UNIVERSIDAD DE CHILE
FACULTAD DE CIENCIAS FÍSICAS Y MATEMÁTICAS
DEPARTAMENTO DE INGENIERÍA ELÉCTRICA

CONTROL OF THE MODULAR MILTILEVEL MATRIX CONVERTER FOR WIND ENERGY CONVERSION SYSTEMS

TESIS PARA OPTAR AL GRADO DE DOCTOR EN INGENIERÍA ELÉCTRICA
TESIS PARA OPTAR AL GRADO DE DOCTOR OF PHILOSOPHY IN ELECTRICAL AND
ELECTRONIC ENGINEERING

MATÍAS DAVID DÍAZ DÍAZ

PROFESOR GUÍA:
ROBERTO CÁRDENAS DOBSON
PATRICK WHEELER

MIEMBROS DE LA COMISIÓN:
DORIS SÁEZ HUEICHAPAN
MARCOS ORCHARD CONCHA
JAVIER PEREDA TORRES
CÉSAR SILVA JIMÉNEZ
PERICLE ZANCHETTA

SANTIAGO DE CHILE
2017

CONTROL OF THE MODULAR MILTILEVEL MATRIX CONVERTER FOR WIND ENERGY CONVERSION SYSTEMS

La potencia nominal de los Sistemas de Conversión de Energía Eólica se ha incrementado constantemente alcanzando niveles de potencia cercanos a los 10 MW. Por tanto, convertidores de potencia de media tensión están reemplazando a los convertidores Back-to-Back de baja tensión habitualmente empleados en la etapa de conversión de energía.

Convertidores Modulares Multinivel se han posicionado como una solución atractiva para Sistemas de Conversión de Energía Eólica de alta potencia debido a sus buenas prestaciones. Algunas de estas prestaciones son la capacidad de alcanzar altos voltajes, modularidad y confiabilidad.

En este contexto, esta tesis discute la aplicación del Convertidor Modular Matricial Multinivel para conectar Sistemas de Conversión de Energía Eólica de alta potencia. Los modelos matemáticos y estrategias de control requeridas para esta aplicación son descritos y discutidos en este documento. Las estrategias de control propuestas habilitan una operación desacoplada del convertidor, proporcionando seguimiento del máximo punto de potencia en el lado del generador eléctrico del sistema eólico, cumplimiento de normas de conexión en el lado de la red eléctrica y regulación de los condensadores flotantes del convertidor.

La efectividad de las estrategias de control propuestas es validada a través de simulaciones y experimentos realizados con un prototipo de laboratorio. Las simulaciones se realizan con un Sistemas de Conversión de Energía Eólica de 10 MW operando a 6.6 kV. Dicho sistema se implementa en el software PLECS. Por otro, se ha desarrollado un prototipo de laboratorio de 6kVA durante el desarrollo de este proyecto.

El prototipo de laboratorio considera un Convertidor Modular Matricial Multinivel de 27 módulos Puente-H . El sistema es controlado empleando una plataforma de control basada en una Digital Signal Processor conectada a tres tarjetas del tipo Field Programmable Gate Array que proveen de 50 mediciones análogo-digital y 108 señales de disparo. La entrada del convertidor es conectada a una fuente programable marca Ametek que emula el comportamiento de la turbina eólica. A su vez, la salida del convertidor es conectada a otra fuente programable con capacidad de producir fallas en la tensión.

Los resultados obtenidos, tanto en el prototipo experimental como en simulación, confirman la operación exitosa del Convertidor Modular Matricial Multinivel en aplicaciones eólicas de alta potencia. En todos los casos, las estrategias de control propuestas aseguran regulación de la tensión en los condensadores flotantes, seguimiento del máximo punto de potencia en el lado del generador eléctrico del sistema eólico y cumplimiento de normas de conexión en el lado de la red eléctrica.

CONTROL OF THE MODULAR MILTILEVEL MATRIX CONVERTER FOR WIND ENERGY CONVERSION SYSTEMS

The nominal power of single Wind Energy Conversion Systems has been steadily growing, reaching power ratings close to 10MW. In the power conversion stage, medium-voltage power converters are replacing the conventional low-voltage back-to-back topology. Modular Multilevel Converters have appeared as a promising solution for Multi-MW WECSs due to their characteristics such as modularity, reliability and the capability to reach high nominal voltages. Thereby, this thesis discusses the application of the Modular Multilevel Matrix Converter (M^3C) to drive Multi-MW Wind Energy Conversion Systems (WECSs).

The modelling and control systems required for this application are extensively analysed and discussed in this document. The proposed control strategies enable decoupled operation of the converter, providing maximum power point tracking capability at the generator-side, grid-code compliance and Low Voltage Ride Through Control at the grid-side and good steady state and dynamic performance for balancing the capacitor voltages of the converter.

The effectiveness of the proposed control strategies is validated through simulations and experimental results. Simulation results are obtained with a 10MW, 6.6 kVM3C based WECS model developed in PLECS software.

Additionally, a 6 kVA downscale prototype has been designed and constructed during this Ph.D. The downscale prototype is composed of 27 H-Bridges power cells. The system is controlled using a Digital Signal Processor connected to three Field Programmable Gate Array which are equipped with 50 analogue-digital channels and 108 gate drive signals. Two programmable AMETEK power supplies emulate the electrical grid and the generator. The wind turbine dynamics is programmed in the generator-side power supply to emulate a generator operating in variable speed/voltage mode. The output port of the M3C is connected to another power source which can generate programmable grid sag-swell conditions.

Simulation and experimental results for variable-speed operation, grid-code compliance, and capacitor voltage regulation have confirmed the successful operation of the M^3C based WECSs. In all the experiments, the proposed control systems ensure proper capacitor voltage balancing, keeping the flying capacitor voltages bounded and with low ripple. Additionally, the performance of the generator-side and grid-side control system have been validated for Maximum Power Point Tracking and Low-Voltage Ride Through, respectively.

Acknowledgements

Contents

List of Tables

List of Figures

CHAPTER 1

Introduction

The economic and social development of modern societies is linked to the accessibility of energy sources. In recent decades, energy consumption supplied mainly by fossil combustibles has been steadily growing. The relatively low cost of converting fossil combustibles to electrical energy means that most countries, both industrialised and developing countries, use fossil fuels as their main source of energy. However, two major problems arise from the use of fossil combustibles. Firstly, natural resources are limited and non-renewable. Therefore, combustible fossil production will struggle to fulfil global energy requirements in the next decades. Secondly, burning fossil fuels to obtain energy produces greenhouse gasses, i.e. carbon dioxide, and waste of water. While carbon dioxide is a natural greenhouse gas, high emissions in the atmosphere have been proven to cause global warming, with consequences such as irregular patterns in climate, the rise of sea levels, reduced food production, increased storm damage, among others [1].

This shortfall in energy generation, combined with environmental concerns about global warming, has resulted in the need for a new paradigm to fulfil the energy needs of our society. In this context, renewable energy sources emerge as a possible answer to the issue of limited fossil fuels and their impact on the environment. Renewable Energy sources are clean, unlimited, and progressively economically competitive forms of energy. However, problems associated with the intermittent nature of many renewable energy sources imposes demanding technical challenges to consistently and reliably meet electric demand. Furthermore, Renewable Energy sources such as the wind, sun and water, have a potential for use anywhere and do not produce greenhouse gasses.

Growth in clean energy is continuous, as reflected in statistics from past years. In 2012, renewable sources represented around 13.2% of the total world energy supply [2]. In 2013 Renewable Energies accounted for almost 22% of global electricity generation, and the International Energy Agency predicts that they should be able to supply at least 26% in 2020. By 2015, the total worldwide power installed capacity reached 1.865 GW [3].

1

GLOBAL CUMULATIVE INSTALLED WIND CAPACITY 2000-2015
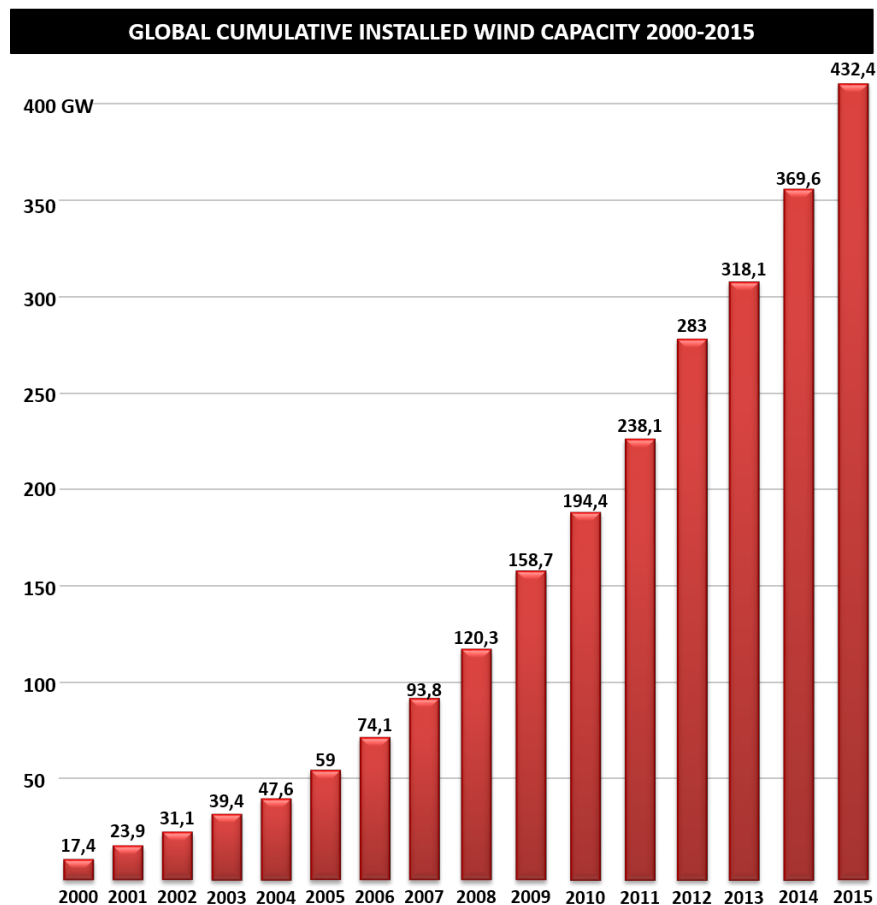
Figure 1.1: Global Cumulative Installed Wind Capacity.

Among all renewable energy sources, wind energy has presented the biggest and fastest growth. The wind power production capacity for the whole world increased from 17.4 GW in 2000 to 432.4 GW in 2015 [4], as shown in Fig.1.1, positioning wind power as a significant and crucial energy source in areas such as Europe, China, and the USA. Powered by 30,5 GW of new installations in China, the global wind power installed in 2015 was 63 GW, representing annual market growth of 22% [5]. A constant increase in wind power capacity is predictable in the immediate future. The European Wind Energy Association (EWEA) plan for the coming years is to make the wind industry the most competitive energy source, onshore by 2020 and offshore by 2030 [6]. EWEA has stated that "wind power would be capable of contributing up to 20% of European Union electricity by 2020, 30% by 2030 and 50% by 2050". Reaching this ambitious plan for wind energy would require a total of 600 GW of wind power capacity, 250 GW would be onshore and 350 GW offshore. Assuming a total electricity demand of 4,000 TWh by 2050, the 600GW of wind power capacity could generate about 2.000 TWh, reaching 50% of the electricity demand of the European Union [7].

When the penetration of Wind Energy is high, its intermittent nature may have a significant influence on the stability of power systems. Therefore, stringent grid codes have been enforced recently, which encompass active power control to support the grid frequency, reactive power control to support the grid voltage, power quality, power controllability, and Fault Ride Through (FRT) capability. FRT requirements regulate the behaviour under Low-Voltage Ride-Through(LVRT), and
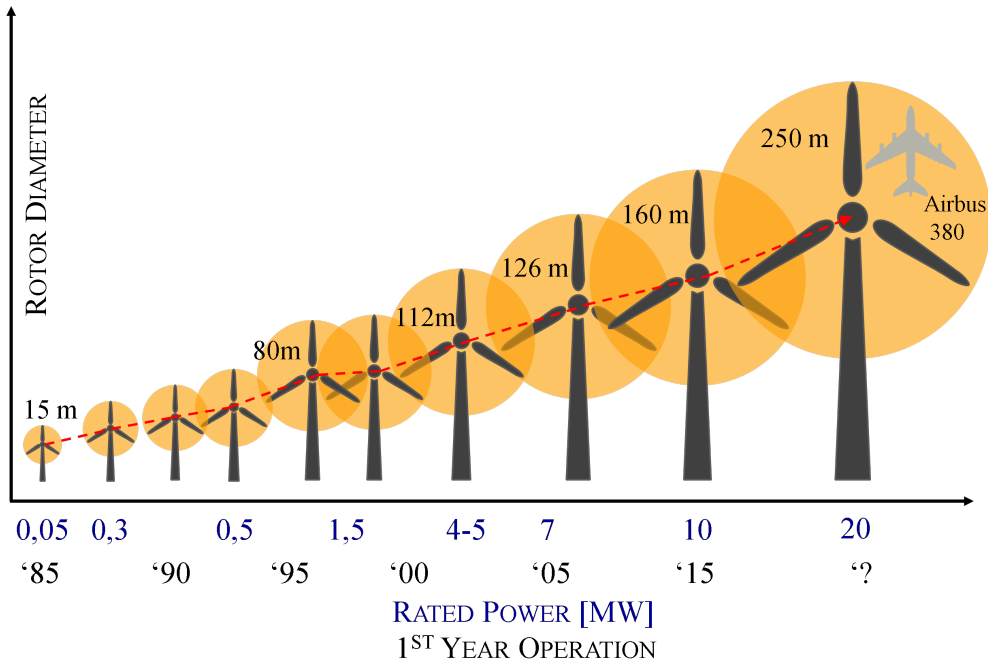
Figure 1.2: Proposed topology to drive Multi-MW Wind Turbines.

High-Voltage Ride Through (HVRT) grid voltage conditions and probably represent the primary concern for wind turbine and power converter manufacturers since grid voltage sag-swell are the most common disturbances present in electrical power systems.

Due to the presence of higher wind power potential and lower environmental impact, some of the future wind power capacity will be installed offshore. For offshore applications, up-scaling wind turbine dimensions, wind park capacities, and electrical infrastructure has become the focus of recent research, because wind turbines output power is related to the cube of wind speed and the square of the rotor diameter. Large Wind Turbines can capture more power with lower installations compared to a group of small wind turbines, and reduce the structure cost of offshore Wind Energy Conversion Systems (WECSs). Owing to this fact, wind turbine nominal powers and rotor diameters have increased approximately to 10MW-160m in 2015, as shown in Fig.1.2 [8, 9]. The largest wind turbine in 2014 was the 8MW Vestas V164, with a rotor diameter of 164 m, currently operating in Denmark.

The new generation of WECSs will substantially increase the power range, reaching power ratios above 10 MW. Manufacturers such as Sway and Windtec are already developing offshore wind turbines rated at 10 MW [10–12]. Additionally, there are projects under study to develop wind turbines up to 20 MW [13].

Despite the trend of Multi-MW Wind Turbines, most of the installed WECSs are based on low-voltage power converters, usually equipped with 1700V Isolated Gate Bipolar Transistor (IGBT) devices for connection to low-voltage networks [8, 9]. The continuous increase in wind turbine power ratings generates larger line current if the low-voltage power converter technology is used. This fact implies several disadvantages, such as high copper losses, low power density, high cable costs and the requirement of step-up transformers before the connection to the grid [9].

3
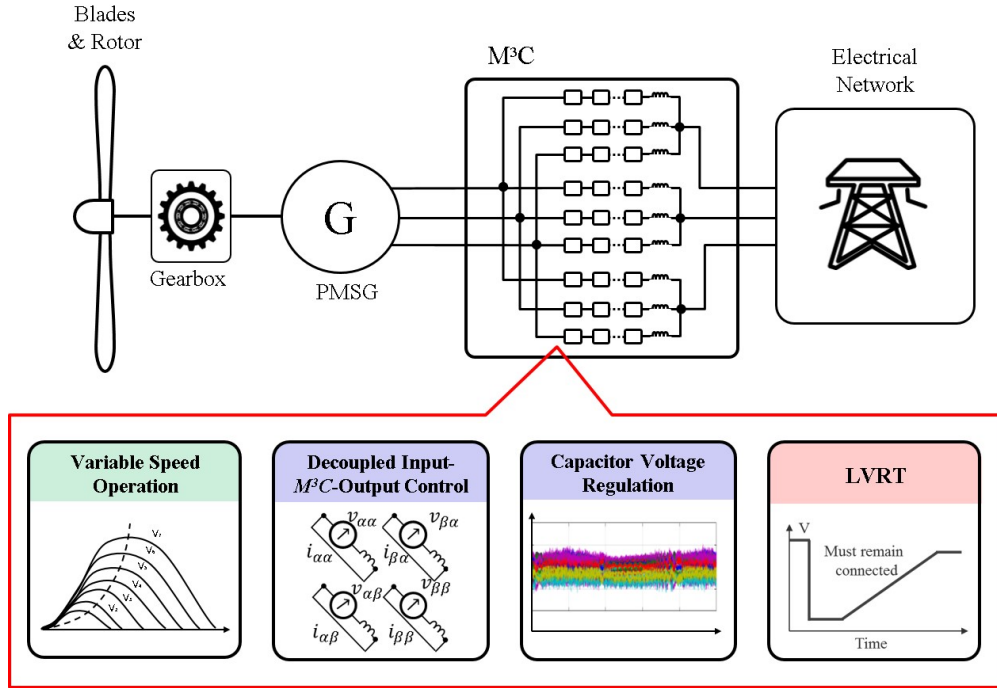
Figure 1.3: Proposed topology to drive Multi-MW Wind Turbines.

Accordingly, wind turbine manufacturers have been incorporating medium-voltage (MV) converters to WECSs above 3 MW because it has been proved that MV operation leads to a decreased energy production cost [14]. In MV applications, Multilevel Converters are an enabling technology which has been extensively validated for drive applications. Recently, the application of these topologies has been introduced in WECSs. For instance, the Neutral-Point Clamped (NPC) converter has become the preferred option for WECS applications above 3 MW [15–17]. However, its implementation can be restricted for offshore applications because of the uneven power losses distribution among the semiconductors and the low reliability of the converter that is particularly important for offshore applications [18].

In addition to traditional multilevel converters, many new converters have been proposed in the literature. The works in [19–21] propose the use of Modular Multilevel Cascade Converters (MMCCs) as a promising solution for Multi-MW WECS. In these topologies, the voltage level can be easily scaled up by cascading more converter cells, reaching voltages in MV range and power ratios beyond 10MW. Besides to the capability to handle higher voltage levels, MMCCs have advantages compared to low-voltage topologies, such as transformer-less capability, lower harmonic distortion of the output voltages, lower switching losses, reduced electromagnetic interference, etc. This converter family has been widely applied in High Voltage Direct Current (HVDC) power transmission [22–25]. Nevertheless, the application of MMCC topologies to drive variable-speed high-power machines have been barely investigated [26].

Multi-MW WECSs should feature power electronic converter capable of ac-ac conversion, MV operation, variable-speed operation, grid code compliance, etc. Consequently, the most well-suited topologies among the MMCC family to fulfil these requirements are the Modular Multilevel Converter (M^2C)in Back-to-Back configuration, the Hexverter and the Modular Multilevel Matrix Converter (M^3C). Technological challenges associated with reliability, efficiency, control com-

plexity and the problem of balancing the flying capacitors have to be solved to enforce the use of MMCCs in Multi-MW WECSs.

In this context, this PhD project is aimed to investigate the application the M^3C in Multi-MW WECSs. This converter is interfaced between the wind turbine generator and the grid, as shown in Fig. 1.3. The M^3C based WECSs must be capable of variable-speed operation, capacitor voltage regulation and fulfilment of grid codes such as LVRT.

1.1   Project Hypotheses

The following hypotheses are stated for this research project:

- The M^3C could be used to drive Multi-MW WECSs providing Medium or High Voltage operation, variable speed operation and grid-code fulfilment.

- The mathematical representation of the M^3C can be extended to implement control strategies that enable the operation of the converter in a broad range of input-output frequencies.

- Owing to the variable-speed nature of WECSs, the control system of the M^3C must have adaptive capabilities. Thereby, the use of adaptive resonant controllers or dq transformations could enhance the performance of the whole system.

- Control methodologies could be developed to regulate the flying capacitors of the converter regardless to the input/output frequencies and without affecting the input/output currents and voltages.

- The voltages and currents of the system connected to the input of the M^3C should be regulated to provide variable-speed operation and Maximum Power Point Tracking (MPPT). Whereas, the voltages and currents of the system connected to the output of the M^3C should be regulated to provide grid-connected operation and grid-code fulfilment.

- Closed-loop control methodologies can be developed to enable the operation of the M^3C when the input frequency is close or equal to the output frequency. In this case, the oscillations in the flying capacitors should be bounded inside and acceptable margin.

1.2   Project Objectives

This Ph.D. research project aims to investigate the operation of the Modular Multilevel Matrix Converter for integration of Multi-MW WECSs. The research described in this thesis pursues to accomplish the following objectives:

- To develop a complete model of the M^3C, considering a decoupled representation of the input, converter and output dynamics.

- To propose control methodologies to allow the operation of the M^3C in variable-speed Multi-MW WECS applications.

- To design and implement a downscale prototype to validate the proposed control strategies for Multi-MW M^3C based WECS in a experimental rig.

1.3   Contributions

The contributions of this work can be summarised as follows:

- A comprehensive model to describe the dynamics of the M^3C is developed in this work. Using this model, a decoupled representation of the dynamics of the capacitor voltages, input and output port voltages and currents is obtained. Furthermore, the model enables the use of the circulating currents and common-mode voltage as degrees of freedom to regulate the operation of the M^3C without affecting the input and output ports.

- A decoupled input/output control for an M^3C based WECS is proposed and thoroughly analysed in this thesis. Similar to the operation of Back-to-Back converters for WECS applications, where the presence of a DC-link allows decoupled control of the AC-DC-AC conversion stages, the control strategies proposed in this thesis enable a decoupled operation of the generator and grid connected to the converter terminals.

- Two control strategies are proposed to regulate the energy balancing of the M^3C for variable-speed applications. The first control proposal, called Scalar Cluster Capacitor Voltage Control, is suitable for Low-Frequency applications. On the other hand, the second control proposal, called Vector Cluster Capacitor Voltage Control, is more appropriate for a broad range of frequencies, including equal input-output frequencies, operation.

- Both control strategies are complemented WECS features. The input-side control system is designed to operate in variable-speed performing MPPT, whereas the output-side control system is designed to provide grid-connected operation and fulfilment of grid-code requirements.

- An enhanced Low Voltage Ride Through (LVRT) algorithm is proposed. This algorithm enables the operation of the converter under symmetrical and unsymmetrical grid voltage sags and can support the grid voltage during the faults through the injection of reactive power.

- Experimental validation of the proposed control schemes is provided, including variable-speed operation, grid code compliance, and regulation of the capacitor voltages. In all the cases, the proposed control structures perform excellent steady-state and transient response.

- To the best of this author knowledge, this is the first research work where LVRT control strategies for M^3C based WECSs (see Fig. 1.3) are discussed, analysed and experimentally validated.

1.4 Thesis Structure

The rest of this work is divided into eight Chapters as follows:

- Chapter 2: A summary of power converters and grid-codes for grid-connected operation of Multi-MW WECSs is presented. Additionally, an overview of MMMC topologies, with attention on the M^3C topology, is addressed in this Chapter.

- Chapter 3: Once the state of the art of the requirements for Multi-MW WECSs and control systems for the M^3C have been presented, the proposal of a new vector model to represent the dynamics of the M^3C is detailed in this Chapter. This vector model is particularly useful to analyse the dynamics of the M^3C in variable-speed applications. Moreover, it enables the identification of the of the degrees of freedom of the converter to control the capacitor voltage oscillations in a broad range of operation frequencies.

- Chapter 4: Two different control systems are proposed for the regulation of the M^3C capacitor voltages. A decoupled representation of the M^3C is used in both cases as a starting point. The first control proposal, called Scalar Control Strategy, could be used for low-frequency operation at the generator-side. The second control proposal, called Vector Control Strategy, is implemented in dq synchronous frames allows operation in a broad range of frequencies, including equal input-output operation frequencies.

- Chapter 5: The generator and grid side control systems are described in this Chapter. The generator-side control system provides variable-speed operation and MPPT. A brief revision of Fault Ride Through (FRT) requirements for grid-connected WECSs is included to bound the requirements for the implementation of LVRT control systems. Grid currents and voltages have to be separated into positive and negative sequence components to perform LVRT control systems. Therefore, a novel fast sequence separation method is proposed and described in this Chapter. Furthermore, a new LVRT control system is introduced for M^3C based WECSs.

- Chapter 6: The simulation validation of the proposed control strategy is presented in this Chapter. A set of simulation tests for variable-speed operation, capacitor voltage balancing, ride through of the unstable operational points and the fulfilment of LVRT requirements are included.

- Chapter 7: This Chapterdescribes the design and construction of an experimental prototype composed of 27 power-cells. The capabilities and characteristics of the control platform, power stage and power sources used to emulated the generator/grid systems are detailed.

- Chapter 8: The experimental validation of the proposed control strategies is presented in this Chapter. A set of experimental tests for variable-speed operation, capacitor voltage balancing, ride through of the unstable operational points, and the fulfilment of LVRT requirements are included.

- Chapter9: The conclusions of this Ph.D. Project and an outlook to the future research on this topic are presented in this section.

CHAPTER 2

State of the art of Power Electronics for Multi-MW WECSs

2.1 Introduction

In this Chapteran extensive review of the state of the art of Multi-MW WECSs is presented. The major components of WECSs, the most recent issues regarding control flexibility and new requirements for grid-connected WECSs are detailed. Accordingly to recent literature, the generator-converter WECSs configurations are classified into four categories and compared based on components number, power converter control complexity, modularity, reliability and operating voltage level.

This Chapteralso provides an overview of existing power electronic converters in WECSs. A particular focus is devoted to those that have the potential for Multi-MW applications. At the end of this Chapter. The latest contributions on Modular Multilevel Converter Topologies are reviewed to introduce a new and promising WECSs based on MMCs.

2.2 Wind Energy Conversion Systems

The development of wind energy conversion technology has evolved significantly through the last decades due to continuous technological advancements aimed to enhance efficiency and reliability. Hence, several new WECS have been emerging since the introduction of the early fixed speed WECSs, which was directly connected to the grid. Nowadays, variable speed WECSs based on power electronic converters are the most popular systems in the wind energy market [9]. The basic configuration of WECSs considers the interaction of mechanical and electrical subsystems, as shown in Fig.2.1. Mechanical components include the tower, nacelle, blades, gearbox, etc. Currently, the three-bladed design is the most efficient and common rotor blade configuration in wind turbines.

The rotor blades capture kinetic energy from the wind and convert it into mechanical energy. The kinetic to mechanical energy conversion has a mechanical limiter which operates in the case of high wind speeds. When the wind speed is above its nominal value, the angle of blades is changed to limit the power captured from the wind. Multi-MW WECSs usually rotate at very low rotational speed and high torque. Therefore, a gearbox is required to increase the low rotational speed of the blade-side to the higher speed required by the electric generator. Gearboxes are one of the most expensive components, counting by itself for about 13% of the overall cost of WECSs [27]. Additionally, they present several drawbacks, such as reduced life span, reduced efficiency, high noise, and the need of periodical maintenance. Matching the speed of the generator with the speed of the blade-side results in the elimination of the gearbox and its drawbacks. Direct-drive or gearless WECSs using multipole generators seems to be a promising configuration for many wind turbine manufacturers [8, 9, 28].

The subsequent step is the conversion of the mechanical energy into electrical energy. The generators conventionally used in WECSs to perform this task are the Squirrel-Cage Induction Generator (SCIG), the Wound Rotor Induction Generator (WRIG), the Doubly Fed Induction Generator (DFIG) and the Permanent Magnet Synchronous Generator (PMSG). The SCIG was extensively used in the first generation of fixed-speed WECSs. Nowadays, the penetration of SCIGs into wind energy generator market is low due to the fact that two full-power converters are required for the operation of this machine and that a multipole direct-drive operation is not technically feasible. In contrast, the DFIG uses a reduced-size power converter rated to a 30% of the machine nominal power to provide limited variable-speed operation. In fact, DFIG is one of the most popular generators for WECSs, representing almost the 50% of wind energy generator market. However, neither SCIG nor DFIG can be used in direct-drive WECSs because low-speed multipole DFIG or SCIG are not technically feasible. On the contrast, multipole PMSGs are feasible and appear to be the configuration to be adopted by most of the large wind turbine manufacturers shortly, gradually replacing the DFIG as the main generator in the wind-energy market [29].
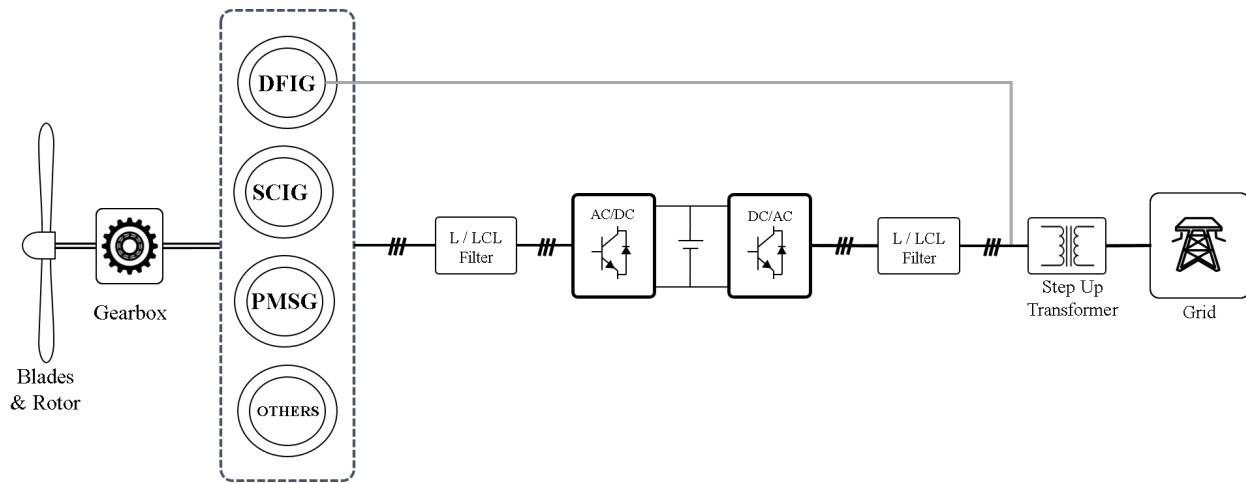
Figure 2.1: WECS main components and control issues.

2.2.1 Topologies

The major electrical components in WECS are the generator and the power electronic converter. Different designs and combinations of generators and power electronic converters yields to a wide variety of WECS configurations, which can be classified as [8, 9, 28]:

- Type I: Fixed-speed WECS with SCIG.

- Type II: Limited-Variable speed WECS with WRIG.

- Type III: Limited-Variable speed WECS with DFIG.

- Type IV: Full-Variable speed WECS.

The above four configurations have been analyzed, documented and commercialized extensively over the past decades. A brief description of each of them is presented in following subsections.

2.2.1.1 Type I: Fixed-speed WECS

A fixed-speed SCIG based WECS is shown in Fig.2.2. This type of WECS, also known as the Danish concept, has been widely used in the first generation of wind turbines since 1990 [30, 31]. As the name suggest, the SCIG operates at constant rotor speed, varying within 2-3% of the synchronous speed at different wind speeds. The rotor of the SCIG is connected to the wind turbine through a fixed ratio gearbox while the stator is connected directly to the grid using a step-up transformer. A soft-starter is usually included during the start-up procedure. As the SCIG draws reactive power from the grid, a shunt capacitor bank is usually installed at its terminals [32]. This configuration is simple, robust and has low initial costs. However, several drawbacks restrict its use, such as: fluctuating output power as the wind speed variates, grid faults cause stress in the mechanical components of the wind turbine, low wind energy conversion efficiency, and an additional power converter is required to fulfill grid codes [9]. The technology status of this configuration is outdated due to its drawbacks. However, some commercial solutions in MW range,

such as Siemens CombiStall 2.3-2.3MW or Bonus 82-2.3MW (now Siemens), could still be found in operation [33].
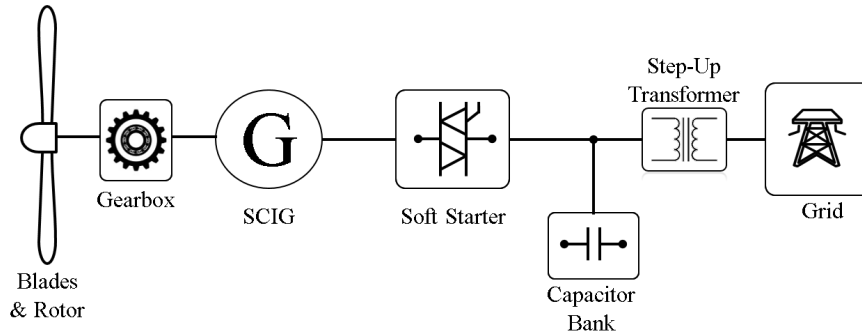
Figure 2.2: Type I WECS.

2.2.1.2 Type II: Limited-Variable speed WECS with WRIG

A Limited-Variable WRIG based WECS is shown Fig.2.3. Similar to fixed-speed SCIG based WECSs, the rotor of the WRIG is connected to the wind turbine through a fixed ratio gearbox, whereas the stator is connected directly to the grid using a step-up transformer. The use of soft-starters and shunt capacitor banks is considered to perform the same role than before [34]. This configuration uses a partially rated power converter to change the rotor resistance, affecting the torque-speed characteristic of the generator to enable a speed adjustment about 10% of its rated speed [35]. This partially rated power converter is composed of a diode rectifier and a chopper. In comparison with Type I WECSs, limited-Variable speed WRIG based WECSs capture more energy from the wind, have a better power quality and reduced mechanical drive-train stresses. The main drawback is that this topology also increases energy losses in the rotor resistance. A few examples of this configuration are the commercial wind turbines Tacke TW 1.5-1.5MW (now Siemens), Vestas V80-1.8MW and Gamesa G80-1.8MW [33].
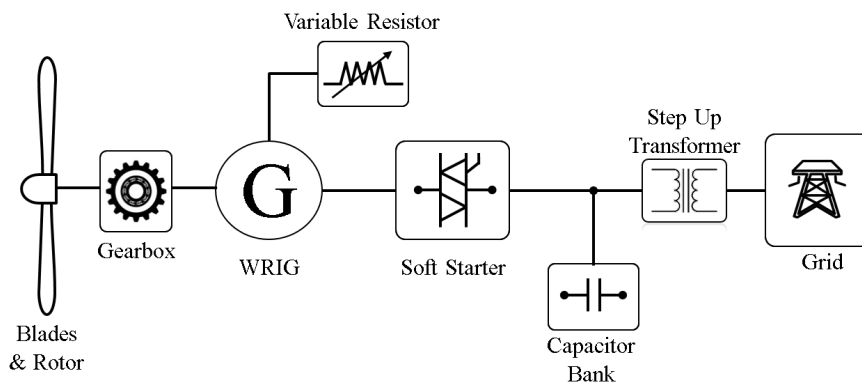
Figure 2.3: Type II WECS.
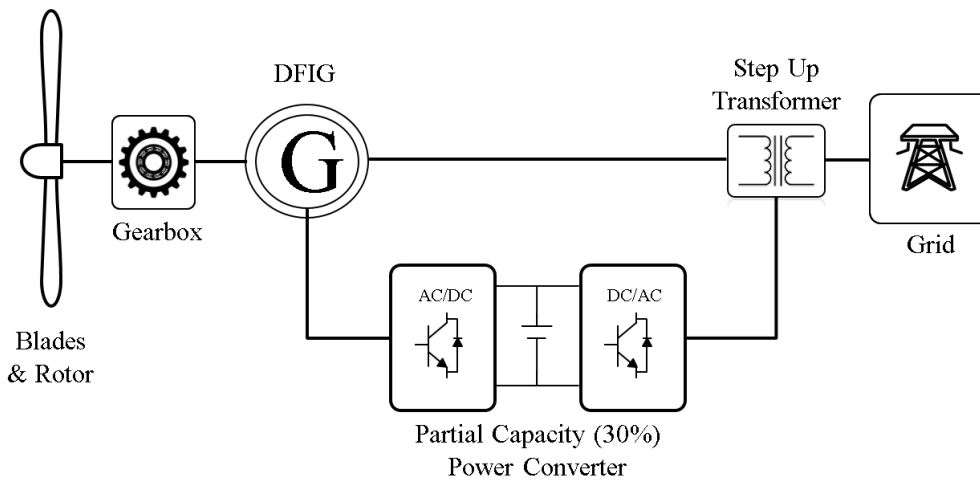
Figure 2.4: Type III WECS with DFIG.

2.2.1.3 Type III: Limited-Variable speed WECS with DFIG

A Limited-Variable DFIG based WECS is shown in Fig.2.4. As the name suggest, the power from the generator is injected into the grid through stator and rotor windings. The rotor is connected to the grid through a partially rated power converter (usually 30% of the nominal power), which is one of the major advantages of this topology [36], [37]. Similar to Type I and Type II WECSs, a gearbox is required to match the wind turbine and generator speeds because multipole DFIG are not technically feasible without oversizing the generator.

The use of partial power converters, usually low-voltage back-to-back converters, allows bidirectional power flow in the rotor and increase the speed adjustment up to about $\pm$ 30% of its synchronous speed. The variable-speed regulation is used to optimise the power extraction from the wind, which is known as maximum power point tracking (MPPT). Moreover, the possibility of controlling the active and reactive power flows gives to this system spining reserve capability on the grid. In comparison with Type I and Type II WECSs, this configuration features higher wind energy conversion efficiency, improved dynamic performance, enhanced disturbance ride-through capability [28, 31].

The characteristic mentioned above make the DFIG based WECS one of the most important generators for wind energy applications. Nowadays, this configuration has a market share of approximately 50% [29]. Table 2.1 shows some of the commercially available WECSs, with a power level in the range of 1.5–3 MW. According to [29], there were 93 models of WECSs based on DFIGs for that power range by 2013. DFIGs are also used in higher power ranges (> 3 MW). For instance, a 7.5 MW model is being developed by Enercon and Repower has two models above 5MW (the model 5M with a total output power of 5 MW and the model 6M with a total output power of 6.150 MW) [33].

As the stator is directly connected to the grid, relatively high currents may be produced in the stator windings under grid faults conditions. Therefore, the capacity of this topology to stay grid-connected in the presence of unbalance voltage conditions or faults is limited. Fault handling components, such as crowbars, are needed to limit to a safe level the currents and voltages in

the rotor circuit [21]. Moreover, DFIG requires regular maintenance due to the power converter is connected to the rotor through slip rings and brushes. Then, the difficulties associated with fulfilling fault ride-through requirements and the need of continuous maintenance, are the major drawbacks that restrict the use of DFIG in future MW-WECSs and off-shore applications [29].

2.2.1.4   Type IV: Full-variable speed WECS

A Full-Variable speed WECS is shown in Fig. 2.5. Several generators can be utilised in this configuration, such as SCIG and Synchronous generators either externally excited or with permanent magnets [38]. Since the power converter and generator are rated at the same level, the generator is fully decoupled from the grid and can operate at full variable speed (0 to 100%). The power converter, usually low-voltage back-to-back converter, has to satisfy the requirements of the generator and the grid. The generator-side converter controls the machine torque current to regulate the rotational speed. Moreover, this converter should handle variable voltage-frequency and perform MPPT [38]. On the other hand, the grid-side converter has as main functions to perform grid-connected operation, power factor regulation and fulfillment of grid codes [39].

In this configuration, the gearbox can be dispensed (usually referred to as direct-drive or gearless technology) using generators with a high number of poles. The multipole capability of PMSG helps to overcome the problems associated to the gearbox (high cost, reduced life span, reduced efficiency and the need for maintenance) [27]. Therefore, multipole PMSGs are becoming the preferred technology for high-power wind turbines manufacturers, especially for offshore applications where the increased reliability and elimination of possible oil spills from the gearbox is another advantage [18, 40].

In comparison with Type I to Type III WECSs, this configuration features the highest conversion efficiency and the best Faut Ride Through (FRT) performance [41–43] when PMSGs are considered. Additionally, PMSG based Type IV WECSs have gearless capability and enhanced power density. Due to its advantages, multipole PMSG based WECS with full power converter seems to be the most promising WECS topology for the foreseeable future [8, 9, 28].

Table 2.1 presents a list of some wind turbines available in the market which features PMSG. These wind turbines reach a range of power up to Multi-MW. Additionally, this topology could be
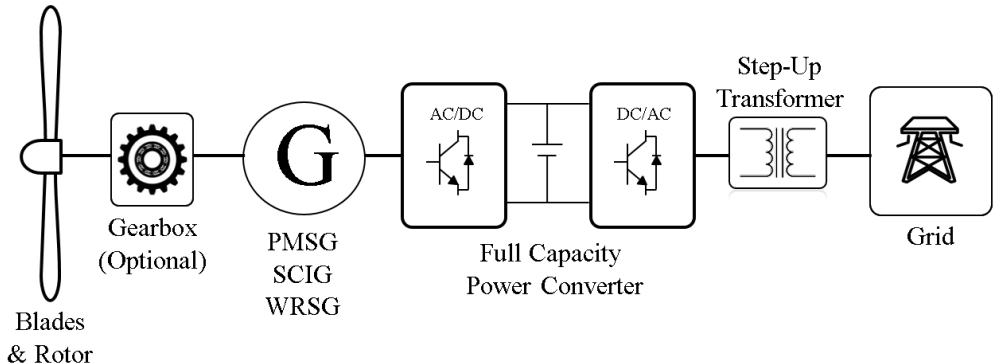
Figure 2.5: Type IV WECS.

DFIG based WECS manufacturers			PMSG based WECSs manufacturers		
Manufacturer	Model	Power Range	Manufacturer	Model	Power Range
AAER	A1500	1.5 MW	Mitsubishi	MWT-1000	1.0 MW
Mingyang	MY1.5	1.5 MW	WindTec	WT	1.65MW
Sinovel	SL 1500	1.5 MW	Dewind	D9.2	2.0 MW
Acciona	AW	1.5/3.0 MW	Unison	U113	2.3 MW
Alstom Power	ECO	1.67/3.0 MW	Avantis	AV 928	2.5 MW
Vestas	V80-V90-V100	1.8-3.0 MW	Goldwind	GW 121	2.5 MW
Dewind	D8.0-D9.0	2.0 MW	Vensys	120	3.0 MW
Gamesa	G114	2.0 MW	WindWind	WWD	3.0MW
Goudian United	UP96	2.0 MW	Vestas	V112.3	3MW
Hyosung	HS-90	2.0 MW	General Electric	4.0-110	4.0 MW
Suzlon	S97	2.1 MW	Gamesa	G128	4.5 MW
Mitsubishi	MWT-2400	2.4 MW	Alstom Power	Haliade 150	6.0 MW
Nordex	N80/2500	2.5 MW	Mingyang	MY6.0	6.0 MW
General Electric	2.85-100	2.8750 MW	Nordex	N150/6000	6.0 MW
United Power	UP6000	6.0 MW	Enercon	E126	7.5 M

Table 2.1: Summary of commercially available DFIG and PMSG based WECSs [10].

designed to reach 10 MW and above. For instance, there are three 10 MW models under development. American manufacturer Clipper is working on 10 MW PMSG based WECS using a two stage gearbox model [33]. Whereas, Norwegian manufacturer Sway and American manufacturer WindTec are developing 10 MW models based on direct-drive PMSG WECSs [11, 12].
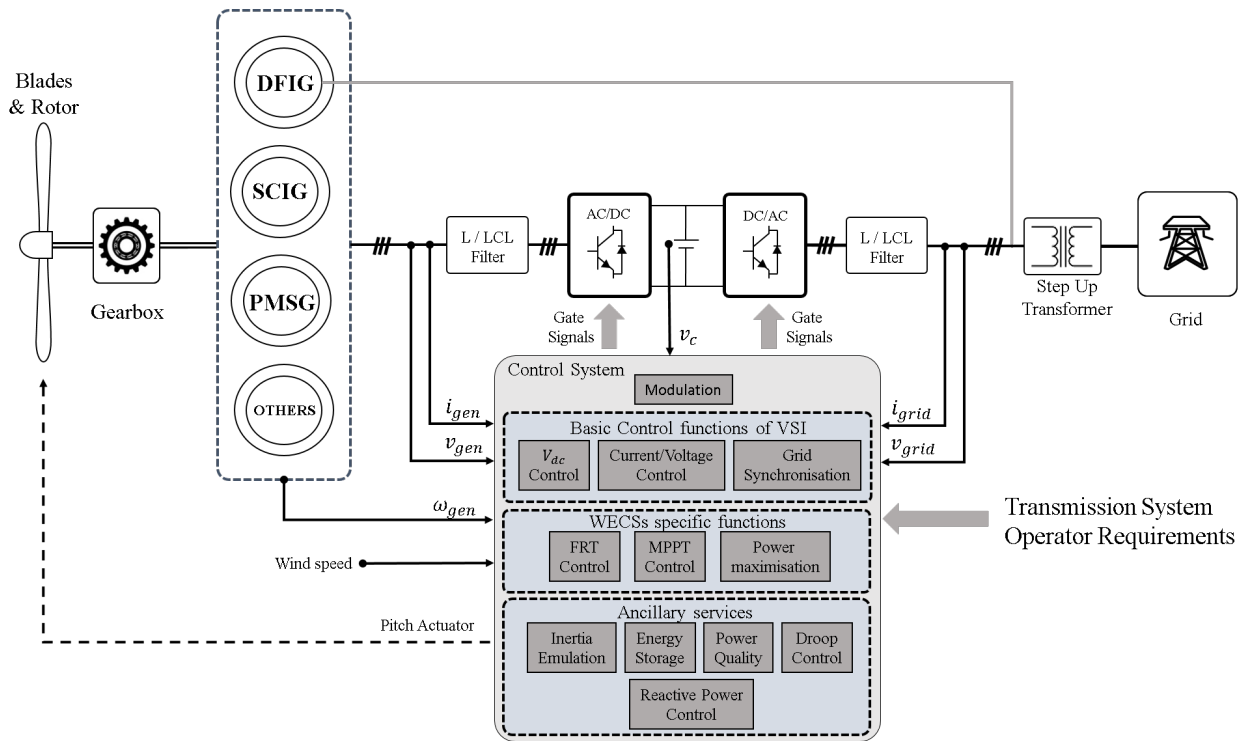
Figure 2.6: WECSs main control functions.

2.2.2 Control of WECSs

Wind Turbine control systems are aimed to achieve efficient dynamic and steady state performance. Several variables, such as wind speed, wind direction, grid voltages and currents, generator voltages and currents, are measured to adjust the system operational point to the desired references. Initially, WECS control systems had very limited functions. Nowadays, they perform a significant number of functions in terms of control flexibility and new grid-code requirements for WECSs, as shown in Fig.2.6 [8, 9, 28].

2.2.2.1 Mechanical Control

Mechanical control systems, such as passive stall, active stall or pitch control, are responsible for the power limitation of the maximum power capture and the reduction of acoustical noise. Type III and Type IV WECSs have incorporated Pitch-Angle Control, which consists of pitching the turbine blades to limit the power extracted from the wind when the wind speed increases beyond the design value. This action reduces mechanical stress on the wind turbine and the drive train. Moreover, MPPT is performed to extract the maximum possible power corresponding to a given wind speed. Then, the generator torque is controlled to track the maximum power point across a broad range of wind speeds [8, 28].

15

2.2.2.2 Electrical Control

The control of the electrical components includes a first control stage to guarantee proper operation of the power converter and generator. In this stage, current-voltage control loops, dc-link control, and grid synchronisation are the main concerns. A second control stage includes WECS specific functions such as maximum power point tracking and grid fault ride-through. A third stage includes functions to contribute to the grid stability and power quality. All these features are illustrated in Fig.2.6.

- Generator-side Control: In both Type III and Type IV WECSs, the turbine speed control is performed by the generator-side converter to maximise the power extracted from the wind, and by the pitch angle controller to limit the power extracted from the wind during periods of high wind speed. Additionally, the reactive power output is controlled in accordance with the generator requirements. In DFIG based WECSs, the active and reactive power reference set the rotor current references, which in turn determines the rotor voltage to be synthesised by the generator-side converter so that the control objectives are fulfilled [29]. In PMSG based WECSs, the active and reactive power references set the stator current references, which in turn determines the stator voltage to be synthesised by the generator-side converter so that the control objectives are fulfilled [39].

- Grid-side Control: The main tasks of the grid-side control are to regulate the DC-Link voltage at the desired value and to perform decoupled control of active and reactive power in steady state and also during grid faults. Using a rotating reference frame, the DC-Link controller commands the direct current, and the reactive power reference commands the quadrature current. Therefore, full control over the output power factor is easily achieved. Moreover, the systems have to be controlled to fulfill stringent grid codes during grid faults [41–43].

2.2.2.3 Grid Codes

In countries with a high penetration of renewable energies, dedicated grid code regulations have been enforced to ensure the proper operation of the electrical networks. These grid codes have focused on power quality, power controllability, and FRT capability. Moreover, in some grid codes, requirements for ancillary services during a network disturbance are stated. For instance, WECSs must be part of primary and secondary frequency control and supply reactive power to the grid. Comprehensive reviews of international grid code requirements for connection of wind turbines to generation and transmission systems are presented in [27, 44]. A summary of these requirements is presented in Table 2.2.

All existing grid codes require fault ride-through capabilities for wind turbines. FRT requirements set the behavior under Low-Voltage Ride-Through (LVRT) and High-Voltage Ride Through (HVRT) conditions. The main concern of wind turbine manufacturers is the LVRT capability of grid connected power converters due to voltage sags conditions are the most common fault in electrical power system. According to recent surveys [45, 46], grid-voltage sags represent 92% of all disturbances into the grid. Moreover, 88% of voltage sags are asymmetrical [46].

FRT requirements from different national grid codes are slightly different in their specifications

Voltage Level	Country	Duration [ms]	Voltage drop level	Recovery time [s]	Voltage profiles	Reactive current support
Distribution/Transmission	Great Britain	140	15%	1,2	Generic	No
Transmission	Spain	500	20%	1	Generic	Up to 100%
> 35 KV	Italy	500	20%	0,3	Generic	No
Transmission	USA	625	15%	2,3	Generic	No
Distribution	Denmark	100	25%	1	2, 3 phase	No
Transmission	Denmark	100	25%	1	1, 2, 3 phase	No
Distribution/Transmission	Ireland	625	15%	3	1, 2, 3 phase	Yes
Distribution/Transmission	Germany	150	0%	1,5	Generic	No

Table 2.2: Summary of Grid Codes from different countries [27,44].
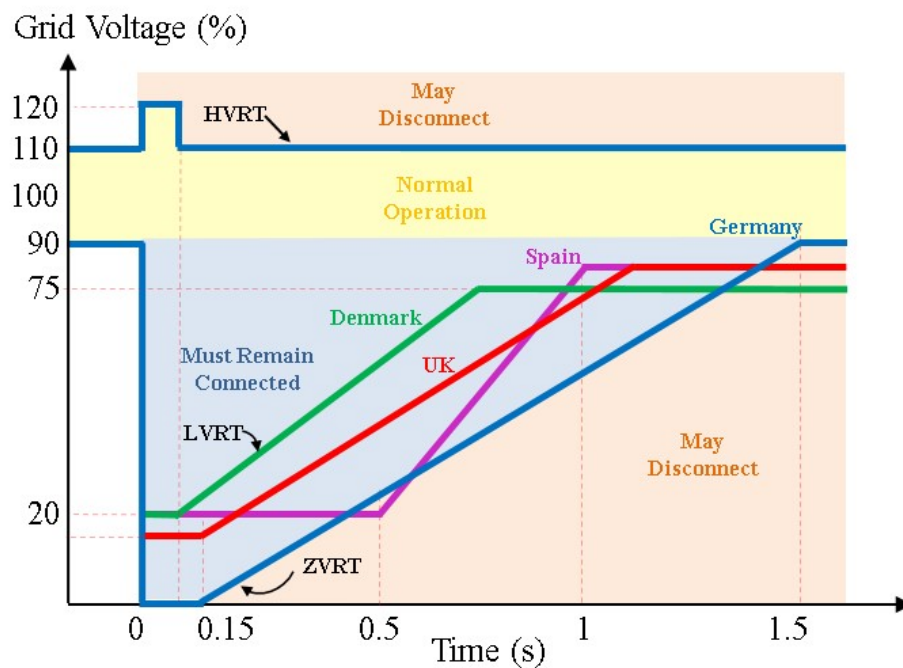
Figure 2.7: LVRT from different countries.

17
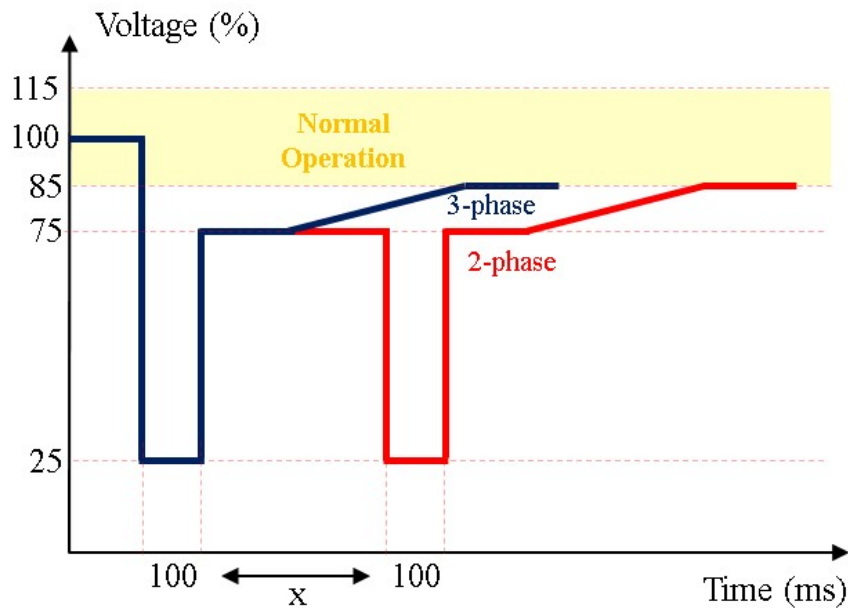
Figure 2.8: LVRT requirements for WECSs connected to the Distribution System in Denmark.

for type, magnitude, and duration of grid-voltage disturbances. Transmission System Operators demand to wind farms to remain connected in the presence of grid voltage sags when the grid voltage is within the specified boundaries of Fig.2.7. Moreover, during the voltage dip, the reactive power control must be changed from normal operation –typically unitary power factor– to a maximum voltage support during grid sags. WECSs must be able to provide full rated reactive power to help to re-establish the normal grid voltage as soon as possible. Some particular situations, when WECs must not be disconnected from the grid, are also specified in [27]. For example, WECSs must be able to remain connected to the grid, in the following cases:

- A 3-phase short-circuit for 100ms.

- A 2-phase short-circuit −with or without ground− for 100ms followed after 300-500ms by a new short-circuit of 100ms duration.

An example of these special conditions is given for the Danish grid-code in Fig.2.8.

2.2.2.4   Other requirements for WECSs

As mentioned before, WECSs perform a significant number of functions in terms of control flexibility and new requirements for grid-connected operation. As Type III and Type IV WECSs are equipped with a power converter to interface the wind turbine with the grid, a broad range of ancillary services can be provided controlling the power converter. Several strategies can be found which enable wind turbines to provide ancillary services [47–53]. The most significant trends are related to the energy storage capability of WECSs to provide grid frequency support. Some of them are briefly explained next:

- Inertia Emulation: the kinetic energy stored in the wind-turbine rotating mass can be used to provide an additional power to the grid in case of frequency variation. When the frequency decreases, the power reference of the WECS is increased by lowering kinetic energy from the rotor. In this way, the power output of the WECSs is temporarily increased and an inertial response is obtained [47, 48] .

- Droop Control: Along with the inertia emulation, usually referred to as synthetic inertia since it resembles the behavior of a synchronous machine in case of a frequency dip, some publications suggest to control the WECS to maintain a reserve of the active power, i.e. regulating the pitch angle to avoid extracting the maximum power from the wind. The frequency regulation is accomplished by regulating the wind-generator electrical torque using this power reserve. However, the droop control counteracts the control action of the MPPT and operates the WECSs at a suboptimal power point during steady state [49].

- Energy Storage Systems: Several energy storage technologies, such as supercapacitors, flywheels, batteries, etc., have been proposed for WECSs [50, 51]. The ESS can be connected either to ac or dc. Then, a power electronic converter is required to interface it to the system. ESSs can be used to provide grid frequency support capability and power smoothing.

- Power smoothing: Due to the power supplied by a WECS is proportional to the cube of the wind speed, the intrinsic variability of the wind produces variations in the power and voltages supplied to the grid. This becomes relevant when the WECSs is connected to either a weak grid or an isolated grid. Then, the ESS is controlled to supply a compensating power to reduce or eliminate the variability in power extracted from the wind [52, 53].

2.3   Power Electronics for Multi-MW WECSs

2.3.1   Multi-MW WECSs

Nowadays, commercially available WECSs are rated around 1.5-6 MW, as shown in Table 2.1. The new generation of WECSs will substantially increase the power range, reaching power ratios above 10 MW, mainly using PMSGs. Manufacturers such as Sway and Windtec are already developing offshore wind turbines rated at 10 MW [33]. Moreover, there are projects under study to develop wind turbines up to 15 MW. A summary of those projects and WECSs around 10 MW is provided in Table 2.3. Despite the trend for Multi-MW Wind Turbines, most of the installed WECSs are based on low-voltage power converters, usually equipped with 1700V IGBT devices for connection to 690V grid [8, 9]. The continuous increase in wind turbine power ratings generates larger line current if the low voltage power converter technology is used. Therefore, the use of low-voltage converters is not convenient for Multi-MW WECSs. For example, from the 1600 A required for a 2 MW systems, the current will increase up to 8810 A for a 10 MW system. Because of this large current value, the diameter of the cables used to connect the converter to the power transformer has to be largely increased. Large current transfer results in high rated power cables going down through the tower (for horizontal axis wind turbines), with significant losses and voltage drops. Parallel cables reduce the loss but increase cost because high current cables are expensive. A step-

Manufacturer	Model	Power Range	Status
Gamesa	NA	15 MW	Design studies
Mingyang	SCD	12 MW	Design studies
WindTec	SeaTitan	10 MW	Under development
Clipper	Britania	10 MW	Under development
Goldwind	NA	10 MW	Design studies
Sinovel	NA	10 MW	Design studies
Siemens	SWT	8.0 MW	Available
Vestas	V164	8.0 MW	Available
Enercon	E126/7580	7.58 MW	Available

Table 2.3: Summary of WECS projects rated at 10 MW and above [10-12].

up transformer located inside the nacelle could avoid some of these disadvantages, but this adds significant mechanical load to the nacelle. This is a drawback for offshore WECSs where expensive platforms must be placed to support the total weight of the structure and the components [18]. Therefore, it is desirable to develop a generator-converter system that can be housed in the nacelle and directly connected to MV networks. Thus, MV or HV converters appears then as a promising solution [8, 9, 18].

2.3.2 Currently available Power Electronics for Multi-MW WECS

The four WECS Types, mentioned in previous sections, show that power electronics technology had played a major role in the evolution of wind energy. Consequently, there is a wide variety of power converter topologies currently available for Multi-MW WECSs. The state of the art solutions are currently available in the form of Type III or Type IV WECSs [8,9,28]. Usually, both configurations are equipped with back-to-back converters (BTB). However, there are other topologies, such as:

- Passive Generator-side Converters.

- Converters for multiphase generators.

- Converters without DC-Link.

A good summary of these configurations is provided in [9].

As far as voltage source BTB converters are concerned, they can be broadly classified as low-voltage (LV) and medium-voltage (MV). Low-voltage BTB converters are the preferred option in Type III and Type IV WECSs for power levels lower than 3 MW [9].

When the nominal power is higher, there are other solutions. For instance, WECSs could be connected to the grid using several BTB converter modules connected in parallel, as shown in Fig.2.9(a) [8, 54]. These modules provide modularity and redundancy, but they increase costs, size and weight of the system. Moreover, circulating currents among the parallel modules lead to technical difficulties and an oversized design.

Other possible solution is the use of MV converters. In the last past years, wind turbine manufacturers have been incorporating MV converters to WECSs above 3 MW because it has been proved that MV operation leads to a decreased energy production cost [14]. In MV applications, Multilevel converters are an enabling technology which has been extensively validated for drive applications [55–57].

The most common multilevel converter topologies are the Neutral-Point-Clamped converter (NPC), the Flying Capacitor converter and the Cascaded H-bridge converter (CHB). The power circuit of a single phase of each of these converters is illustrated in Fig.2.10. Usually, NPC and FC converters are equipped with MV semiconductor devices, such as Integrated Gate Commutated Thyristor (IGCT) and MV-Insulated Gate Bipolar Transistor (IGBT), whereas CHB converter features LV-IGBTs [55].

Several control methods for NPC, FC or CHB topologies are available, each of them strongly depending on the application. For example, the CHB has been successfully commercialised for reactive power compensation [58], and photovoltaic power conversion [59]. The CHB is well suited for high-power applications because its modular structure enables higher voltage operation. However, it requires a significant number of isolated DC sources fed from phase-shifting isolated transformers, increasing costs and weight.

The NPC converter has a significant market participation in high-power motor drive applica-
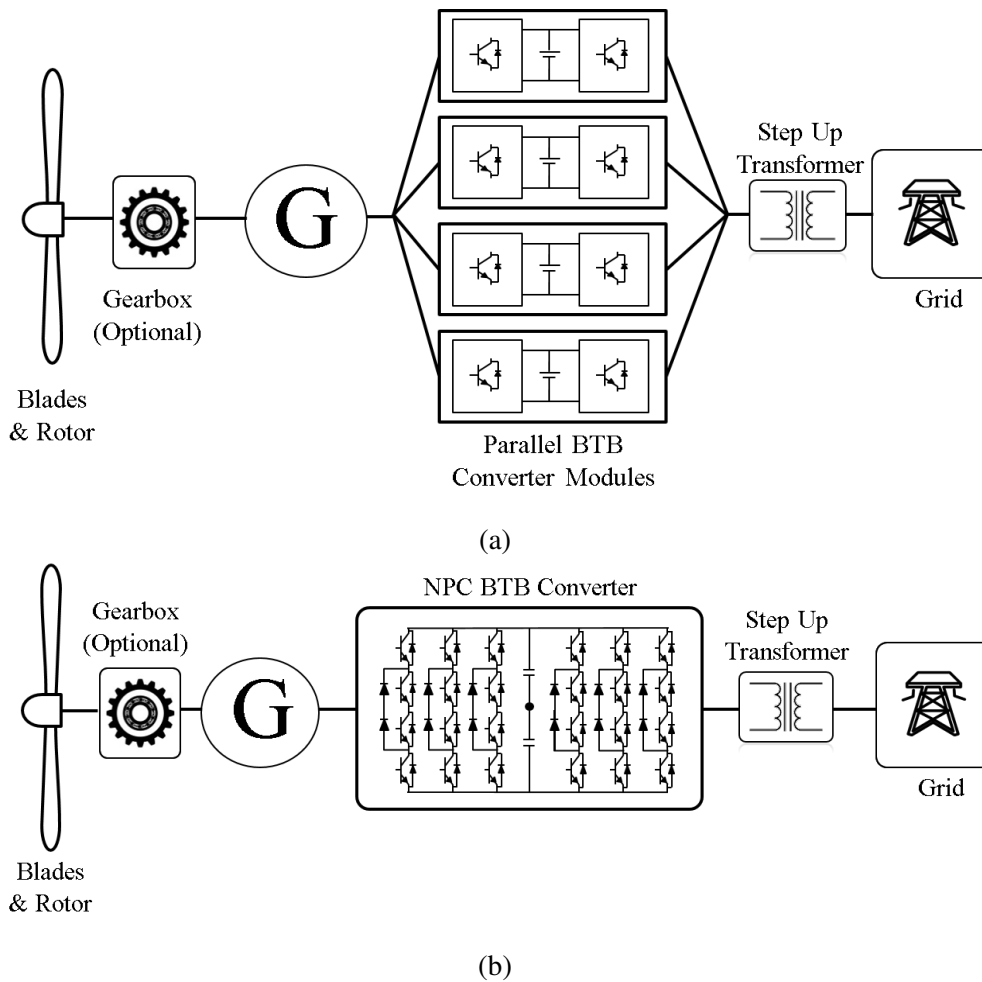
Figure 2.9: Reported Multilevel Converter for high power wind turbines. (a) Parallel back-to-back Converter based WECS. (b) NPC back-to-back Converter based WECS.

tions, such as mills, pumps, conveyors, etc. This converter is suitable for a BTB configuration in bidirectional power applications. In fact, the NPC converter has become the preferred option for WECS applications above 3 MW [15–17]. Fig. 2.9(b) shows a BTB NPC converter for a Type IV WECSs. The major drawbacks of the NPC converter for wind energy applications are the uneven power losses distribution among the semiconductors and the low reliability of the converter that is particularly important for offshore applications [18].

Finally, it is worth to mention that the FC converter has found less industrial development, mainly because the high switching frequency, required to maintain its DC capacitors balanced, restricts its use in high-power applications.

A good summary of generalities, applications, and characteristics of Multilevel Converter is presented in [55, 57].
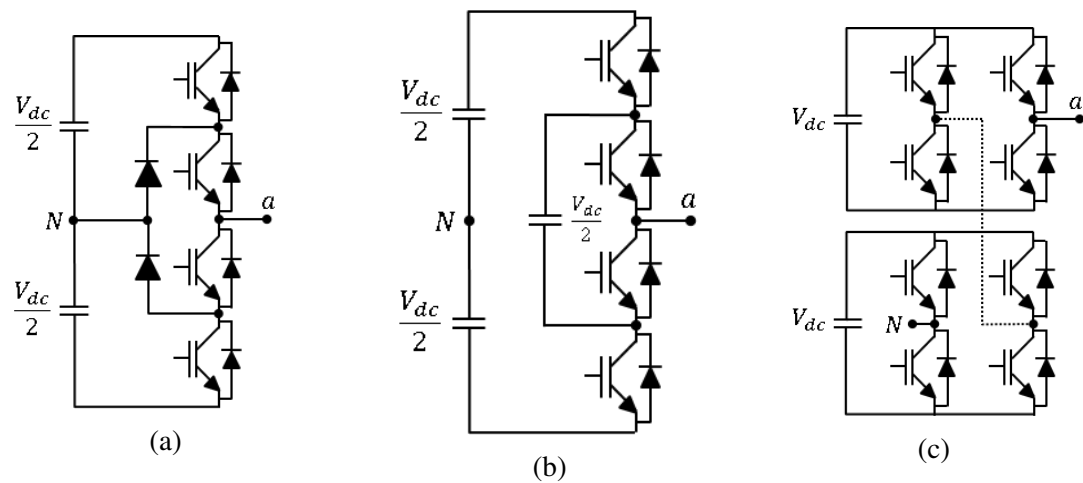
Figure 2.10: Traditional multilevel converter topologies. (a) NPC Converter. (b) FC Converter. (c) CHB Converter.

2.3.3 Future trends in Power Electronics for Multi-MW WECS

The continuous increase in the power level of WECSs is driving the power electronics technology towards MV operation. Accordingly, MV power converters will be dominant in the next generation Multi-MW WECSs, mainly because they offer cost-effectiveness and compact design. In addition to traditional multilevel converter topologies (NPC, FC and CHB), many new converters have been proposed in the literature, either as hybrid topologies or new topologies. For example, a five-level hybrid NPC converter with increasing number of devices is proposed to reach power rates up to 6 MW [60]. An hybrid between the NPC and the FC converter, called nested neutral-point-clamped (NNPC) converter, has been proposed to provide MV operation of WECSs [61]. The scholarly works in [20, 62, 63] propose the application of the Modular Multilevel Cascade Converters, which have been extensively used in High Voltage Direct Current (HVDC) Transmission, for Multi-MW WECSs. Among other characteristics, MMCCs converters offer modular structure, simple extension, redundancy, MV or high voltage operation − that can lead to transformer-less grid integration−, and improved power quality.

There are several operational and technical requirements that must be accomplished for wind turbine power converters. The most important requirements are listed bellow:

- Initial Cost: The initial cost of the power converter, which is only a fraction of the overall WECS cost, should be minimised to improve the cost of energy of WECSs to be competitive with other energy sources.

- Maintenance: the need of maintenance of the power converter should be as low as possible. This is particularly significant in offshore installations where the accessibility and logistics are complex.

- Efficiency: at Multi-MW rates, efficiency is an important factor reducing the cost of energy of WECSs. Therefore, the power converter has to feature high-efficiency switching devices, optimal control schemes and modulation, etc.

- Reliability and Modularity: Power converters for wind turbines, especially for offshore turbines, must have high reliability. Power converters having a modular structure are preferable because even when one power converter fails, the wind turbine can still work and the downtime of the system is decreased.

- Power Quality: voltages and currents synthesised for the power converter have to fulfill power quality standards. The total harmonics distortion and the dv/dt can be decreased as the number of levels of the converter is increased. By doing so, the requirement for output filter decreases and the power density and cost of energy of the system are enhanced.

- Size and weight: A limited space is available in the nacelle of wind turbine. Therefore, the power converter must feature high power density to reduce weight and size. This is particularly significant in offshore installations where expensive platforms must be placed to support the total weight of the WECS structure.

- Grid code compliance: this is one of the most important requirements for grid-connected WECSs. The power converter must provide fault-ride through capability, reactive power compensation, voltage/frequency support, among other requirements.

Therefore, the prevalence of one particular power converter topology in the wind energy industry is related to the trade-off among all the above-mentioned requirements. Research works on novel MV power converters and advanced control schemes will play a major role in the development of the new generation of WECSs.

2.4 Modular Multilevel Cascade Converters

MMCCs are a relatively new family of power converters proposed initially for HVDC transmission [22, 64]. However, similar configurations have been proposed since middle of the 1990s for MV drives and STATCOMs [65, 66].

The MMCC family is characterised by a cascade connection of power cells forming a cluster. These power cells are usually single-phase H-bridges or bidirectional choppers, and the converter voltage rating can be easily enlarged by increasing the number of cells per cluster. The capacitor voltage of each power cell is floating and could charge-discharge during the operation of the converter. Therefore, one of the most important control aims is to maintain the voltage in each capacitor within an acceptable range, particularly for variable-speed operation. Different connection of cluster and power cells, i.e. choppers or full-bridges, lead to different MMCCs topologies. A good overview of the the MMCC family is presented in [26].

The terms "modular" and "multilevel" can be used to refer several configurations, but they are mainly used to refer to the configuration shown in Fig. 2.11. This converter is generally referred to as Modular Multilevel Converter or M^2C. The M^2C is composed of an ac port, a DC port and six clusters. Each cluster has n cascaded power cells and one inductor. Each power cell is composed of a bidirectional chopper (half bridge) and its associated flying capacitor, as shown in Fig. 2.11(b). H-Bridge power cell can be also used in this topology (see Fig. 2.11(c). The power cells within a cluster are controlled to generate the required AC output voltage whereas the cluster inductor
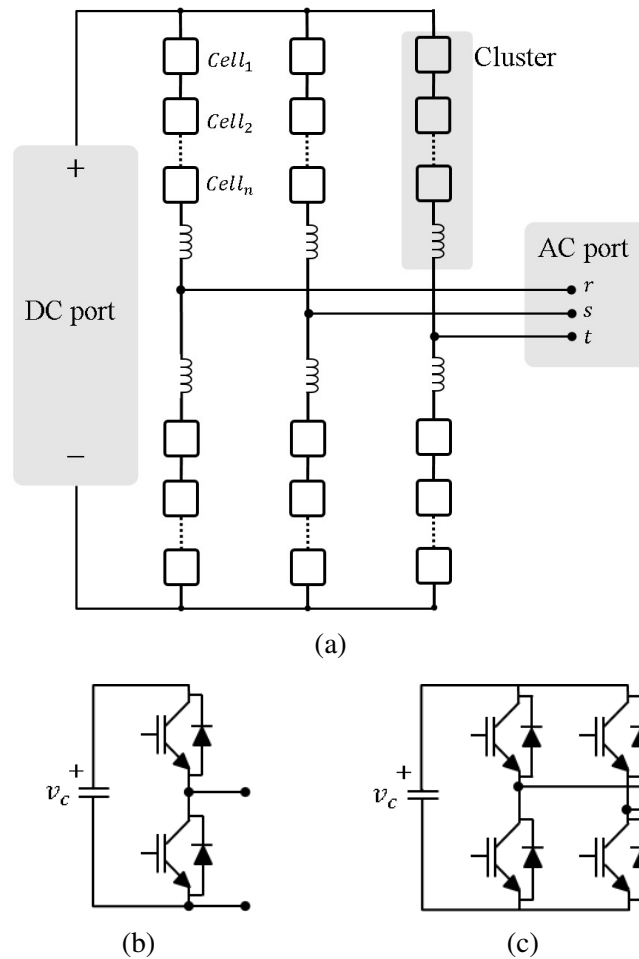
Figure 2.11: Modular Multilevel Converter or M^2C. (a) Whole converter. (b) Half-Bridge power cell. (c) H-Bridge power cell.

suppresses the high-frequency components of the cluster current.

The M^2C has been extensively used in HVDC transmission systems [22–25]. In 2010, the first commercial application of this converter was presented by Siemens, implementing a HVDC transmission line of 400-MW with 200kV DC voltage between Pittsburgh and San Francisco in USA [67].

2.4.1 AC-to-AC Modular Multilevel Converters

Most of the reported applications of the MMCC family are in the field of HVDC transmission. Consequently, the application of these converters for high-power drives has been barely investigated. Recent studies indicates that MMCCs are well suited for high-power variable-speed applications such as sag mills, mine hoists and large wind turbines, due to their several advantages over tradional topologies: full modularity and easy extensibility to reach high voltage levels, redundancy, control flexibility and power quality [26].

In accordance with the requirements mentioned in previous section, Multi-MW WECSs should

feature power electronic converter capable of AC-to-AC conversion, MV operation, variable speed operation, grid code compliance, etc. Consequently, the most appropriate MMCC topologies to fulfil these requirements are:

- M^2C in BTB configuration

- Hexverter

- M^3C

2.4.1.1 Back-to-Back MMC

The BTB M^2C is shown in Fig.2.12. This converter is composed of two M^2C connected by their DC ports to enable AC-to-AC conversion. Each converter has six clusters composed of n power cells connected in cascade with one inductor. The power cells are composed of bidirectional choppers and a flying capacitor. Among the MMCC family, the BTB M^2C is the only topology currently available on the market [67]. There are ongoing research works studying its application to MV drive systems [24, 26, 68, 69] and the scholarly works presented in [63, 70] have proposed the application of the BTB M^2C for Multi-MW WECSs.

In this converter, the control of the flying capacitors is difficult to perform when the one of the ac systems connected to its ports is operating at zero or very low frequency [68]. In this situation, high magnitude circulating currents or common mode voltage are required to mitigate the oscillations in the capacitors [24, 68, 69]. Therefore, the problem using this topology in Multi-MW WECSs is the comparatively small output frequency of modern wind energy generators that usually are around 10–20 Hz [71]. Consequently, the generator-side M^2C must be designed to accommodate the extra currents and common-mode voltage, which can decrease the efficiency and increase the built-in rate of the system.
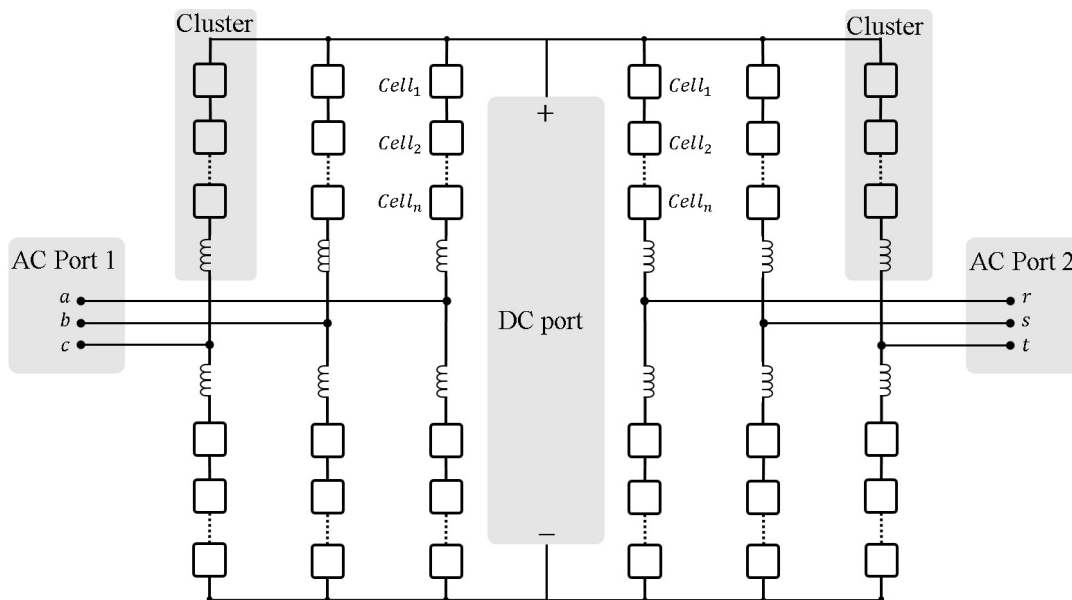
Figure 2.12: Modular Multilevel Converter in BTB configuration.

2.4.1.2 Hexverter

The Hexverter circuit is shown in Fig.2.13. This converter is composed of six cluster connecting each input phase to two output phases. Then, six identical cluster forms a hexagonal ring. Each cluster is composed of a stack of n power cells connected in cascade with one inductor. The power cells comprise a full bridge and a flying capacitor. As each power cell can produce both polarities, AC-to-AC conversion is enabled.

This converter was firstly proposed in 2013 for high-power AC-to-AC conversion [72]. Few publications have reported experimental implementations of this topology [72, 73] and the Hexverter has not been used in practice so far. Adjacent clusters have different active power components depending on the difference of reactive power connected to both ports [73] . Therefore, an adjacent power component, i.e. combination of circulating current and common-mode voltage, has to be considered to regulate the average capacitor voltage of the converter. This leads to an oversized design of the converter components and it is a disadvantage of the Hexverter compared to others modular multilevel converters [74].
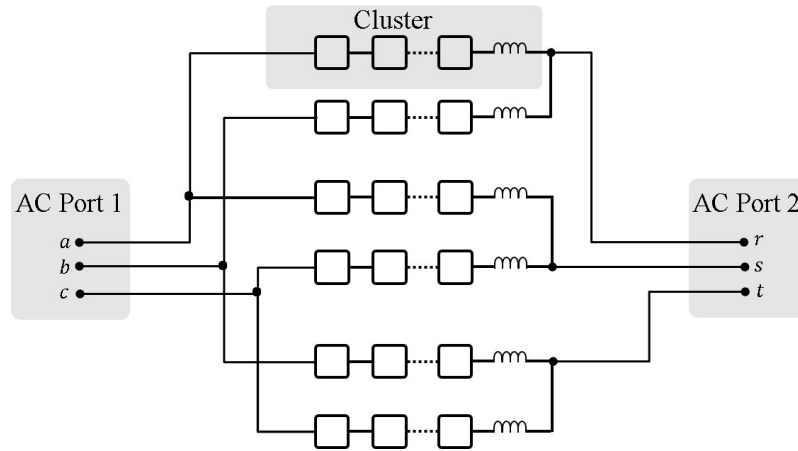
Figure 2.13: Hexverter.

2.4.1.3 Modular Multilevel Matrix Converter

The M^3C is shown Fig.2.14. This converter consists of nine clusters linking one phase of the input system (e.g. phase a), to the three phases of the output system (r, s, t). Each cluster is composed of a stack of n power cells connected in cascade with one inductor. The power cells comprise a full bridge and a flying capacitor. As each power cell can produce both polarities, AC-to-AC conversion is enabled and this converter is usually referred to as Direct M^2C.

This converter is more suitable for low-speed high-power applications because lower circulating currents are required to mitigate the oscillations in the capacitors, in comparison with the BTB M^2C [72, 74]. However, the M^3C has an inherent problem when the machine frequency is close to the grid frequency, leading to dangerous capacitor voltage oscillations and instability.
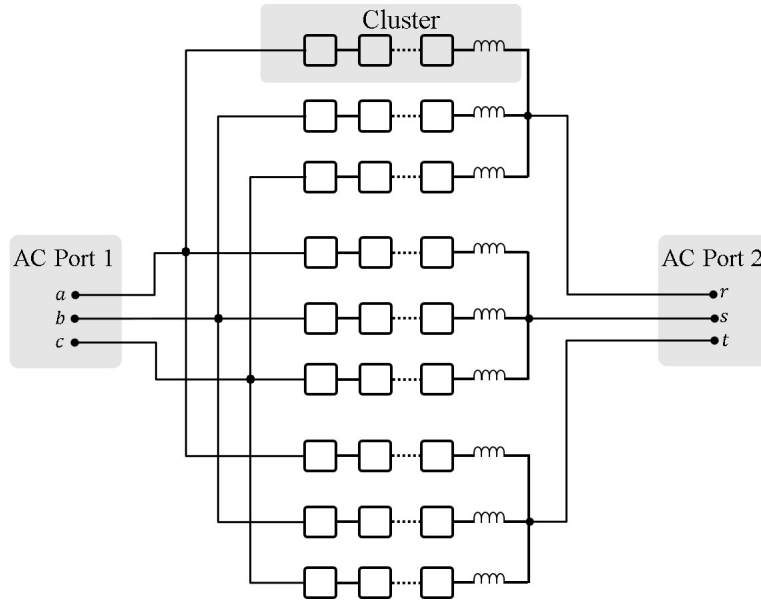
Figure 2.14: Modular Multilevel Matrix Converters.

2.4.2 Benchmarking of Modular Multilevel Converters for Multi-MW WECSs

In this section, a comparison of the most popular converters for a power range of 3-7MW is conducted. Comparisons between power converters for WECSs in this power range have been presented in recent literature [8, 9]. The selected converters are the parallel two-level BTB converter and the NPC converter [16, 18, 54]. Moreover, the three AC-to-AC MMCCs described in the previous section are compared for a 10 MW WECSs. For all the converters, the performance indicators are the nominal power, grid-voltage connection level, number of converter or power cells, number of switching devices, requirement of circulating currents, reliability, converter complexity, grid-code compliance, transformer-less capability and the technology status.

The analysis presented in Table 2.4 summarises the advantages/disadvantages of applying different power converters in LV or MV depending on the power rating of the WECS. The commercially practised power converters in the present wind industry are limited to low-voltage BTB converters, parallel low-voltage BTB converters and NPC converters (equipped with MV switches) .

The M^2C, Hexverter and M^3C are compared for a 10 MW WECS considering the connection to a 6.6 kV grid and an internal composition of 9 power cells per cluster. In this example, the M^2C has the same semiconductor demand than the Hexverter and the M^3C. This is because the M^2C is equipped with 12 half-bridge based clusters and the Hexverter is equipped with 6 H-Bridge based clusters. Then, the requirement of DC capacitors of the M^2C is twice the one of the Hexverter. The M^2C requires injection of common-mode voltage and higher circulating currents to operate at low frequencies, leading to an oversized design [68].

Even though the Hexverter needs fewer modules M^3C, there are operational conditions, such as independent power factor in the ac systems connected to the converter ports, where a compensating power is required to regulate the flying capacitor of the Hexverter. This compensation power is achieving injecting circulating current and common mode voltage and also leads to oversized

design. Moreover, this drawback also results in the fact that the grid code compliance capability of the Hexaverter is poor because fully controllable power factor the grid-side implies huge over-dimensioning of the power cells [74].

Despite the high number of power cells required by the M^3C, its constructive characteristics allow low-frequency operation with low circulating current requirements and without the injection of common-mode voltage. Moreover, the reliability of the converter and its grid-code compliance performance are the best among the MMCC family. In fact, the M^3C is advantageously compared with others high power converter topologies for high-power wind energy applications [72, 74]. Consequently, the M^3C could be successfully employed in WECSs application of 10MW and beyond. In the next Subsection a revision of control strategies for the M^3C will be detailed.

Finally, it is important to mention that the comparison presented above depend on the initial suppositions. Different scenarios can lead to rather different results in the comparison. Accordingly, detailed comparisons including technical and economic analysis of the converters, such as nominal voltage, number of cells, type of semiconductors, switching frequency, efficiency, require additional information that is usually managed by industry manufacturers.

	Parallel 2L-VSC	3L-NPC	BTB M²C	Hexverter	M³C
Typical Power	3-7.5 MW	3.0-6.0 MW	10 MW and above	10 MW and above	10 MW and above
Typical Voltage	up to 1kV	up to 4 kV	6.6 kV	6.6 kV	6.6 kV
Number of Converters	up to 10	1	84 power cells	42 power cells	63 power cells
Number of Switches	up to 120	24	168	168	252
Switching Devices	LV-IGBTs	MV-IGBTs MV-IGCTs	LV-IGBTs	LV-IGBTs	LV-IGBTs
Circulating currents	High	-	High	High	Low
Common-Mode Voltage	No	No	Required	Required	No
Reliability of the system	Medium	Low	High	Medium-High	High
Converter Complexity	Medium	Medium	High	High	High
Grid-Code Compliance	Medium	Good	Excellent	Low	Excellent
Transformerless operation	No	Possible	Yes	Yes	Yes
Technology Status	Highly Mature	Well Established	Research only	Research only	Research only
Commercial example	Enercon E-126	Nordex N150	Siemens HVDC plus	-	-

Table 2.4: Comparison of power converters for Multi-MW WECSs [16,18,54,70-74].

,

29

2.5 Control Systems for the Modular Multilevel Matrix Converter

Owing to the high complexity of the M^3C, few publications have reported experimental implementations of this topology. An overview of the papers published so far is presented in Table 2.5. The principal research works related to the M^3C have proposed its application for for Wind Energy Conversion Systems [75, 76], low-frequency variable speed drive applications [77–80], ac transmission [81, 82].

The control strategies presented in the aforementioned papers can be broadly classified into the following categories:

- Conventional Control Strategies: the capacitor voltage regulation is performed affecting either the input or the output systems connected to the ports of the M^3C [75, 76, 79, 81, 83–86]

- Decoupled Control Strategies: there is an usage of the degrees of freedom of the M^3C enabling a decoupled control of capacitor voltage of the M^3C. Consequently, the input and output systems are not affected by the regulation of the flying capacitors of the converter [77, 78, 80, 87–93].

Paper Title	Year	Exp. Validation Power rate	Control Features			Type of Publication	Ref. Number
			Variable Speed	Equal Frequency	LVRT		
A New Family of Multilevel Matrix Converters	2001	No	No	No	No	Conference	[75]
A New Family of Multilevel Matrix Converters for Wind Power Applications	2006	Yes, 24 kVA	No	No	No	Report	[76]
Direct Modular Multi-Level Converter for Gearless Low-Speed Drives	2011	No	No	No	No	Conference	[84]
A novel cascaded vector control scheme for the Modular Multilevel Matrix Converter	2011	No	No	No	No	Conference	[87]
Control of a Modular Multilevel Matrix Converter for High Power Applications	2012	Yes, 0,4 kVA	Yes	No	No	Studies in Informatics and Control	[86]
Fully decoupled current control and energy balancing of the Modular Multilevel Matrix Converter	2012	Yes, 5 kVA	No	No	No	Conference	[77]
Decoupled control of a three-phase to three-phase modular multilevel matrix converter	2013	No	No	No	No	Conference	[85]
Modular multilevel matrix converter for low frequency AC transmission	2013	Yes, 1 kVA	No	No	No	Conference	[81]
Independent control of input current and output voltage for Modular Matrix Converter	2013	Yes, 1 kVA	No	No	No	Conference	[83]
A broad range of frequency control for the modular multilevel cascade converter based on triple-star bridge-cells (MMCC-TSBC)	2013	Yes, 15 kVA	Yes	Yes, restricted	No	Conference	[90]
Energy balancing of the Modular Multilevel Matrix Converter based on a new transformed arm power analysis	2014	Yes, 4 kVA	No	Yes	No	Conference	[88]
Control and Experiment of a Modular Multilevel Cascade Converter Based on Triple-Star Bridge Cells	2014	Yes, 15 kVA	Yes	No	No	IEEE Trans. on Ind. Applic	[78]
Independent Control of Input Current, Output Voltage, and Capacitor Voltage Balancing for a Modular Matrix Converter	2015	Yes, 3 kVA	No	No	No	IEEE Trans. On Ind. Applic	[79]
A Low-Speed, High-Torque Motor Drive Using a Modular Multilevel Cascade Converter Based on Triple-Star Bridge Cells (MMCC-TSBC)	2015	Yes, 15 kVA	Yes	No	No	IEEE Trans. On Ind. Applic	[91]
A broad range of speed control of a permanent magnet synchronous motor driven by a modular multilevel TSBC converter	2016	Yes, 15 kVA	Yes	Yes	No	IEEE Trans. On Ind. Applic.	[80]
A Branch Current Reallocation Based Energy Balancing Strategy for the Modular Multilevel Matrix Converter Operating Around Equal Frequency	2017	Yes, 5 kVA	No	Yes, restricted	No	IEEE Trans. On Power Electronics	[82]
Experimental Verification of an Electrical Drive Fed by a Modular Multilevel TSBC Converter When the Motor Frequency Gets Closer or Equal to the Supply Frequency	2017	Yes, 15 kVA	Yes	Yes	No	IEEE Trans. on Ind. Applic.	[92]

Table 2.5: Overview of published research works of the M^3C.

2.5.1 Conventional Control Strategies

The simplest approach to balance the capacitor voltages of the M^3C is the injection of negative-sequence currents. In [79, 84], the capacitor voltage imbalances among different clusters are controlled by injecting a negative-sequence current in phase with the voltage connected to one of the ports of the converter. Then, active power flows between one cluster and another regulate the imbalances among capacitor voltages. Additionally, a positive-sequence current component in phase with the voltage connected to the same port than before is regulated to control the average value of the capacitor voltages.

Control strategies based on Space Vector Modulation have been proposed to synthesise the cluster voltages [75, 76, 81]. Considering that an M^3C composed of n cells has 3^{9n} possible switching states, Space Vector Modulation is hardly feasible for more than two power-cells because of the extremely high number of possible vectors. Furthermore, neither the variable speed operation nor the grid-connected operation of the M^3C is considered in these papers.

The control proposals of [85, 86] are validated through simulations. In [75, 76, 79, 81, 83, 84], control strategies are experimentally validated considering M^3Cs composed of 1 power cell per cluster, feeding RL loads or connecting two AC systems. In general, these scholarly works propose cascaded control strategies with an inner cluster current control and an outer control loop for balancing the capacitor voltages. Nevertheless, all these control proposals do not use the full degrees of freedom of the M^3C. Therefore, the balancing of the flying capacitor voltages results in unbalanced currents flowing into the input or output systems, which is undesirable for a grid-connected M^3C driving electrical machines.

2.5.2 Decoupled Control Strategies based on the $\alpha\beta0$ Transformation

Control strategies based on decoupled modelling of the M^3C using the Double $\alpha\beta0$ Transformation have been reported recently [77, 78]. The concept of the Double $\alpha\beta0$ Transformation was firstly proposed in [77] and further complemented in [87,88] by the same research group. However, [78] is probably the best research work published so far, because it considers the experimental validation of the proposal through experiments conducted with a M^3C composed of four power cells per cluster rated at 15 kVA. The same authors of [78] have also published this decoupled control system of the M^3C for STATCOM applications [89], permanent magnet motor drives [80], induction machines [90–92] and a comparison between the M^2C and the M^3C is provided in [93].

In all these scholarly works, control strategies are applied to a system that relates the transformed voltages and currents of the M^3C in the Double $\alpha\beta0$ frame. This linear transformation makes the analysis simpler and also it also enables the use of the common-mode voltage and the currents that circulate in the converter (circulating currents) as degrees of freedom. Moreover, the representation of the M^3C in the Double $\alpha\beta0$ frame is decoupled, meaning that the input and output systems connected to the ports of the converter, can be controlled independently of the M^3C. Then, it is possible to regulate the flying capacitor of the M^3C without affecting the input or output systems. The methodology and definitions of this approach will be thoughtfully explained in the next Chapter.

(a)

(b) .
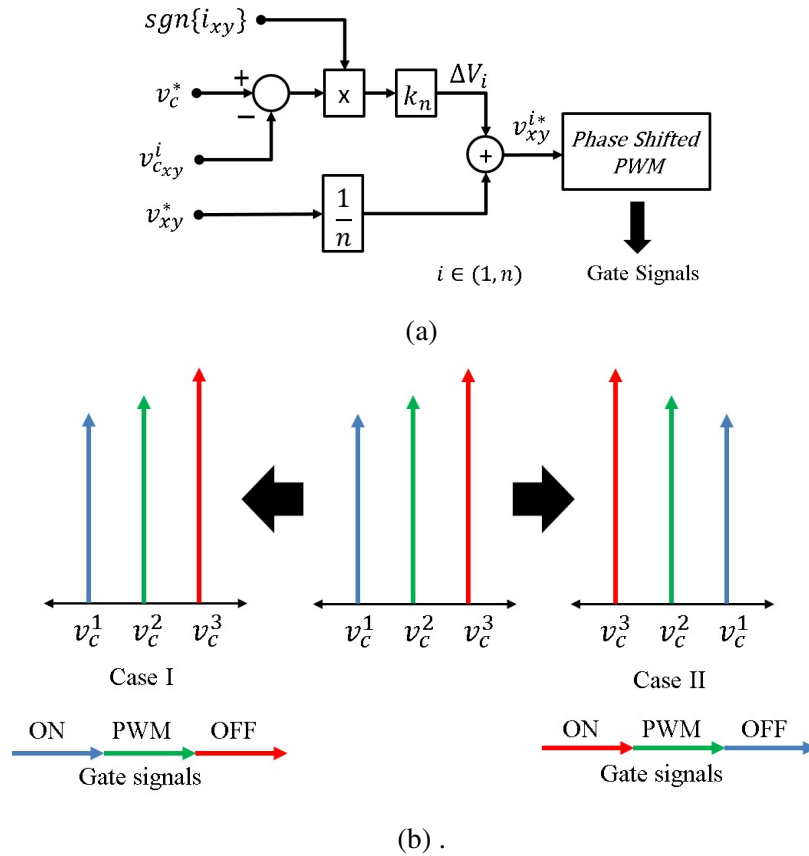
Figure 2.15: Published options for Single-Cell Capacitor Voltage Control. (a) Single-cell Capacitor Voltage Control proposed in [89]. (b) Single-Cell Capacitor Voltage Control based on the sorting algorithm of [77].

The control systems based on the representation of the M^3C in the Double $\alpha\beta0$ frame are composed of the following sub-systems:

- **Average Capacitor Voltage Control:**

  In both, [77, 78], the control system regulates the average value of all the capacitor voltages using a PI controller that set the reference of the input current control system. This maintains the energy store in the converter cluster constant at a desired level by imposing a direct current reference. The reference value for the reactive power at the input port can be set to zero or to any desired value for working additionally as a STATCOM [89].

- **Control of the capacitor voltage imbalances:**

  The voltage imbalances between flying capacitors of different clusters must be regulated to ensure equal capacitor voltage distribution. The imbalances are controlled to zero using either Proportional-Integral [77] or Proportional [78] controllers that set the amplitude and phase of the circulating current. The circulating current control system tracks its references using proportional controllers which generate voltage references to be synthesised by each cluster.

33

- **Input-side and Output-side Control Systems:**

The input system is controlled using a regular $\mathrm{d}q$ control structure that receives its references from the Average Capacitor Voltage Control. In the most of the cases, e.g. [77,78], the system connected to the output port considers an electrical machine. The electrical machine can be controlled using a conventional field-oriented control system. Therefore, the measured output currents are rotated into their corresponding synchronous reference frame to control the magnetic flux and electric torque independently. The torque current reference value is specified by an external speed controller which has to be designed depending on the requirements of the mechanical process.

- **Single-Cell Control**:

There are two main options to balance the capacitor voltages of the same cluster.

The control loops mentioned above produce voltage references for each cluster. Here, the additional loop presented in Fig. 2.15(a) is applied [89]. The capacitor voltage v_c^{i} of the ith power cell (where $\mathrm{i} \in (1, n)$ and n stands for the number of cell within a cluster) is compared to the desired value v_c^*. The resulting error is multiplied by the cluster current producing an incremental voltage ΔV_{i} which is added to the power cell reference voltage v_{xy}^*/n. Thereafter, phase-shifted PWM is used to synthesise the voltage references. This modulation is simple to implement in a commercial FPGA-based control platform and produces power losses evenly distributed among the cells within a cluster. Moreover, phase-shifted unipolar modulation generates an output switching frequency of $2n$ times the carrier frequency.

Another alternative is proposed in [77]. This algorithm is shown in Fig.2.15(b), where an example for a cluster with three power cell is illustrated as a demonstrative example. Firstly, the capacitor voltages (v_c^1, v_c^2, v_c^3) are measured and sorted ascending or descending depending on the cluster power polarity. If the power cell is absorbing active power, the power cell with the lowest capacitor voltages is switched on, and the cell with the higher is switched off. The opposite case is selected when the power cell is injecting active power, i.e. the power cell with the higher voltage is switched on, and the one with the lowest is switched off. For both cases, the power cell with the closest value to the set-point is modulated. Using this sorting algorithm, the power cell-balancing is always ensured because the cells with the lowest capacitor voltages are charged, and the cells with the highest voltages are discharged.

2.6 Summary

This Chapterhas presented a literary review on Wind Energy Conversion Systems and Modular Multilevel Converters. This review includes WECS topologies, control systems, grid codes and other requirements such as inertia emulation and power smoothing. Attention has been paid to power electronics converter topologies suitable for Multi-MW WECS applications.

A Comparison between power converters for Multi-MW WECSs was presented showing that MMCCs are an attractive solution for the foreseen Multi-MW WECSs. Among the MMCC family, it has been stated that the M^3C is the best option for low-speed high-power applications. The M^3C could be successfully employed in WECS applications of 10 MW and beyond due to its characteristics such as scalability, control flexibility and FRT capability.

A brief overview of control strategies for the operation of the M^3C has also been presented in this chapter. From this analysis, it can be concluded that there remains an absent of studies and experimental validation of control schemes including variable speed operation, grid code compliance, and capacitor voltage regulation for WECSs.

CHAPTER 3

Proposed Modelling of the M^3C

3.1 Introduction

In this Chapterthe modelling of the M^3C is firstly introduced based on the early research works that propose the use of the Double $\alpha\beta0$ Transformation to represent a decoupled dynamics of the converter [77, 78]. Thereafter, a detailed analysis of the capacitor voltage oscillations as a function of the input/output frequencies is given.

An additional linear transformation is introduced to improve the representation of M^3C for any generator-grid frequencies condition. The $\Sigma\Delta$ Transformation is used to obtain a vector representation of the M^3C that allows a simple analysis and consequently implementation of control strategies using vector control.

3.2 Modelling of the M^3C

The M^3C circuit configuration is presented in Fig. 3.1. Each module or power cell is composed of an H-bridge connected to a flying capacitor, as shown in Fig. 3.1(a). The power cells are connected in a stack of n full bridges and one inductor, forming a cluster [see Fig. 3.1(b)]. Three clusters form a Sub-Converter, which is also known as a single-phase M^3C [83]. In a Sub-Converter, the clusters are organised to link the three phases of the system connected to the input port to one of the phases of the system connected to the output port. Fig. 3.1(c shows a Sub-Converter connecting the phases $\{a, b, c\}$ to the output phase r. Finally, the full circuit of the M^3C is presented in Fig. 3.1(d). This converter is well suited for high-power applications due to its characteristics. In a M^3C with a high number of power cells, the voltage synthesised by the converter has small voltage steps and low harmonic distortion. This converter also has another characteristics, for instance, full modularity, simplicity to reach high voltage levels, control flexibility, power quality and redundancy [77, 78].

In this topology, the capacitor voltages of the power cells are floating and can charge-discharge through the operation of the converter. This fact becomes the major control concern to provide proper operation of the converter in variable-speed applications.

Considering the output voltage v_{xy} of a generic cluster where $x \in \{a, b, c\}$ and $y \in \{r, s, t\}$, the following relationship is deduced:

$$v_{xy} = \sum_{i=1}^{n} v_{xy_i} = \sum_{i=1}^{n} s_i v_{c_{xy_i}} \tag{3.1}$$

Where n stands for the number of power cell in the cluster. The variables v_{xy_i}, $s_i \in \{-1, 0, 1\}$ and $v_{c_{xy_i}}$ are the output voltage, the switching state and the capacitor voltage of each power cell, respectively. Therefore, the output voltage of a single cluster is restricted to the total voltage available in the cluster as follows:

$$-v_{c_{xy}} \leq v_{xy} \leq v_{c_{xy}} \tag{3.2}$$

The term $v_{c_{xy}}$ is defined as the sum of the n capacitor voltages and it represents the available capacitor voltage in the xy cluster. In the following chapters, $v_{c_{xy}}$ is called Cluster Capacitor Voltage.

At this point, it is straightforward to conclude that the available capacitor voltage $v_{c_{xy}}$ must be the same in all the clusters to synthesise symmetrical voltages. Moreover, the capacitor voltages of the power cells within a cluster should be controlled to the same level. Therefore, there are two conditions to be satisfied to provide correct operation of the converter:

- The nine Cluster Capacitor Voltages have to be controlled to the same value. This control task is referred to as Cluster Capacitor Voltage balancing.

- The n Capacitor Voltages within a cluster have to be controlled to the same value. This
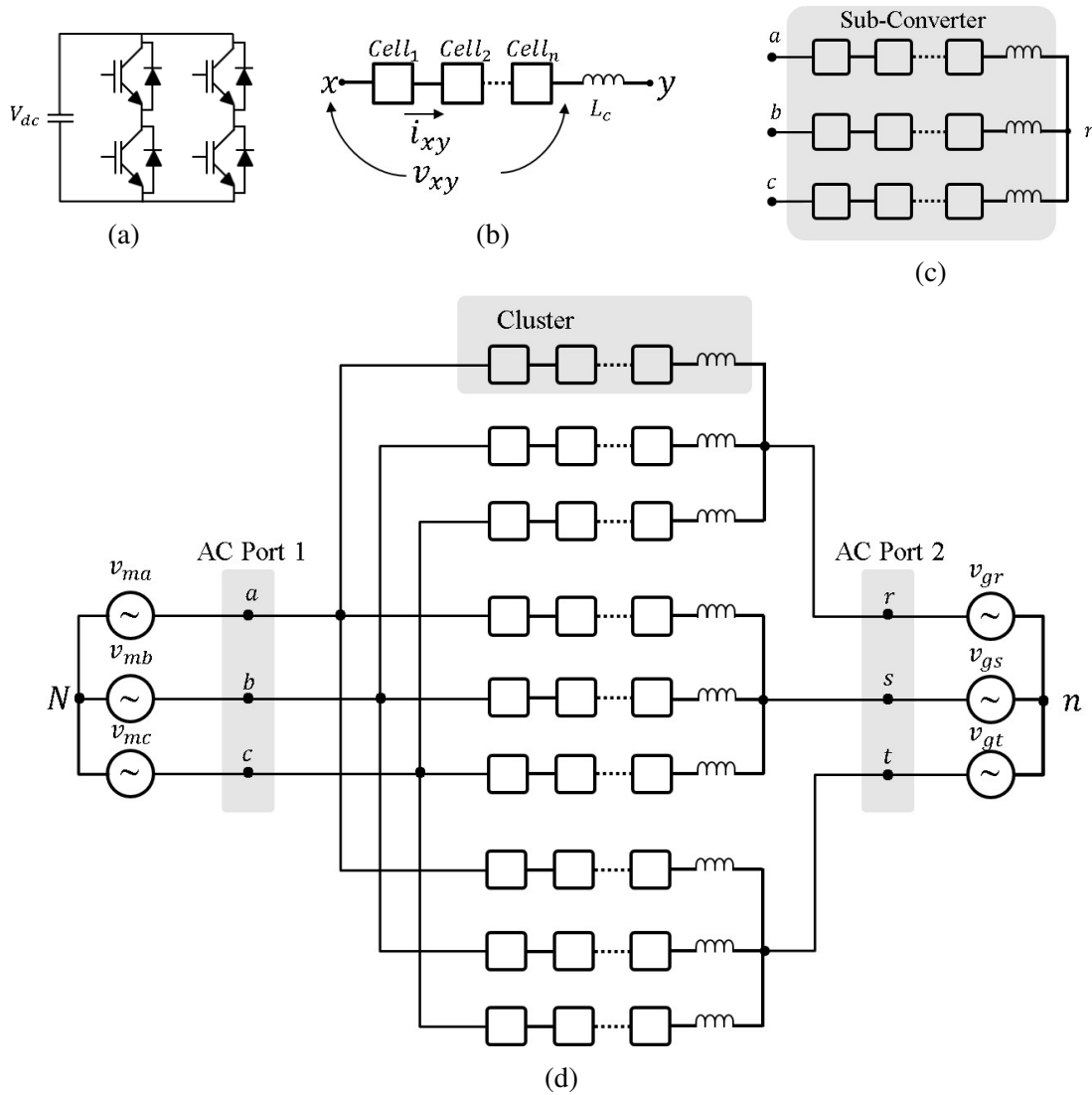
Figure 3.1: M^3C composition. (a) H-Bridge based power cell. (b) Cluster composition. (c) Sub-Converter. (d) Full converter

control task is referred to as Single-cell balancing.

When both conditions are satisfied the M^3C is 'Balanced' and the clusters can be considered as controlled voltage sources. Accordingly, the reduced representation of the M^3C presented in Fig. 3.2 is used to simplify the analyses.

In this and the following analyses, it is considered that an electrical machine is connected to the input port of the M^3C, and the output port is connected to the grid.

The dynamics modelling of the M^3C is required to perform the Cluster Capacitor Voltages and Single-Cell balancing control. Consequently, two models are described to represent the dynamics of the currents/voltages and the Cluster Capacitor Voltages of the M^3C.
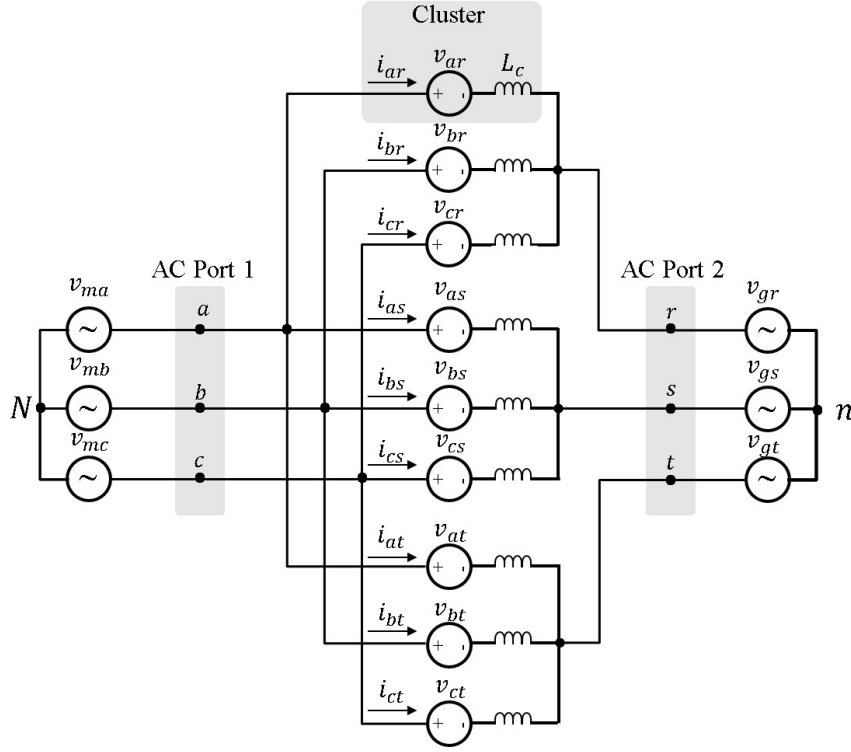
Figure 3.2: Simplified circuit of the M^3C.

3.2.1 Voltage-Current Model of the M^3C

The first model represents the currents and voltages of the M^3C. For simplicity, the clusters are replaced by controlled voltage sources as shown in Fig.3.2. Using Kirchhoff's Voltage Law on this circuit, and assuming that the grid and the generator are ideal voltage sources, the following expression is obtained:

$$
\begin{bmatrix} v_{ma} & v_{mb} & v_{mc} \\ v_{ma} & v_{mb} & v_{mc} \\ v_{ma} & v_{mb} & v_{mc} \end{bmatrix} = L_c \frac{\mathrm{d}}{\mathrm{d}t} \begin{bmatrix} i_{ar} & i_{br} & i_{cr} \\ i_{as} & i_{bs} & i_{cs} \\ i_{at} & i_{bt} & i_{ct} \end{bmatrix} + \begin{bmatrix} v_{ar} & v_{br} & v_{cr} \\ v_{as} & v_{bs} & v_{cs} \\ v_{at} & v_{bt} & v_{ct} \end{bmatrix}
$$
$$
+ \begin{bmatrix} v_{gr} & v_{gr} & v_{gr} \\ v_{gs} & v_{gs} & v_{gs} \\ v_{gt} & v_{gt} & v_{gt} \end{bmatrix} + v_n \begin{bmatrix} 1 & 1 & 1 \\ 1 & 1 & 1 \\ 1 & 1 & 1 \end{bmatrix}
\tag{3.3}
$$

Where the subscript m represents the machine-side voltages and currents and the subscript g stands for the grid-side variables. The voltage drops at the terminal of the cluster are represented by v_{xy}, with $x \in \{a, b, c\}$, $y \in \{r, s, t\}$, L_c stands for the cluster inductor inductance, and the common-mode voltage between the neutral points N and n is symbolised by v_n.

Decoupled modelling of the M^3C have been reported recently in the literature [77,78]. In these papers, the main task is to obtain a decoupled representation of the M^3C using linear transformations based on the Clarke Transformation.

In this work, a similar approach is used. Firstly, the system connected to the input port is transformed from $\{a, b, c\}$ to $\{\alpha, \beta, 0\}$ using the power invariant Clarke transformation. This transformation is defined as follows:

$$\mathbf{C}_{\alpha\beta 0} = \sqrt{\frac{2}{3}} \begin{bmatrix} 1 & -1/2 & -1/2 \\ 0 & \sqrt{3}/2 & -\sqrt{3}/2 \\ 1/\sqrt{2} & 1/\sqrt{2} & 1/\sqrt{2} \end{bmatrix} \tag{3.4}$$

Secondly, the same Clarke transformation is applied to the resulting system to transform output system from $\{r, s, t\}$ to $\{\alpha, \beta, 0\}$. The complete description of this procedure is explained in Appendix A.

This two steps $\alpha\beta 0$ transformation is equivalent to pre-multiply (3.3) by $\mathbf{C}_{\alpha\beta 0}^T$ ($\{a, b, c\} \rightarrow \{\alpha, \beta, 0\}$) and post-multiply it by $\mathbf{C}_{\alpha\beta 0}$ ($\{r, s, t\} \rightarrow \{\alpha, \beta, 0\}$) [77, 78]. In this document, the pre and post multiplication by $\mathbf{C}_{\alpha\beta 0}^T$ and $\mathbf{C}_{\alpha\beta 0}$ are referred to as Double $\alpha\beta 0$ Transformation.

Applying the Double $\alpha\beta 0$ Transformation to (3.3) results in:

$$\sqrt{3} \begin{bmatrix} 0 & 0 & 0 \\ 0 & 0 & 0 \\ v_{m\alpha} & v_{m\beta} & v_{m0} \end{bmatrix} = L_c \frac{\mathrm{d}}{\mathrm{d}t} \begin{bmatrix} i_{\alpha\alpha} & i_{\beta\alpha} & i_{0\alpha} \\ i_{\alpha\beta} & i_{\beta\beta} & i_{0\beta} \\ i_{\alpha 0} & i_{\beta 0} & i_{00} \end{bmatrix} + \begin{bmatrix} v_{\alpha\alpha} & v_{\beta\alpha} & v_{0\alpha} \\ v_{\alpha\beta} & v_{\beta\beta} & v_{0\beta} \\ v_{\alpha 0} & v_{\beta 0} & v_{00} \end{bmatrix} + \sqrt{3} \begin{bmatrix} 0 & 0 & v_{g\alpha} \\ 0 & 0 & v_{g\beta} \\ 0 & 0 & v_{g0} \end{bmatrix}$$
$$+ \begin{bmatrix} 0 & 0 & 0 \\ 0 & 0 & 0 \\ 0 & 0 & 3v_n \end{bmatrix} \tag{3.5}$$

The system of (3.5) is called Voltage-Current model of the M^3C in the Double $\alpha\beta 0$ coordinates. One of the main advantages of this representation is the fact that it enables the use of the transformed cluster currents and voltages as degrees of freedom to regulate the converter [77, 78].

Considering that voltages connected to the input-output ports are balanced (i.e. $v_{g0} = v_{m0} = 0$) and there is not current path between neutral points N and n (i.e. $i_{00} = 0$), the Voltage-Current model of (3.5) can be re-written as four independent equations:

$$\sqrt{3} \begin{bmatrix} v_{m\alpha} \\ v_{m\beta} \end{bmatrix} = \begin{bmatrix} v_{\alpha 0} \\ v_{\beta 0} \end{bmatrix} + L_c \frac{\mathrm{d}}{\mathrm{d}t} \begin{bmatrix} i_{\alpha 0} \\ i_{\beta 0} \end{bmatrix} \tag{3.6}$$

$$-\sqrt{3} \begin{bmatrix} v_{g\alpha} \\ v_{g\beta} \end{bmatrix} = \begin{bmatrix} v_{0\alpha} \\ v_{0\beta} \end{bmatrix} + L_c \frac{\mathrm{d}}{\mathrm{d}t} \begin{bmatrix} i_{0\alpha} \\ i_{0\beta} \end{bmatrix} \tag{3.7}$$

$$\begin{bmatrix} v_{\alpha\alpha} & v_{\beta\alpha} \\ v_{\alpha\beta} & v_{\beta\beta} \end{bmatrix} = -L_c \frac{\mathrm{d}}{\mathrm{d}t} \begin{bmatrix} i_{\alpha\alpha} & i_{\beta\alpha} \\ i_{\alpha\beta} & i_{\beta\beta} \end{bmatrix} \tag{3.8}$$

$$\sqrt{3} v_{m0} = L_c \frac{\mathrm{d}}{\mathrm{d}t} i_{00} + v_{00} + \sqrt{3} v_{g0} + 3 v_n \tag{3.9}$$

Analysing (3.9), it is concluded that $v_{00} = -3 v_n$. Additionally, using Kirchhoff current law in Fig. 3.2 (see Appendix A), the following relationships are obtained:

$$i_{m\alpha} = \sqrt{3}\, i_{\alpha 0} \; ; \; i_{m\beta} = \sqrt{3}\, i_{\beta 0} \tag{3.10}$$

$$i_{g\alpha} = \sqrt{3}\, i_{0\alpha} \; ; \; i_{g\beta} = \sqrt{3}\, i_{0\beta} \tag{3.11}$$

At this point, the following definitions are made:

- $i_{\alpha 0}$ and $i_{\beta 0}$ are proportional to the machine-side currents.

- $i_{0\alpha}$ and $i_{0\beta}$ are proportional to the grid-side currents

- The currents $i_{\alpha\alpha}$, $i_{\beta\alpha}$, $i_{\alpha\beta}$ and $i_{\beta\beta}$ do not appears either at the input or output ports. Consequently, they are referred to as Circulating Currents.

Replacing (3.10) into (3.6) and (3.11) into (3.7), the Voltage-Current model of the M^3C can be re-written as a function of the input and output currents as follows:

$$\begin{bmatrix} v_{m\alpha} \\ v_{m\beta} \end{bmatrix} = \frac{1}{\sqrt{3}} \begin{bmatrix} v_{\alpha 0} \\ v_{\beta 0} \end{bmatrix} + \frac{L_c}{3} \frac{\mathrm{d}}{\mathrm{d}t} \begin{bmatrix} i_{m\alpha} \\ i_{m\beta} \end{bmatrix} \tag{3.12}$$

$$-\begin{bmatrix} v_{g\alpha} \\ v_{g\beta} \end{bmatrix} = \frac{1}{\sqrt{3}} \begin{bmatrix} v_{0\alpha} \\ v_{0\beta} \end{bmatrix} + \frac{L_c}{3} \frac{\mathrm{d}}{\mathrm{d}t} \begin{bmatrix} i_{g\alpha} \\ i_{g\beta} \end{bmatrix} \tag{3.13}$$

In this manner, decoupled equations are obtained to represent the voltages and currents of the machine-side system, (3.12). The currents and voltages of the grid-side system are represented by (3.13). The transformed cluster voltages and currents of the M^3C are represented by (3.8) and the common-mode voltage (3.9).

The equivalent circuits of the equations mentioned above are presented in Fig. 3.3. Using this representation, it is straightforward to implement conventional control systems. For instance, the equivalent circuit of the machine-side can be regulated using a conventional dq control scheme rotating at the machine frequency.
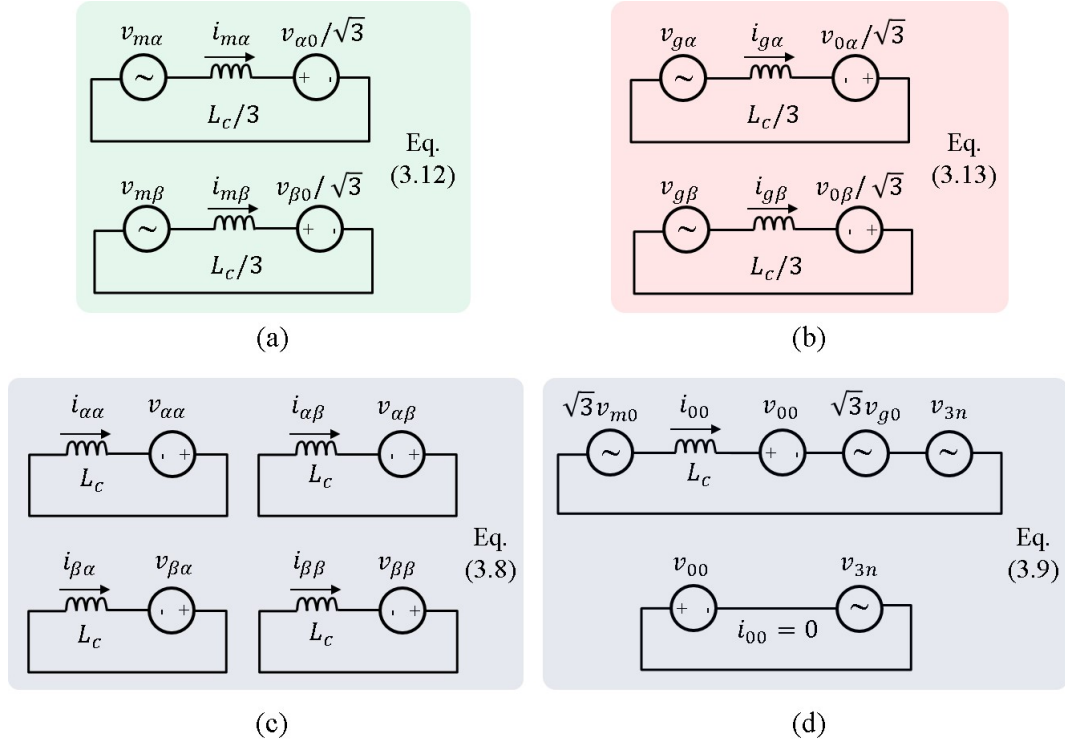
Figure 3.3: Equivalent circuits of the Voltage-Current model of the M^3C in Double-$\alpha\beta0$ coordinates. (a) Machine-side equivalent circuit. (b) Grid-side equivalent circuit. (c) Circulating currents equivalent circuit. (d) Common-mode voltage equivalent circuits.

3.2.2 Power-Capacitor Voltage Model

The flying capacitors of the M^3C are not connected to external voltage sources and should be regulated to provide proper operation of the converter. Then, a dynamics model to regulate the capacitor voltages of the M^3C is required. In this section, it is assumed that the problem of Single-Cell balancing is able to regulate to the same value all the capacitor voltages within a cluster. Then, the focus is to ensure equal Cluster Capacitor Voltage (CCV) distribution.

As it was mentioned before, the CCVs represent the sum of capacitor voltages in each cluster. In matrix notation, the nine the CCVs of the M^3C are defined as:

$$
\begin{bmatrix}
v_{c_{ar}} & v_{c_{as}} & v_{c_{at}} \\
v_{c_{br}} & v_{c_{bs}} & v_{c_{bt}} \\
v_{c_{cr}} & v_{c_{cs}} & v_{c_{ct}}
\end{bmatrix}
=
\begin{bmatrix}
\sum_{i=1}^{n} v_{c_{ar}}^{i} & \sum_{i=1}^{n} v_{c_{as}}^{i} & \sum_{i=1}^{n} v_{c_{at}}^{i} \\
\sum_{i=1}^{n} v_{c_{br}}^{i} & \sum_{i=1}^{n} v_{c_{bs}}^{i} & \sum_{i=1}^{n} v_{c_{bt}}^{i} \\
\sum_{i=1}^{n} v_{c_{cr}}^{i} & \sum_{i=1}^{n} v_{c_{cs}}^{i} & \sum_{i=1}^{n} v_{c_{ct}}^{i}
\end{bmatrix}
\tag{3.14}
$$

Where n stands for the number of power cells per cluster.

The relation between the CCVs and the power flows in their corresponding cluster is used to obtain a dynamics model of (3.14). Considering a generic cluster as a representative example [see Fig.3.1b], the cluster energy W_{xy} is related to the capacitor voltage as follows:

$$
W_{xy} = \frac{1}{2}C\sum_{i=1}^{n} v_{c_{xy}}^{i2}
\tag{3.15}
$$

Where $x \in \{a, b, c\}$ and $y \in \{r, s, t\}$. Additionally, it is assumed that the power cells have the same capacitance C and their capacitors are controlled to the desired value v_c^*. Neglecting internal losses and the power dissipated in the cluster inductor, the relationship between the CCV and the cluster power yields to:

$$
\frac{\mathrm{d}}{\mathrm{d}t}v_{c_{xy}} \approx \frac{P_{xy}}{Cv_c^*}
\tag{3.16}
$$

By inspection of (3.15) and (3.16), it is concluded that control of the M^3C can be done indistinctly using the energy or Cluster Capacitor Voltages when the capacitance C is equal for all the power cells.

Extending (3.16) to the nine Cluster Capacitor Voltages yields to:

$$
\frac{\mathrm{d}}{\mathrm{d}t}
\begin{bmatrix}
v_{c_{ar}} & v_{c_{as}} & v_{c_{at}} \\
v_{c_{br}} & v_{c_{bs}} & v_{c_{bt}} \\
v_{c_{cr}} & v_{c_{cs}} & v_{c_{ct}}
\end{bmatrix}
\approx \frac{1}{Cv_c^*}
\begin{bmatrix}
P_{ar} & P_{as} & P_{at} \\
P_{br} & P_{bs} & P_{bt} \\
P_{cr} & P_{cs} & P_{ct}
\end{bmatrix}
\tag{3.17}
$$

It is usefull to consider that CCVs are composed of an average value $\bar{v}_{c_{xy}}$ and a ripple component $\tilde{v}_{c_{xy}}$:

$$v_{c_{xy}} = \bar{v}_{c_{xy}} + \tilde{v}_{c_{xy}} \tag{3.18}$$

Then, (3.17) can be reformuled as follows:

$$\begin{bmatrix} v_{c_{ar}} & v_{c_{as}} & v_{c_{at}} \\ v_{c_{br}} & v_{c_{bs}} & v_{c_{bt}} \\ v_{c_{cr}} & v_{c_{cs}} & v_{c_{ct}} \end{bmatrix} \approx \frac{1}{Cv_c^*} \int \begin{bmatrix} P_{ar} & P_{as} & P_{at} \\ P_{br} & P_{bs} & P_{bt} \\ P_{cr} & P_{cs} & P_{ct} \end{bmatrix} \mathrm{d}t + nv_c^* \begin{bmatrix} 1 & 1 & 1 \\ 1 & 1 & 1 \\ 1 & 1 & 1 \end{bmatrix} \tag{3.19}$$

Either (3.17) or (3.19) are refered to as Power-CCV model of the M^3C. By simple inspection of (3.19), it is straightforward realise that the ripple components of the Cluster Capacitor Voltages depends on the cluster instanstaneous power, whereas the average value tends to $\bar{v}_{c_{xy}} = nv_c^*$.

At this point, the Double $\alpha\beta0$ Transformation is applied to the Power-CCV model of (3.19) because it enables a decoupled representation of the energy interaction among all the clusters of the M^3C [77,78]. Therefore, (3.19) is pre-multiplied by $\mathbf{C}_{\alpha\beta0}^T$ and post-multiplied by $\mathbf{C}_{\alpha\beta0}$ to obtain:

$$\begin{bmatrix} v_{c_{\alpha\alpha}} & v_{c_{\beta\alpha}} & v_{c_{0\alpha}} \\ v_{c_{\alpha\beta}} & v_{c_{\beta\beta}} & v_{c_{0\beta}} \\ v_{c_{\alpha0}} & v_{c_{\beta0}} & v_{c_{00}} \end{bmatrix} \approx \frac{1}{Cv_c^*} \int \begin{bmatrix} P_{\alpha\alpha} & P_{\beta\alpha} & P_{0\alpha} \\ P_{\alpha\beta} & P_{\beta\beta} & P_{0\beta} \\ P_{\alpha0} & P_{\beta0} & P_{00} \end{bmatrix} \mathrm{d}t + \begin{bmatrix} 0 & 0 & 0 \\ 0 & 0 & 0 \\ 0 & 0 & 3nv_c^* \end{bmatrix} \tag{3.20}$$

The relation of (3.20) represents the Power-CCV model of the M^3C in Double-$\alpha\beta0$ coordinates. More details about this procedure are given in Appendix B.

The voltage terms of the left side of (3.20) have the following physical meaning:

- The voltage terms $v_{c_{\alpha\alpha}}$, $v_{c_{\beta\alpha}}$, $v_{c_{\alpha\beta}}$, $v_{c_{\beta\beta}}$ represent the CCV imbalances inside a Sub-Converter, called *Intra-CCV Imbalance terms*.

- The terms $v_{c_{0\alpha}}$, $v_{c_{0\beta}}$, $v_{c_{\alpha0}}$ and $v_{c_{\beta0}}$ represent the CCV imbalances between different Sub-Converters , called *Inter-CCV Imbalance terms*.

- Finally, the term $v_{c_{00}}$ is related to the total active power flowing into/from the M^3C and can be regulated to set the average value of all the CCVs.

3.2.2.1 Ripple power components

The power components in the right side of (3.19) represents the energy interactions among different clusters and produce the ripple component of the CCV. These components can be expressed as a function of the voltages and currents of the M^3C as follows:

$$
\begin{bmatrix}
P_{ar} & P_{as} & P_{at} \\
P_{br} & P_{bs} & P_{bt} \\
P_{cr} & P_{cs} & P_{ct}
\end{bmatrix}
=
\begin{bmatrix}
v_{ar}i_{ar} & v_{as}i_{as} & v_{at}i_{at} \\
v_{br}i_{br} & v_{bs}i_{bs} & v_{bt}i_{bt} \\
v_{cr}i_{cr} & v_{cs}i_{cs} & v_{ct}i_{ct}
\end{bmatrix}
\tag{3.21}
$$

Being v_{xy} the cluster output voltages and i_{xy} the cluster currents, with $x \in \{a, b, c\}$ and $y \in \{r, s, t\}$.

Applying the Double $\alpha\beta0$ Transformation to (3.21) and after some manipulations/simplifications (see Appendix C), the power components of the right side of (3.20) are expressed as a function of the transformed currents and voltages of the M^3C in Double-$\alpha\beta0$ coordinates [78].

$$
P_{\alpha\alpha} = \frac{1}{3}(v_{m\alpha}i_{g\alpha} - v_{g\alpha}i_{m\alpha}) + \frac{1}{\sqrt{6}}(v_{m\alpha}i_{\alpha\alpha} - v_{m\beta}i_{\beta\alpha}) - \frac{1}{\sqrt{6}}(v_{g\alpha}i_{\alpha\alpha} - v_{g\beta}i_{\alpha}) - v_n i_{\alpha\alpha} \tag{3.22}
$$

$$
P_{\alpha\beta} = \frac{1}{3}(v_{m\alpha}i_{g\beta} - v_{g\beta}i_{m\alpha}) + \frac{1}{\sqrt{6}}(v_{m\alpha}i_{\alpha\beta} - v_{m\beta}i_{\beta\beta}) + \frac{1}{\sqrt{6}}(v_{g\alpha}i_{\alpha\beta} + v_{g\beta}i_{\alpha\alpha}) - v_n i_{\alpha\beta} \tag{3.23}
$$

$$
P_{\beta\alpha} = \frac{1}{3}(v_{m\beta}i_{g\alpha} - v_{g\alpha}i_{m\beta}) - \frac{1}{\sqrt{6}}(v_{m\alpha}i_{\beta\alpha} + v_{m\beta}i_{\alpha\alpha}) - \frac{1}{\sqrt{6}}(v_{g\alpha}i_{\beta\alpha} - v_{g\beta}i_{\beta\beta}) - v_n i_{\beta\alpha} \tag{3.24}
$$

$$
P_{\beta\beta} = \frac{1}{3}(v_{m\beta}i_{g\beta} - v_{g\beta}i_{m\beta}) - \frac{1}{\sqrt{6}}(v_{m\alpha}i_{\beta\beta} + v_{m\beta}i_{\alpha\beta}) + \frac{1}{\sqrt{6}}(v_{g\alpha}i_{\beta\beta} + v_{g\beta}i_{\beta\alpha}) - v_n i_{\beta\beta} \tag{3.25}
$$

$$
P_{\alpha0} = \frac{1}{3\sqrt{2}}(v_{m\alpha}i_{m\alpha} - v_{m\beta}i_{m\beta}) - \frac{1}{\sqrt{3}}(v_{g\alpha}i_{\alpha\alpha} + v_{g\beta}i_{\alpha\beta}) - \frac{1}{\sqrt{3}}v_n i_{m\alpha} \tag{3.26}
$$

$$
P_{\beta0} = -\frac{1}{3\sqrt{2}}(v_{m\alpha}i_{m\beta} + v_{m\beta}i_{m\alpha}) - \frac{1}{\sqrt{3}}(v_{g\alpha}i_{\beta\alpha} + v_{g\beta}i_{\beta\beta}) - \frac{1}{\sqrt{3}}v_n i_{m\beta} \tag{3.27}
$$

$$
P_{0\alpha} = -\frac{1}{3\sqrt{2}}(v_{g\alpha}i_{g\alpha} - v_{g\beta}i_{g\beta}) + \frac{1}{\sqrt{3}}(v_{m\alpha}i_{\alpha\alpha} + v_{m\beta}i_{\beta\alpha}) - \frac{1}{\sqrt{3}}v_n i_{g\alpha} \tag{3.28}
$$

$$
P_{0\beta} = \frac{1}{3\sqrt{2}}(v_{g\alpha}i_{g\beta} + v_{g\beta}i_{g\alpha}) + \frac{1}{\sqrt{3}}(v_{m\alpha}i_{\alpha\beta} + v_{m\beta}i_{\beta\beta}) - \frac{1}{\sqrt{3}}v_n i_{g\beta} \tag{3.29}
$$

$$
P_{00} = \frac{1}{3}(v_{m\alpha}i_{m\alpha} + v_{m\beta}i_{m\beta}) - \frac{1}{3}(v_{g\alpha}i_{g\alpha} + v_{g\beta}i_{g\beta}) \tag{3.30}
$$

The power components given in (3.22)−(3.30) represent the energy changes in the M^3C. For instance, the power flow P_{00} defines the total power flowing into/from the M^3C. The components $P_{\alpha\alpha}, P_{\alpha\beta}, P_{\beta\alpha}, P_{\beta\beta}$ represent power flows inside a sub-converter (Intra-CCV). Whereas, the components $P_{\alpha0}, P_{\beta0}, P_{0\alpha}, P_{0\beta}$ represent power flows from one Sub-Converter to the others (Inter-CCV).

For correct operation of the M^3C, all the capacitors should be regulated to the same voltage level. When this condition is satisfied, i.e. all the capacitor voltages are equal to v_c^*, the power flows (3.22)−(3.30) tends to zero, and (3.20) becomes:

$$
\begin{bmatrix} v_{c\alpha\alpha} & v_{c\beta\alpha} & v_{c0\alpha} \\ v_{c\alpha\beta} & v_{c\beta\beta} & v_{c0\beta} \\ v_{c\alpha0} & v_{c\beta0} & v_{c00} \end{bmatrix} = \begin{bmatrix} 0 & 0 & 0 \\ 0 & 0 & 0 \\ 0 & 0 & 3nv_c^* \end{bmatrix} \tag{3.31}
$$

In steady state, the M^3C is 'Balanced' when (3.31) is achieved. Then, a suitable control system for the M^3C must be able to control the CCV imbalance terms to zero and the component v_{c00} to $3nv_c^*$.

3.3 CCV ripple analysis

3.3.1 CCV ripple in $abc - rst$ coordinates

Depending on the operational conditions of the M^3C, the ripple component of the CCVs can present large fluctuations that must be prevented to ensure proper and safe operation of the M^3C. These fluctuations are analysed in this Subsection using the cluster ar as a representative example.

Assuming neither circulating current nor common-mode voltage is injected, and neglecting the effect of the cluster inductor, the instantaneous active power of the cluster ar is given by:

$$
P_{ar} = v_{ar}i_{ar} = (v_{ma} - v_{gr})\frac{1}{3}(i_{ma} + i_{gr}) \tag{3.32}
$$

Additionally, the input/output voltage and current are defined as follows:

$$
v_{ma} = V_m \cos(\omega_m t + \delta) \tag{3.33}
$$

$$
i_{ma} = I_m \cos(\omega_m t + \delta + \phi_m) \tag{3.34}
$$

$$
v_{gr} = V_g \cos(\omega_g t) \tag{3.35}
$$

$$
i_{gr} = I_g \cos(\omega_g t + \phi_g) \tag{3.36}
$$

where $\omega_m = 2\pi f_m$ and $\omega_g = 2\pi f_g$. Note that V_m and V_g are the machine and grid-side phase-to-neutral peak voltage magnitudes, respectively. I_m and I_g are the machine and grid-side peak current magnitudes, respectively. f_m and f_g are the machine and grid-side frequencies. The angles ϕ_m and ϕ_g are the machine and grid-side phase angles, and δ is the initial phase of the machine with respect to the grid at $t=0$.

From (3.19), the ripple component of $v_{c_{ar}}$ can be calculated replacing (3.33)−(3.36) into (3.32) yielding to:

$$\tilde{v}_{c_{ar}} \approx \frac{V_g I_g}{4\omega_g C v_c^*} \sin(2\omega_g t + \phi_g) + \frac{V_m I_m}{4\omega_m C v_c^*} \sin(2\omega_m t + \phi_m)$$

$$+ \frac{I_g V_m}{C v_c^*(\omega_g^2 - \omega_m^2)} \left[(\omega_g \sin(\omega_g t + \phi_g) \cos(\omega_m t)) - (\omega_m \cos(\omega_g t + \phi_g) \sin(\omega_m t)) \right] \quad (3.37)$$

$$+ \frac{I_m V_g}{C v_c^*(\omega_g^2 - \omega_m^2)} \left[(\omega_m \sin(\omega_m t + \phi_m) \cos(\omega_g t)) - (\omega_g \cos(\omega_m t + \phi_m) \sin(\omega_g t)) \right]$$

Analysing (3.37), $\tilde{v}_{c_{ar}}$ contains components that are inversely proportional to the machine and grid frequencies. Then, the components of frequencies f_m, f_g and $f_m \pm f_g$ can lead to large voltage fluctuations in the following situations:

- $f_g = 0$

- $f_m = 0$

- $f_m = f_g$

- $f_m = -f_g$

Therefore, the M^3C has an inherent problem when the machine frequency is close or equal to $\pm$ the grid frequency. The condition when f_m is zero is not complex to control because this oscillation also depend on the voltage and current magnitudes (generally, a low f_m implies a low $V_m I_m$). Additionally, it is assumed that the output port of the M^3C is connected to the electrical network with a frequency of, for example, 50 Hz. Then, the case of f_g=0 is not very likely.

From a control point of view, the operation of the M^3C will be divided into a Low-Frequency Mode (LFM) and an Equal-Frequency Mode (EFM). The LFM is enabled when the machine frequency is $f_m < \pm 0.8 f_g$ (this threshold depends on the parameters of the M^3C [94]). In the LFM, the voltage oscillations in the capacitors are within an acceptable range and the main control task to regulate the average component of the CCVs as shown in (3.31). This process is called 'Balancing'. On the other hand, the EFM is enabled when the machine frequency is close to $\pm$ the grid frequency. In this case, the voltage fluctuations can be complex to control and power flows produced by the circulating currents and common-mode voltage have to be used to mitigate the voltage oscillations. This task is called 'Mitigation'.

3.3.2 CCV ripple in Double-$\alpha\beta0$ coordinates

Assuming neither circulating current nor common-mode voltage is injected, the instantaneous power flows of (3.22)−(3.29) are simplified to:

$$P_{\alpha\alpha} = \frac{1}{3}(v_{m\alpha} i_{g\alpha} - v_{g\alpha} i_{m\alpha}) \quad (3.38)$$

$$P_{\alpha\beta} = \frac{1}{3}(v_{m\alpha}\mathrm{i}_{g\beta} - v_{g\beta}\mathrm{i}_{m\alpha}) \tag{3.39}$$

$$P_{\beta\alpha} = \frac{1}{3}(v_{m\beta}\mathrm{i}_{g\alpha} - v_{g\alpha}\mathrm{i}_{m\beta}) \tag{3.40}$$

$$P_{\beta\beta} = \frac{1}{3}(v_{m\beta}\mathrm{i}_{g\beta} - v_{g\beta}\mathrm{i}_{m\beta}) \tag{3.41}$$

$$P_{\alpha 0} = \frac{1}{3\sqrt{2}}(v_{m\alpha}\mathrm{i}_{m\alpha} - v_{m\beta}\mathrm{i}_{m\beta}) \tag{3.42}$$

$$P_{\beta 0} = -\frac{1}{3\sqrt{2}}(v_{m\alpha}\mathrm{i}_{m\beta} + v_{m\beta}\mathrm{i}_{m\alpha}) \tag{3.43}$$

$$P_{0\alpha} = -\frac{1}{3\sqrt{2}}(v_{g\alpha}\mathrm{i}_{g\alpha} - v_{g\beta}\mathrm{i}_{g\beta}) \tag{3.44}$$

$$P_{0\beta} = \frac{1}{3\sqrt{2}}(v_{g\alpha}\mathrm{i}_{g\beta} + v_{g\beta}\mathrm{i}_{g\alpha}) \tag{3.45}$$

Replacing (3.38)$-$(3.45) into the Power-CCV model of (3.20), the ripple components of the CCVs in Double-$\alpha\beta 0$ coordinates are given by:

$$
\tilde{v}_{c_{\alpha\alpha}} \approx \frac{1}{3Cv_c^*}\Big[\frac{V_m I_g \sin(\phi_g + (\omega_g - \omega_m)t) + V_g I_m \sin(\phi_m - (\omega_g - \omega_m)t)}{2(\omega_g - \omega_m)} \\
+ \frac{V_m I_g \sin(\phi_g + (\omega_g + \omega_m)t) - V_g I_m \sin(\phi_m + (\omega_g + \omega_m)t)}{2(\omega_g + \omega_m)}\Big] \tag{3.46}
$$

$$
\tilde{v}_{c_{\alpha\beta}} \approx \frac{1}{3Cv_c^*}\Big[\frac{V_g I_m \cos(\phi_m - (\omega_g - \omega_m)t) - V_m I_g \cos(\phi_g + (\omega_g - \omega_m)t)}{2(\omega_g - \omega_m)} \\
+ \frac{V_g I_m \cos(\phi_m + (\omega_g + \omega_m)t) - V_m I_g \cos(\phi_g + (\omega_g + \omega_m)t)+}{2(\omega_g + \omega_m)}\Big] \tag{3.47}
$$

$$
\tilde{v}_{c_{\beta\alpha}} \approx \frac{1}{3Cv_c^*}\Big[\frac{V_m I_g \cos(\phi_g + (\omega_g - \omega_m)t) - V_g I_m \cos(\phi_m - (\omega_g - \omega_m)t)}{2(\omega_g - \omega_m)} \\
+ \frac{V_g I_m \cos(\phi_m + (\omega_g + \omega_m)t) - V_m I_g \cos(\phi_g + (\omega_g + \omega_m)t)+}{2(\omega_g + \omega_m)}\Big] \tag{3.48}
$$

$$
\tilde{v}_{c_{\beta\beta}} \approx \frac{1}{3Cv_c^*}\Big[\frac{V_m I_g \sin(\phi_g + (\omega_g - \omega_m)t) + V_g I_m \sin(\phi_m - (\omega_g - \omega_m)t)}{2(\omega_g - \omega_m)} \\
+ \frac{V_g I_m \sin(\phi_m + (\omega_g + \omega_m)t) - V_m I_g \sin(\phi_g + (\omega_g + \omega_m)t)}{2(\omega_g + \omega_m)}\Big] \tag{3.49}
$$

$$\tilde{v}_{c_{\alpha 0}} \approx \frac{1}{3\sqrt{2}Cv_c^*}\left[\frac{V_m I_m \sin(\phi_m + 2\omega_m t)}{2\omega_m}\right] \tag{3.50}$$

$$\tilde{v}_{c_{\beta 0}} \approx \frac{1}{3\sqrt{2}Cv_c^*}\left[\frac{V_m I_m \cos(\phi_m + 2\omega_m t)}{2\omega_m}\right] \tag{3.51}$$

$$\tilde{v}_{c_{0\alpha}} \approx \frac{-1}{3\sqrt{2}Cv_c^*}\left[\frac{V_g I_g \sin(\phi_g + 2\omega_g t)}{2\omega_g}\right] \tag{3.52}$$

$$\tilde{v}_{c_{0\beta}} \approx \frac{-1}{3\sqrt{2}Cv_c^*} \left[\frac{V_g I_g \cos(\phi_g + 2\omega_g t)}{2\omega_g} \right] \tag{3.53}$$

The first four ripple components (3.46)−(3.49) leads to unacceptable voltage oscillations when $f_m = \pm f_g$. Whereas, the components of (3.50)−(3.51) are unstable when $f_m = 0$. Finally, the terms (3.52)−3.53 become undefined when $f_g = 0$.

3.4   Classification of the voltage fluctuations

In Subsections 3.3.1 and 3.3.2, it had been shown that the ripple components of the CCVs are produced for a part of the instantaneous power flows because neither circulating current nor common-mode voltage injection is considered. Consequently, the components of (3.22)−(3.29) are classified into the three following categories:

- Non-Controllable: These components depend on the machine or grid voltages and currents and cannot be regulated without affecting the input or the output systems.

- Semi-Controllable: These components are a combination of circulating currents or common mode voltage with the input or the output voltages. The SC components can be partially regulated without affecting the input and output ports.

- Fully-Controllable: These components are composed of the combination of common mode voltage and circulating currents. Then, they can be regulated without any effect at the input or output systems.

Table 3.1 shows this classification considering the extended form of the (3.22)−(3.29). Note that the term P_{00} is not included since it is not related to the CCV Imbalance terms.

By simple inspection of Table 3.1 and (3.46)−(3.53), it is concluded that the oscillations in the capacitors are produced by the Non-controllable components. The Semi-controllable and Fully-controllable components are degrees of freedom to control the converter and their influence in the oscillations can be used to compensate the oscillations.

Power Term	Non-Controllable	Semi-Controllable	Fully Controllable
$P_{\alpha\alpha}$	$\dfrac{v_{m\alpha} i_{g\alpha} - v_{g\alpha} i_{m\alpha}}{3}$	$\dfrac{1}{\sqrt{6}}\left(v_{m\alpha} i_{\alpha\alpha} - v_{m\beta} i_{\beta\alpha}\right)$ $\dfrac{-1}{\sqrt{6}}\left(v_{g\alpha} i_{\alpha\alpha} - v_{g\beta} i_{\alpha\beta}\right)$	$-v_n i_{\alpha\alpha}$
$P_{\alpha\beta}$	$\dfrac{v_{m\alpha} i_{g\beta} - v_{g\beta} i_{m\alpha}}{3}$	$\dfrac{1}{\sqrt{6}}\left(v_{m\alpha} i_{\alpha\beta} - v_{m\beta} i_{\beta\beta}\right)$ $\dfrac{+1}{\sqrt{6}}\left(v_{g\alpha} i_{\alpha\beta} + v_{g\beta} i_{\alpha\alpha}\right)$	$-v_n i_{\alpha\beta}$
$P_{\beta\alpha}$	$\dfrac{v_{m\beta} i_{g\alpha} - v_{g\alpha} i_{m\beta}}{3}$	$\dfrac{-1}{\sqrt{6}}\left(v_{m\alpha} i_{\beta\alpha} + v_{m\beta} i_{\alpha\alpha}\right)$ $\dfrac{-1}{\sqrt{6}}\left(v_{g\alpha} i_{\beta\alpha} - v_{g\beta} i_{\beta\beta}\right)$	$-v_n i_{\beta\alpha}$
$P_{\beta\beta}$	$\dfrac{v_{m\beta} i_{g\beta} - v_{g\beta} i_{m\beta}}{3}$	$\dfrac{-1}{\sqrt{6}}\left(v_{m\alpha} i_{\beta\beta} + v_{m\beta} i_{\alpha\beta}\right)$ $\dfrac{+1}{\sqrt{6}}\left(v_{g\alpha} i_{\beta\beta} + v_{g\beta} i_{\beta\alpha}\right)$	$-v_n i_{\beta\beta}$
$P_{\alpha 0}$	$\dfrac{v_{m\alpha} i_{m\alpha} - v_{m\beta} i_{m\beta}}{3\sqrt{2}}$	$\dfrac{-v_{g\alpha} i_{\alpha\alpha} - v_{g\beta} i_{\alpha\beta} - v_n i_{m\beta}}{\sqrt{3}}$	
$P_{\beta 0}$	$\dfrac{-v_{m\alpha} i_{m\beta} - v_{m\beta} i_{m\alpha}}{3\sqrt{2}}$	$\dfrac{-v_{g\alpha} i_{\beta\alpha} - v_{g\beta} i_{\beta\beta} - v_n i_{m\beta}}{\sqrt{3}}$	
$P_{0\alpha}$	$\dfrac{-v_{g\alpha} i_{g\alpha} + v_{g\beta} i_{g\beta}}{3\sqrt{2}}$	$\dfrac{v_{m\alpha} i_{\alpha\alpha} + v_{m\beta} i_{\beta\alpha} - v_n i_{g\alpha}}{\sqrt{3}}$	
$P_{0\beta}$	$\dfrac{v_{g\alpha} i_{g\beta} + v_{g\beta} i_{g\alpha}}{3\sqrt{2}}$	$\dfrac{v_{m\alpha} i_{\alpha\beta} + v_{m\beta} i_{\beta\beta} - v_n i_{g\beta}}{\sqrt{3}}$	
P_{00}	$\dfrac{\left(v_{g\alpha} i_{g\alpha} + v_{g\beta} i_{g\beta}\right) - \left(v_{g\alpha} i_{g\alpha} + v_{g\beta} i_{g\beta}\right)}{3}$		

Table 3.1: Classification of the Cluster Capacitor Voltage components.

3.5 $\Sigma\Delta$ Transformation applied to the M^3C

In several applications related to power electronics, the analyses become easier using different reference frames (abc, $\alpha\beta$, dq, etc.). Consequently, this proposal introduces the use of an additional linear transformation, called $\Sigma\Delta$ Transformation, to enable a vector representation of the CCVs.

The $\Sigma\Delta$ Transformation has been introduced previously in M^2C control systems to consider the interaction of the electrical variables among the converter poles [95], representing the sum and difference of two variables. Additionally, this transformation has been used to obtain a geometrical orientation of the four circulating currents of the M^3C [88].

The $\Sigma\Delta$ Transformation can be written in matrix form to transform a generic vector $\vec{X}$ from the Double $\alpha\beta0$ frame to the $\Sigma\Delta$ frame as follow:

$$\begin{bmatrix} X_{1\alpha}^{\Sigma\Delta} \\ X_{1\beta}^{\Sigma\Delta} \\ X_{2\alpha}^{\Sigma\Delta} \\ X_{2\beta}^{\Sigma\Delta} \end{bmatrix} = \frac{1}{2} \begin{bmatrix} 1 & 0 & 0 & 1 \\ 0 & 1 & -1 & 0 \\ 1 & 0 & 0 & -1 \\ 0 & 1 & 1 & 0 \end{bmatrix} \begin{bmatrix} X_{\alpha\alpha} \\ X_{\alpha\beta} \\ X_{\beta\alpha} \\ X_{\beta\beta} \end{bmatrix} \tag{3.54}$$

3.5.1 CCV ripple in $\Sigma\Delta$ Double-$\alpha\beta 0$ coordinates

The $\Sigma\Delta$ Transformation is applied to the four ripple components (3.46)$-$(3.49), leading to:

$$\tilde{v}_{c_{1\alpha}}^{\Sigma\Delta}=\frac{1}{2}(\tilde{v}_{c_{\alpha\alpha}}+\tilde{v}_{c_{\beta\beta}})\approx\frac{1}{3Cv_c^*}\left[\frac{V_mI_g\sin(\phi_g+(\omega_g-\omega_m)t)+V_gI_m\sin(\phi_m-(\omega_g-\omega_m)t)}{2(\omega_g-\omega_m)}\right] \quad (3.55)$$

$$\tilde{v}_{c_{1\beta}}^{\Sigma\Delta}=\frac{1}{2}(\tilde{v}_{c_{\alpha\beta}}-\tilde{v}_{c_{\beta\alpha}})\approx\frac{1}{3Cv_c^*}\left[\frac{V_gI_m\cos(\phi_m-(\omega_g-\omega_m)t)-V_mI_g\cos(\phi_g+(\omega_g-\omega_m)t)}{2(\omega_g-\omega_m)}\right] \quad (3.56)$$

$$\tilde{v}_{c_{2\alpha}}^{\Sigma\Delta}=\frac{1}{2}(\tilde{v}_{c_{\alpha\alpha}}-\tilde{v}_{c_{\beta\beta}})\approx\frac{1}{3Cv_c^*}\left[\frac{V_gI_m\sin(\phi_m+(\omega_g+\omega_m)t)-V_mI_g\sin(\phi_g+(\omega_g+\omega_m)t)}{2(\omega_g+\omega_m)}\right] \quad (3.57)$$

$$\tilde{v}_{c_{2\beta}}^{\Sigma\Delta}=\frac{1}{2}(\tilde{v}_{c_{\alpha\beta}}+\tilde{v}_{c_{\beta\alpha}})\approx\frac{1}{3Cv_c^*}\left[\frac{V_gI_m\cos(\phi_m+(\omega_g+\omega_m)t)-V_mI_g\cos(\phi_g+(\omega_g+\omega_m)t)}{2(\omega_g+\omega_m)}\right] \quad (3.58)$$

The use of the $\Sigma\Delta$ Transformation enables a better representation of the CCVs in terms of the machine-grid frequencies because a pair of of CCV ripple terms is obtained for each unstable condition. Summarising:

- The ripple components of (3.55) and (3.56) lead to unacceptable voltage oscillations when $f_m=f_g$.

- The ripple components of (3.57) and (3.58) lead to unacceptable voltage oscillations when $f_m=-f_g$.

- The ripple components of (3.50) and (3.51) lead to unacceptable voltage oscillations when $f_m=0$.

- The ripple components of (3.52) and (3.53) leads to unacceptable voltage oscillations when $f_g=0$.

Analysing the case when $f_m=f_g$, it can be concluded that (3.55) tends to zero when the following operational restrictions are satisfied:

- $\phi_m=-\phi_g$.

- $V_mI_g=V_gI_m$.

The first condition can be achieved adjusting the reactive current of the ports of the M^3C to operate with complementary power factor ($Q_m=-Q_g$). The second condition means that the input port voltage is equal to the output port voltage, which is not probably for a broad range of input-output frequencies operation of electrical machines. However, $V_m=V_g$ can be achieved if the electrical machine has the same rated voltage and frequency than the grid. Notice that a control strategy using these same operational restrictions but in Double-$\alpha\beta 0$ coordinates is described in [92].

3.5.2 Power-CCV model of the M^3C in $\Sigma\Delta$ Double-$\alpha\beta 0$ coordinates

The Power-CCV of the M^3C is expressed in $\Sigma\Delta$ Double-$\alpha\beta 0$ coordinates as follows:

$$
\begin{bmatrix} v_{c_{1\alpha}}^{\Sigma\Delta} & v_{c_{1\beta}}^{\Sigma\Delta} & v_{c_{0\alpha}} \\ v_{c_{2\alpha}}^{\Sigma\Delta} & v_{c_{2\beta}}^{\Sigma\Delta} & v_{c_{0\beta}} \\ v_{c_{\alpha 0}} & v_{c_{\beta 0}} & v_{c_{00}} \end{bmatrix} \approx \frac{1}{Cv_c^*} \int \begin{bmatrix} P_{1\alpha}^{\Sigma\Delta} & p_{1\beta}^{\Sigma\Delta} & P_{0\alpha} \\ P_{2\alpha}^{\Sigma\Delta} & p_{2\beta}^{\Sigma\Delta} & P_{0\beta} \\ P_{\alpha 0} & P_{\beta 0} & P_{00} \end{bmatrix} \mathrm{d}t + \begin{bmatrix} 0 & 0 & 0 \\ 0 & 0 & 0 \\ 0 & 0 & 3nv_c^* \end{bmatrix} \tag{3.59}
$$

The power components of the right side of (3.59) are expressed as a function of the transformed currents and voltages of the M^3C in $\Sigma\Delta$ Double-$\alpha\beta 0$ coordinates as follows:

$$
\begin{aligned}
P_{1\alpha}^{\Sigma\Delta} &= \frac{1}{6}[(v_{m\alpha}i_{g\alpha} - v_{g\alpha}i_{m\alpha}) + (v_{m\beta}i_{g\beta} - v_{g\beta}i_{m\beta})] + \frac{1}{\sqrt{6}}(v_{m\alpha}i_{2\alpha}^{\Sigma\Delta} - v_{m\beta}i_{2\beta}^{\Sigma\Delta}) \\
&\quad + \frac{1}{\sqrt{6}}(-v_{g\alpha}i_{2\alpha}^{\Sigma\Delta} + v_{g\beta}i_{2\beta}^{\Sigma\Delta}) - v_n i_{1\alpha}^{\Sigma\Delta}
\end{aligned} \tag{3.60}
$$

$$
\begin{aligned}
P_{1\beta}^{\Sigma\Delta} &= \frac{1}{6}\left[(v_{m\alpha}i_{g\beta} - v_{g\beta}i_{m\alpha}) - (v_{m\beta}i_{g\alpha} - v_{g\alpha}i_{m\beta})\right] + \frac{1}{\sqrt{6}}(v_{m\alpha}i_{2\beta}^{\Sigma\Delta} + v_{m\beta}i_{2\alpha}^{\Sigma\Delta}) \\
&\quad + \frac{1}{\sqrt{6}}(v_{g\alpha}i_{2\beta}^{\Sigma\Delta} + v_{g\beta}i_{2\alpha}^{\Sigma\Delta}) - v_n i_{1\beta}^{\Sigma\Delta}
\end{aligned} \tag{3.61}
$$

$$
\begin{aligned}
P_{2\alpha}^{\Sigma\Delta} &= \frac{1}{6}\left[(v_{m\beta}i_{g\alpha} - v_{g\alpha}i_{m\beta}) - (v_{m\beta}i_{g\beta} - v_{g\beta}i_{m\beta})\right] + \frac{1}{\sqrt{6}}(v_{m\alpha}i_{1\alpha}^{\Sigma\Delta} + v_{m\beta}i_{1\beta}^{\Sigma\Delta}) \\
&\quad + \frac{1}{\sqrt{6}}(-v_{g\alpha}i_{1\alpha}^{\Sigma\Delta} + v_{g\beta}i_{1\beta}^{\Sigma\Delta}) - v_n i_{2\alpha}^{\Sigma\Delta}
\end{aligned} \tag{3.62}
$$

$$
\begin{aligned}
P_{2\beta}^{\Sigma\Delta} &= \frac{1}{6}\left[(v_{m\beta}i_{g\beta} - v_{g\beta}i_{m\beta}) + (v_{m\beta}i_{g\alpha} - v_{g\alpha}i_{m\beta})\right] + \frac{1}{\sqrt{6}}(v_{m\alpha}i_{1\beta}^{\Sigma\Delta} - v_{m\beta}i_{1\alpha}^{\Sigma\Delta}) \\
&\quad + \frac{1}{\sqrt{6}}(v_{g\alpha}i_{1\beta}^{\Sigma\Delta} + v_{g\beta}i_{1\alpha}^{\Sigma\Delta}) - v_n i_{2\beta}^{\Sigma\Delta}
\end{aligned} \tag{3.63}
$$

$$
\begin{aligned}
P_{\alpha 0} &= \frac{1}{3\sqrt{2}}(v_{m\alpha}i_{m\alpha} - v_{m\beta}i_{m\beta}) - \frac{1}{\sqrt{3}}\left[v_{g\alpha}(i_{1\alpha}^{\Sigma\Delta} + i_{2\alpha}^{\Sigma\Delta}) + v_{g\beta}(i_{1\beta}^{\Sigma\Delta} + i_{2\beta}^{\Sigma\Delta})\right] \\
&\quad - \frac{1}{\sqrt{3}}v_n i_{m\alpha}
\end{aligned} \tag{3.64}
$$

$$
\begin{aligned}
P_{\beta 0} &= -\frac{1}{3\sqrt{2}}(v_{m\alpha}i_{m\beta} + v_{m\beta}i_{m\alpha}) - \frac{1}{\sqrt{3}}\left[v_{g\alpha}(-i_{1\beta}^{\Sigma\Delta} + i_{2\beta}^{\Sigma\Delta}) + v_{g\beta}(i_{1\alpha}^{\Sigma\Delta} - i_{2\alpha}^{\Sigma\Delta})\right] \\
&\quad - \frac{1}{\sqrt{3}}v_n i_{m\beta}
\end{aligned} \tag{3.65}
$$

$$
\begin{aligned}
P_{0\alpha} &= -\frac{1}{3\sqrt{2}}(v_{g\alpha}i_{g\alpha} - v_{g\beta}i_{g\beta}) + \frac{1}{\sqrt{3}}\left[v_{m\alpha}(i_{1\alpha}^{\Sigma\Delta} + i_{2\alpha}^{\Sigma\Delta}) + v_{m\beta}(-i_{1\beta}^{\Sigma\Delta} + i_{2\beta}^{\Sigma\Delta})\right] \\
&\quad - \frac{1}{\sqrt{3}}v_n i_{g\alpha}
\end{aligned} \tag{3.66}
$$

$$P_{0\beta} = \frac{1}{3\sqrt{2}}(v_{g\alpha}\mathrm{i}_{g\beta} + v_{g\beta}\mathrm{i}_{g\alpha}) + \frac{1}{\sqrt{3}}\left[v_{m\alpha}(\mathrm{i}_{1\beta}^{\Sigma\Delta} + \mathrm{i}_{2\beta}^{\Sigma\Delta}) + v_{m\beta}(\mathrm{i}_{1\alpha}^{\Sigma\Delta} - \mathrm{i}_{2\alpha}^{\Sigma\Delta})\right]$$
$$- \frac{1}{\sqrt{3}}v_n\mathrm{i}_{g\beta} \tag{3.67}$$

3.6 Vector Power-CCV model of the M^3C

In this Subsection, a vector representation for the Power-CCV model of M^3C is proposed. The first step consist in using conventional vector notation for the the currents and voltages of the M^3C:

$$
\begin{aligned}
\vec{P}_{1\alpha\beta}^{\Sigma\Delta} &= P_{1\alpha}^{\Sigma\Delta} + jP_{1\beta}^{\Sigma\Delta}\\
\vec{P}_{2\alpha\beta}^{\Sigma\Delta} &= P_{2\alpha}^{\Sigma\Delta} + jP_{2\beta}^{\Sigma\Delta}\\
\vec{P}_0^{\alpha\beta} &= P_{\alpha0} + jP_{\beta0}\\
\vec{P}_{\alpha\beta}^0 &= P_{0\alpha} + jP_{0\beta}\\
\vec{v}_{c_1\alpha\beta}^{\Sigma\Delta} &= v_{c_1\alpha}^{\Sigma\Delta} + jv_{c_1\beta}^{\Sigma\Delta}\\
\vec{v}_{c_2\alpha\beta}^{\Sigma\Delta} &= v_{c_2\alpha}^{\Sigma\Delta} + jv_{c_2\beta}^{\Sigma\Delta}\\
\vec{v}_{m_{\alpha\beta}} &= v_{m\alpha} + jv_{m\beta}\\
\vec{\mathrm{i}}_{m_{\alpha\beta}} &= \mathrm{i}_{m\alpha} + j\mathrm{i}_{m\beta}\\
\vec{v}_{g_{\alpha\beta}} &= v_{g\alpha} + jv_{g\beta}\\
\vec{\mathrm{i}}_{g_{\alpha\beta}} &= \mathrm{i}_{g\alpha} + j\mathrm{i}_{g\beta}
\end{aligned}
\tag{3.68}
$$

Then, it is possible to obtain a vector representation of $(3.60)-(3.67)$ as follows:

$$\vec{P}_{1\alpha\beta}^{\Sigma\Delta} = \frac{1}{6}(\vec{v}_{m_{\alpha\beta}}^{\,c}\,\vec{\mathrm{i}}_{g_{\alpha\beta}} - \vec{v}_{g_{\alpha\beta}}\vec{\mathrm{i}}_{m_{\alpha\beta}}^{\,c}) + \frac{1}{\sqrt{6}}(\vec{v}_{m_{\alpha\beta}}\vec{\mathrm{i}}_{2\alpha\beta}^{\Sigma\Delta} - \vec{v}_{g_{\alpha\beta}}^{\,c}\,\vec{\mathrm{i}}_{2\alpha\beta}^{\Sigma\Delta^c}) - v_n\vec{\mathrm{i}}_{1\alpha\beta}^{\Sigma\Delta} \tag{3.69}$$

$$\vec{P}_{2\alpha\beta}^{\Sigma\Delta} = \frac{1}{6}(\vec{v}_{m_{\alpha\beta}}\vec{\mathrm{i}}_{g_{\alpha\beta}} - \vec{v}_{g_{\alpha\beta}}\vec{\mathrm{i}}_{m_{\alpha\beta}}) + \frac{1}{\sqrt{6}}(\vec{v}_{m_{\alpha\beta}}^{\,c}\,\vec{\mathrm{i}}_{1\alpha\beta}^{\Sigma\Delta} - \vec{v}_{g_{\alpha\beta}}^{\,c}\,\vec{\mathrm{i}}_{1\alpha\beta}^{\Sigma\Delta^c}) - v_n\vec{\mathrm{i}}_{2\alpha\beta}^{\Sigma\Delta} \tag{3.70}$$

$$\vec{P}_0^{\alpha\beta} = \frac{1}{3\sqrt{2}}(\vec{v}_{m_{\alpha\beta}}^{\,c}\,\vec{\mathrm{i}}_{m_{\alpha\beta}}^{\,c}) - \frac{1}{\sqrt{3}}(\vec{v}_{g_{\alpha\beta}}\vec{\mathrm{i}}_{1\alpha\beta}^{\Sigma\Delta^c} + \vec{v}_{g_{\alpha\beta}}^{\,c}\,\vec{\mathrm{i}}_{2\alpha\beta}^{\Sigma\Delta} + v_n\vec{\mathrm{i}}_{m_{\alpha\beta}}) \tag{3.71}$$

$$\vec{P}_{\alpha\beta}^0 = \frac{-1}{3\sqrt{2}}(\vec{v}_{g_{\alpha\beta}}^{\,c}\,\vec{\mathrm{i}}_{g_{\alpha\beta}}^{\,c}) + \frac{1}{\sqrt{3}}(\vec{v}_{m_{\alpha\beta}}\vec{\mathrm{i}}_{1\alpha\beta}^{\Sigma\Delta} + \vec{v}_{m_{\alpha\beta}}^{\,c}\,\vec{\mathrm{i}}_{2\alpha\beta}^{\Sigma\Delta} - v_n\vec{\mathrm{i}}_{g_{\alpha\beta}}) \tag{3.72}$$

Where the superscript c stands for the complex conjugate operator.

Considering the integral relationship between the CCVs and the power terms of (3.59), the Power-CCV model is written in terms of the CCVs:

$$Cv_c^*\frac{\mathrm{d}\vec{v}_{c_1\alpha\beta}^{\Sigma\Delta}}{\mathrm{d}t} \approx \frac{1}{6}(\vec{v}_{m_{\alpha\beta}}^{\,c}\,\vec{\mathrm{i}}_{g_{\alpha\beta}} - \vec{v}_{g_{\alpha\beta}}\vec{\mathrm{i}}_{m_{\alpha\beta}}^{\,c}) + \frac{1}{\sqrt{6}}(\vec{v}_{m_{\alpha\beta}}\vec{\mathrm{i}}_{2\alpha\beta}^{\Sigma\Delta} - \vec{v}_{g_{\alpha\beta}}^{\,c}\,\vec{\mathrm{i}}_{2\alpha\beta}^{\Sigma\Delta^c}) - v_n\vec{\mathrm{i}}_{1\alpha\beta}^{\Sigma\Delta} \tag{3.73}$$

$$C v_c^* \frac{\mathrm{d}\vec{v}_{c_{2\alpha\beta}}^{\Sigma\Delta}}{\mathrm{d}t} \approx \frac{1}{6}(\vec{v}_{m_{\alpha\beta}}\vec{\mathrm{i}}_{g_{\alpha\beta}} - \vec{v}_{g_{\alpha\beta}}\vec{\mathrm{i}}_{m_{\alpha\beta}}) + \frac{1}{\sqrt{6}}(\vec{v}_{m_{\alpha\beta}}^{c}\,\vec{\mathrm{i}}_{1\alpha\beta}^{\Sigma\Delta} - \vec{v}_{g_{\alpha\beta}}^{c}\,\vec{\mathrm{i}}_{1\alpha\beta}^{\Sigma\Delta^c}) - v_n\vec{\mathrm{i}}_{2\alpha\beta}^{\Sigma\Delta} \tag{3.74}$$

$$C v_c^* \frac{\mathrm{d}\vec{v}_{c_0}^{\alpha\beta}}{\mathrm{d}t} \approx \frac{1}{3\sqrt{2}}(\vec{v}_{m_{\alpha\beta}}^{c}\,\vec{\mathrm{i}}_{m_{\alpha\beta}}^{c}) - \frac{1}{\sqrt{3}}(\vec{v}_{g_{\alpha\beta}}\vec{\mathrm{i}}_{1\alpha\beta}^{\Sigma\Delta^c} + \vec{v}_{g_{\alpha\beta}}^{c}\,\vec{\mathrm{i}}_{2\alpha\beta}^{\Sigma\Delta} + v_n\vec{\mathrm{i}}_{m_{\alpha\beta}}) \tag{3.75}$$

$$C v_c^* \frac{\mathrm{d}\vec{v}_{c_{\alpha\beta}}^{0}}{\mathrm{d}t} \approx \frac{-1}{3\sqrt{2}}(\vec{v}_{g_{\alpha\beta}}^{c}\,\vec{\mathrm{i}}_{g_{\alpha\beta}}^{c}) + \frac{1}{\sqrt{3}}(\vec{v}_{m_{\alpha\beta}}\vec{\mathrm{i}}_{1\alpha\beta}^{\Sigma\Delta} + \vec{v}_{m_{\alpha\beta}}^{c}\,\vec{\mathrm{i}}_{2\alpha\beta}^{\Sigma\Delta} - v_n\vec{\mathrm{i}}_{g_{\alpha\beta}}) \tag{3.76}$$

Equations $(3.73)-(3.76)$ represent the Power-CCV model of M^3C in $\Sigma\Delta$ Double-$\alpha\beta0$ coordinates. The same classification as in Table 3.1, i.e. Non-controllable, Semi-controllable and Fully-controllable, is applied to $(3.73)-(3.76)$. At this point, the following conclusions are elaborated:

- The Non-Controllable component of the vector $\vec{v}_{c_{1\alpha\beta}}^{\Sigma\Delta}$ can lead to unacceptable voltage oscillations when $f_g = f_m$. It is possible to mitigate these oscillations using either the Semi-controllable or the Fully-controllable component of the same vector.

- The Non-Controllable component of the vector $\vec{v}_{c_{2\alpha\beta}}^{\Sigma\Delta}$ leads to unacceptable voltage oscillations when $f_g = -f_m$. . It is possible to mitigate these oscillations using either the SC or the FC component of the same vector.

- The NC component of the vector $\vec{v}_{c_0}^{\alpha\beta}$ leads to unacceptable voltage oscillations when $f_m = 0$. It is possible to mitigate these oscillations using the Semi-controllable component of the same vector.

- The NC component of the vector $\vec{v}_{c_{\alpha\beta}}^{0}$ leads to unacceptable voltage oscillations when $f_g = 0$. (not feasible case for grid-connected applications). It is possible to mitigate these oscillations using the Semi-controllable component of the same vector.

- The term $v_n\vec{\mathrm{i}}_{m}^{\alpha\beta}$ could also generate unacceptable voltage oscillations if n^{th} order harmonic common mode voltage is used and $f_g = \frac{1}{n}f_m$. This should not be complex to handle because the frequency of the common-mode voltage can be freely chosen.

Furthermore, the above-mentioned Semi-controllable or Fully-controllable terms can be used to balance (the average value of the CCVs) and to mitigate (the voltage oscillation at unstable frequency conditions) at the same time. Therefore, proper voltage regulation can be guaranteed regardless the machine frequency if suitable control strategies are developed based on the vector Power-CCV model.

Finally, it is important to note that the vector Power-CCV model of the M^3C in $\Sigma\Delta$ Double-$\alpha\beta0$ coordinates represents the dynamics of the converter using a compact notation with only four vector equations. The balancing and mitigation task can be linked to conventional $\mathrm{d}q$ based control systems.

3.7 Summary

This Chapterhas described a detailed modelling of the M^3C. Firstly, the Voltage-Current model of the M^3C is presented to represent the dynamics of the converter currents and voltages. This model is transformed to Double-$\alpha\beta0$ coordinates to obtain a decoupled representation of input, output and converter dynamics.

After that, the Power-CCV model of the M^3C is introduced. The behaviour of the CCVs is analysed in abc-rst and Double-$\alpha\beta0$ coordinates to identify the frequency conditions that might lead to unstable operation of the converter.

An additional linear transformation has been presented to enhance the modelling of the M^3C for a broad range of input-output frequencies. The use of $\Sigma\Delta$ Transformation yields a compact vector representation of the converter dynamics with just four vector equations. Moreover, the vector Power-CCV model of the M^3C in the $\Sigma\Delta$ Double-$\alpha\beta0$ coordinates allows a simple analysis and implementation of control strategies using vector control, as will be discussed in next Chapter.

CHAPTER 4

Proposed Control Strategies for M^3C based WECS - Converter Control

4.1 Introduction

This Chapterdiscusses the application of the M^3C to drive Multi-MW WECSs. The proposed control strategies enable decoupled operation of the converter, providing MPPT capability at the generator-side, grid code compliance at the grid-side, and good steady state and transient regulation of the capacitor voltages.

An overview of the overall control systems is illustrated in Fig.4.1, considering a hierarchical structure of the following sub-control loops:

1. CCV Control Systems.

    CCV Balancing Control System.

    CCV Mitigation Control System.

2. Average CCV Control System.

3. Generator-side Control System and MTTP algorithm.

4. Grid-side Control System and LVRT algorithm.

5. Single-Cell Balancing and Modulation.

Two different control systems are proposed for the regulation of the CCVs. The first control
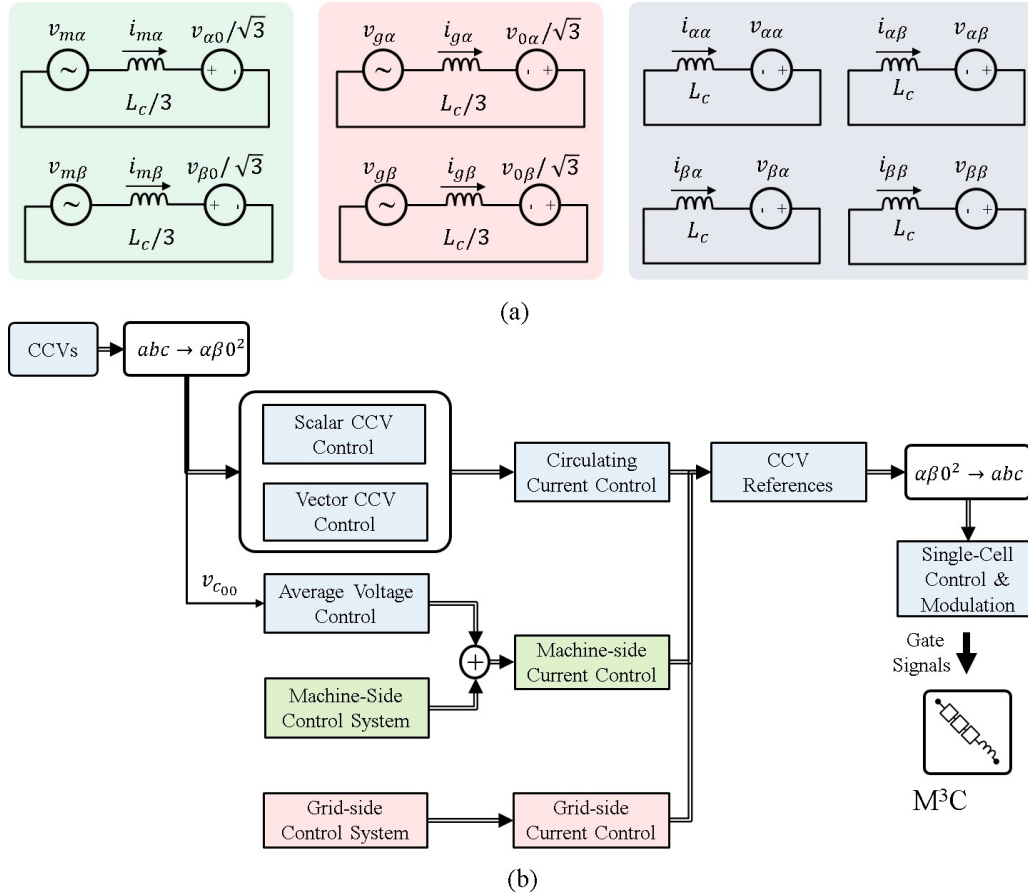
Figure 4.1: Proposed control strategy. (a) Decoupled Electric Circuits of the M^3C in Double-$\alpha\beta0$ coordinates. (b) Block diagrams of the proposed control strategy.

proposal, referred as to Scalar Control Strategy, performs balancing of the CCVs based on the Voltage-Current and the Power-CCV models of the M^3C in Double-$\alpha\beta0$ coordinates. Additionally, the mitigation of the CCVs for EFM is performed using an open-loop control system. Details of this control are provided in Section 4.2.1

The second control proposal, refereed to as Vector Control Strategy, is based on the vector Power-CCV model on $\Sigma\Delta$ Double-$\alpha\beta0$ coordinates. This control system perform balancing of the CCVs. The mitigation is carried out using a closed-loop control system implemented in $\mathrm{d}q$ synchronous frames which allows operation of the converter in a broad range of frequencies, including equal frequency. See details in Section 4.2.2.

Because of the length of the Chapter, the Generator-side Control System and the Grid-side Control System are briefly introduced in this chapter and their analysis will be detailed in Chapter5.

4.2 CCV Control Systems

All capacitors should be regulated to the same voltage level to have an accurate operation of the M^3C. When this condition is fulfilled (i.e. all the capacitor voltages are equal to v_c^*), (3.31) is achieved and the vector voltages of $(3.73)-(3.76)$ tend to:

$$\vec{v}_{c_{1\alpha\beta}}^{\Sigma\Delta} = \vec{v}_{c_{2\alpha\beta}}^{\Sigma\Delta} = \vec{v}_{c0}^{\alpha\beta} = \vec{v}_{c_{\alpha\beta}}^{0} = 0, v_{c00} = 3v_c^* \tag{4.1}$$

Moreover, significant voltage oscillation should be avoided when the input and the output frequencies are close to any of the unstable conditions, i.e. $f_g = f_m$, $f_g = -f_m$, $f_g = 0$, $f_m = 0$. Nested control systems, considering outer CCVs controllers and inner circulating current control loop, are used to regulate the inbalance capacitor voltages as stated in Subsection 2.5.2. Therefore, zero steady state error and good dynamic control of the CCVs imbalance terms are fundamental to operate in a broad range of frequency (including the unstable frequency conditions).

In the following Subsections, the Scalar and the Vector control strategies are detailed including operation in LFM and EFM.
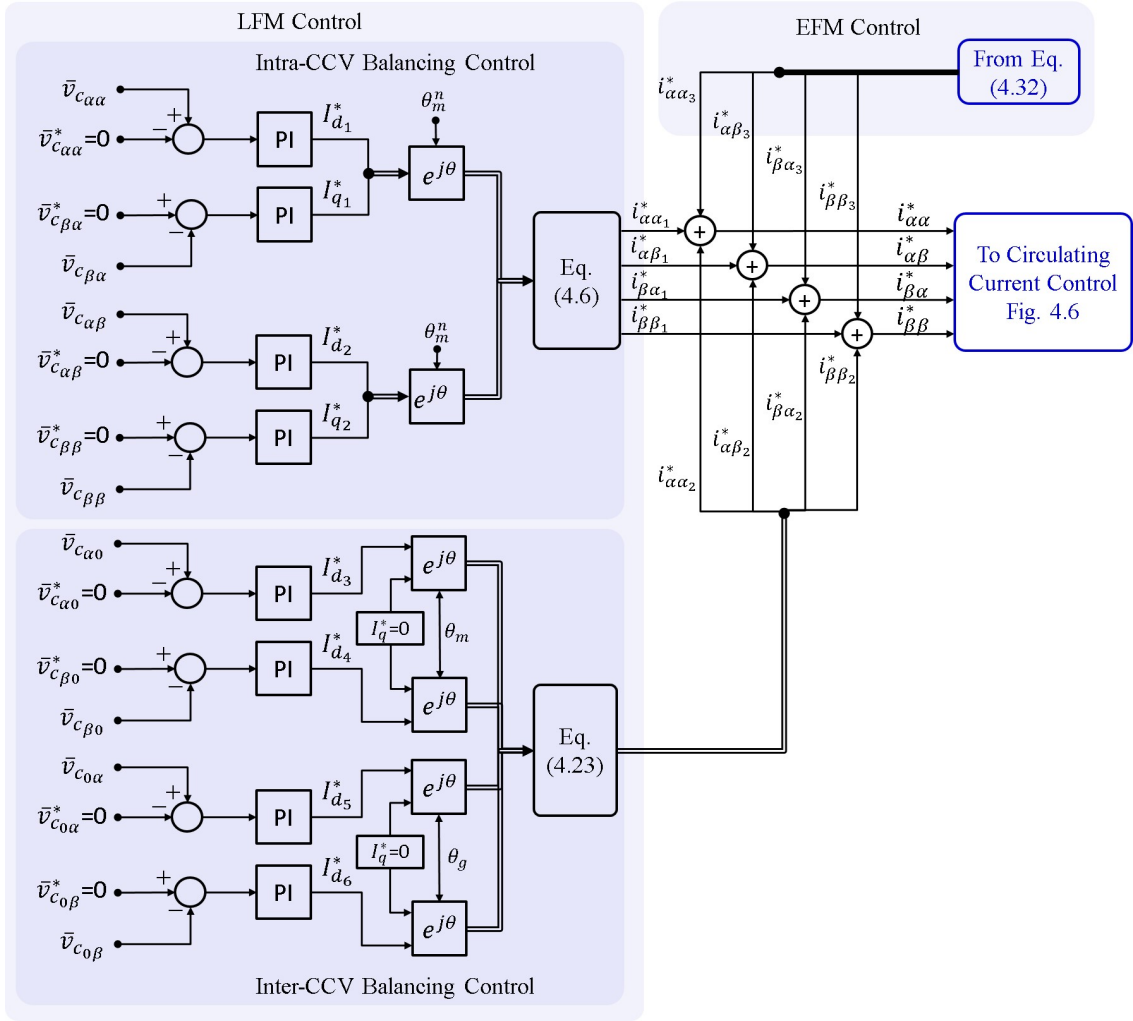
Figure 4.2: Proposed Scalar CCV Control Strategy.

4.2.1 Scalar CCV Control Strategy

The average components of the eight CCV imbalance terms in (3.20) (i.e. $v_{c_{\alpha\alpha}}$, $v_{c_{\beta\alpha}}$, $v_{c_{0\alpha}}$, $v_{c_{\alpha\beta}}$, $v_{c_{\beta\beta}}$, $v_{c_{0\beta}}$, $v_{c_{\alpha 0}}$, $v_{c_{\beta 0}}$) have to be regulated to zero to balance the converter. The Intra-CCV imbalance terms ($v_{c_{\alpha\alpha}}$, $v_{c_{\beta\alpha}}$, $v_{c_{\alpha\beta}}$, $v_{c_{\beta\beta}}$) and the Inter-CCV imbalance terms ($v_{c_{0\alpha}}$, $v_{c_{0\beta}}$, $v_{c_{\alpha 0}}$, $v_{c_{\beta 0}}$) could be regulated using either circulating currents or the common mode voltage (see [77, 78]). In this strategy, circulating currents alone have been used to regulate the balance the CCVs avoiding then the injection of common-mode voltage.

The diagram block of the Scalar Control Strategy is shown in Fig. 4.2 and it is explained in the following next.

4.2.1.1 Scalar CCV Control Strategy, LFM

Intra-CCV balancing control:

Considering $v_n = 0$, the power terms presented in (3.22)−(3.25) tends to:

$$P_{\alpha\alpha} = \frac{1}{3} \overbrace{(v_{m\alpha}\mathrm{i}_{g\alpha} - v_{g\alpha}\mathrm{i}_{m\alpha})}^{\text{NC terms}} + \frac{1}{\sqrt{6}}(v_{m\alpha}\mathrm{i}_{\alpha\alpha} - v_{m\beta}\mathrm{i}_{\beta\alpha}) - \frac{1}{\sqrt{6}}(v_{g\alpha}\mathrm{i}_{\alpha\alpha} - v_{g\beta}\mathrm{i}_{\alpha\beta}) \tag{4.2}$$

$$P_{\alpha\beta} = \frac{1}{3}(v_{m\alpha}\mathrm{i}_{g\beta} - v_{g\beta}\mathrm{i}_{m\alpha}) + \frac{1}{\sqrt{6}}(v_{m\alpha}\mathrm{i}_{\alpha\beta} - v_{m\beta}\mathrm{i}_{\beta\beta}) + \frac{1}{\sqrt{6}}(v_{g\alpha}\mathrm{i}_{\alpha\beta} + v_{g\beta}\mathrm{i}_{\alpha\alpha}) \tag{4.3}$$

$$P_{\beta\alpha} = \frac{1}{3}(v_{m\beta}\mathrm{i}_{g\alpha} - v_{g\alpha}\mathrm{i}_{m\beta}) - \frac{1}{\sqrt{6}}(v_{m\alpha}\mathrm{i}_{\beta\alpha} + v_{m\beta}\mathrm{i}_{\alpha\alpha}) - \frac{1}{\sqrt{6}}(v_{g\alpha}\mathrm{i}_{\beta\alpha} - v_{g\beta}\mathrm{i}_{\beta\beta}) \tag{4.4}$$

$$P_{\beta\beta} = \frac{1}{3}(v_{m\beta}\mathrm{i}_{g\beta} - v_{g\beta}\mathrm{i}_{m\beta}) - \frac{1}{\sqrt{6}}(v_{m\alpha}\mathrm{i}_{\beta\beta} + v_{m\beta}\mathrm{i}_{\alpha\beta}) + \frac{1}{\sqrt{6}}(v_{g\alpha}\mathrm{i}_{\beta\beta} + v_{g\beta}\mathrm{i}_{\beta\alpha}) \tag{4.5}$$

These power components are used to regulate Intra-CCV imbalance terms of (3.20). At this point, some simplifications to (4.2)−(4.5) can be considered. As the NC terms possess components of frequencies $f_g \pm f_m$ (see Section 3.3), they do not lead to large voltage oscillations if the power cell capacitors are properly designed and the rotational speed of the WECS is restricted within a suitable range. Accordingly, the Non-controllable components are filtered by the capacitors in LFM and their influence is neglected from (4.2)−(4.5).

Additionally, circulating currents are designed to generate non-zero mean active power components in (4.2)−(4.5) which can be used to regulate any possible dc-drift or close-to-dc components in these power terms. The dc-drifts could be produced, for instance, by non linearities in the converter cells, offsets in the measured signals, etc. Notice that, due to the integral effect produced in the capacitors, even small dc-components in the powers of (4.2)−(4.5) could produce significant voltage imbalances.

Accordingly, the following circulating currents of negative-sequence in-phase with the generator voltage are imposed:

$$\begin{aligned}
\mathrm{i}^*_{\alpha\alpha_1} &= I_{d_1}\cos\omega_m t + I_{q_1}\sin\omega_m t \\
\mathrm{i}^*_{\beta\alpha_1} &= -I_{d_1}\sin\omega_m t + I_{q_1}\cos\omega_m t \\
\mathrm{i}^*_{\alpha\beta_1} &= I_{d_2}\cos\omega_m t + I_{q_2}\sin\omega_m t \\
\mathrm{i}^*_{\beta\beta_1} &= -I_{d_2}\sin\omega_m t + I_{q_2}\cos\omega_m t
\end{aligned} \tag{4.6}$$

When the circulating currents are imposed as (4.6), (4.2)−(4.5) become:

$$P_{\alpha\alpha} = \frac{V_m I_{d_1}}{\sqrt{6}} - \frac{1}{\sqrt{6}}\overbrace{(v_{g\alpha}\mathrm{i}_{\alpha\alpha} - v_{g\beta}\mathrm{i}_{\alpha\beta})}^{\text{AC Components } f_g \pm f_m} + \frac{1}{3}\overbrace{(v_{m\alpha}\mathrm{i}_{g\alpha} - v_{g\alpha}\mathrm{i}_{m\alpha})}^{\text{AC Components } f_g \pm f_m} \tag{4.7}$$

$$P_{\alpha\beta} = \frac{V_m I_{q_1}}{\sqrt{6}} + \frac{1}{\sqrt{6}}\overbrace{(v_{g\alpha}\mathrm{i}_{\alpha\beta} + v_{g\beta}\mathrm{i}_{\alpha\alpha})}^{\text{AC Components } f_g \pm f_m} + \frac{1}{3}\overbrace{(v_{m\alpha}\mathrm{i}_{g\beta} - v_{g\beta}\mathrm{i}_{m\alpha})}^{\text{AC Components } f_g \pm f_m} \tag{4.8}$$

$$P_{\beta\alpha} = -\frac{V_m I_{d_2}}{\sqrt{6}} - \frac{1}{\sqrt{6}} \overbrace{(v_{g\alpha}\mathrm{i}_{\beta\alpha} - v_{g\beta}\mathrm{i}_{\beta\beta})}^{\text{AC Components } f_g \pm f_m} + \frac{1}{3} \overbrace{(v_{m\beta}\mathrm{i}_{g\alpha} - v_{g\alpha}\mathrm{i}_{m\beta})}^{\text{AC Components } f_g \pm f_m} \tag{4.9}$$

$$P_{\beta\beta} = -\frac{V_m I_{q_2}}{\sqrt{6}} + \frac{1}{\sqrt{6}} \overbrace{(v_{g\alpha}\mathrm{i}_{\beta\beta} + v_{g\beta}\mathrm{i}_{\beta\alpha})}^{\text{AC Components } f_g \pm f_m} + \frac{1}{3} \overbrace{(v_{m\beta}\mathrm{i}_{g\beta} - v_{g\beta}\mathrm{i}_{m\beta})}^{\text{AC Components } f_g \pm f_m} \tag{4.10}$$

Therefore, non-zero mean active power components are obtained. Filtering the ripple components in (4.7)−(4.10) and using (3.20), the following relationships are obtained:

$$\frac{\mathrm{d}\bar{v}_{c_{\alpha\alpha}}}{\mathrm{d}t} \approx \frac{\bar{P}_{\alpha\alpha}}{Cv_c^*} = \frac{V_m I_{d_1}}{\sqrt{6}Cv_c^*} \tag{4.11}$$

$$\frac{\mathrm{d}\bar{v}_{c_{\alpha\beta}}}{\mathrm{d}t} \approx \frac{\bar{P}_{\alpha\beta}}{Cv_c^*} = \frac{V_m I_{q_1}}{\sqrt{6}Cv_c^*} \tag{4.12}$$

$$\frac{\mathrm{d}\bar{v}_{c_{\beta\alpha}}}{\mathrm{d}t} \approx \frac{\bar{P}_{\beta\alpha}}{Cv_c^*} = \frac{-V_m I_{d_2}}{\sqrt{6}Cv_c^*} \tag{4.13}$$

$$\frac{\mathrm{d}\bar{v}_{c_{\beta\beta}}}{\mathrm{d}t} \approx \frac{\bar{P}_{\beta\beta}}{Cv_c^*} = \frac{-V_m I_{q_2}}{\sqrt{6}Cv_c^*} \tag{4.14}$$

where $\bar{v}_{c_{\alpha\alpha}}$, $\bar{v}_{c_{\alpha\beta}}$, $\bar{v}_{c_{\beta\alpha}}$ and $\bar{v}_{c_{\beta\beta}}$ are filtered versions of $v_{c_{\alpha\alpha}}$, $v_{c_{\alpha\beta}}$, $v_{c_{\beta\alpha}}$ and $v_{c_{\beta\beta}}$ that represent close-to-dc components of the Intra-CCV Imbalance terms. Analogously, $\bar{P}_{\alpha\alpha}$, $\bar{P}_{\alpha\beta}$, $\bar{P}_{\beta\alpha}$, $\bar{P}_{\beta\beta}$ are filtered versions of $P_{\alpha\alpha}$, $P_{\alpha\beta}$, $P_{\beta\alpha}$, $P_{\beta\beta}$.

The Intra-CCV Control System is shown in Fig. 4.2. Four PI controllers regulate to 0 the close-to-dc components of the Intra-CCV Imbalance terms by imposing circulating current references of negative-sequence of frequency f_m that generate the manipulable non-zero mean active power components of (4.11)−(4.14). Notice that circulating currents of frequency f_g could be also applied to regulate the Intra-CCV Imbalance terms. However, in this application it is assumed that the WECS has to be synchronised to the grid before being connected. Therefore, before synchronisation well-regulated grid voltages are not available in the cluster voltages and better results can be achieved by using the generator voltages and circulating currents of frequency f_m.

Inter-CCV balancing control A similar process is carried out to analyse the Inter-CCV imbalance terms. Considering $v_n=0$, the power flows related to this CCVs are described by:

$$P_{\alpha 0} = \frac{1}{3\sqrt{2}} \overbrace{(v_{m\alpha}\mathrm{i}_{m\alpha} - v_{m\beta}\mathrm{i}_{m\beta})}^{\text{NC terms}} - \frac{1}{\sqrt{3}} (v_{g\alpha}\mathrm{i}_{\alpha\alpha} + v_{g\beta}\mathrm{i}_{\alpha\beta}) \tag{4.15}$$

$$P_{\beta 0} = -\frac{1}{3\sqrt{2}} (v_{m\alpha}\mathrm{i}_{m\beta} + v_{m\beta}\mathrm{i}_{m\alpha}) - \frac{1}{\sqrt{3}} (v_{g\alpha}\mathrm{i}_{\beta\alpha} + v_{g\beta}\mathrm{i}_{\beta\beta}) \tag{4.16}$$

$$P_{0\alpha} = -\frac{1}{3\sqrt{2}} (v_{g\alpha}\mathrm{i}_{g\alpha} - v_{g\beta}\mathrm{i}_{g\beta}) + \frac{1}{\sqrt{3}} (v_{m\alpha}\mathrm{i}_{\alpha\alpha} + v_{m\beta}\mathrm{i}_{\beta\alpha}) \tag{4.17}$$

$$P_{0\beta} = \frac{1}{3\sqrt{2}} \left(v_{g\alpha} i_{g\beta} + v_{g\beta} i_{g\alpha} \right) + \frac{1}{\sqrt{3}} \left(v_{m\alpha} i_{\alpha\beta} + v_{m\beta} i_{\beta\beta} \right) \tag{4.18}$$

The NC terms of (4.15)−(4.18) possess components of frequencies $2f_g$ or $2f_m$ that do not lead to large voltage oscillations if the power cell capacitors are properly designed and the rotational speed of the WECS is restricted within a suitable range. Accordingly, these components are filtered by the capacitors in LFM and their influence is neglected.

Additionally, circulating currents are designed to generate non-zero mean active power components which can be used to regulate any possible dc-drift or close-to-dc components in the Inter-CCV Imbalance Terms.

Therefore, the following circulating current are imposed for $P_{\alpha 0}$:

$$
\begin{aligned}
i^*_{\alpha\alpha_{2a}} &= I_{d_3} \cos \omega_g t - 0 \sin \omega_g t \\
i^*_{\alpha\beta_{2a}} &= I_{d_3} \sin \omega_g t + 0 \cos \omega_g t
\end{aligned} \tag{4.19}
$$

and for $P_{\beta 0}$:

$$
\begin{aligned}
i^*_{\beta\alpha_{2a}} &= I_{d_4} \cos \omega_g t - 0 \sin \omega_g t \\
i^*_{\beta\beta_{2a}} &= I_{d_4} \sin \omega_g t + 0 \sin \omega_g t
\end{aligned} \tag{4.20}
$$

and for $P_{0\alpha}$:

$$
\begin{aligned}
i^*_{\alpha\alpha_{2b}} &= I_{d_5} \cos \omega_m t - 0 \sin \omega_m t \\
i^*_{\beta\alpha_{2b}} &= I_{d_5} \sin \omega_m t + 0 \cos \omega_m t
\end{aligned} \tag{4.21}
$$

and for $P_{0\beta}$:

$$
\begin{aligned}
i^*_{\alpha\beta_{2b}} &= I_{d_6} \cos \omega_m t - 0 \sin \omega_m t \\
i^*_{\beta\beta_{2b}} &= I_{d_6} \sin \omega_m t + 0 \cos \omega_m t
\end{aligned} \tag{4.22}
$$

Then, the following circulating current references of positive-sequence are imposed:

$$
\begin{aligned}
i^*_{\alpha\alpha_2} &= I_{d_3} \cos \omega_g t + I_{d_5} \cos \omega_m t \\
i^*_{\alpha\beta_2} &= I_{d_3} \sin \omega_g t + I_{d_6} \cos \omega_m t \\
i^*_{\beta\alpha_2} &= I_{d_4} \cos \omega_g t + I_{d_5} \sin \omega_m t \\
i^*_{\beta\beta_2} &= I_{d_4} \sin \omega_g t + I_{d_6} \sin \omega_m t
\end{aligned} \tag{4.23}
$$

When the circulating currents are imposed as (4.23), (4.15)−(4.18) become:

$$P_{\alpha 0} = -\frac{V_g I_{d_3}}{\sqrt{3}} - \overbrace{\frac{V_g I_{d_5} cos\omega_g t cos\omega_m t - V_g I_{d_6} sin\omega_g t cos\omega_m t}{\sqrt{3}}}^{\text{AC Components } f_m \pm f_g} + \frac{1}{3\sqrt{2}} \overbrace{\left(v_{m\alpha} i_{m\alpha} - v_{m\beta} i_{m\beta} \right)}^{\text{AC Components } 2f_m} \tag{4.24}$$

$$P_{\beta 0} = -\frac{V_g I_{d_4}}{\sqrt{3}} - \overbrace{\frac{V_g I_{d_5} cos\omega_g t sin\omega_m t - V_g I_{d_6} sin\omega_g t sin\omega_m t}{\sqrt{3}}}^{\text{AC Components } f_m \pm f_g} - \frac{1}{3\sqrt{2}} \overbrace{\left(v_{m\alpha} i_{m\beta} + v_{m\beta} i_{m\alpha} \right)}^{\text{AC Components } 2f_m} \tag{4.25}$$

$$P_{0\alpha} = \frac{V_m I_{d_5}}{\sqrt{3}} - \overbrace{\frac{V_m I_{d_3} cos\omega_g t cos\omega_m t - V_m I_{d_4} sin\omega_m t cos\omega_g t}{\sqrt{3}}}^{\text{AC Components } f_m \pm f_g} - \frac{1}{3\sqrt{2}} \overbrace{\left(v_{g\alpha} i_{g\alpha} - v_{g\beta} i_{g\beta}\right)}^{\text{AC Components } 2f_g} \qquad (4.26)$$

$$P_{0\beta} = \frac{V_m I_{d_6}}{\sqrt{3}} - \overbrace{\frac{V_m I_{d_3} cos\omega_m t sin\omega_g t - V_m I_{d_4} sin\omega_m t sin\omega_g t}{\sqrt{3}}}^{\text{AC Components } f_m \pm f_g} + \frac{1}{3\sqrt{2}} \overbrace{\left(v_{g\alpha} i_{g\beta} + v_{g\beta} i_{g\alpha}\right)}^{\text{AC Components } 2f_g} \qquad (4.27)$$

Filtering the ripple components in (4.24)−(4.27) and using (3.20), the following relationship are obtained:

$$\frac{d\bar{v}_{c_{\alpha 0}}}{dt} \approx \frac{\bar{P}_{\alpha 0}}{Cv_c^*} = \frac{-V_g I_{d_3}}{\sqrt{3} Cv_c^*} \qquad (4.28)$$

$$\frac{d\bar{v}_{c_{\beta 0}}}{dt} \approx \frac{\bar{P}_{\beta 0}}{Cv_c^*} = \frac{-V_g I_{d_4}}{\sqrt{3} Cv_c^*} \qquad (4.29)$$

$$\frac{d\bar{v}_{c_{0\alpha}}}{dt} \approx \frac{\bar{P}_{0\alpha}}{Cv_c^*} = \frac{V_m I_{d_5}}{\sqrt{3} Cv_c^*} \qquad (4.30)$$

$$\frac{d\bar{v}_{c_{0\beta}}}{dt} \approx \frac{\bar{P}_{0\beta}}{Cv_c^*} = \frac{V_m I_{d_6}}{\sqrt{3} Cv_c^*} \qquad (4.31)$$

Being $\bar{v}_{c_{\alpha 0}}$, $\bar{v}_{c_{\beta 0}}$, $\bar{v}_{c_{0\alpha}}$ and $\bar{v}_{c_{0\beta}}$ are filtered versions of $v_{c_{\alpha 0}}$, $v_{c_{\beta 0}}$, $v_{c_{0\alpha}}$ and $v_{c_{0\beta}}$ that represent close-to-dc components of the Inter-CCV Imbalance terms. Analogously, $\bar{P}_{\alpha 0}$, $\bar{P}_{\beta 0}$, $\bar{P}_{0\alpha}$, $\bar{P}_{0\beta}$ are filtered versions of $P_{\alpha 0}$, $P_{\beta 0}$, $P_{0\alpha}$, $P_{0\beta}$.

Positive-sequence circulating current references are controlled to generate non-zero mean active power values that drive the close-to-dc components of the Inter-CCVs. The diagram block of the Inter-CCV control systems is presented in Fig. 4.2. In this case, the current references are referred into positive sequence reference frames using the machine-side electrical angle θ_m and the grid-side electrical angle θ_g.

4.2.1.2 Scalar CCV Control Strategy, EFM

As explained in Subsection 3.3.2, the four ripple components of $(3.46)-(3.49)$ ($\tilde{v}_{c_{\alpha\alpha}}$, $\tilde{v}_{c_{\alpha\beta}}$, $\tilde{v}_{c_{\beta\alpha}}$ and $\tilde{v}_{c_{\beta\beta}}$) leads to unacceptable voltage oscillations when $f_m = \pm f_g$. Then, extra circulating currents must be superimposed to mitigate capacitor-voltage fluctuations when the machine frequency gets closer to the grid frequency.

In this control proposal, a third component of the circulating current references is used to generate an additional power flow to cancel $(3.38)-(3.41)$. Those components are calculated as:

$$
\begin{aligned}
i^*_{\alpha\alpha3} &= -\frac{\sqrt{6}}{3V_m}(v_{m\alpha}i_{g\alpha} - v_{g\alpha}i_{m\alpha}) \\
i^*_{\alpha\beta3} &= -\frac{\sqrt{6}}{3V_m}(v_{m\alpha}i_{g\beta} - v_{g\beta}i_{m\alpha}) \\
i^*_{\beta\alpha3} &= \frac{\sqrt{6}}{3V_m}(v_{m\beta}i_{g\alpha} - v_{g\alpha}i_{m\beta}) \\
i^*_{\beta\beta3} &= \frac{\sqrt{6}}{3V_m}(v_{m\beta}i_{g\beta} - v_{g\beta}i_{m\beta})
\end{aligned}
\tag{4.32}
$$

The diagram block of the EFM implementation is presented in Fig. 4.2. The set-points for the mitigation currents are predefined off-line. Consequently, this proposal does not have any sort of closed loop adaptation capability which is required to compensate possible changes in the parameters or operational points of the M^3C.

Note that similar approaches have been proposed in [90, 92]. In fact, the additional power flow required to mitigate the voltage oscillations can be generated using the common-mode voltage.

4.2.2 Vector CCV Control Strategy

A closed-loop vector control system for the regulation of the vector voltages $\vec{v}_{c_{1\alpha\beta}}^{\Sigma\Delta}$, $\vec{v}_{c_{2\alpha\beta}}^{\Sigma\Delta}$, $\vec{v}_{c0}^{\alpha\beta}$, $\vec{v}_{c_{\alpha\beta}}^{0}$ is proposed in this Section. When the frequencies are not close to the unstable operational points, the average value of all the vectors is regulated to zero using the Semi-controllable terms of the Power-CCV model of the M^3C in $\Sigma\Delta$ Double-$\alpha\beta0$ coordinates presented in (3.73)$-$(3.76). On the other hand, to allow operation at the unstable operational frequencies, the oscillations in the vector voltages are regulated using the Fully-controllable terms of (3.73)$-$(3.76); this control task is referred to as "Mitigation". Consequently, the separation of the vector voltages into their close-to-dc (to balance) and ripple (to mitigate) components is required. Moreover, zero steady state error is ensured since the vector voltage terms are controlled in $\mathrm{d}q$ coordinates using PI controllers.

4.2.2.1 Vector CCV Control Strategy, LFM

Balancing Control of $\vec{v}_{c_{1\alpha\beta}}^{\Sigma\Delta}$ and $\vec{v}_{c_{2\alpha\beta}}^{\Sigma\Delta}$.

The close-to-dc components of the vectors $\vec{v}_{c_{1\alpha\beta}}^{\Sigma\Delta}$ and $\vec{v}_{c_{2\alpha\beta}}^{\Sigma\Delta}$ are regulated using circulating currents in-phase with the generator-side voltage, similarly to the proposed in the Scalar Vector Strategy. Defining each vector in $\Sigma\Delta$ Double-$\alpha\beta0$ coordinates as $\vec{x}_{\alpha\beta}^{\Sigma\Delta}=\vec{x}_{dq}^{\Sigma\Delta}e^{j\theta_e}$, where θ_e is the angle of vector, (3.73) and (3.74) can be re-write as:

$$Cv_c^* \frac{\mathrm{d}\vec{v}_{c_{1\alpha\beta}}^{\Sigma\Delta}}{\mathrm{d}t} \approx \frac{1}{6}(\vec{v}_{m_{dq}}\vec{i}_{g_{dq}} - \vec{v}_{g_{dq}}\vec{i}_{m_{dq}})e^{j(\theta_g-\theta_m)} + \frac{1}{\sqrt{6}}(\vec{v}_{m_{dq}}\vec{i}_{2dq}^{\Sigma\Delta}$$
$$- \vec{v}_{g_{dq}}\,\vec{i}_{2dq}^{\Sigma\Delta}e^{-j(\theta_g-\theta_m)}) - v_n\vec{i}_{1dq}^{\Sigma\Delta}e^{j\theta_m} \tag{4.33}$$

$$Cv_c^* \frac{\mathrm{d}\vec{v}_{c_{2\alpha\beta}}^{\Sigma\Delta}}{\mathrm{d}t} \approx \frac{1}{6}(\vec{v}_{m_{dq}}\vec{i}_{g_{dq}} - \vec{v}_{g_{dq}}\vec{i}_{m_{dq}})e^{j(\theta_g+\theta_m)} + \frac{1}{\sqrt{6}}(\vec{v}_{m_{dq}}\vec{i}_{1dq}^{\Sigma\Delta}$$
$$- \vec{v}_{g_{dq}}\vec{i}_{1dq}^{\Sigma\Delta})e^{j(-\theta_g+\theta_m)} - v_n\vec{i}_{2dq}^{\Sigma\Delta}e^{-j\theta_m} \tag{4.34}$$

Where:

$$\vec{i}_{1\alpha\beta_1}^{\Sigma\Delta*} = \vec{i}_{1dq_1}^{\Sigma\Delta*}e^{j\theta_m}$$
$$\vec{i}_{2\alpha\beta_1}^{\Sigma\Delta*} = \vec{i}_{2dq_1}^{\Sigma\Delta*}e^{-j\theta_m} \tag{4.35}$$

Imposing the circulating current references as (4.35), setting the common mode voltage $v_n= 0$ and filtering the ripple components, the system presented in (4.33)$-$(4.34) becomes:

$$Cv_c^* \frac{\mathrm{d}}{\mathrm{d}t}\vec{v}_{c_{1\alpha\beta}}^{\Sigma\Delta_{dc}} \approx \frac{1}{\sqrt{6}}\vec{v}_{m_{dq}}\vec{i}_{2dq_1}^{\Sigma\Delta*} \tag{4.36}$$

$$Cv_c^* \frac{\mathrm{d}}{\mathrm{d}t}\vec{v}_{c_{2\alpha\beta}}^{\Sigma\Delta_{dc}} \approx \frac{1}{\sqrt{6}}\vec{v}_{m_{dq}}\vec{i}_{1dq_1}^{\Sigma\Delta*} \tag{4.37}$$

Notice that $\vec{v}_{g_{dq}}\vec{i}_{2dq}^{\Sigma\Delta}e^{-j(\theta_g-\theta_m)}$ and $\vec{v}_{g_{dq}}\vec{i}_{1dq}^{\Sigma\Delta}e^{-j(\theta_g+\theta_m)}$ in (4.33)$-$(4.34) produce frequency oscil-

lations that can be filtered out by the capacitors reason why they are neglected from $(4.36)-(4.37)$. In addition, the Non-controllable components of the vectors $\vec{v}_{c_{1\alpha\beta}}^{\Sigma\Delta}$ and $\vec{v}_{c_{2\alpha\beta}}^{\Sigma\Delta}$ can be approximated as:

$$Cv_c^* \frac{\mathrm{d}}{\mathrm{d}t} \vec{v}_{c_{1\alpha\beta}}^{\Sigma\Delta\sim} \approx \frac{1}{6}(\vec{v}_{m_{\mathrm{d}q}}\vec{i}_{g_{\mathrm{d}q}} - \vec{v}_{g_{\mathrm{d}q}}\vec{i}_{m_{\mathrm{d}q}})\mathrm{e}^{j(\theta_g - \theta_m)} \tag{4.38}$$

$$Cv_c^* \frac{\mathrm{d}}{\mathrm{d}t} \vec{v}_{c_{2\alpha\beta}}^{\Sigma\Delta\sim} \approx \frac{1}{6}(\vec{v}_{m_{\mathrm{d}q}}\vec{i}_{g_{\mathrm{d}q}} - \vec{v}_{g_{\mathrm{d}q}}\vec{i}_{m_{\mathrm{d}q}})\mathrm{e}^{j(\theta_g + \theta_m)} \tag{4.39}$$

The balancing control is enabled when the frequencies are not close to the critical points. Thus, the Non-controllable components of the vectors are within an acceptable range and they are neglected from $(4.36)-(4.37)$.

Regarding the filtering procedure of the CCV vectors, it is worth to mention that the separation of the CCVs into their close-to-dc and ripple components has been proposed using low pass filters [77, 78]. However, low pass filters loose effectiveness when the CCVs have low-frequency components and they can introduce inaccurate circulating current references. Accordingly, the separation of the close-to-dc and ripple components of the vectors is performed using synchronous reference frame notch filters [68]. These filters are implemented in reference frames rotating at $\theta_{u1} = \int (\omega_g - \omega_m)\mathrm{d}t$ and $\theta_{u2} = \int (\omega_g + \omega_m)\mathrm{d}t$.

The proposed balancing control system is depicted in Fig.4.3. The outer control loop regulates with zero steady state error, using PI controllers, the dc components of the vectors $\vec{v}_{c_{1\alpha\beta}}^{\Sigma\Delta}$ and $\vec{v}_{c_{2\alpha\beta}}^{\Sigma\Delta}$. The outputs of these external loops are used to calculate the reference of the $\mathrm{d}q$ circulating currents. Moreover, the gains to enable the Balancing Control are $k_b = 1$ and $k_m = 0$. Afterward, the circulating current references are transformed from the $\Sigma\Delta$ frame to the $\alpha\beta0^2$ frame, where proportional controllers are used to tracking the references.

Balancing Control of $\vec{v}_{c0}^{\alpha\beta}$ and $\vec{v}_{c_{\alpha\beta}}^{0}$.

The dynamics of the vectors $\vec{v}_{c0}^{\alpha\beta}$ and $\vec{v}_{c_{\alpha\beta}}^{0}$ [presented in $(3.75)-(3.76)$] can be re-written as:

$$Cv_c^* \frac{\mathrm{d}\vec{v}_{c0}^{\alpha\beta}}{\mathrm{d}t} \approx \frac{1}{3\sqrt{2}}\vec{v}_{m_{\mathrm{d}q}}\vec{i}_{m_{\mathrm{d}q}}\mathrm{e}^{-j2\theta_m} - \frac{1}{\sqrt{3}}(\vec{v}_{g_{\mathrm{d}q}}\vec{i}_{1\mathrm{d}q}^{\Sigma\Delta} + \vec{v}_{g_{\mathrm{d}q}}\vec{i}_{2\mathrm{d}q}^{\Sigma\Delta}) \tag{4.40}$$

$$Cv_c^* \frac{\mathrm{d}\vec{v}_{c_{\alpha\beta}}^{0}}{\mathrm{d}t} \approx \frac{-1}{3\sqrt{2}}\vec{v}_{g_{\mathrm{d}q}}\vec{i}_{g_{\mathrm{d}q}}\mathrm{e}^{-j2\theta_g} + \frac{1}{\sqrt{3}}(\vec{v}_{m_{\mathrm{d}q}}\vec{i}_{1\mathrm{d}q}^{\Sigma\Delta} + \vec{v}_{m_{\mathrm{d}q}}\vec{i}_{2\mathrm{d}q}^{\Sigma\Delta}) \tag{4.41}$$

when the circulating current references are imposed as:

$$\vec{i}_{1\alpha\beta_2}^{\Sigma\Delta*} = \vec{i}_{1\mathrm{d}q_2}^{\Sigma\Delta*}\mathrm{e}^{j\theta_g} \tag{4.42}$$

$$\vec{i}_{2\alpha\beta_2}^{\Sigma\Delta*} = \vec{i}_{2\mathrm{d}q_2}^{\Sigma\Delta*}\mathrm{e}^{j\theta_m} \tag{4.43}$$
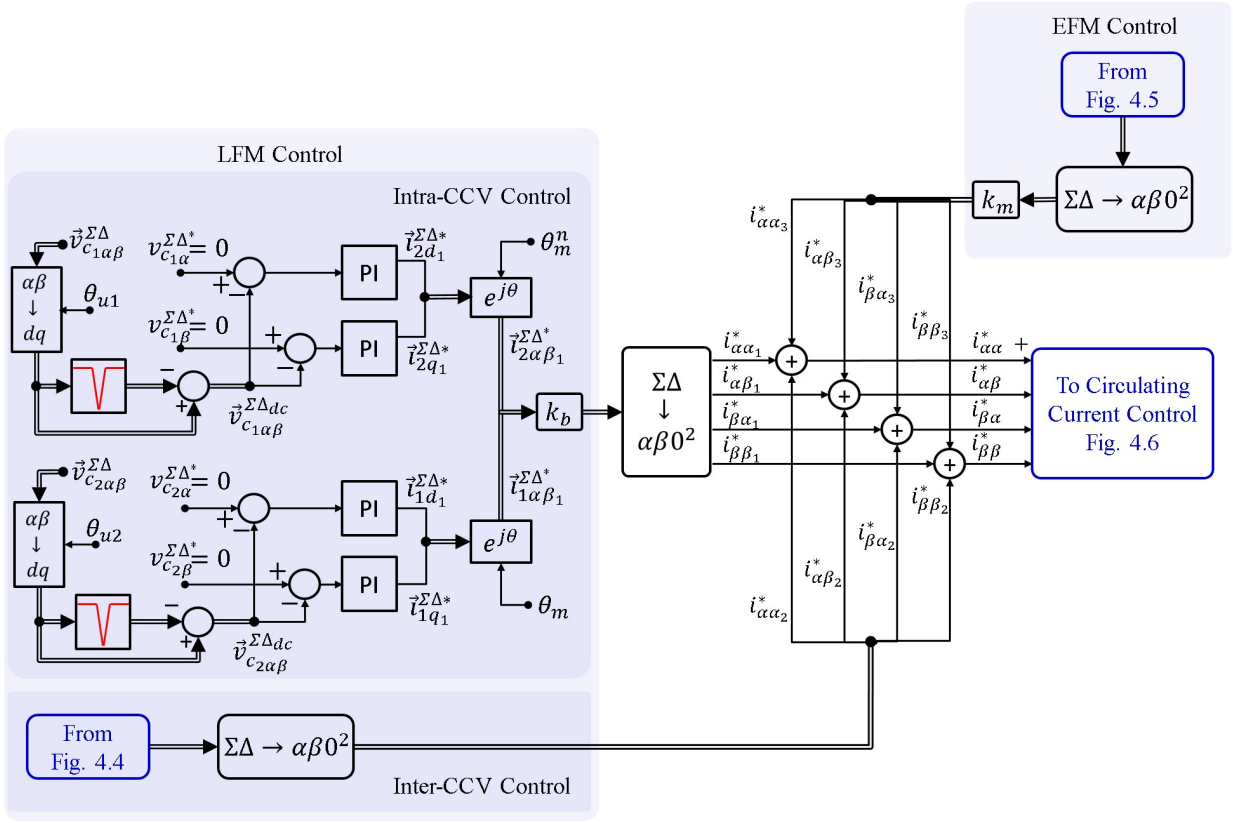
Figure 4.3: Proposed Vector CCV Control Strategy.

and the common mode voltage is $v_n = 0$.

As mentioned before, the balancing control is enabled when the frequencies are not close to the critical points. In this case, it is assumed that neither f_m nor f_g are close to zero. Therefore, the Non-controllable components of the vectors $\vec{v}_{c_0}^{\alpha\beta}$ and $\vec{v}_{c_{\alpha\beta}}^{0}$ [see (4.44)−(4.45)] are inside an acceptable range and are neglected for control purposes because they are filtered by the capacitors.

$$Cv_c^* \frac{\mathrm{d}}{\mathrm{d}t} \vec{v}_{c_0}^{\alpha\beta\sim} \approx \frac{1}{3\sqrt{2}} \vec{v}_{m_{dq}} \vec{\mathrm{i}}_{m_{dq}} e^{-j2\theta_m} \tag{4.44}$$

$$Cv_c^* \frac{\mathrm{d}}{\mathrm{d}t} \vec{v}_{c_{\alpha\beta}}^{0\sim} \approx \frac{1}{3\sqrt{2}} \vec{v}_{g_{dq}} \vec{\mathrm{i}}_{g_{dq}} e^{-j2\theta_g} \tag{4.45}$$

Therefore, (4.40)−(4.41) become:

$$Cv_c^* \frac{\mathrm{d}}{\mathrm{d}t} \vec{v}_{c_0}^{\alpha\beta_{dc}} \approx -\frac{1}{\sqrt{3}} \vec{v}_{g_{dq}} \vec{\mathrm{i}}_{1d_{q2}}^{\Sigma\Delta} \tag{4.46}$$

$$Cv_c^* \frac{\mathrm{d}}{\mathrm{d}t} \vec{v}_{c_{\alpha\beta}}^{0_{dc}} \approx -\frac{1}{\sqrt{3}} \vec{v}_{m_{dq}} \vec{\mathrm{i}}_{2d_{q2}}^{\Sigma\Delta} \tag{4.47}$$

The proposed balancing control system is presented in Fig. 4.4. The close-to-dc component $\vec{v}_{c_0}^{\alpha\beta_{dc}}$ is regulated to zero using a power flow in phase with the grid angle θ_g. The same effect is achieved for $\vec{v}_{c_{\alpha\beta}}^{0_{dc}}$ manipulating a non-zero mean active power in phase with the machine angle θ_m. The
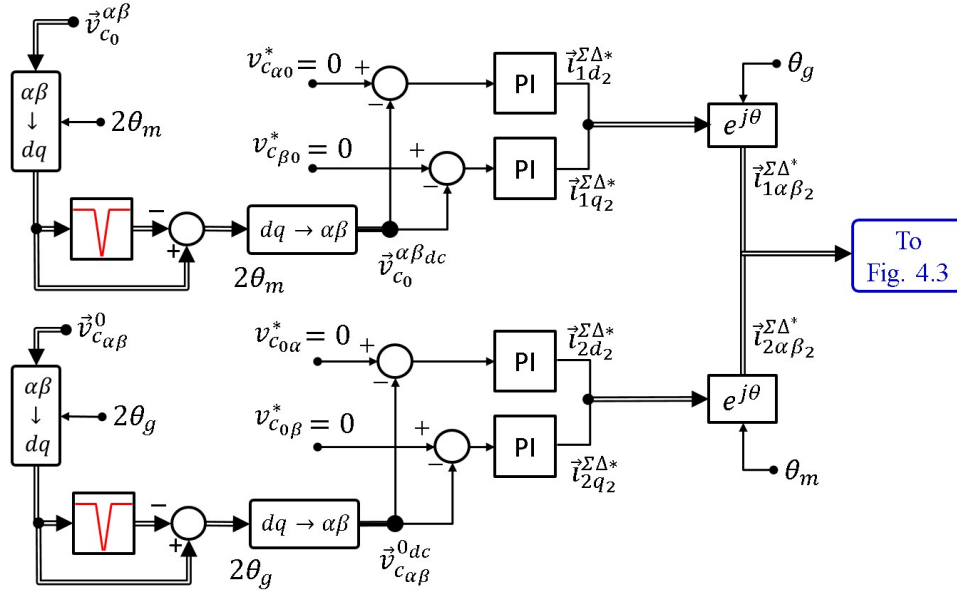
Figure 4.4: Proposed Balancing Control of $\vec{v}_{c_0}^{\alpha\beta}$ and $\vec{v}_{c_{\alpha\beta}}^0$

outputs of these outer loops are used to calculate the reference of the circulating currents.

4.2.2.2 Vector CCV Control Strategy, EFM

Mitigation Control of $\vec{v}_{c_{1\alpha\beta}}^{\Sigma\Delta}$ and $\vec{v}_{c_{2\alpha\beta}}^{\Sigma\Delta}$

The vectors $\vec{v}_{c_{1\alpha\beta}}^{\Sigma\Delta}$ and $\vec{v}_{c_{2\alpha\beta}}^{\Sigma\Delta}$ have been referred to rotating frames to implement the proposed control system. Accordingly, (3.73) is referred to a dq-frame rotating at $\theta_{u1} = \int (\omega_g - \omega_m) \mathrm{d}t$, and (3.74) is referred to a dq-frame rotating at $\theta_{u2} = \int (\omega_g + \omega_m) \mathrm{d}t$.

$$
\begin{aligned}
Cv_c^* &\left[\frac{\mathrm{d}\vec{v}_{c_{1dq}}^{\Sigma\Delta}}{\mathrm{d}t} + j\omega_{u1}\vec{v}_{c_{1dq}}^{\Sigma\Delta} \right] \approx \frac{1}{6}(\vec{v}_{m_{dq}} \vec{i}_{g_{dq}} - \vec{v}_{g_{dq}} \vec{i}_{m_{dq}}) \\
&+ \frac{1}{\sqrt{6}}(\vec{v}_{m_{dq}}\vec{i}_{2_{dq}}^{\Sigma\Delta}e^{j3\theta_m} - \vec{v}_{g_{dq}}\vec{i}_{2_{dq}}^{\Sigma\Delta}e^{-j3\theta_g}) - v_n\vec{i}_{1_{dq}}^{\Sigma\Delta}
\end{aligned}
\tag{4.48}
$$

$$
\begin{aligned}
Cv_c^* &\left[\frac{\mathrm{d}\vec{v}_{c_{2dq}}^{\Sigma\Delta}}{\mathrm{d}t} + j\omega_{u2}\vec{v}_{c_{2dq}}^{\Sigma\Delta} \right] \approx \frac{1}{6}(\vec{v}_{m_{dq}}\vec{i}_{g_{dq}} - \vec{v}_{g_{dq}}\vec{i}_{m_{dq}}) \\
&+ \frac{1}{\sqrt{6}}(\vec{v}_{m_{dq}}\vec{i}_{1_{dq}}^{\Sigma\Delta}e^{-j3\theta_m} - \vec{v}_{g_{dq}}\vec{i}_{1_{dq}}^{\Sigma\Delta}e^{-j3\theta_g}) - v_n\vec{i}_{2_{dq}}^{\Sigma\Delta}
\end{aligned}
\tag{4.49}
$$

Being:

$$
\begin{aligned}
\vec{i}_{1\alpha\beta_3}^{\Sigma\Delta*} &= \vec{i}_{1dq_3}^{\Sigma\Delta*}e^{j(\theta_g-\theta_m)} \\
\vec{i}_{2\alpha\beta_3}^{\Sigma\Delta*} &= \vec{i}_{2dq_3}^{\Sigma\Delta*}e^{j(\theta_g+\theta_m)}
\end{aligned}
\tag{4.50}
$$

68

The power flows produced by the last terms of (4.48)−(4.49) are used to regulate the vectors $\vec{v}_{c_{1\alpha\beta}}^{\Sigma\Delta}$ and $\vec{v}_{c_{2\alpha\beta}}^{\Sigma\Delta}$ when the frequencies are close to the critical points $f_g = f_m$ and $f_m = -f_g$.

If both vectors are referred to $\mathrm{d}q$ frames, the common-mode voltage and the $\mathrm{d}q$ circulating currents should be in phase to produce adjustable power flows. Moreover, when $\vec{\mathrm{i}}_{1_{\mathrm{d}q}}^{\Sigma\Delta}$ and $\vec{\mathrm{i}}_{2_{\mathrm{d}q}}^{\Sigma\Delta}$ are redefined as high frequency signals, the power flows produced by Semi-controllable terms of (4.48)−(4.49) could be neglected since the capacitors can filter them out. Therefore, the $\mathrm{d}q$ circulating currents and the common-mode voltage are defined as:

$$
\begin{aligned}
\vec{\mathrm{i}}_{1\mathrm{d}q3}^{\Sigma\Delta*} &= \vec{I}_{1\mathrm{d}q3}^{\Sigma\Delta*} f(t) \\
\vec{\mathrm{i}}_{2\mathrm{d}q3}^{\Sigma\Delta*} &= \vec{I}_{2\mathrm{d}q3}^{\Sigma\Delta*} f(t) \\
v_n &= V_0 g(t)
\end{aligned}
\tag{4.51}
$$

Where $f(t)$ and $g(t)$ must be in-phase. What is more, $f(t) = A_1 \sin\theta_n + A_2 \sin\theta_n$, θ_n must change with high frequency, and $g(t) = sgn\{f(t\}$ (sgn is the sign function). The amplitudes of the constants A_1, A_2 and V_0 are chosen to maximise the modulation index accordingly to the criteria presented in [96]. These definitions imply than the mean value of $f(t)g(t) \approx 1$.

Then, (4.48)−(4.49) becomes:

$$
Cv_c^* \frac{\mathrm{d}\vec{v}_{c_{1\mathrm{d}q}}^{\Sigma\Delta}}{\mathrm{d}t} \approx \frac{1}{6}(\vec{v}_{m_{\mathrm{d}q}}\vec{\mathrm{i}}_{g_{\mathrm{d}q}} - \vec{v}_{g_{\mathrm{d}q}}\vec{\mathrm{i}}_{m_{\mathrm{d}q}}) - V_0 \vec{I}_{1\mathrm{d}q3}^{\Sigma\Delta}
\tag{4.52}
$$

$$
Cv_c^* \frac{\mathrm{d}\vec{v}_{c_{2\mathrm{d}q}}^{\Sigma\Delta}}{\mathrm{d}t} \approx \frac{1}{6}(\vec{v}_{m_{\mathrm{d}q}}\vec{\mathrm{i}}_{g_{\mathrm{d}q}} - \vec{v}_{g_{\mathrm{d}q}}\vec{\mathrm{i}}_{m_{\mathrm{d}q}}) - V_0 \vec{I}_{2\mathrm{d}q3}^{\Sigma\Delta}
\tag{4.53}
$$

Note that the coupling terms $j\omega_{u1}\vec{v}_{c_{1\mathrm{d}q}}^{\Sigma\Delta}$ and $j\omega_{u2}\vec{v}_{c_{2\mathrm{d}q}}^{\Sigma\Delta}$ are neglected from (4.52)−(4.53). For instance, when $f_m \approx f_g$, ω_{u1} tends to zero and ω_{u2} tends to $2\omega_g$. Consequently $j\omega_{u1}\vec{v}_{c_{1\mathrm{d}q}}^{\Sigma\Delta} \rightarrow 0$ and $j\omega_{u2}\vec{v}_{c_{2\mathrm{d}q}}^{\Sigma\Delta}$ is a high frequency component that is filtered by the capacitors.

The NC terms in (4.52)−(4.53) can be considered as disturbances from a control point of view. This interpretation leads to the redefinition of the $\mathrm{d}q$ circulating including the next feed-forward components:

$$
\vec{I}_{1\mathrm{d}q3}^{\Sigma\Delta} = \vec{I}_{1\mathrm{d}q_c}^{\Sigma\Delta} + \vec{I}_{1\mathrm{d}q_f}^{\Sigma\Delta}; \ \vec{I}_{1\mathrm{d}q_f}^{\Sigma\Delta} = \frac{1}{6V_0}(\vec{v}_{m_{\mathrm{d}q}}\vec{\mathrm{i}}_{g_{\mathrm{d}q}} - \vec{v}_{g_{\mathrm{d}q}}\vec{\mathrm{i}}_{m_{\mathrm{d}q}})
\tag{4.54}
$$

$$
\vec{I}_{2\mathrm{d}q3}^{\Sigma\Delta} = \vec{I}_{2\mathrm{d}q_c}^{\Sigma\Delta} + \vec{I}_{2\mathrm{d}q_f}^{\Sigma\Delta}; \ \vec{I}_{2\mathrm{d}q_f}^{\Sigma\Delta} = \frac{1}{6V_0}(\vec{v}_{m_{\mathrm{d}q}}\vec{\mathrm{i}}_{g_{\mathrm{d}q}} - \vec{v}_{g_{\mathrm{d}q}}\vec{\mathrm{i}}_{m_{\mathrm{d}q}})
\tag{4.55}
$$

Finally, using (4.54)−(4.55) in (4.52)−(4.53):
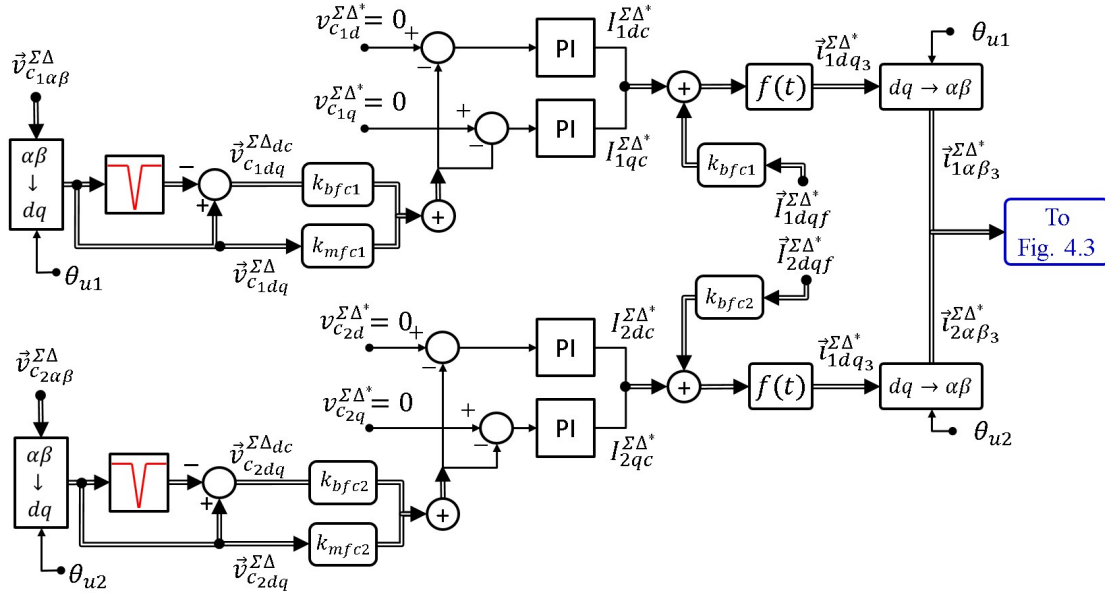
Figure 4.5: Proposed Mitigation Control of $\vec{v}_{c_{1\alpha\beta}}^{\Sigma\Delta}$ and $\vec{v}_{c_{2\alpha\beta}}^{\Sigma\Delta}$

$$Cv_c^* \frac{\mathrm{d}\vec{v}_{c_{1dq}}^{\Sigma\Delta}}{\mathrm{d}t} \approx -V_0 \vec{I}_{1\mathrm{d}q_c}^{\Sigma\Delta*} \tag{4.56}$$

$$Cv_c^* \frac{\mathrm{d}\vec{v}_{c_{2dq}}^{\Sigma\Delta}}{\mathrm{d}t} \approx -V_0 \vec{I}_{2\mathrm{d}q_c}^{\Sigma\Delta*} \tag{4.57}$$

The control system for the operation at the critical frequencies is presented in Fig. 4.5. When the generator-side frequency is close to $f_m=f_g$, (4.56) is applied and the vector $\vec{v}_{c_{1\alpha\beta}}^{\Sigma\Delta}$ is regulated in the $\mathrm{d}q$ frame using PI controllers. The dynamic regulation is improved by feed-forwarding the component $\vec{I}_{1\mathrm{d}q_f}^{\Sigma\Delta}$, which represent the oscillations of the NC term. The output of the external control loop is multiplied by $f(t)$ and the common-mode voltage is imposed as (4.51). In this case, the weighting factors are selected to be $k_{bfc1}=0$ and $k_{mfc1}=1$.

Notice that in this case, the vector $\vec{v}_{c_{2\alpha\beta}}^{\Sigma\Delta}$ could be regulated using (4.37) because large oscillations appear just in $\vec{v}_{c_{1\alpha\beta}}^{\Sigma\Delta}$. However, since the M^3C is synthetising common-mode voltage the assumption made in (4.51) is no longer valid and the weighting factors are $k_{bfc2}=1$ and $k_{mfc2}=0$. Therefore, the vector $\vec{v}_{c_{2\alpha\beta}}^{\Sigma\Delta}$ must be controlled by (4.57) using just the dc component of the vector and the feed-forward current $\vec{I}_{2\mathrm{d}q_f}^{\Sigma\Delta}$ is not included.

4.2.2.3 Transition Control for a broad range of frequency operation

Table 4.1 summarises the type of control applied to each vector in the M³C for each frequency conditions. In each case, the weighting factors (i.e. k_b, k_m, k_{bfc1}, k_{mfc1}, k_{bfc2}, k_{mfc2}) are used to select the corresponding control actions for a broad range of frequency operation.

Interval	$\vec{v}_{c_1\alpha\beta}^{\Sigma\Delta}$	$\vec{v}_{c_2\alpha\beta}^{\Sigma\Delta}$	$\vec{v}_{c_0}^{\alpha\beta}$	$\vec{v}_{c_{\alpha\beta}}^{0}$
Interval I $-f_g \leq f_m \leq -f_t$ $k_m=1, k_b=0$	Balancing using (4.56) $k_{bfc1}=1, k_{mfc1}=0$	Mitigation using (4.57) $k_{bfc2}=0, k_{mfc2}=1$	Balancing using (4.46)	Balancing using (4.47)
Interval II $-f_t < f_m < f_t$ $k_m=0, k_b=1$	Balancing using (4.36)	Balancing using (4.37)	Balancing (4.46) If $\theta_m=0$, Mitigation could be required	Balancing using (4.47)
Interval III $f_t \leq f_m \leq f_g$ $k_m=1, k_b=0$	Mitigation using (4.56) $k_{bfc1}=0, k_{mfc1}=1$	Balancing using (4.57) $k_{bfc2}=1, k_{mfc2}=0$	Balancing using (4.46)	Balancing using (4.47)

Table 4.1: Transition Control for a broad range of frequency operation.

The frequency f_t is defined as the maximum frequency to switch between balancing and mitigation control. The selection of f_t depend on the parameters of the converter such as power cell capacitance, generator and grid side voltages and power factors. An anaysis of the influence of this parameters for WECS is given in [74]. For this work, f_t is considered as $f_t \approx 0.8 f_g$ including an hysteresis interval of 0.1 Hz to avoid possible undesired transitions.

When the generator-side frequency is close to $f_m=-f_g$, dangerous oscillations appear in $\vec{v}_{c_2\alpha\beta}^{\Sigma\Delta}$. Consequently, the mitigation control proposed in (4.57) has to be applied. As the common-mode voltage is being synthetised by the M^3C, the close-to-dc components of $\vec{v}_{c_1\alpha\beta}^{\Sigma\Delta}$ are controlled using the FC term, as shown in (4.56). In this case, the feed-forward current $\vec{I}_{1dq_f}^{\Sigma\Delta}$ is not include by selecting $k_{bfc1}=1$ and $k_{mfc1}=0$.

The same situation, but with reversal functions, is applied when frequencies are close to $f_m=f_g$. The mitigation proposed in (4.56) is applied to $\vec{v}_{c_1\alpha\beta}^{\Sigma\Delta}$ selecting $k_{bfc1}=0$ and $k_{mfc1}=1$, whereas balancing of $\vec{v}_{c_2\alpha\beta}^{\Sigma\Delta}$ is performed using (4.57) and selecting $k_{bfc2}=1$ and $k_{mfc2}=0$.

For Interval II, the frequency is among the interval $-f_t<f_m<f_t$. Then, the balancing control of (4.36)$-$(4.37) is used to command the vectors $\vec{v}_{c_1\alpha\beta}^{\Sigma\Delta}$ and $\vec{v}_{c_2\alpha\beta}^{\Sigma\Delta}$. The weighting factor are set to $k_b=1$ and $k_m=0$ to disable the circulating current references produced by the mitigation control.

In all intervals, the vectors $\vec{v}_{c_0}^{\alpha\beta}$ and $\vec{v}_{c_{\alpha\beta}}^{0}$ are regulated using (4.46)$-$(4.47). If θ_m is close to zero, (4.46) could be modified to regulate both, dc and ac, components of $\vec{v}_{c_0}^{\alpha\beta}$.

4.3 Circulating Current Control

The equivalent circuit presented in Fig.3.3 and the decoupled model of (3.8) are used to regulate the circulating currents. Fig. 4.6 presents the diagram block of the circulating current control system. The cluster currents are transformed to Double $\alpha\beta0$ coordinates where the components
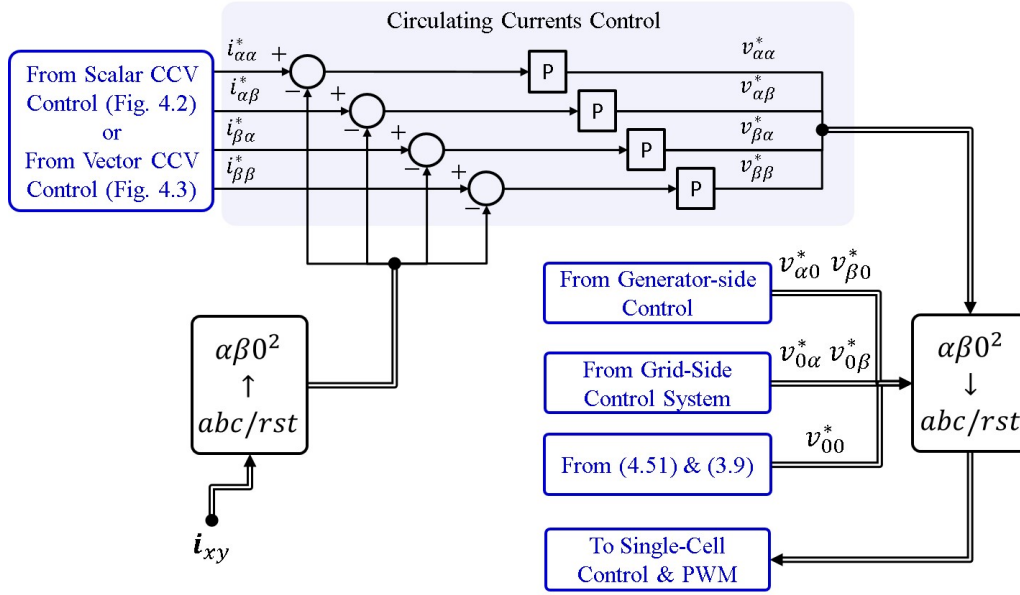
Figure 4.6: Circulating Current Control System.

$i_{\alpha\alpha}$, $i_{\beta\alpha}$, $i_{\alpha\beta}$ and $i_{\beta\beta}$ are compared to their respective references. Due to integrative nature of the plants that defines the dynamics of the four circulating currents, proportional controllers are used to track the circulating current references obtained using either the Scalar CCV Control or the Vector CCV Control. The output of the proportional controllers are the CCV references in Double-$\alpha\beta0$ coordinates. These voltage references are referred to the abc-rst frame using the inverse Double-$\alpha\beta0$ Transformation to be processed by the Single-cell balancing control.

4.4 Control of the average CCV component

The term $v_{c_{00}}$ represent the average voltage in all the capacitor of the M^3C and it is related to the active power flowing into the converter P_{00}, which is defined in (3.30) and represents the difference between the input and output power. Therefore, the following expression is written:

$$Cv_c^* \frac{dv_{c00}}{dt} \approx P_{00} = \frac{1}{3} \overbrace{(v_{m\alpha}i_{m\alpha} + v_{m\beta}i_{m\beta})}^{\text{Input Power}=P_{in}} - \frac{1}{3} \overbrace{(v_{g\alpha}i_{g\alpha} + v_{g\beta}i_{g\beta})}^{\text{Output Power}=P_{out}} \tag{4.58}$$

The term P_{out} represents the M^3C output power. It is considered as a disturbance that can be neglected, or feedforwarded, for control purposes. Additionallity, the generator-side variables can be referred to a dq frame rotating at θ_m and oriented along the rotor flux for the case of a PMSG connected to the input port of the M^3C (please see the complete explanation of the generator-side control system in next Chapter). Therefore, (4.58) becomes:

$$Cv_c^* \frac{dv_{c00}}{dt} \approx P_{00} = \frac{1}{3} v_{mq} i_{mq} \tag{4.59}$$

72

Accordingly, a component of the generator-side current $i^*_{mq_1}$ can be calculated as follows for energy balancing purposes:

$$i^*_{mq_1} = \frac{3Cv^*_c}{v_{mq}} \frac{dv_{c00}}{dt} \tag{4.60}$$

Therefore, the control system proposed in this work uses a component of the machine current $i^*_{mq_1}$ to regulate the average value of the CCVs.

4.5 Single-Cell Control and Modulation Scheme

The voltage references obtained by the control systems presented in the previous Subsection s (i.e. $v^*_{\alpha\alpha}$, $v^*_{\beta\alpha}$, $v^*_{\alpha\beta}$, $v^*_{\beta\beta}$, $v^*_{\alpha0}$, $v^*_{\beta0}$, $v^*_{0\alpha}$ and $v^*_{0\beta}$) are transformed to the natural reference frame using the inverse $\alpha\beta0^2$ Transformation. Then, the CCV references for each cluster in the abc-rst frame are obtained (i.e. v^*_{ar}, v^*_{br}, v^*_{cr}, v^*_{as}, v^*_{bs}, v^*_{cs}, v^*_{at}, v^*_{bt}, v^*_{ct}).

In the natural frame, the cluster references are divided by the number of cells to obtain a voltage reference for each power cell. Here, an additional control loop is utilised to regulate at the same level the capacitor voltages within a cluster. The single-cell control scheme presented in Fig.4.7 is responsible for the capacitor voltage balancing of the capacitors within a cluster. The capacitor voltage of the ith $i \in (1, n)$ power cell is compared to algebraic-mean value of the corresponding CCV. The resulting error is multiplied by the sign of the cluster current (and by the gain k_n) producing either an in-phase or 180° out-of-phase voltage with respect to the cluster current, resulting in a release/absorption of power from/to each power cell. Therefore, an incremental voltage ΔV_i is added to the cell reference voltage v^*_{xy}/n.

This strategy is similar to Single-Cell balancing proposed in [89]. However, there are some incremental differences between this proposal and [89] which are listed below:

- The incremental voltage ΔV_i is produced by the sign of the cluster current instead of the cluster currents to reduce the oscillations in the control signals.

- The capacitor voltage is compared to the algebraic mean value of capacitor voltage available in the cluster instead of the desired value v^*_c. By this means that the sum of ΔV_i in the same cluster tends to zero and does not affect the Cluster Capacitor Voltage reference. Therefore, the Cluster Capacitor Voltage control is decoupled from the Single-Cell Control.

Finally, phase-shifted unipolar sinusoidal PWM is used to synthesise the voltage references for each power cell [89]. The single-cell voltage references of the same cluster are compared to triangular carrier signals shifted by $2\pi/n$ from each other. This modulation algorithm gives expansion for a high number of power cells, and it is simple to implement in commercial FPGA-based control platforms. Moreover, phase-shifted PWM produces power losses evenly distributed among the cells of the same cluster, and it generates an output switching frequency of $2n$ times the carrier frequency.
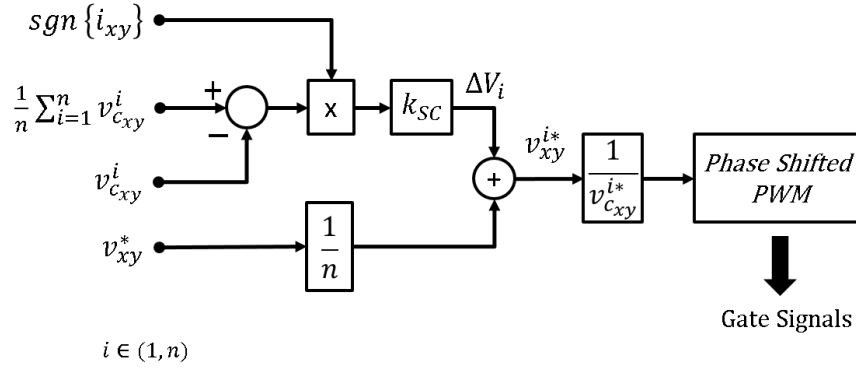
Figure 4.7: Proposed Single-Cell Balancing Control.

4.6 Summary

The Chapterhas presented a cascade control strategy for M^3C based WECSs. This proposal considers a cascade structure, where the outer loops regulate the capacitor voltages by setting the references of the circulating currents. Moreover, they can be linked to the input and output current control loops.

Especial attention had been paid to the CCV control system. Two control proposals are introduced to achieve operation in LFM as well as in EFM. The first control proposal performs balancing using the Semi-controllable terms of the Power-CCV model in Double-$\alpha\beta0$ coordinates. Moreover, the EFM control is based on open-loop circulating current references that mitigate the voltage oscillations produced by the EF operation.

The Vector CCV Control Strategy introduces a novel $\mathrm{d}q$ based vector control which is especially useful for EFM operation. In this strategy, the dynamics of the CCVs is analysed in $\Sigma\Delta$ Double-$\alpha\beta0$ coordinates. When the machine frequency is not close to the unstable points, the average values of the vectors are balanced using the Semi-controllable terms of the Power-CCV model. The EFM control is performed using a closed-loop control system implemented in $\mathrm{d}q$ coordinates which allow operation of the converter in a broad range of frequencies, including equal frequency.

CHAPTER 5

Proposed Control Strategies for based M^3C WECS - WECS Control

5.1 Introduction

This Chapter discusses the application of the M^3C to drive Multi-MW WECSs, focusing on the control structures that enable MPPT capability at the generator-side and grid code compliance at the grid-side.

The generator-side control system comprises a cascaded structure where an outer control loop performs MPPT, and an inner control loop regulates the generator current using a dq based control system suitable for PMSG based WECSs.

The grid-side control system considers LVRT control in the presence of symmetrical or asymmetrical faults. Unlike conventional LVRT algorithms in the dq frame, this proposal considers the use of Resonant Controllers to regulate the positive and negative sequence components of the grid voltage. Sequence component separation is achieved using a new fast-convergence Delayed Signal Cancellation (DSC) method which is also discussed in this chapter.

Finally, a brief explanation of the controller design criteria used to tune the cascade control systems is presented. Notice that this section includes also the control structures detailed in Chapter 4.
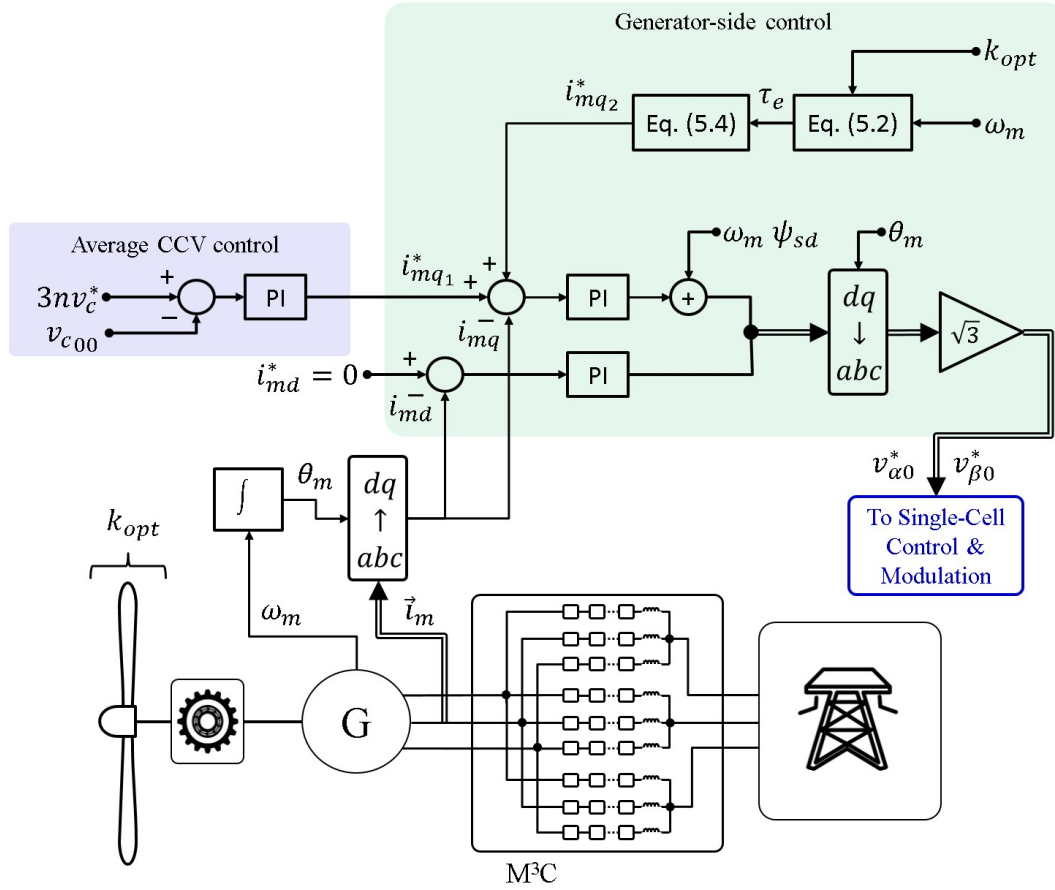
Figure 5.1: Proposed Control Strategy Generator-side control strategy.

5.2 Wind Turbine Control System

5.2.1 MPPT

The modelling of PMSG based WECSs have been extensively discussed in the literature [27,38,39]. For completeness, a brief discussion is presented in this section.

The mechanical torque and the power produced by a wind turbine are expressed as:

$$P_m = 0.5\pi\rho r_{wt}^2 C_p(\lambda, \beta)v_w^3 \tag{5.1}$$

where v_w is the wind speed, β correspond to the blade pitch angle and r_{wt} is the blades ratio. $C_p(\lambda, \beta)$ is the power coefficient and λ represents the tip-speed ratio. The power characteristic $C_p(\lambda, \beta)$ reported in [36, 39] is used in this work. For each wind velocity, there is a point of maximum power capture from the wind and, in steady state, the wind turbine operates at a maximum power point when the electrical generator torque is regulated as:

$$\tau_{\mathrm{e}} = K_{opt}\omega_m^2 \rightarrow P_m = K_{opt}\omega_m^3 \tag{5.2}$$

being K_{opt} a constant that depends on the blade aerodynamic, gear box ratio and wind turbine parameters. This variable can be calculated as the ratio between the nominal power P_m and the nominal generator rotational speed ω_m.

In this proposal, the generator-side variables are referred to a $\mathrm{d}q$ frame rotating at θ_m and oriented along the rotor flux [39] because a PMSG is connected to the input port of the M^3C. Accordingly, the torque-current relationship can be expressed as :

$$\tau_{\mathrm{e}} = \frac{3}{2}p\psi_{mr}\mathrm{i}_{mq_2} \tag{5.3}$$

Being p the generator pair of poles, ψ_{mr} the rotor flux and i_{mq_2} the generator torque current in $\mathrm{d}q$ coordinates.

Replacing (5.2) in (5.3), the PMSG current reference for MPPT purposes is calculated as follow:

$$\mathrm{i}_{mq_2}^* = \frac{2}{3}\frac{K_{opt}\omega_m^2}{p\psi_{mr}} \tag{5.4}$$

The proposed generator-side control system is illustrated in Fig.5.1. This control system regulates the quadrature current $\mathrm{i}_{mq_2}^*$ to operates in MPPT.

5.2.2   Generator-side current control

The dynamics of the generator-side Voltage-Current model presented in (3.12) can be controlled using conventional $\mathrm{d}q$ control systems implemented in $\mathrm{d}q$ coordinates rotating at θ_m. Then, (3.12) becomes:

$$\begin{bmatrix} v_{md} \\ v_{mq} \end{bmatrix} = \frac{1}{\sqrt{3}}\begin{bmatrix} v_{d0} \\ v_{q0} \end{bmatrix} + \frac{L_c}{3}\frac{\mathrm{d}}{\mathrm{d}t}\begin{bmatrix} \frac{\mathrm{d}}{\mathrm{d}t} & -\omega_m \\ \omega_m & \frac{\mathrm{d}}{\mathrm{d}t} \end{bmatrix}\begin{bmatrix} \mathrm{i}_{md} \\ \mathrm{i}_{mq} \end{bmatrix} \tag{5.5}$$

Being $v_{\mathrm{d}0}$ and v_{q0} stand for the CCVs $v_{\alpha 0}$ and $v_{\beta 0}$ in $\mathrm{d}q$ coordinates.

To achieve decoupled generator-side current control, the voltage commands are:

$$\frac{1}{\sqrt{3}}\begin{bmatrix} v_{\mathrm{d}0}^* \\ v_{q0}^* \end{bmatrix} = \begin{bmatrix} v_{md} \\ v_{mq} \end{bmatrix} - \begin{bmatrix} 0 & \frac{-L_c\omega_m}{3} \\ \frac{L_c\omega_m}{3} & 0 \end{bmatrix}\begin{bmatrix} \mathrm{i}_{md} \\ \mathrm{i}_{mq} \end{bmatrix} - PI_m\left\{\begin{bmatrix} \mathrm{i}_{md}^* \\ \mathrm{i}_{mq}^* \end{bmatrix} - \begin{bmatrix} \mathrm{i}_{md} \\ \mathrm{i}_{mq} \end{bmatrix}\right\} \tag{5.6}$$

Where PI_m stands for the transfer function of the PI controller used to regulate the currents.

This control structure is shown in Fig. 5.1. The generator-side control system is implemented

in a dq frame orientated along the rotor flux vector. For simplicity, the dq decoupling terms have not been displayed in Fig. 5.1, but they are considered. The output of the PI controller represents the voltage references $\vec{v}_0^{\alpha\beta*}$, which are rotated back to the natural frame. These voltage references are sent to the Single-Cell Control as shown in Fig. 4.6.

Grid currents can be regulated using a similar structure than in Fig. 5.1. However, Resonant Controllers are preferred due to the LVRT requirements imposed to grid-connected WECSs. This is be further explained in next Section.
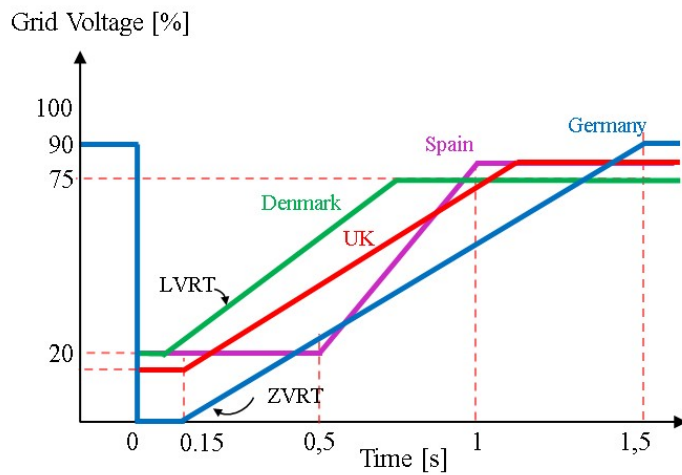
(a)
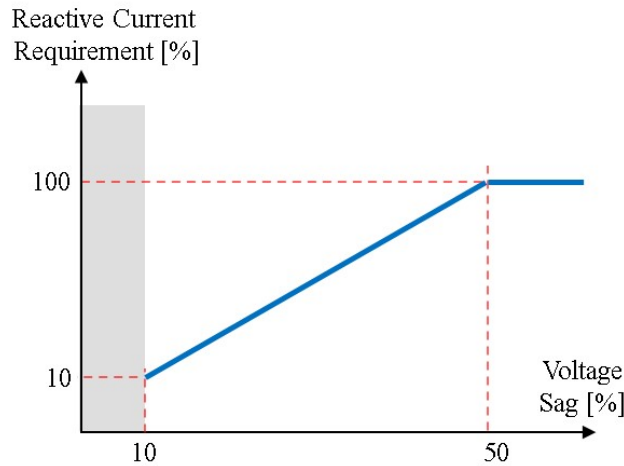
(b)

Figure 5.2: Low Voltage Ride-Through Requirements from different national codes. (a) Magnitude and duration limits of the grid voltage sags. (b) Required Reactive current injection of German Grid-Code.

78

5.3   Grid-side Control System

5.3.1   LVRT Requirements for grid-connected WECSs

There are different LVRT requirements which are imposed by several countries around the world. A good summary of standard LVRT requirements was presented in Subsection 2.2.2.3. Summarising, to implement an LVRT control strategy, the system should be able to:

- WECS should remain connected in the presence of grid-voltage sags when the grid voltage is within the boundaries specified in Fig. 5.2(a).

- Reactive power control must be changed from normal operation –typically unitary power factor– to a maximum voltage support during grid sags, as shown in Fig. 5.2(b). WECSs must be able to provide full rated reactive power to help to re-establish the normal grid voltage as soon as possible.

5.3.2   Grid-side Control Strategy

The proposed control system for LVRT operation of the M^3C is shown in Fig. 5.3. For asymmetrical grid-voltage sag conditions, the currents flowing into the grid are regulated to provide LVRT behaviour. In Fig. 5.3, this is represented by the block "LVRT calculation". The current calculation method is presented in Subsection 5.3.3. Moreover, the positive and negative components of the grid voltage have to be estimated to be able to calculate $(5.18)-(5.21)$. Instead of using $\mathrm{d}q$ frame controllers, the use of Resonant Controllers is preferred because no orientation along any voltage/current vector is needed, and only two Resonant Controllers are required. In a typical $\mathrm{d}q$ implementation four controllers have to be implemented to deal with the positive and negative components.

The positive and negative sequence components of voltages/currents have to be separated to calculate the current references and also to guarantee correct grid frequency estimation. Then, sequence components of the grid voltage vector and current are estimated using a modified Delayed Signal Cancellation algorithm, which can be used with a programmable delay angle. This is further explained in Section 5.3.4. The positive sequence voltage is the input to a Phase-Locked Loop (PLL) algorithm designed to estimate the grid frequency f_g required to maintain tuning of the resonant controllers in the current control system.

Finally, the voltage references $v_{0\alpha}^*$ and $v_{0\beta}^*$ are sent to the Single-Cell Control.
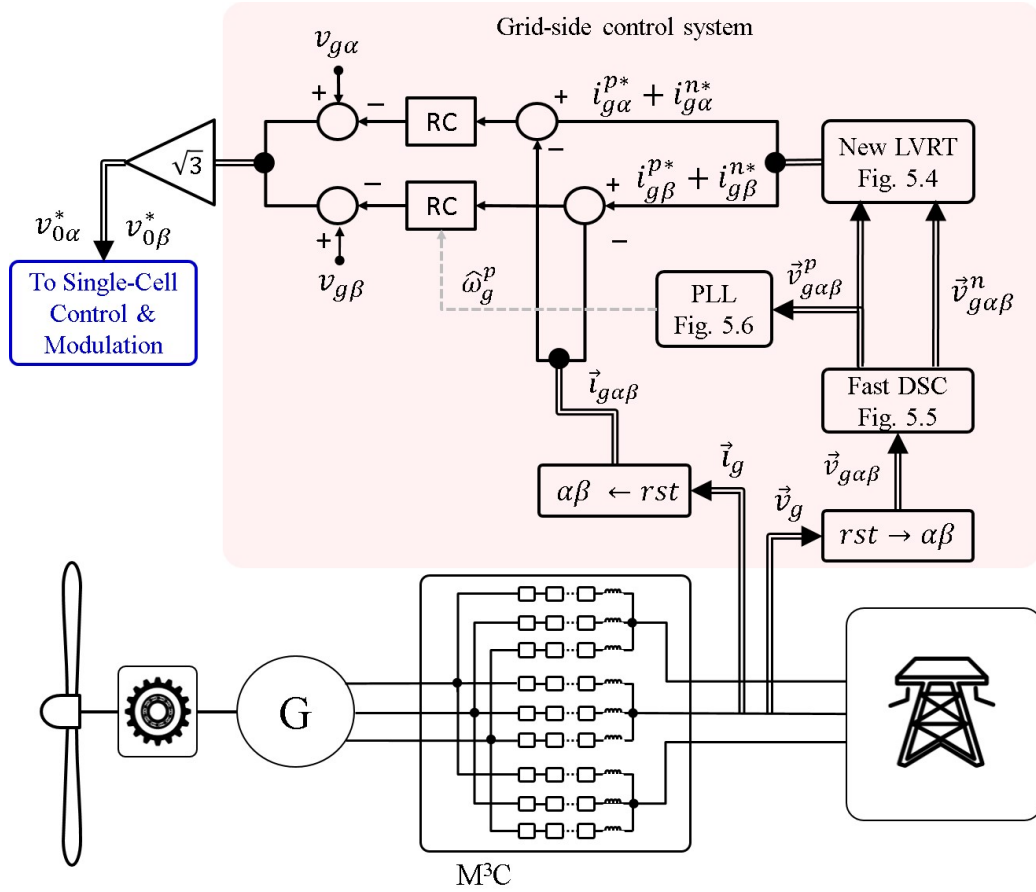
Figure 5.3: Proposed grid-side LVRT control strategy.

5.3.2.1 Complex Power Considerations

For the implementation of LVRT control systems, the measured currents and voltages must be separated into positive and negative sequence components to eliminate the power oscillations in the active $-$or reactive$-$ power injected into the grid.

The apparent power at grid terminal, calculated considering a three-leg unbalanced system with positive -and negative- sequence components, can be calculated as:

$$P_g + jQ_g = k_{\alpha\beta}(\vec{v}_{g_{\alpha\beta}}^{\,p} + \vec{v}_{g_{\alpha\beta}}^{\,n})(\vec{i}_{g_{\alpha\beta}}^{\,p} + \vec{i}_{g_{\alpha\beta}}^{\,n})^c \tag{5.7}$$

The value of $k_{\alpha\beta}$ depends on the $\alpha\beta$ transform being used, e.g. $k_{\alpha\beta} = \sqrt{\frac{2}{3}}$ for the power invariant transformation and $k_{\alpha\beta} = 1$ for the conventional $\alpha\beta$ transformation. Moreover, the superscript c stands for the complex conjugate operator.

In (5.7), $\vec{v}_{g_{\alpha\beta}}^{\,p} = v_{g\alpha}^p + jv_{g\beta}^p$ and $\vec{i}_{g_{\alpha\beta}}^{\,p} = i_{g\alpha}^p + ji_{g\beta}^p$ represent the positive sequence voltage and current vectors. On the other hand, $\vec{v}_{g_{\alpha\beta}}^{\,n}, \vec{i}_{g_{\alpha\beta}}^{\,n}$ are the negative sequence voltage and current vectors. In the stationary $\alpha\beta$ frame, $(v_{g\alpha}^p, v_{g\beta}^p)$ are defined as the real and imaginary components of $\vec{v}_{g_{\alpha\beta}}^{\,p}$,

80

respectively. Similarly, $(v^n_{g\alpha}, v^n_{g\beta})$ are defined as the real and imaginary components of $\vec{v}^{\,n}_{g\alpha\beta}$

Expanding (5.7) yields to:

$$P_g(t) = P_{g0} + P_{gc2}cos2\omega_g t + P_{gs2}sin2\omega_g t \tag{5.8}$$

$$Q_g(t) = Q_{g0} + Q_{gc2}cos2\omega_g t + Q_{gs2}sin2\omega_g t \tag{5.9}$$

where $P_g(t)$, $Q_g(t)$ are the active and reactive power, respectively, which are time dependent functions, and P_{g0} and Q_{g0} are the dc components of the active/reactive power. The other terms in (5.8)−(5.9) are double frequency components rotating at $(2\omega_g)$.

Using (5.7)−(5.9), the terms P_{g0}, Q_{g0}, P_{gc2}, P_{gs2}, Q_{gc2} and Q_{gs2} are obtained as:

$$P_{g0} = k_{\alpha\beta}(v^p_{g\alpha}i^p_{g\alpha} + v^p_{g\beta}i^p_{g\beta} + v^n_{g\alpha}i^n_{g\alpha} + v^n_{g\beta}i^n_{g\beta}) \tag{5.10}$$

$$P_{gc2} = k_{\alpha\beta}(v^p_{g\alpha}i^n_{g\alpha} + v^p_{g\beta}i^n_{g\beta} + v^n_{g\alpha}i^p_{g\alpha} + v^n_{g\beta}i^p_{g\beta}) \tag{5.11}$$

$$P_{gs2} = k_{\alpha\beta}(v^n_{g\beta}i^p_{g\alpha} - v^n_{g\alpha}i^p_{g\beta} - v^p_{g\beta}i^n_{g\alpha} + v^p_{g\alpha}i^n_{g\beta}) \tag{5.12}$$

$$Q_{g0} = k_{\alpha\beta}(v^p_{g\beta}i^p_{g\alpha} - v^p_{g\alpha}i^p_{g\beta} + v^n_{g\beta}i^n_{g\alpha} - v^n_{g\alpha}i^n_{g\beta}) \tag{5.13}$$

$$Q_{gc2} = k_{\alpha\beta}(v^p_{g\beta}i^n_{g\alpha} - v^p_{g\alpha}i^n_{g\beta} + v^n_{g\beta}i^p_{g\alpha} - v^n_{g\alpha}i^p_{g\beta}) \tag{5.14}$$

$$Q_{gs2} = k_{\alpha\beta}(v^p_{g\alpha}i^n_{g\alpha} + v^p_{g\beta}i^n_{g\beta} - v^n_{g\alpha}i^p_{g\alpha} - v^n_{g\beta}i^p_{g\beta}) \tag{5.15}$$

The grid-side currents have four degrees of freedom $(i^p_{g\alpha}, i^p_{g\beta}, i^n_{g\alpha}, i^n_{g\beta})$ that cannot be used to control the six variables $(P_{g0}, Q_{g0}, P_{gc2}, P_{gs2}, Q_{gc2}, Q_{gs2})$ at the same time. Therefore it is necessary to make a choice of variables to control.

5.3.2.2 Calculation of the current references for LVRT control

In this proposal, the grid current references are calculated to regulate the dc components of the active and reactive power (P^*_{g0}, Q^*_{g0}), and to eliminate the double frequency oscillations in the active power $(P_{gc2}=0, P_{gs2}=0)$ supplied to the grid. Additionally, when this control methodology is used, the double frequency oscillations in the capacitors of the M^3C are reduced or even eliminated when the currents are calculated using (5.25). However, reactive power oscillations (Q_{gc2}, Q_{gs2}) cannot be simultaneously controlled if undistorted sinusoidal currents are required at the M^3C output. In matrix form, the required references can be defined as:

$$\begin{bmatrix} P^*_{g0} \\ Q^*_{g0} \\ P_{gs2} = 0 \\ P_{gc2} = 0 \end{bmatrix} = k_{\alpha\beta} \begin{bmatrix} v^p_{g\alpha} & v^p_{g\beta} & v^n_{g\alpha} & v^n_{g\beta} \\ v^p_{g\beta} & -v^p_{g\alpha} & v^n_{g\beta} & -v^n_{g\alpha} \\ v^n_{g\beta} & -v^n_{g\alpha} & -v^p_{g\beta} & v^p_{g\alpha} \\ v^n_{g\alpha} & v^n_{g\beta} & v^p_{g\alpha} & v^p_{g\beta} \end{bmatrix} \begin{bmatrix} i^p_{g\alpha} \\ i^p_{g\beta} \\ i^n_{g\alpha} \\ i^n_{g\beta} \end{bmatrix} \tag{5.16}$$

Using (5.16), the reference currents are calculated using:

81

$$
\begin{bmatrix} \mathrm{i}_{g\alpha}^{p*} \\ \mathrm{i}_{g\beta}^{p*} \\ \mathrm{i}_{g\alpha}^{n*} \\ \mathrm{i}_{g\beta}^{n*} \end{bmatrix} = \frac{1}{k_{\alpha\beta}} \begin{bmatrix} v_{g\alpha}^p & v_{g\beta}^p & v_{g\alpha}^n & v_{g\beta}^n \\ v_{g\beta}^p & -v_{g\alpha}^p & v_{g\beta}^n & -v_{g\alpha}^n \\ v_{g\beta}^n & -v_{g\alpha}^n & -v_{g\beta}^p & v_{g\alpha}^p \\ v_{g\alpha}^n & v_{g\beta}^n & v_{g\alpha}^p & v_{g\beta}^p \end{bmatrix}^{-1} \begin{bmatrix} P_{g0}^* \\ Q_{g0}^* \\ 0 \\ 0 \end{bmatrix}
\tag{5.17}
$$

Expanding (5.17), the reference currents are obtained as:

$$
\mathrm{i}_{g\alpha}^{p*} = \frac{1}{k_{\alpha\beta}} \left[\frac{v_{g\alpha}^p\, P_{g0}^*}{v_{g\alpha}^{p\,2} + v_{g\beta}^{p\,2} - v_{g\alpha}^{n\,2} - v_{g\beta}^{n\,2}} + \frac{v_{g\beta}^p\, Q_{g0}^*}{v_{g\alpha}^{p2} + v_{g\beta}^{p\,2} + v_{g\alpha}^{n\,2} + v_{g\beta}^{n\,2}} \right]
\tag{5.18}
$$

$$
\mathrm{i}_{g\beta}^{p*} = \frac{1}{k_{\alpha\beta}} \left[\frac{v_{g\beta}^p\, P_{g0}^*}{v_{g\alpha}^{p\,2} + v_{g\beta}^{p\,2} - v_{g\alpha}^{n\,2} - v_{g\beta}^{n\,2}} - \frac{v_{g\alpha}^p\, Q_{g0}^*}{v_{g\alpha}^{p\,2} + v_{g\beta}^{p\,2} + v_{g\alpha}^{n\,2} + v_{g\beta}^{n\,2}} \right]
\tag{5.19}
$$

$$
\mathrm{i}_{g\alpha}^{n*} = \frac{1}{k_{\alpha\beta}} \left[\frac{-v_{g\alpha}^n\, P_{g0}^*}{v_{g\alpha}^{p\,2} + v_{g\beta}^{p\,2} - v_{g\alpha}^{n\,2} - v_{g\beta}^{n\,2}} + \frac{v_{g\beta}^n\, Q_{g0}^*}{v_{g\alpha}^{p\,2} + v_{g\beta}^{p\,2} + v_{g\alpha}^{n\,2} + v_{g\beta}^{n\,2}} \right]
\tag{5.20}
$$

$$
\mathrm{i}_{g\beta}^{n} = \frac{1}{k_{\alpha\beta}} \left[\frac{-v_{g\beta}^n\, P_{g0}^*}{v_{g\alpha}^{p\,2} + v_{g\beta}^{p\,2} - v_{g\alpha}^{n\,2} - v_{g\beta}^{n\,2}} - \frac{v_{g\alpha}^n\, Q_{g0}^*}{v_{g\alpha}^{p\,2} + v_{g\beta}^{p\,2} + v_{g\alpha}^{n\,2} + v_{g\beta}^{n\,2}} \right]
\tag{5.21}
$$

Notice that (5.18)−(5.21) are simple to implement in a Digital Signal Processor. The reference values P_{g0}^*, Q_{g0}^* are considered as inputs to the control system shown in Fig. 5.3. They can be obtained from the grid-code LVRT requirements, using the curves depicted in Fig. 5.2.

If the currents calculated from (5.17) are imposed by the current control system, the double frequency oscillations in the capacitor of the M^3C are not eliminated. This is because the M^3C supplies the oscillatory active power consumed by the filter. These power oscillations can be calculated as:

$$
\Delta P_{g_{c2}} = \left[2R_{g_1}\left(\mathrm{i}_{g\alpha}^p \mathrm{i}_{g\alpha}^n + \mathrm{i}_{g\beta}^p \mathrm{i}_{g\beta}^n\right) + 2\omega_g L_{g_1}\left(\mathrm{i}_{g\alpha}^p \mathrm{i}_{g\beta}^n - \mathrm{i}_{g\beta}^p \mathrm{i}_{g\alpha}^n\right) \right]
\tag{5.22}
$$

$$
\Delta P_{g_{s2}} = \left[R_{g_1}\left(\mathrm{i}_{g\alpha}^p \mathrm{i}_{g\beta}^n - \mathrm{i}_{g\beta}^p \mathrm{i}_{g\alpha}^n\right) + 2\omega_g L_{g_1}\left(-\mathrm{i}_{g\alpha}^p \mathrm{i}_{g\alpha}^n - \mathrm{i}_{g\beta}^p \mathrm{i}_{g\beta}^n\right) \right]
\tag{5.23}
$$

where L_{g_1} and R_{g_1} are the equivalent grid-side inductance and its intrinsic resistance . The equivalent grid-side inductance is:

$$
L_{g_1} = \frac{1}{3} L_c + L_g
\tag{5.24}
$$

where the term $(1/3)L_c$ is obtained from the Voltage-Current model of (3.13). The term L_g stands for any additional inductance connected between the M^3C output and the grid.

Consequently, the values of $\Delta P_{g_{c2}}$ and $\Delta P_{g_{s2}}$ have to be considered in the calculation of the reference currents to eliminate the double frequency active power components at the converter terminals. This means that the grid has to supply these oscillations. Then, the values of $\Delta P_{g_{c2}}$ and $\Delta P_{g_{s2}}$ should be considered in the calculation of the reference current in (5.17):

$$
\begin{bmatrix} i^{p*}_{g\alpha} \\ i^{p*}_{g\beta} \\ i^{n*}_{g\alpha} \\ i^{n*}_{g\beta} \end{bmatrix} = \frac{1}{k_{\alpha\beta}} \begin{bmatrix} v^p_{g\alpha} & v^p_{g\beta} & v^n_{g\alpha} & v^n_{g\beta} \\ v^p_{g\beta} & -v^p_{g\alpha} & v^n_{g\beta} & -v^n_{g\alpha} \\ v^n_{g\beta} & -v^n_{g\alpha} & -v^p_{g\beta} & v^p_{g\alpha} \\ v^n_{g\alpha} & v^n_{g\beta} & v^p_{g\alpha} & v^p_{g\beta} \end{bmatrix}^{-1} \begin{bmatrix} P^*_{g0} \\ Q^*_{g0} \\ P^*_{gs2} = -\Delta P_{gs2} \\ P^*_{gc2} = -\Delta P_{gc2} \end{bmatrix} \tag{5.25}
$$

If the currents are obtained using (5.25), the output port of the M^3C is free of the double frequency oscillations produced by the filter. To calculate either (5.17) or (5.25), the positive and negative components of the currents have to be estimated using an additional implementation of the DSC algorithm discussed in Section 5.3.4. Additionally, the calculation of (5.25) implies that a more complicated inverse matrix operation has to be implemented. Nevertheless, these calculations are still simple to implement using modern DSPs [41, 42, 97].

5.3.3 Proposed LVRT control strategy for the M^3C based WECS

The double frequency active power components ($\Delta P_{g_{c2}}$ and $\Delta P_{g_{s2}}$) are calculated using (5.22) and (5.23). The main drawback of this calculation is the fact that the power references ($P^*_{g_{c2}}$, $P^*_{g_{s2}}$) which set the current references, depend on the current measurements. Consequently, delayed sample-time current measurements are used in the calculation to avoid algebraic loops [41,98–100].

Here, a new LVRT algorithm is proposed. The control diagram is shown in Fig. 5.4. The double frequency power components are rotated to the dq frame using $\theta_{LVRT} = tan^{-1}(\frac{\Delta P_{gs2}}{\Delta P_{gc2}})$. As $\Delta P_{g_{c2}}$ and $\Delta P_{g_{s2}}$ are orthogonal, the resulting terms ΔP_{g_d} and ΔP_{g_q} are oriented in the direct component ($\Delta P_{gq} = 0$). The magnitude of the component ΔP_{g_d} is normalised and compared with a mitigation constant k_{LVRT}. When $k_{LVRT} = 0$, ΔP_{g_d} is controlled to zero using a PI controller. The output of this PI controller is rotated back from the dq frame and then used as power reference:

$$
\begin{bmatrix} i^{p*}_{g\alpha} \\ i^{p*}_{g\beta} \\ i^{n*}_{g\alpha} \\ i^{n*}_{g\beta} \end{bmatrix} = \frac{1}{k_{\alpha\beta}} \begin{bmatrix} v^p_{g\alpha} & v^p_{g\beta} & v^n_{g\alpha} & v^n_{g\beta} \\ v^p_{g\beta} & -v^p_{g\alpha} & v^n_{g\beta} & -v^n_{g\alpha} \\ v^n_{g\beta} & -v^n_{g\alpha} & -v^p_{g\beta} & v^p_{g\alpha} \\ v^n_{g\alpha} & v^n_{g\beta} & v^p_{g\alpha} & v^p_{g\beta} \end{bmatrix}^{-1} \begin{bmatrix} P^*_{g0} \\ Q^*_{g0} \\ P^*_{gd} \\ P^*_{gq} \end{bmatrix} \tag{5.26}
$$

Selecting $K_{LVRT} = 0$ results in null active power double frequency oscillations at the grid point of connection. However, the active power double frequency oscillation in the filter are supplied for the M^3C. In some cases, e.g., weak grids or massive short circuits, these oscillations could be dangerous for the converter and should be mitigated. This task can easily be achieved regulating $k_{LVRT} = 1$, which implies that the oscillations at the M^3C output are zero.
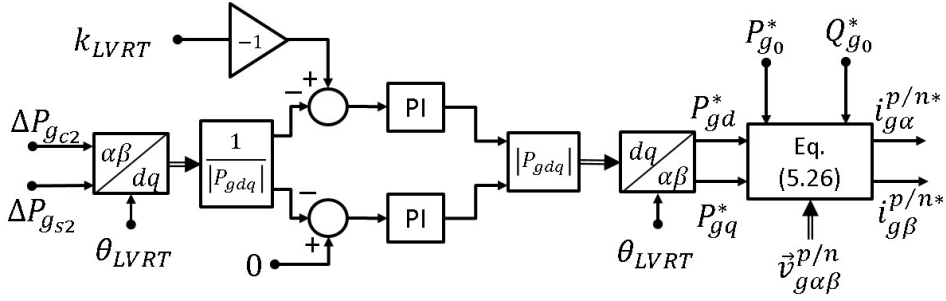
Figure 5.4: Proposed LVRT Control Strategy.

Finally, the current references $i_{g\alpha}^{p*}$, $i_{g\beta}^{p*}$, $i_{g\alpha}^{n*}$ and $i_{g\beta}^{n*}$ are obtained using (5.26). As depicted in Fig. 5.3, only two resonant controllers are required to regulate the current supplied to the grid. The reference currents are obtained as:

$$ i_{g\alpha}^* = i_{g\alpha}^{p*} + i_{g\alpha}^{n*} \tag{5.27} $$

$$ i_{g\beta}^* = i_{g\beta}^{p*} + i_{g\beta}^{n*} \tag{5.28} $$

5.3.4 Sequence Component Separation Method

Conventional Delayed-signal-cancellation methods reported in the literature separate the positive and negative sequence components using (5.29) and (5.30) [101, 102].

$$ \hat{v}_{g\alpha\beta}^p = \frac{1}{2}\left[\vec{v}_g(t) + j\vec{v}_g(t - \frac{T}{4})\right] \tag{5.29} $$

$$ \hat{v}_{g\alpha\beta}^n = \frac{1}{2}\left[\vec{v}_g(t) - j\vec{v}_g(t - \frac{T}{4})\right] \tag{5.30} $$

Where $\hat{v}_{g\alpha\beta}^p$, $\hat{v}_{g\alpha\beta}^n$ are estimations of the positive and negative sequence signals, respectively. The vector $\vec{v}_g$ is the total voltage vector, and T is the signal period. The delayed-signal-cancellation method is probably the best-suited method to separate sequences, and it has been used in grid-connected WECS applications [41, 42, 98].

The main disadvantage of using (5.29)−(5.30) is that a significant delay of $\frac{T}{4}$ (i.e. 5*ms* for 50Hz) is created in the result. Additionally, in digital implementations the ratio $\frac{T}{4t_s}$ (where t_s is the sampling period) has to be an integer, which is not always feasible [101]. Moreover, another disadvantage of the conventional DSC method is that a relatively large number of memory positions could be required to store the vector $\vec{v}_g(t - \frac{T}{4})$.

Conventional DSC methods, as well as the fast method presented in this Chapter, are affected by harmonic distortion in the signals [101]. Filtering has to be applied before using, or a complex generalised DSC (which has a high computational burden) has to be implemented [102]. The

filtering or pre-processing stage is considered outside the scope of this work, and it is assumed that the signals at the DSC input have reduced harmonic distortion. Consequently, the voltage vector $\vec{v}_g$ is composed of positive and negative sequence components as follows:

$$\vec{v}_g = V_1 \mathrm{e}^{j\omega t + \emptyset_1} + V_2 \mathrm{e}^{-j\omega t + \emptyset_2} \tag{5.31}$$

Using (5.31), it can be shown that the positive and negative sequence signals can be obtained as:

$$\vec{v}^{\,p}_{g\alpha\beta} = \frac{1}{2} \left[\vec{v}_g(t) + \frac{j}{\omega} \frac{\partial \vec{v}_g(t)}{\partial t} \right] \tag{5.32}$$

$$\vec{v}^{\,n}_{g\alpha\beta} = \frac{1}{2} \left[\vec{v}_g(t) - \frac{j}{\omega} \frac{\partial \vec{v}_g(t)}{\partial t} \right] \tag{5.33}$$

It is well known that in a digital implementation direct differentiation of the voltage amplifies the noise in $\vec{v}_g$. Therefore, an alternative is to use the following expression:

$$\vec{v}_s = \vec{v}_g(\omega t) - \mathrm{e}^{-j\theta_\mathrm{d}} \vec{v}_g(\omega t - \theta_\mathrm{d}) \tag{5.34}$$

where θ_d is the delay angle. In an experimental implementation this angle is calculated as $\theta_\mathrm{d} = 2T/(mt_s)$ where m is an integer. Using (5.31) in (5.34), and assuming that $\emptyset_1 = \emptyset_2 = 0$, the vector $\vec{v}_s$ is obtained as:

$$\vec{v}_s = V_1 \mathrm{e}^{j\omega t} + V_2 \mathrm{e}^{-j\omega t} - \mathrm{e}^{-j\theta_\mathrm{d}} \left[V_1 \mathrm{e}^{j(\omega t - \theta_\mathrm{d})} + V_2 \mathrm{e}^{-j(\omega t - \theta_\mathrm{d})} \right] \tag{5.35}$$

By simple inspection of (5.34)−(5.35) it is concluded that the negative sequence component is canceled, yielding to:

$$\hat{v}^{\,p}_{g\alpha\beta} = \frac{\vec{v}_s}{[1 - \mathrm{e}^{-j2\theta_\mathrm{d}}]} = \frac{1}{2} \frac{\left[\vec{v}_g(\omega t) - \mathrm{e}^{-j\theta_\mathrm{d}} \vec{v}_g(\omega t - \theta_\mathrm{d}) \right] (1 - \mathrm{e}^{j2\theta_\mathrm{d}})}{[1 - 2\cos(2\theta_\mathrm{d})]} \tag{5.36}$$

where $\hat{v}_{1\beta}$ is an estimation of the positive sequence signal. The negative sequence component of the signal is estimated using:

$$\hat{v}^{\,n}_{g\alpha\beta} = \frac{1}{2} \frac{\left[\vec{v}_g(\omega t) + \mathrm{e}^{-j\theta_\mathrm{d}} \vec{v}_g(\omega t - \theta_\mathrm{d}) \right] (1 - \mathrm{e}^{-j2\theta_\mathrm{d}})}{[1 - 2\cos(2\theta_\mathrm{d})]} \tag{5.37}$$

It can be shown that (5.32)−(5.33) are equivalent to (5.36)−(5.37) when $\theta_\mathrm{d} \to 0$. The implementation of the proposed fast DSC, based on (5.36)−(5.37), is shown in Fig. 5.5. The time delay of mt_s seconds corresponds to a delay angle of θ_d rads. The conventional DSC of (5.29)−(5.30)
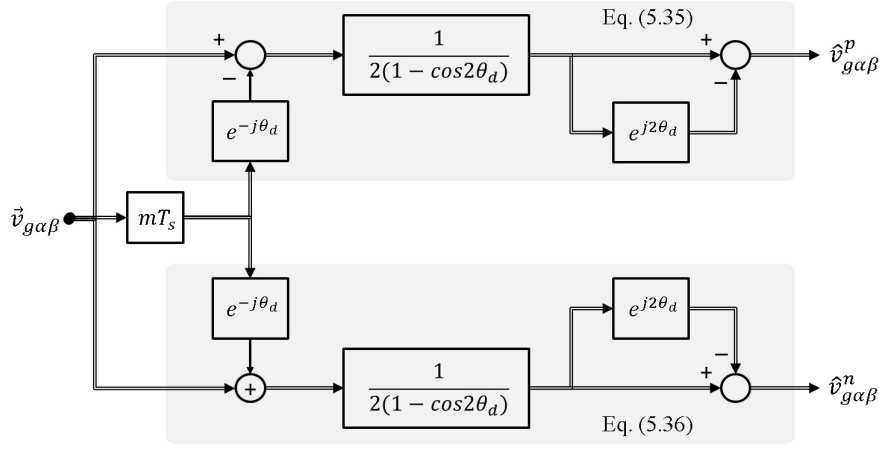
Figure 5.5: Proposed DSC algorithm.

is obtained using $\theta_\mathrm{d} = \pi/2$. Notice that the use of $\theta_\mathrm{d} > \pi/2$ is also possible, which could be an alternative for sequence separation with very noisy signals (i.e. delays >5 ms).

The estimation of the sequence components can be obtained using the equations (5.32)$-$(5.33). The extended expression of those equations is presented in (5.38)$-$(5.41). For compactness, $\vec{v}_g^{\,\theta_\mathrm{d}}$ stands for $\vec{v}_g(\omega t - \theta_\mathrm{d})$ and the subscripts p and n stand for the positive and negative sequence components, respectively. Notice that m samples of the signal $\vec{v}_g(t)$ have to be stored in the DSP memory for the implementation of this fast DSC algorithm.

$$
\begin{aligned}
\hat{v}_{g\alpha}^{p} = {} & \frac{v_{g\alpha} - v_{g\alpha}^{\theta_\mathrm{d}} \cos\theta_\mathrm{d} - v_{g\beta}^{\theta_\mathrm{d}} \sin\theta_\mathrm{d} - (v_{g\alpha} - v_{g\alpha}^{\theta_\mathrm{d}} \cos\theta_\mathrm{d} - v_{g\beta}^{\theta_\mathrm{d}} \sin\theta_\mathrm{d}) \cos2\theta_\mathrm{d}}{2(1 - \cos2\theta_\mathrm{d})} \\
& + \frac{(v_{g\beta} - v_{g\beta}^{\theta_\mathrm{d}} \cos\theta_\mathrm{d} + v_{g\alpha}^{\theta_\mathrm{d}} \sin\theta_\mathrm{d}) \sin2\theta_\mathrm{d}}{2(1 - \cos2\theta_\mathrm{d})}
\end{aligned}
\tag{5.38}
$$

$$
\begin{aligned}
\hat{v}_{g\beta}^{p} = {} & \frac{v_{g\beta} - v_{g\beta}^{\theta_\mathrm{d}} \cos\theta_\mathrm{d} + v_{g\alpha}^{\theta_\mathrm{d}} \sin\theta_\mathrm{d} - (v_{g\beta} - v_{g\beta}^{\theta_\mathrm{d}} \cos\theta_\mathrm{d} + v_{g\alpha}^{\theta_\mathrm{d}} \sin\theta_\mathrm{d}) \cos2\theta_\mathrm{d}}{2(1 - \cos2\theta_\mathrm{d})} \\
& - \frac{(v_{g\alpha} - v_{g\alpha}^{\theta_\mathrm{d}} \cos\theta_\mathrm{d} - v_{g\beta}^{\theta_\mathrm{d}} \sin\theta_\mathrm{d}) \sin2\theta_\mathrm{d}}{2(1 - \cos2\theta_\mathrm{d})}
\end{aligned}
\tag{5.39}
$$

$$
\begin{aligned}
\hat{v}_{g\alpha}^{n} = {} & \frac{v_{g\alpha} - v_{g\alpha}^{\theta_\mathrm{d}} \cos\theta_\mathrm{d} + v_{g\beta}^{\theta_\mathrm{d}} \sin\theta_\mathrm{d} - (v_{g\alpha} - v_{g\alpha}^{\theta_\mathrm{d}} \cos\theta_\mathrm{d} + v_{g\beta}^{\theta_\mathrm{d}} \sin\theta_\mathrm{d}) \cos2\theta_\mathrm{d}}{2(1 - \cos2\theta_\mathrm{d})} \\
& + \frac{(v_{g\beta} - v_{g\beta}^{\theta_\mathrm{d}} \cos\theta_\mathrm{d} - v_{g\alpha}^{\theta_\mathrm{d}} \sin\theta_\mathrm{d}) \sin2\theta_\mathrm{d}}{2(1 - \cos2\theta_\mathrm{d})}
\end{aligned}
\tag{5.40}
$$

$$
\begin{aligned}
\hat{v}_{g\beta}^{n} = {} & \frac{v_{g\beta} - v_{g\beta}^{\theta_\mathrm{d}} \cos\theta_\mathrm{d} - v_{g\alpha}^{\theta_\mathrm{d}} \sin\theta_\mathrm{d} - (v_{g\beta} - v_{g\beta}^{\theta_\mathrm{d}} \cos\theta_\mathrm{d} - v_{g\alpha}^{\theta_\mathrm{d}} \sin\theta_\mathrm{d}) \cos2\theta_\mathrm{d}}{2(1 - \cos2\theta_\mathrm{d})} \\
& - \frac{(v_{g\alpha} - v_{g\alpha}^{\theta_\mathrm{d}} \cos\theta_\mathrm{d} + v_{g\beta}^{\theta_\mathrm{d}} \sin\theta_\mathrm{d}) \sin2\theta_\mathrm{d}}{2(1 - \cos2\theta_\mathrm{d})}
\end{aligned}
\tag{5.41}
$$

Figure 5.6: Proposed DSC algorithm.

5.3.5 Frequency estimation under unbalance conditions

In conventional grid-connected dq frame control system, the orientation is performed in the positive sequence component of the grid voltage. Consequently, Phase Locked Loops (PLLs) are widely employed to identify the frequency of the positive sequence component of the grid voltage. The proposed LVRT control system is implemented using RCs in the $\alpha\beta$ frame, then no orientation along any voltage/current vector is required. However, the electrical frequency ω_g^p is still needed to tuning the RCs of the current control system.

Fig. 5.6 shows the diagram block of the PLL used in this work to synchronise the M^3C converter with the grid voltage. It is important to mention that there are several topologies of PLL proposed in the literature, and the PLL presented in Fig. 5.6 is just one of them. The positive sequence voltage $v_{g\alpha\beta}^p$ estimated with the Fast DSC algorithm presented in the previous Subsection, is the input to the PLL algorithm designed to estimate the electrical frequency ω_g^p. The symbol $\otimes$ represents the cross product between the normalised grid voltage vector and a unitary vector generated by the PLL.

$$\xi = \frac{(\hat{v}_{g\alpha}^p + j\hat{v}_{g\beta}^p)}{\left|\hat{v}_{g\alpha\beta}^p\right|} \otimes (sin\hat{\theta}_g^p + jcos\hat{\theta}_g^p) \tag{5.42}$$

Then, the cross product is zero when both vectors are in phase and the PLL "lock" the grid voltage ensuring zero steady state error due to the integral action of the PI controller.

5.4 Controllers Design

The proposed control systems are designed using the root-locus method and the transfer functions obtained in Chapters 3 to 5. The outer control loops are designed with a closed-loop bandwidth $\approx$ 10 Hz, whereas the internal control loops are designed with a closed-loop bandwidth of about 100 Hz. A summary of the proposed controllers is shown in Table 5.1 with the designed closed-loop bandwidth (Hz) indicated by f_n. In general, either proportional or PI controllers are used, except the grid-side control system where RC have been preferred.

Control Loop	Type	f_n[Hz]
Average Voltage	1 PI Controller	10
Cap.Voltage Balancing	4 PI Controllers (outer control loops)	5
Machine-side Current	2 PI Controllers (dq frame)	100
Grid-side current	2 Resonant Controllers	100
Circulating Currents	4 P Controllers (inner control loops)	100
Single-Cell Voltage	27 Proportional Controller	5

Table 5.1: Summary of the Control Systems implemented.

5.4.1 Design of the CCV Control System

5.4.1.1 Scalar CCV Control System

Operation in LFM
The Scalar CCV balancing control is shown in Fig. 4.2. This strategy features PI controllers designed with a bandwidth of 5 Hz. Equations $(4.11)-(4.14)$ are used to tune the controllers of the Intra-CCV Imbalance terms. Whereas, $(4.28)-(4.28)$ are used to tune the controllers of the Inter-CCV.

Operation in EFM
Due to the mitigation control proposed in the Scalar CCV Control System is based on an open-loop calculation of the circulating current references, there is not any closed loop behaviour for EF operation.

5.4.1.2 Vector CCV Control System

Operation in LFM
The Vector CCV balancing control is shown in Fig. 4.3. This strategy features PI controllers designed with a bandwidth of 5 Hz. Equations $(4.36)-(4.36)$ are used to tuning the controllers of the vector $\vec{v}_{c_{1\alpha\beta}}^{\Sigma\Delta}$ and $\vec{v}_{c_{2\alpha\beta}}^{\Sigma\Delta}$ (Intra-CCV Imbalance terms).

The Inter-CCV balancing control is shown in Fig.4.4. In this case, the vectors $\vec{v}_{c_0}^{\alpha\beta}$ and $\vec{v}_{c_{\alpha\beta}}^{0}$ are balanced using PI controllers designed with a bandwidth of 5 Hz and the plants of $(4.46)-(4.47)$.

Operation in EFM

The Vector CCV mitigation control is illustrated in Fig. 4.5. In this case, $(4.56)-(4.57)$ are used to tuning the PI controllers of the vectors $\vec{v}_{c_{1\alpha\beta}}^{\Sigma\Delta}$ and $\vec{v}_{c_{2\alpha\beta}}^{\Sigma\Delta}$ (Intra-CCV Imbalance). In this case, the bandwidth of the controllers is also selected to 5 Hz.

5.4.2 Design of the Average CCV Control System.

This control loop is presented in Fig. 5.1. Equation (4.60) is used to tuning the PI controller that imposes an additional component to the generator torque current to regulate the average value of the cell capacitor voltages (i.e. similar to the conventional control methodologies used in back-to-back converters [39]). In this case, the controller is designed with a bandwidth of 10 Hz to be slightly faster than the imbalance control systems.

5.4.3 Design of the Circulating Current Control System.

The circulating current loops are shown in Fig. 4.6. Due to the fact that the plant of (3.8) is integrative, and that the circulating currents contain at least two frequency components, proportional controllers designed with a bandwidth of 100 Hz are selected.

5.4.4 Design of the Generator-side Control System

The generator-side control systems is shown in Fig. 5.1. This strategy is based standard field orientated control strategies implemented in $\mathrm{d}q$ coordinates that uses PI controllers. In this case, the PI controllers have been designed with a bandwidth of 100 Hz and the plants of (3.12) are used for tuning purposes.

5.5 Design of the Grid-side Control System

The grid-side control system regulates the grid-connected operation using RCs designed with a bandwidth of 100Hz. More details regarding the implementation design criteria of RCs are discussed in next Subsection 5.6.1.

5.6 Design of the Single-Cell Balancing

This control system is shown in Fig. 4.7. This uses the Power-CCV relationship of (3.16). Due to the integrative nature of the plant, proportional controllers designed with a bandwidth of 10 Hz are used. Notice that the Single-Cell control is decoupled of the CCV control.

5.6.1 Resonant Controllers Design

In this thesis, resonant controllers are used to achieving zero steady-state error when sinusoidal reference signals are provided to the LVRT control system [103]. Most of the design methods for

resonant controllers reported in the literature are usually based on the Laplace domain and transformed to the Z-domain using some of the discretization methods discussed in [104]. However, with this methodology the Z-domain controllers obtained using discretization algorithms (e.g. bilinear transform), do not necessarily maintain the dynamics response of the original s-plane design unless the sampling frequency is relatively high. This is particularly difficult to achieve in applications involving high power converters where the switching frequency could be relatively low to limit the converter losses. To avoid these drawbacks, the resonant controllers of Fig. 5.3 have been directly designed in the z-plane using the zero-pole placement method.

The proposed Z-plane resonant controller is shown in Fig. 5.7. There is a pole (complex conjugate pair) located on the z-plane unit circle and a zero (complex conjugate pair) located at a distance r from the origin. The transfer function of this controller is:

$$RC(z) = K_r \frac{(z - r\mathrm{e}^{j\omega_g T_s})(z - r\mathrm{e}^{-j\omega_g T_s})}{(z - \mathrm{e}^{j\omega_g T_s})(z - \mathrm{e}^{-j\omega_g T_s})} \tag{5.43}$$

which is equivalent to the following second order transfer function:

$$RC(z) = K_r \frac{(z^2 + 2rcos(\omega_g T_s)z + r^2)}{(z^2 + 2cos(\omega_g T_s)z + 1)} \tag{5.44}$$

where ω_g is the grid frequency, and K_r is the controller gain. If the controller is well designed, the poles of the resonant notch are located at the grid frequency ω_g. However, if the grid frequency changes, a self-tuning resonant controller is appropriate, i.e. the transfer function of (5.44) is calculated online using $\hat{\omega}_g^p$, which is the electrical frequency estimated by the PLL algorithm (see Fig. 5.6). This is further discussed in [105], where a self-tuning resonant controller to regulate the stator current of a generator operating over a wide speed range is presented.

The design of the grid current controller is performed using root locus and Bode diagrams. In order to increase the dynamics performance, a lead-lag network can be used [106]. Considering this lead-lag, the transfer function of the controller is:

$$G_c(z) = K_r \frac{(z^2 + 2rcos(\hat{\omega}_g T_s)z + r^2)}{(z^2 + 2cos(\hat{\omega}_g T_s)z + 1)} \frac{(z^2 + az + b)}{(z^2 + cz + \mathrm{d})} \tag{5.45}$$

Two controllers with transfer function $G_c(z)$ are sufficient to regulate both currents $i_{g\alpha}^*$ and $i_{g\beta}^*$ [see (5.27) and (5.28)]. For the design used in this work the current control loop has a bandwidth of approximately 100 Hz, and a phase margin of more than $60°$.
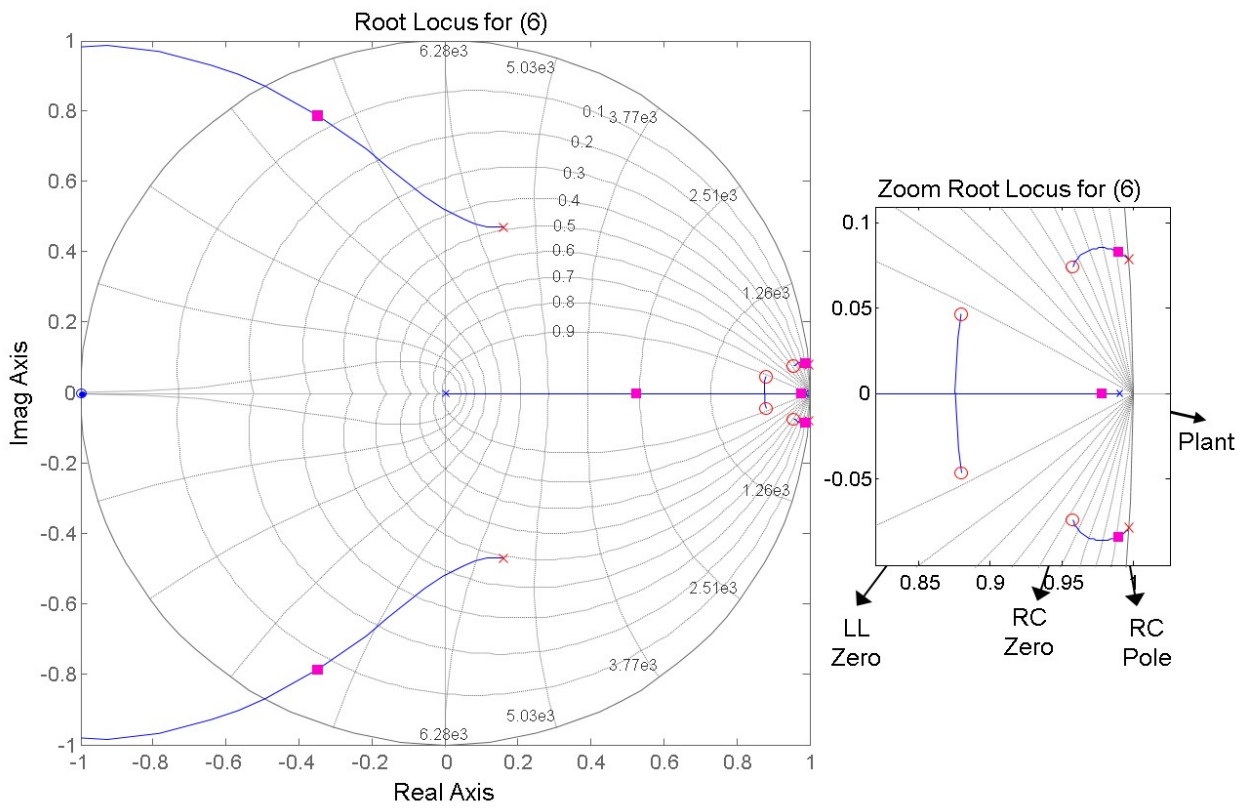
Figure 5.7: Resonant control system pole and zero diagram.

5.7 Summary

This Chapter has presented control structures for the regulation of the systems connected to the generator and grid-side ports of the M^3C.

The Generator-side Control System comprises a cascaded structure where an outer control loop performs MPPT, and an inner control loop regulates the generator current using a dq based control system suitable for PMSG based WECSs.

The Grid-side Control System includes a new control methodology based on self-tuning RCs that require only controllers to regulate the four degrees of freedom ($i^p_{g\alpha}$, $i^p_{g\beta}$, $i^n_{g\alpha}$, $i^n_{g\beta}$) available in grid-side system. One of the advantages of this control structure is the fact that neither counter-revolving dq coordinates nor a notch filters to achieve sequence separation are required.

Additionally, a fast convergence modified DSC algorithm has been proposed. This DSC algorithm can be used to separate the positive and negative sequence components of the unbalanced voltages and currents with a programmable delay. The proposed control system is simple to implement.

Finally, the global overview of the control design of the nested control loops proposed in this Chapter as well as in Chapter 4 is presented.

CHAPTER 6

Simulations

6.1 Introduction

A M^3C based Multi-MW WECS is implemented to verify the theoretical work proposed in this thesis. Several simulations have been conducted to validate the Control Strategies proposed in Chapters 4-5. The following tests are detailed in this Chapter:

- Fixed-Speed Steady State Operation

- Variable-Speed WECS emulation

- Grid-code compliance tests, including Symmetric and Asymmetric LVRT operation

- Equal Input-Output Frequencies Operation

The tests mentioned above are conducted to validate proper capacitor voltage balancing, variable speed operation and fulfilment of grid codes for M^3C based Multi-MW WECS.

Although it is not likely that a M^3C based Multi-MW WECS operate with equal generator-grid frequencies, the system is tested in equal-frequency mode to analyse the performance of the proposed control strategies to ride-through the more demanding operational conditions that can lead to high voltage oscillations in the capacitor of the converter.

The general parameters considered for all simulation tests are shown in Table 6.1. The model of the M^3C is designed using PLECS software. The simulated M^3C has a nominal power of 10 MW and it features seven power cells per cluster. Each power cell capacitor operates at 1.71 kV with a capacitance of 7 mF. In accordance with the index used to compare dimensioning of

Parameters	Nominal Value
Nominal Power	10 MVA
Cells per branch	7
Input Voltage	5.39 kV
Input Frequency	10-40 Hz
Cluster Inductor	1.2 mH
Single cell Capacitance	7 mF
Nominal Capacitor Voltage	1715 V
Output Voltage	4580 V
Output Frequency	50 Hz
Switching frequency	0.8 kHz

Table 6.1: Parameters of the M^3C simulated using PLECS.

Multilevel Converters presented in [107], the simulated model has an H index of 64.8 ms, which is a normal value for AC-to-AC conversion. The power cells are controlled using unipolar phase-shifted modulation. Additionally, the H-bridges are composed of four ideal IGBT modules (with anti-parallel diodes) and their associates flying capacitors.

In the following Subsections, all the simulation results are discussed to ensure that the control system is tested in the most realistic terms possible.

6.1.1 Equivalence of the control strategies for Low Frequency Operation

When the generator frequency is not close to the grid frequency, the oscillations in the capacitors of the M^3C are within an acceptable margin. In this situation, either Scalar of Vector control strategies regulate the average voltage of the CCVs using the SC power components. In fact, both strategies use circulating currents in phase with the generator voltage to generate manipulable power flows which drive the imbalance terms (either in vector or scalar form) to zero. What is more, the major advantage of the $\Sigma\Delta$ Transformation is to decouple Intra-CCV Imbalances when the unstable operational conditions are reached. Therefore, it can be stated that both strategies produce similar results when the frequency at the generator side is low. Accordingly, the results obtained in this Section are obtained using the Vector Control Strategy in low-frequency mode.
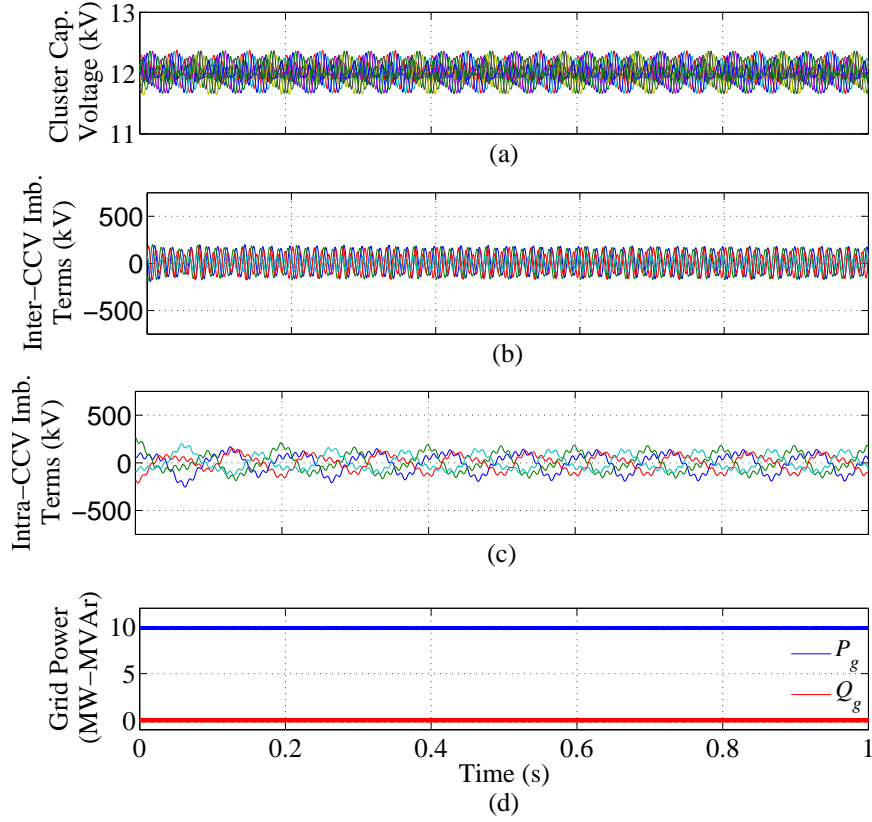
Figure 6.1: Simulation Results for Steady State Operation in LFM. (a) 27 Power Cells Capacitor Voltages. (b) Inter-CCV imbalance terms. (c) Intra-CCV imbalance terms. (d) Power Injected into the Grid.

6.2 Simulation Results for Fixed-Speed Steady State Operation

The steady state operation of the M^3C in LFM is evaluated in this test. The generator-side frequency is set to 40 Hz, whereas the grid frequency is 50 Hz. The capacitor voltages of the 63 power cells are regulated to 1715 V. Consequently, the Cluster Capacitor Voltage is regulated to 12 kV, as shown in Fig. 6.1(a). The Inter-CCV imbalance terms (i.e. $v_{c_{0\alpha}}$, $v_{c_{0\beta}}$, $v_{c_{\alpha 0}}$, $v_{c_{\beta 0}}$) are presented in Fig. 6.1(b), whereas the Intra-CCV imbalance terms (i.e $v_{c_{\alpha\alpha}}$, $v_{c_{\alpha\beta}}$, $v_{c_{\alpha\beta}}$, $v_{c_{\beta\beta}}$) are shown in Fig. 6.1(c). The eight imbalance terms are successfully regulated inside a $\pm$ 200 V band, which represents oscillations of $\approx 1.6\%$ of the Cluster Capacitor Voltage. Finally, Fig. 6.1(d) illustrates the unity power factor operation of the system injecting 10 MW into the grid.

The average CCV control loop presents excellent steady state tracking, as shown in Fig. 6.2. The term $v_{c_{00}}$ is regulated to $3nv_c^* = 36$ kV in accordance with (3.20).

The Single-cell control performance is shown in Fig. 6.3. The balancing of the capacitor voltages within a cluster is achieved and there almost not drift or imbalances between the capacitors within a cluster. Moreover, the tracking of the Cluster Capacitor Voltagereference for cluster v_{ar}
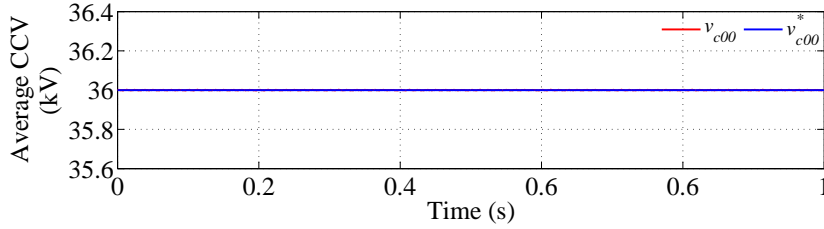
Figure 6.2: Simulation Results for Steady State Operation in LFM. Average CCV Tracking.
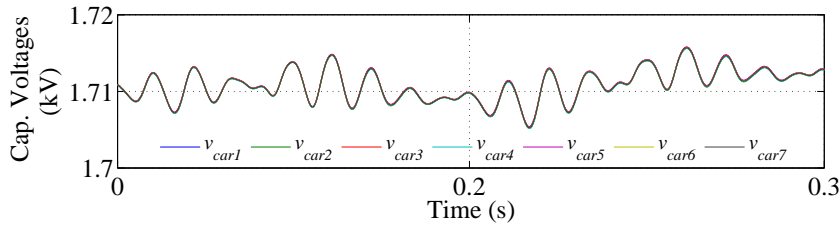
Figure 6.3: Simulation Results for Steady State Operation in LFM. Single-Cell balancing performance for cluster v_{ar}

is illustrated in Fig. 6.4(a). The phase-shifted modulation can track the reference that has the frequency components of the generator (40 Hz) and the grid (50Hz). The use of this modulation technique implies an output voltage of $2n + 1 = 15$ levels and an equivalent output switching frequency of $2nf_{sw} = 11.2$ kHz. Due to the M^3C implemented in simulations features seven power cell per cluster, the synthesised waveform has $2n + 1 = 15$ levels, as shown in Fig. 6.4(b).

As stated in Subsection 7.3.3.1, the Cluster Capacitor Voltage and the Single-Cell balancing of the power cells within a cluster are decoupled. Accordingly, the Cluster Capacitor Voltage is replaced by a controllable voltage source to simplify the simulations of following tests. This assumption is equivalent to simulate the simplified version of the M^3C illustrated in Fig. 3.2.

The generator and grid voltages are set to 5.39 and 4.58 kV (peak phase to neutral values), respectively, as shown in Fig. 6.5(a)−(b). The input and output currents are not affected by the circulating currents produced by the balancing algorithms. As shown in Fig. 6.5(c)−(d), the input and output currents are balanced and present low harmonic distortion (THD $\approx 0.5\%$).

Due to the balancing of the Cluster Capacitor Voltage is performed using a component of the circulating currents in phase with the generator voltages, any drift in the circulating current tracking can be reflected in the generator currents. Therefore, the circulating current reference tracking has to be as accurate as possible, which is achieved using the circulating control loop proposed in Subsection 4.3. As illustrated in Fig. 6.6, circulating currents effectively track the control references.
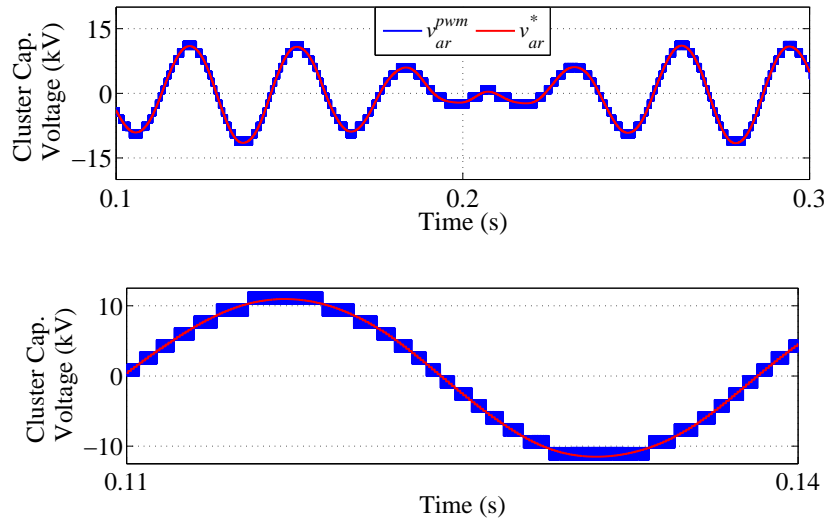
Figure 6.4: Simulation Results for Steady State Operation in LFM. (a) Synthesised Cluster Capacitor Voltage v_ar vs its reference. (b) Amplified view of (a).

Figure 6.5: Simulation Results for Steady State Operation in LFM. (a) Grid Voltages. (b) Generator Voltages. (c) Grid Currents. (d) Generator Currents.
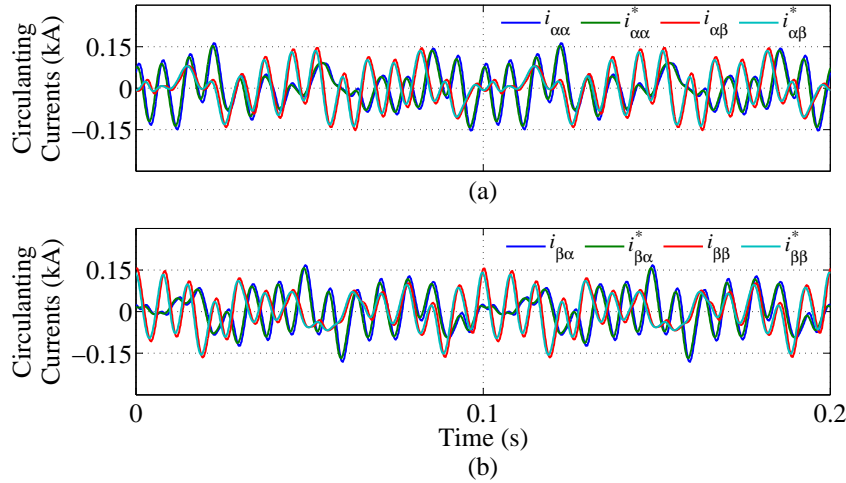
Figure 6.6: Simulation Results for Steady State Operation in LFM. (a)-(b) Circulating Currents tracking.

Wind Turbine Parameters	Nominal Value
Average wind speed	9.5ms
Generator Type	PMSG
Blades Radio	89m
Generator Inertia	750m/kg2
L	0.12 mH
R	0.15 Ohm
Nominal Speed (after gear box)	375 rpm

Table 6.2: Parameters of the Simulated Wind Turbine.

6.3   Simulation Results for Variable-Speed WECS Emulation

The operation of a 10 MW PMSG based variable-speed wind turbine is simulated using a wind speed profile from Rutherford Appleton Laboratories. The parameters used for the PMSG are depicted in Table 6.2.

The wind speed profile used in this test has an average value of 9.5ms, as shown in Fig. 6.7(a), it generates a variable rotational speed at the generator-side, whereas the grid frequency remains constant at 50 Hz [Fig. 6.7(b)]. The CCVs keep their voltage references throughout the test, regardless the generator frequency, as is depicted in Fig. 6.7(c). The dq frame currents and voltages of the PMSG are shown in Fig. 6.7(d). The generator-side control system is orientated in the rotor flux and, consequently, MPPT operation is achieved through the regulation of the quadrature current [see (4.60)]. Finally, Fig. 6.7(e) shows the power injected into the grid, which is regulated to operate with unitary power factor.

98

Figure 6.7: Simulation Results for Variable-Speed Wind Turbine Emulation. (a) 27 Power Cells Capacitor Voltages. (b) Inter-CCV imbalance terms. (c) Intra-CCV imbalance terms. (d) Power Injected into the Grid.

An amplified view of the voltages and currents of the generator and grid side is presented in Fig. 6.8. The grid voltage is set to 5.39 kV, and the generator voltage depends on the wind turbine rotational speed, as shown in Fig. 6.8(a)−(b). The grid and generator currents, which are illustrated in Fig. 6.5(c)−(d), are not affected by the circulating currents produced by the balancing algorithms. In fact, both currents are balanced and present low harmonic distortion. The circulating current reference tracking is presented in Fig. 6.6 in a time windows of 0.2 s. As can be easily observed, circulating currents effectively track the control references and their peak is small in comparison with the nominal of the current.

Figure 6.8: Simulation Results for Variable-Speed Wind Turbine Emulation. (a) Grid Voltages. (b) Generator Voltages. (c) Grid Currents. (d) Generator Currents.

Figure 6.9: Simulation Results for Variable-Speed Wind Turbine Emulation. (a)-(b) Circulating Currents tracking.

Figure 6.10: Simulation Results for LVRT. (a) 27 Power Cells Capacitor Voltages. (b) Inter-CCV imbalance terms. (c) Intra-CCV imbalance terms. (d) Power Injected into the Grid.

6.4 Simulation Results for Symmetric LVRT operation

Similarly to previous tests, the system injects 10 MW into the grid for normal operation. In $t=0.22s$, a symmetrical grid voltage fault is applied. The voltage of the three phases is decreased to a 0% of the nominal value for $0.15s$. During the next 0.4s, a profile for the recovery of the grid voltage is applied [see Fig. 6.11(a)].

The power references are set to full reactive power injection to fulfill international grid codes depicted in Subsection 5.3.1, Fig. 5.2.

For this test, Fig. 6.10(a) shows the proper regulation of the CCVs, which are controlled to 12 kV. The CCV Imbalance terms are successfully bounded inside a ± 350 V, as is shown in Fig. 6.10(b)-(c), respectively. When the fault is applied, the active power is regulated to 0 MW, and the M^3C starts supporting the grid voltage through the injection of reactive power, as shown in Fig. 6.10(d).

During the fault, the generator and grid currents are regulated to generate the active and reactive power of Fig. 6.10(d). Accordingly, the grid current set-point is modified to inject 100% of reactive current, and the generator current reference is reduced to 0A. The grid and generator current waveforms are shown in Fig. 6.11(c)-(d), where it can be seen that both control loops have good dynamics responses and the synthesised currents are balanced and effectively regulated to the references.
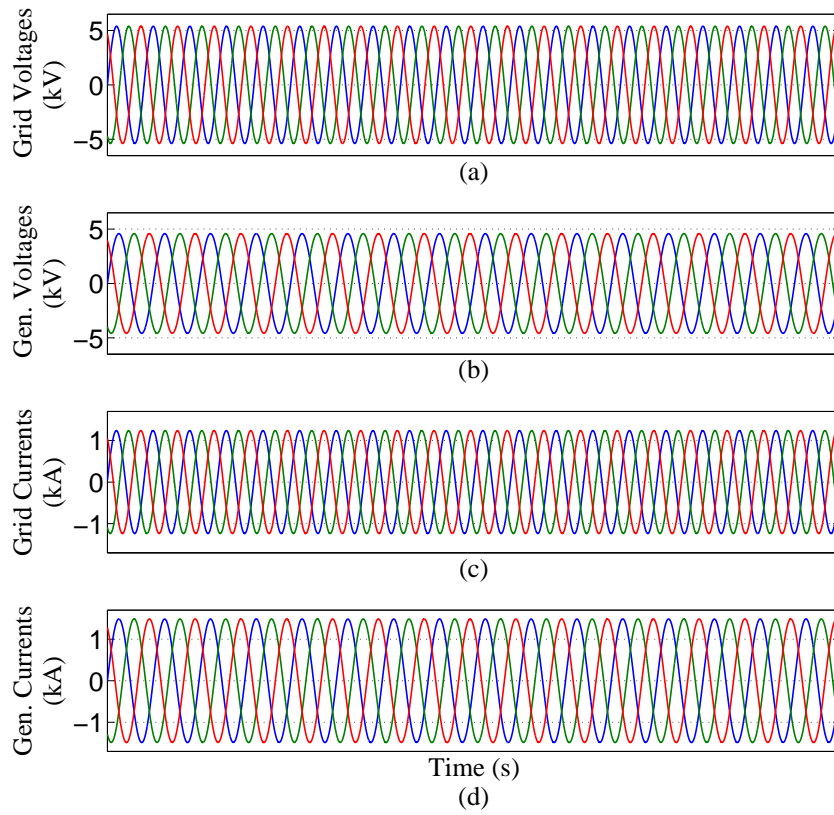
Figure 6.11: Simulation Results for LVRT Control. (a) Grid Voltages. (b) Generator Voltages. (c) Grid Currents. (d) Generator Currents.

Figure 6.12: Grid Voltages for a 50% Dip Type C. (a) Grid Voltages. (b) Positive and Negative sequence components estimation using θ_d =2m. (c) Amplified view of $\hat{v}_{g\alpha}^n$.

6.5 Simulation Results for Asymmetric LVRT operation

In this case, the proposed control strategy is tested considering a Type C grid voltage sag, which means that two grid phases decrease their voltages to a 50% of the nominal value for 0.15s. During the next 0.4s, the profile recovery shown in Fig. 6.12(a) is applied.

As stated before, asymmetrical faults produce positive and negative sequence components in the grid voltages. Therefore, the positive sequence component of the grid voltage have to be estimated to ensure proper synchronisation. Moreover, the negative sequence component is needed to implement the control. Accordingly, the DSC algorithm proposed in section 5.3.4 is used to estimate the positive and negative sequence components of the grid voltage. Its performance is presented in Fig. 6.12(b). In this test, the delay of the DSC algorithm is set to be 2ms. Moreover, three additional cases have been included, i.e. $\theta_\mathrm{d} = 0.4ms$, $\theta_\mathrm{d} = 1.2ms$ and the traditional delay of $\theta_\mathrm{d} = 4.8ms$, just for illustrative purposes. Note that the experimental converter will be operated using a sample time of 400 μs and, consequently, it is not possible to apply the delay of 5ms used in the conventional DSC algorithm.

For simplicity, only the estimations of $v_{g\alpha}^n$ (using the four aforementioned delay angles) are illustrated in Fig. 6.12(c). From this graphic, it is concluded that the overshoot of the DSC estimator is increased when the delay angle θ_d is smaller. This is because the numerical implementation of $\partial v_g(t)/\partial t$ is implicit in (5.32)−(5.33) amplifies the high frequency components of the grid voltage [106].

The performance of the M^3C control system is illustrated in Fig. 6.13. The CCVs are properly regulated to the desired set point during the fault, as shown in Fig. 6.13. The Inter-SC and the
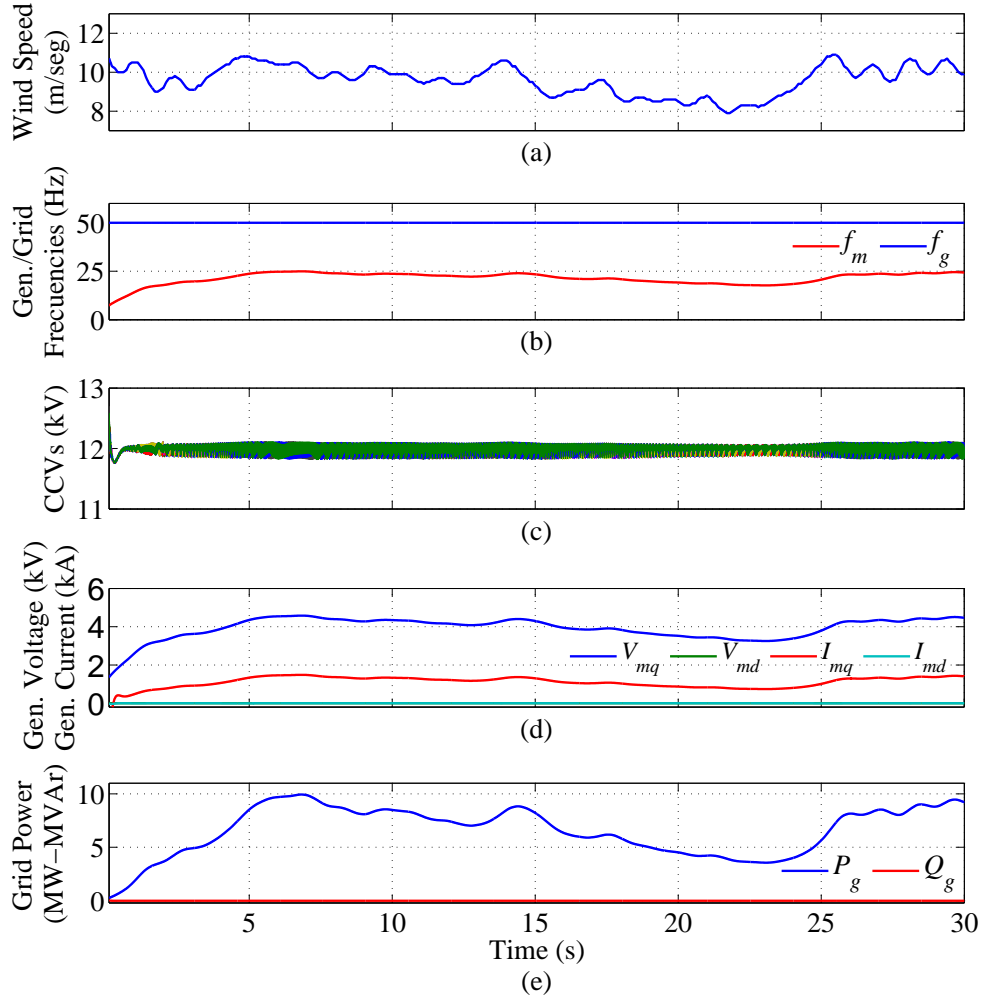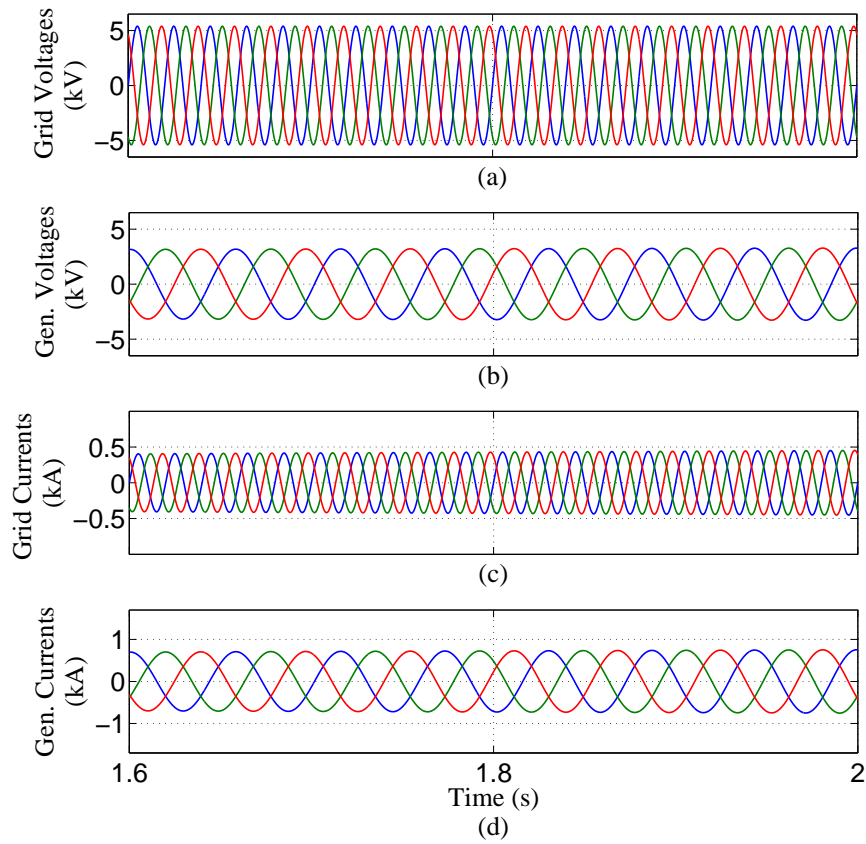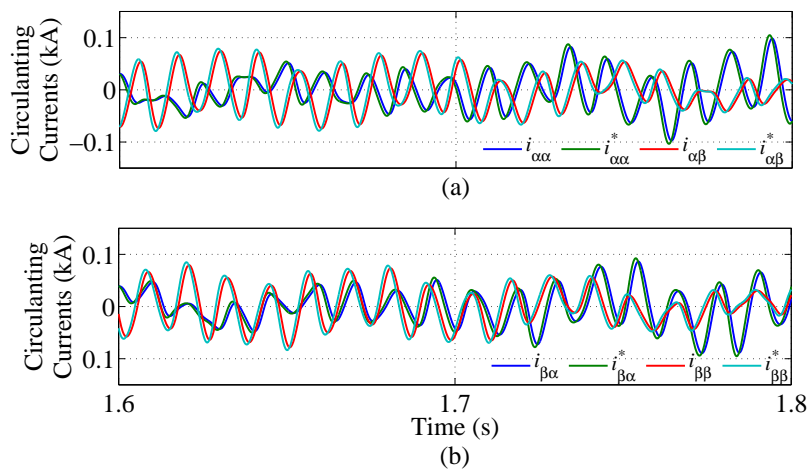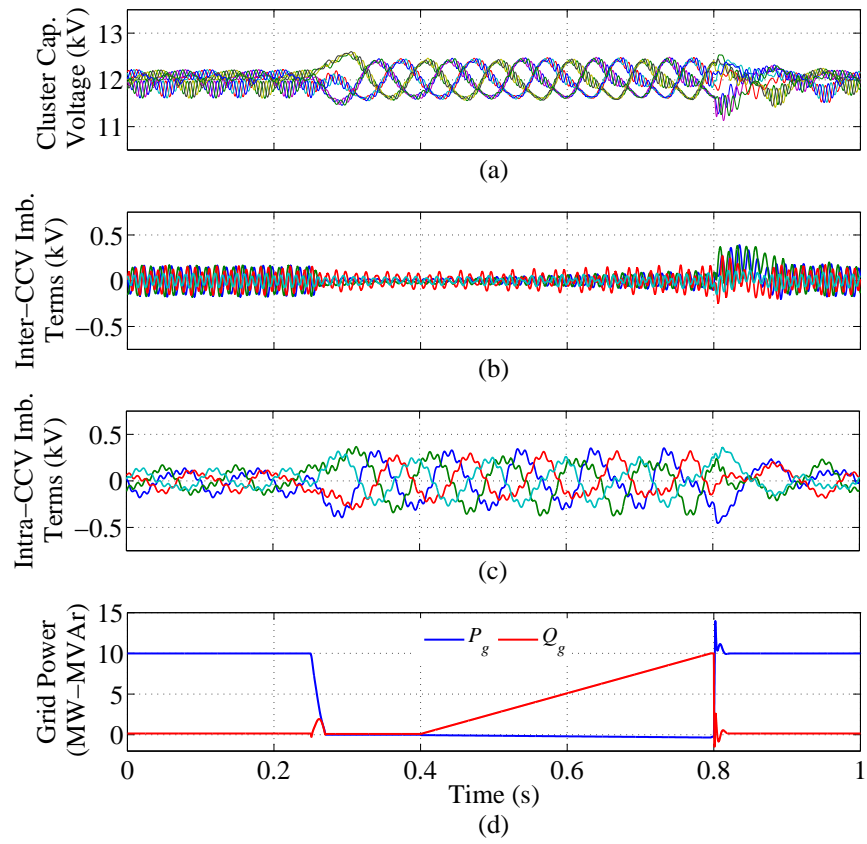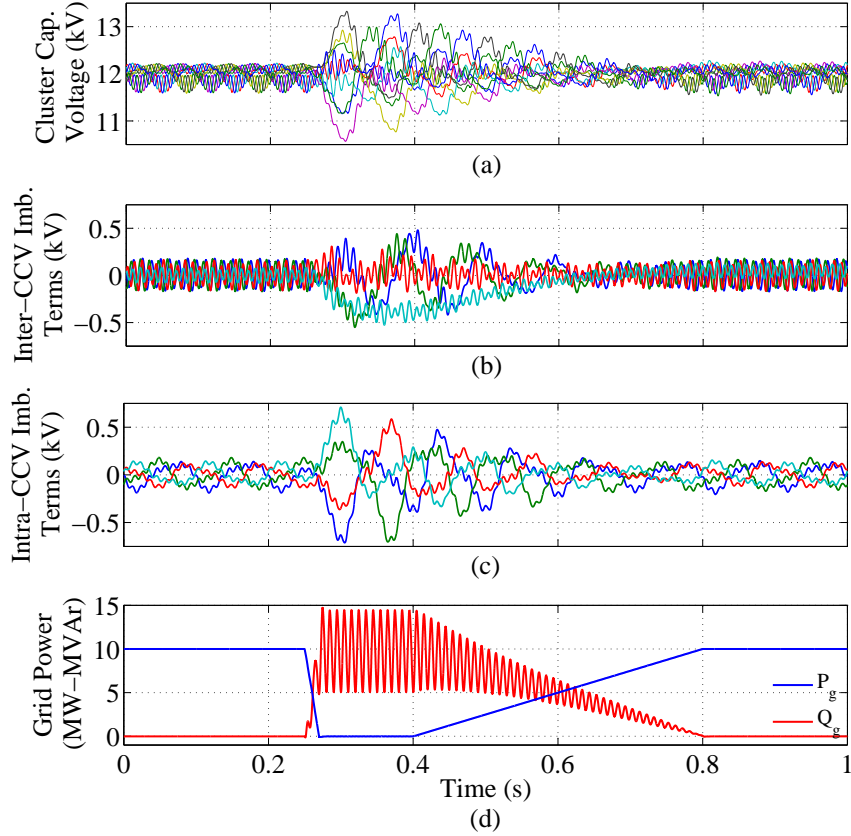
Figure 6.13: Simulation Results for LVRT Control. (a) 27 Power Cells Capacitor Voltages. (b) Inter-CCV imbalance terms. (c) Intra-CCV imbalance terms. (d) Power Injected into the Grid.

Intra-CCV imbalance terms are presented in Fig. 6.13(b)-(c), respectively. The average value of those imbalance terms is successfully regulated to zero, and the oscillations generated during the fault are maintained inside a ± 500 V band. Active and reactive powers injected into the grid during the fault are presented in Fig. 6.13(d). When the fault appears, the M^3C supplies only reactive power. However, as mentioned in Subsection 5.3.2.2, the four $\alpha\beta$ grid currents do not provide enough degrees of freedom to eliminate the oscillations in the reactive power which has a noticeable 100Hz component. On the other hand, active power supplied to the grid is virtually free of double frequency oscillations because the current calculation of (5.17) is obtained selecting $k_{LVRT}=0$. However, the oscillations required by the impedance between the M^3C output and the grid has to be supplied by the converter.

As discussed in the Section 5.3.3, the grid-side control system regulates the positive and negative currents to mitigate the double-frequency power pulsations in the active power. Considering that two grid voltage phases decrease their voltages in 50%, the unbalanced grid currents presented in Fig. 6.14(c) need to be synthesised to inject full reactive power capacity. However, the peak of the grid current reaches 2 kA during the fault, which is almost 150% higher than the pre-fault current value. The generator currents are shown in Fig. 6.14(d), where it can be seen that the current is effectively reduced to 0 A through the fault.
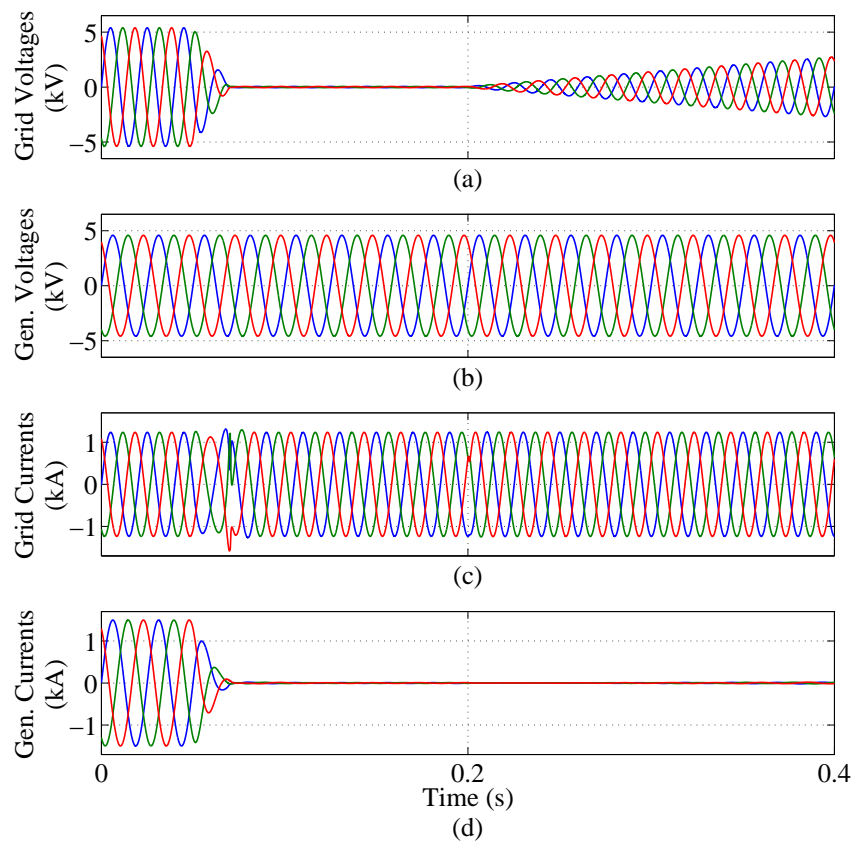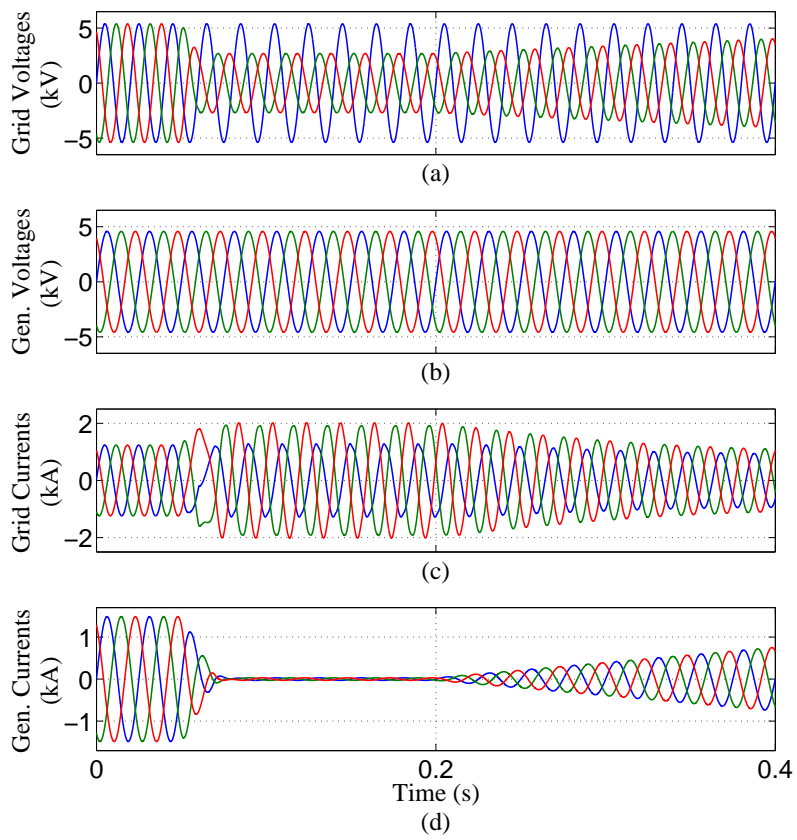
Figure 6.14: Simulation Results for LVRT Control. (a) Grid Voltages. (b) Generator Voltages. (c) Grid Currents. (d) Generator Currents.
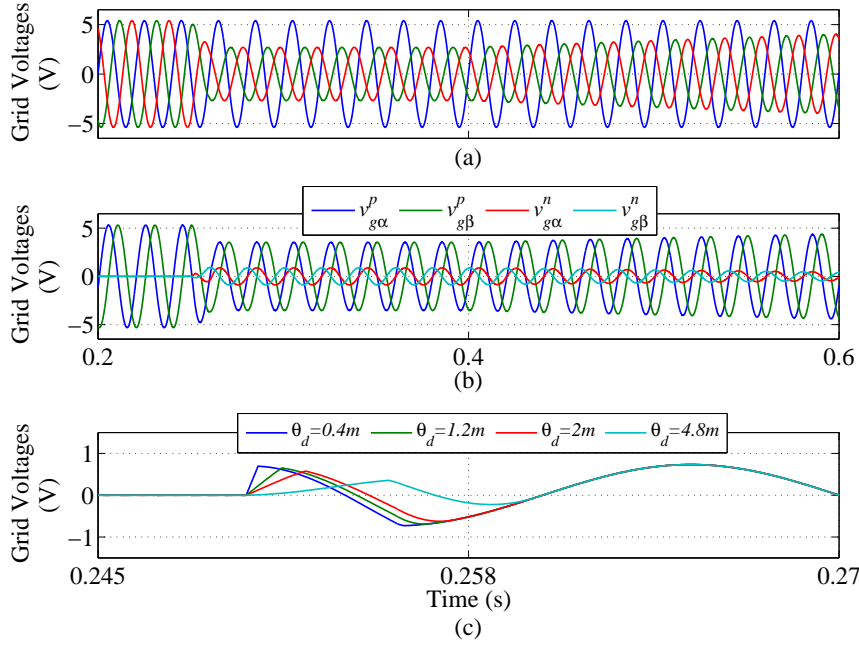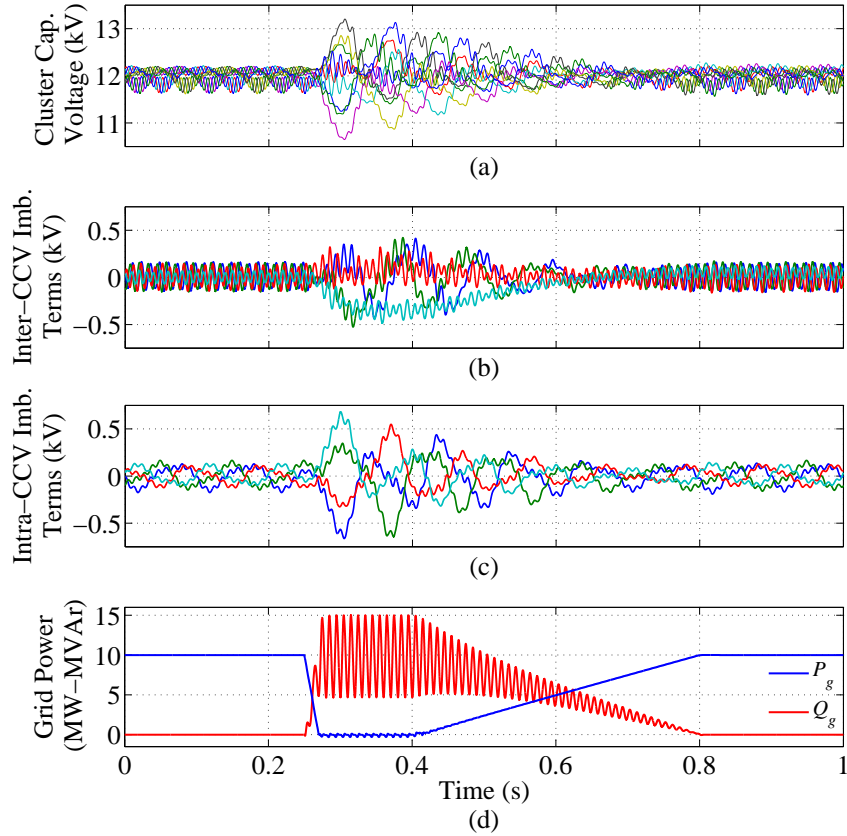
Figure 6.15: Simulation Results for LVRT Control (with oscillations). (a) 27 Power Cells Capacitor Voltages. (b) Inter-CCV imbalance terms. (c) Intra-CCV imbalance terms. (d) Power Injected into the Grid.

The LVRT control system presented in Fig. 5.4 is alternatively configured to eliminate the oscillations required by the impedance at the converter terminals. In this case, $k_{LVRT}=1$ and the grid has to supply the active power oscillations requested by the impedance. The simulation results are shown in Fig. 6.15. In general, results are pretty much the same than in Fig. 6.13 when $k_{LVRT} = 0$ is selected. This is due to the filter between the M^3C and the grid has a low internal resistance ($R_g = 0.1\Omega$). Therefore, small active power oscillations are produced in the filter when the grid voltage Dip appears. However, a slight reduction can be observed in the capacitor waveforms when Fig. 6.15(a)−(c). A zoomed view of the active power delivered to the grid in both cases is shown in Fig. 6.16 for better understanding. The red-line waveforms correspond to the case when $k_{LVRT} = 0$ and the blue line corresponds to the case when $k_{LVRT} = 1$. From the inspection of Fig. 6.16, it is concluded that when $k_{LVRT} = 1$ the active power oscillations are supplied by the grid and, consequently, the oscillations at the M^3C output are successfully reduced. In some cases, e.g., weak grids, resistive lines or massive short circuits, the oscillations in active power could be dangerous for the converter and is desirable to mitigate them at the converter terminals.
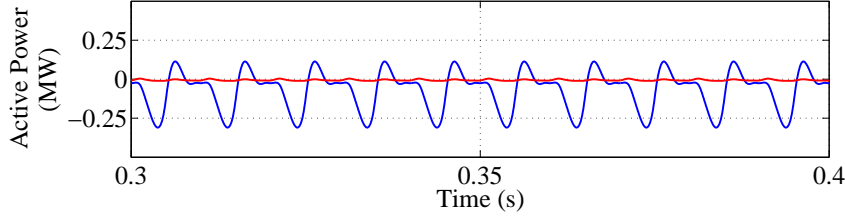
Figure 6.16: Blue line: Amplified view of Active Power Injected when $k_{LVRT} = 1$. Red line: Amplified view of Active Power Injected when $k_{LVRT} = 0$.

6.6 Simulation Results for Equal Input-Output Frequencies Operation

In this section, equal frequency operation of the M^3C is tested for Scalar and Vector control strategies. In both cases, the mitigation control is activated when $f_m \leq 40$Hz. Below this condition, just balancing control is performed in both cases. For the frequency range $40 \leq f_m \leq 50$ Hz, the mitigation control system is performed injecting extra circulating currents for mitigating the oscillation in the capacitors, in the case of the scalar control strategy. Those mitigation currents are calculated as described in section 4.2.1, which means that they are predefined off-line. On the other hand, Vector Control strategy consist of a closed loop structure that uses the Fully-controllable terms of the power terms.

It is important to note that the vector control strategy has to synthesise common-mode voltage, which is set to an amplitude of 2.5kV. Then, each cluster has to be able to synthesise the generator voltage plus the grid voltage plus the common-mode voltage. Accordingly, the reference of the CCV is increased to 14 kV, which means that each capacitor increases its voltage from 1.71 kV to 2 kV.

6.6.1 Scalar Control Strategy

Results for the equal frequency operation of the M^3C using the Scalar Control Strategy are presented in Fig. 6.17 and Fig. 6.18. The generator frequency f_m is increased in 2 Hz each 2 seconds until it reaches 50 Hz. The Cluster Capacitor Voltages are regulated to 14 kV, as shown in Fig. 6.17(a). The Inter-CCV imbalance terms (i.e. $v_{c_{0\alpha}}$, $v_{c_{0\beta}}$, $v_{c_{\alpha 0}}$, $v_{c_{\beta 0}}$) are presented in Fig. 6.17(b), whereas the Intra-CCV imbalance terms (i.e $v_{c_{\alpha\alpha}}$, $v_{c_{\alpha\beta}}$, $v_{c_{\alpha\beta}}$, $v_{c_{\beta\beta}}$) are shown in Fig. 6.17(c). The imbalance terms ripple is increased as f_m gets closer to f_g. In fact, the Intra-SC terms are not properly controlled to zero when f_m=50 Hz, as shown in the right side of Fig. 6.17(c). However, the eight imbalance terms are bounded inside a $\pm$ 1 kV band, which represents oscillations of a 14% of the Cluster Capacitor Voltage nominal value. Finally, Fig. 6.17(d) illustrates the unity power factor operation of the system injecting 10 MW into the grid.

The main issue using this method is that the amplitude of the circulating currents is heavily

Figure 6.17: Simulation Results for Equal Frequency Operation using Scalar Control. (a) Generator and Grid Frequencies. (b) 27 Power Cells Capacitor Voltages. (c) Inter-CCV imbalance terms. (d) Intra-CCV imbalance terms. (e) Power Injected into the Grid.

Figure 6.18: Simulation Results for Equal Input-Output Frequencies Operation using Scalar Control. (a) $i_{\alpha\alpha}$ and $i_{\beta\alpha}$. (b) $i_{\alpha\beta}$ and $i_{\beta\beta}$.

increased to allow operation in equal frequency conditions. Fig. 6.18 shows the circulating currents for this test. When the mitigation is activated, the circulating current peak is increased from ≈ 150 A to 1.7 kA, which implies a cluster current increment of almost 200%. Additionally, it is important to note that this strategy requires complementary power factor at the input and output of the M^3C (i.e. $Q_m = - Q_g$). Due to this test is performed using unitary power factor in both sides, this condition is accomplished. However, the performance of the Scalar Control Strategy is decreased as the difference of the power factors increases.

6.6.2 Vector Control Strategy

Results for the equal frequency operation of the M^3C using the Vector Control Strategy are presented in Fig. 6.19 and Fig. 6.20. Similarly to the previous test, the generator frequency f_m is increased in 2 Hz each 2 seconds until it reaches 50 Hz, as illustrated in Fig. 6.19(a). For $t \leq 1s$, $f_m = 40$ Hz and the Cluster Capacitor Voltages are controlled using the dc component of the vectors $\vec{v}_{c_0}^{\alpha\beta}$, $\vec{v}_{c_{\alpha\beta}}^0$, $\vec{v}_{c_{1\alpha\beta}}^{\Sigma\Delta}$ and $\vec{v}_{c_{2\alpha\beta}}^{\Sigma\Delta}$. Lately, $t>1$, mitigation techniques are applied accordingly to the proposed in Section 4.2.2.2. Accordingly, the oscillations in $\vec{v}_{c_{1\alpha\beta}}^{\Sigma\Delta}$ are mitigated using the power terms produced by the circulating current and the common-mode voltage from $t>1$.

During all this test, the Cluster Capacitor Voltages are successfully regulated to 14 kV, as shown in Fig. 6.19(a). The Inter-CCV imbalance terms ($v_{c_{0\alpha}}$, $v_{c_{0\beta}}$, $v_{c_{\alpha0}}$, $v_{c_{\beta0}}$) and the Intra-CCV imbalance terms ($v_{c_{\alpha\alpha}}$, $v_{c_{\alpha\beta}}$, $v_{c_{\alpha\beta}}$, $v_{c_{\beta\beta}}$) are illustrated in Fig. 6.19(b)−(c), respectively. The ripple of the imbalance terms is properly bounded and it is not increased as f_m gets closer to f_g. In fact, the eight imbalance terms are bounded inside a ± 350 V band, which represents oscillations of $\approx 4\%$ of the Cluster Capacitor Voltage nominal value. Finally, Fig. 6.19(d) illustrates the unity power factor operation of the system injecting 10 MW into the grid.

Fig. 6.20(a)−(b) shows the circulating currents for this test. When the mitigation is activated, the circulating current peak is bounded at the same amplitude than the pre-equal frequency value $\approx$
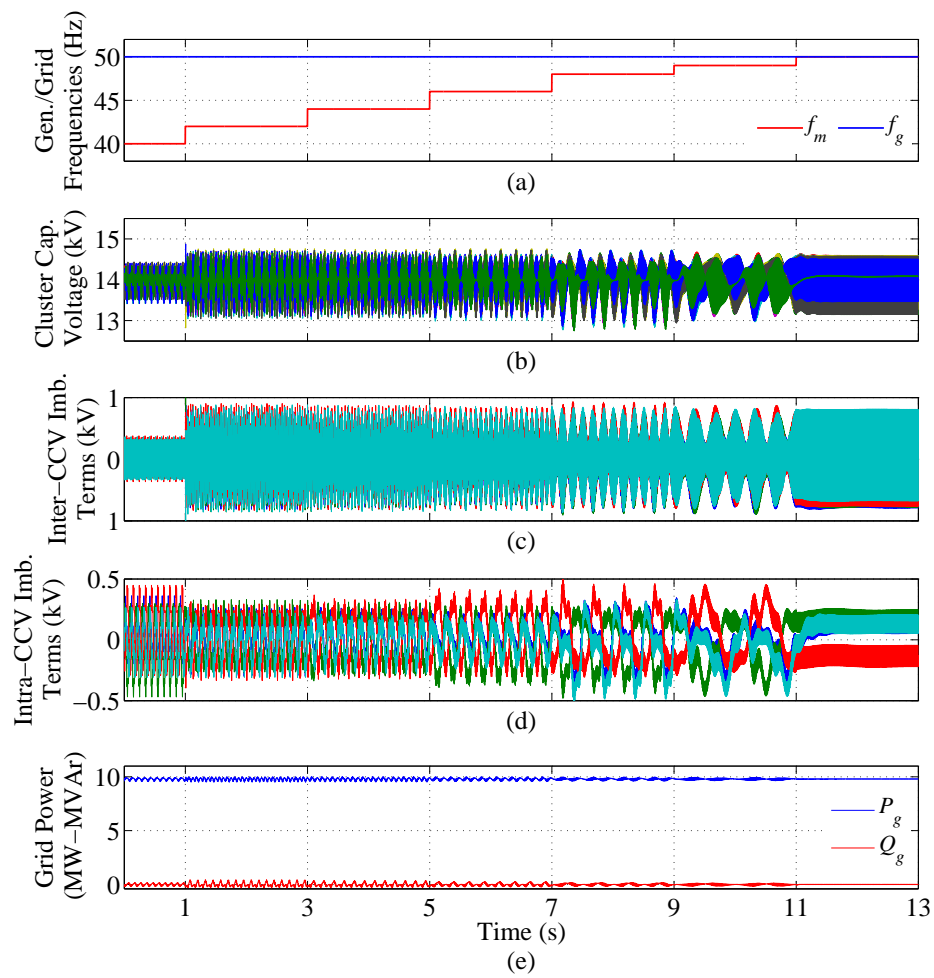
110
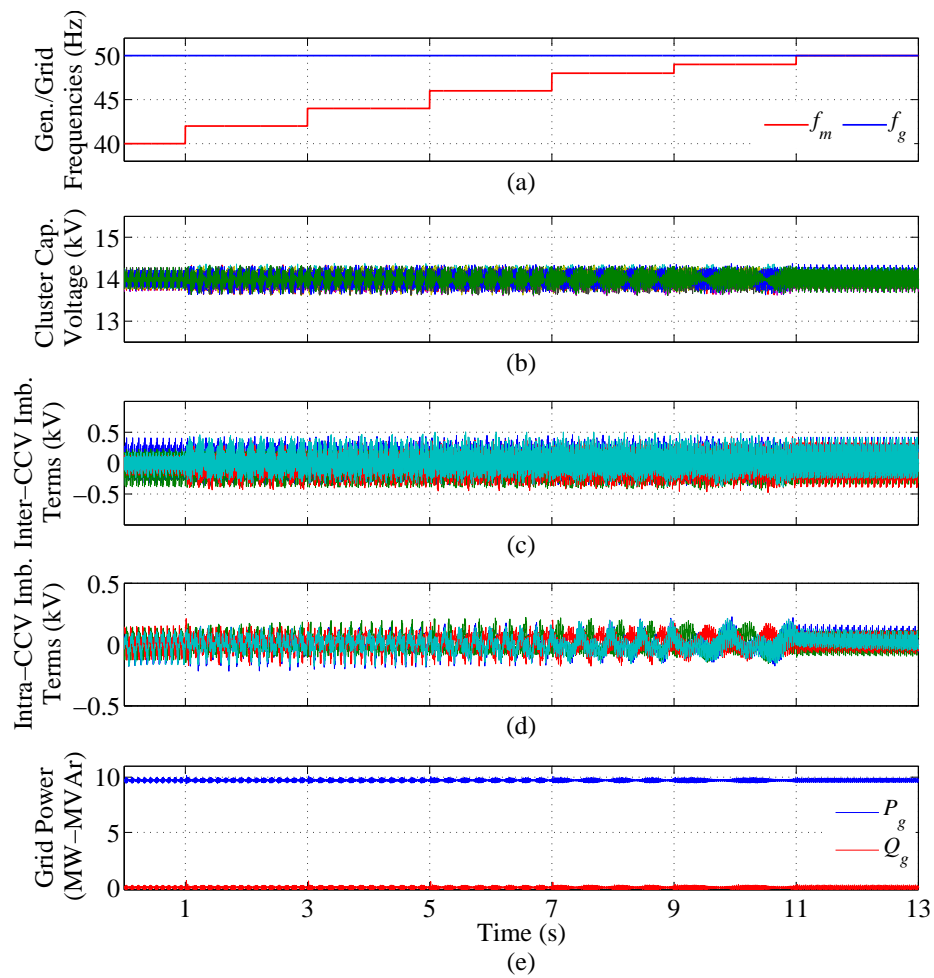
Figure 6.19: Simulation Results for Equal Input-Output Frequencies Operation using Vector Control. (a) Generator and Grid Frequencies. (b) 27 Power Cells Capacitor Voltages. (c) Inter-CCV imbalance terms. (d) Intra-CCV imbalance terms. (e) Power Injected into the Grid.
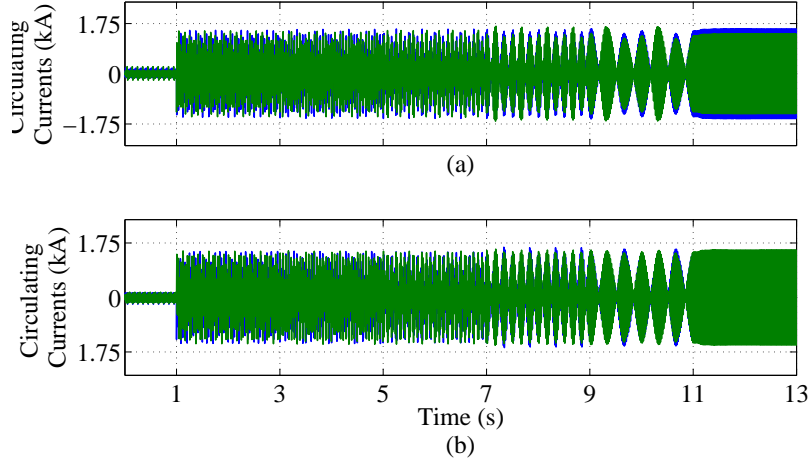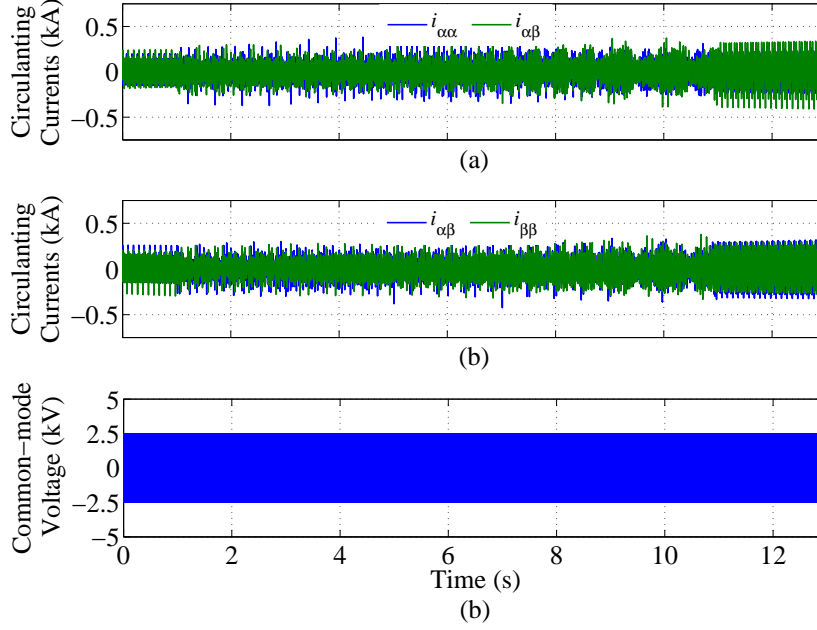
Figure 6.20: Simulation Results for Equal Input-Output Frequencies Operation using Vector Control. (a) $i_{\alpha\alpha}$ and $i_{\beta\alpha}$. (b) $i_{\alpha\beta}$ and $i_{\beta\beta}$. (c) Common-mode Voltage

0.15 kA. Due to the mitigation control is performed using the Fully-controllable terms of the vector model of (3.73)−(3.76), the circulating currents are not increased. Accordingly, the common-mode voltage of Fig. 6.20(c) is synthesised to generate manipulable power flows that allow to balance and to mitigate the oscillation produced by the equal frequency operation. In this case, the common-mode voltage is selected to have an amplitude of 2.5 kV and a fundamental frequency of 120 Hz.

Finally, it is important to mention that the Vector Control strategy considers closed loop control of the CCV Imbalance terms whereas the Scalar Control strategy enables equal frequency operation using open-loop mitigation signals. Consequently, 0 steady state error is achieved in the regulation of the Inter-SC and Intra-CCV imbalance terms even when f_m=50 Hz for the Vector Control Strategy. However, this condition is fulfilled when the Scalar Control strategy is selected. To better understanding, an amplified view of Fig. 6.19 and Fig. 6.17 is presented in Fig. 6.21 a mode of comparison of Vector and Scalar control strategies. From the inspection of Fig. 6.21, it is evident the better performance of the Vector Control Strategy over the Scalar Control Strategy for equal frequency operation. The CCV imbalance terms are successfully controlled with 0 steady state error, and the ripple in the CCVs is lower for the Vector Control Strategy. Furthermore, Vector Control Strategy does not impose additional requirements, such as complementary power factor, for its correct operation.
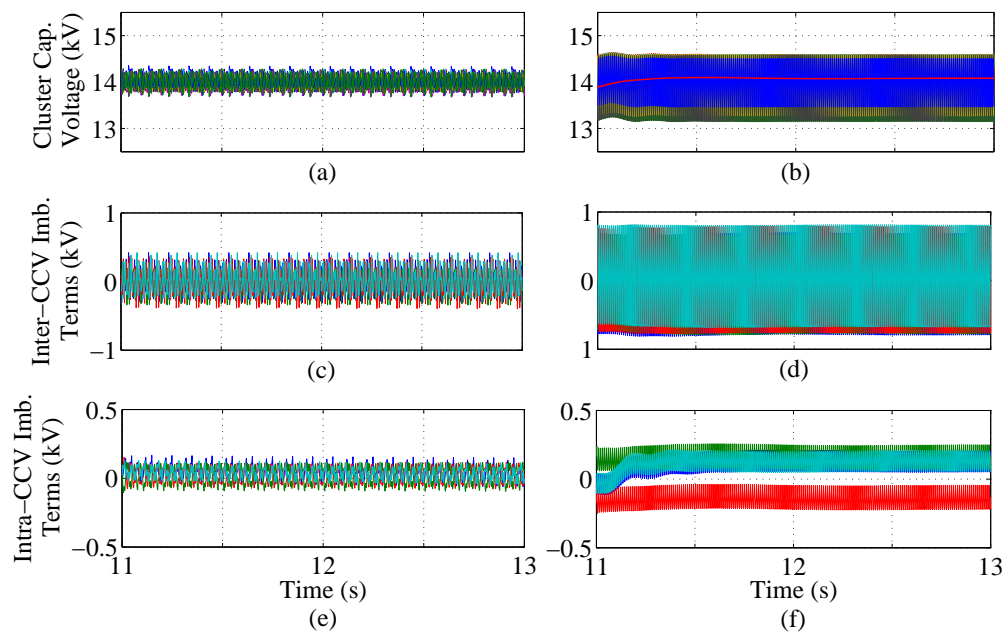
Figure 6.21: Comparison of Scalar and Vector Control Strategies. (a)-(c)-(e) CCV and CCV imbalance terms using Vector Control Strategy. (b)-(d)-(f) CCV and CCV imbalance terms using Scalar Control Strategy.

6.7 Summary

This chapter has presented a set of simulation tests conducted with a 10 MW M^3C to validate the effectiveness of the control strategies proposed in Chapters 4-5. Simulations results for variable speed operation, grid code compliance, and capacitor voltage regulation have been presented and discussed in this Chapter.

As a first conclusion, it can be stated that both control strategies are equivalent for low-frequency operation of the M^3C. In LFM, fixed speed operation, variable-speed operation and the fulfilment of grid codes, such as LVRT and ZVRT, have been successfully tested for the implemented model. In all tests, the proposed control systems ensure proper capacitor voltage balancing, keeping the CCVs bounded and with low ripple. Additionally, the performance of the generator-side and grid-side control system have been validated for MPPT and grid-code compliance.

As far as equal-frequency operation is concerned, it can be stated that Vector Control Strategy has a better performance than Scalar Control Strategy and it is more flexible because it does not require operational condition such as complimentary power factor at the generator and grid sides.

CHAPTER 7

Experimental Converter

7.1 Introduction

This Chapterpresents the design and construction of the experimental M^3C used to validate the control strategies proposed in this thesis. Due to the high complexity of the converter, a control platform with expanded capabilities is developed, and its key features are described. Details of the power electronics circuits are presented with emphasis on the key areas of the converter such as H-bridge design and capacitor dimensioning.

Parameters	Specification	Quantity
DSP	TMS320C6713	1
FPGA	ProASIC3 A3P1000	3
External AD board	20 AD channels	1
Voltage Transducer	LEM LV 25-P	33
Current Transducer	LEM LA 55-P	9
MOSFETs	IRFP4868PBF / 70 A	108
Cell capacitor	4.7 mF / 200 V	27
Cluster inductor	2.5 mH / 20 A	9
Machine-side Power Supply	Ametek CSW5550	1
Grid-side Power Supply	Ametek MX45	1

Table 7.1: Key components of the Laboratory prototype.

7.2 Overview of the prototype

A simplified diagram of the implemented M^3C is presented in Fig. 7.1(a) and a photograph of it is illustrated in Fig. 7.1(b). The key components of the prototype are given in Table 7.1. As shown in Fig. 7.1 and Table 7.1, the prototype is composed of a control platform and a power stage. The control platform is composed of a Digital Signal Processor (DSP) Texas Instrument board, three FPGA boards, and some additional external boards for computer communication and external analogue-digital (A/D) conversion. On the other hand, the power stage of the M^3C prototype is composed of nine clusters based on the series connection of three full-H-bridge cells and one inductor. Therefore, the converter has 27 power cells, each of them connected to a flying capacitor of 4.7mF. The input of the M^3C has been connected to an Ametek Programmable power source, Model CSW5550. The grid-side has been connected to another Ametek Programmable Power Source, Model MX45. Design consideration of the M^3C such as nominal power, voltage, frequency as well as cell capacitance and cluster inductance will be presented in next sections.

(a)

(b)
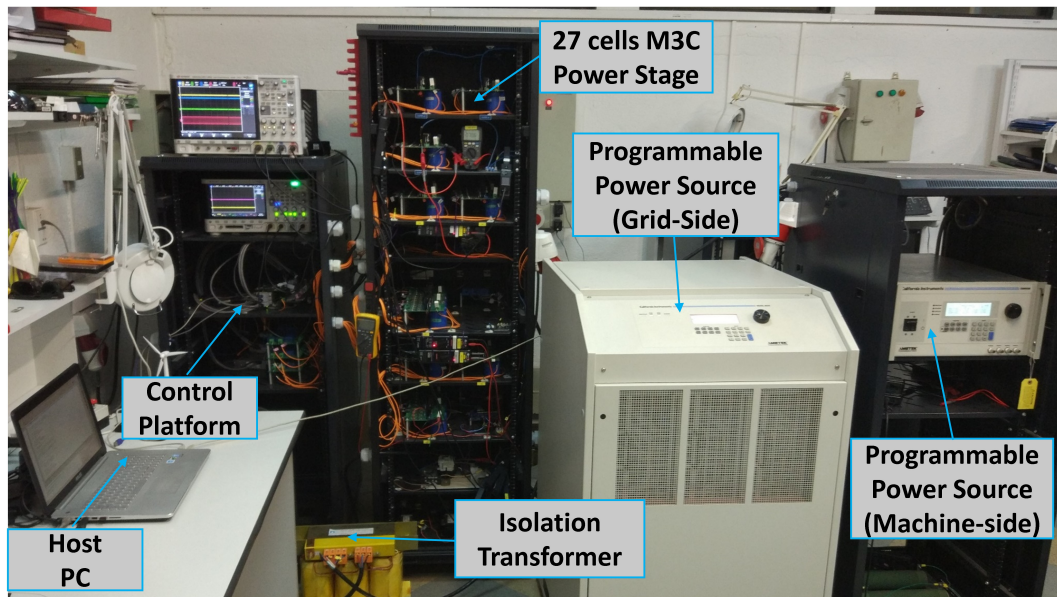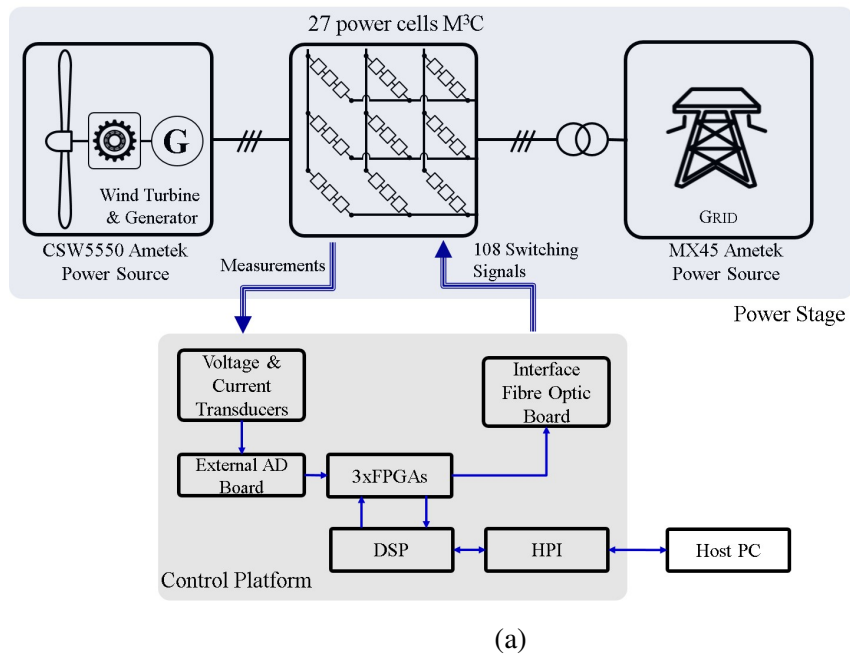
Figure 7.1: Downscaled Laboratoy Prototype. (a) Diagram of the experimental system. (b) Photograph of the experimental system.

Measurements	Quantity
DC voltage capacitors	27
Cluster Currents	9
Input Voltages	3
Output Voltages	3
Total	42

Table 7.2: Signals to be measured by the Control Platform of the experimental M^3C.

7.3 Control Platform

The control platform comprises a TMS320C6713 Texas Instrument DSP, three FPGA boards, an external analogue-digital board, and interface board with fibre optic transmitters and an HPI (Host Port Interface) daughter board. A photograph of the control platform mounted in the experimental setup is shown in Fig. 7.2 and a description of its components is presented in the following Sub-sections. Furthermore, a photograph of each of the control platform main components is shown in Fig. 7.4.

The control platform must be able to measure all the electrical variables of the M^3C to implement the feedback control proposed in Chapter4 and Chapter5. These measurement requirements are summarised in Table 7.2, where is shown that 42 signals have to be processed by the control system of the M^3C to measure capacitor voltages, cluster currents and input/output voltages and currents of the M^3C prototype presented in Fig. 7.1. It is important to mention that the input and output currents are not directly measured because they are dependent on the circulating currents, as the Voltage-Current model of $(3.6)-(3.8)$ indicates.

On the other hand, a three cells per clusters M^3C implies that at least 54 gate-drive signals have to be switched (there are 108 MOSFETs in total). Accordingly, the control platform shall be able to measure 42 analogue signals and to synthesise 54 gate-drive signals.
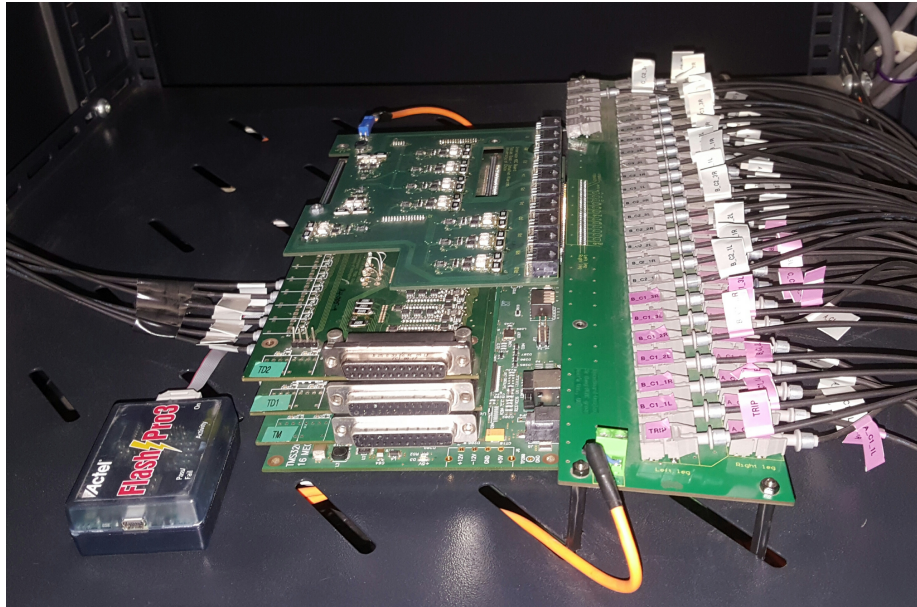
Figure 7.2: Control platform used in this project.

7.3.1 DSP

The TMS320C6713 is a 32-bit floating point DSP able to process 1350 million of floating point instructions per second, which runs at 225 MHz. This DSP can be programmed in C using Code Composer Studio from Texas Instruments and it is used for the real-time implementation of all the control structures proposed in this thesis.

The TMS320C6713 DSP is integrated into a development kit (DSK C6713) with interfaces to add external peripherals. The general structure of the DSK C6713 is shown in Fig. 7.3. One of the major advantages of this development kit is that the External Memory Interface (EMIF) supports 64MB of on board SDRAM memory, Flash ROM, and I/O port but also expands the memory interface through an connector for a daughter board. Then, the FPGAs are mapped into the DSK's memory using EMIF connectors on the DSK. The DSP has four dedicated address spaces which allow both the onboard devices and the expansion memory interface to be selected. The access to the EMIF is clocked at up to 100MHz while the CPU is clocked at 225MHz.
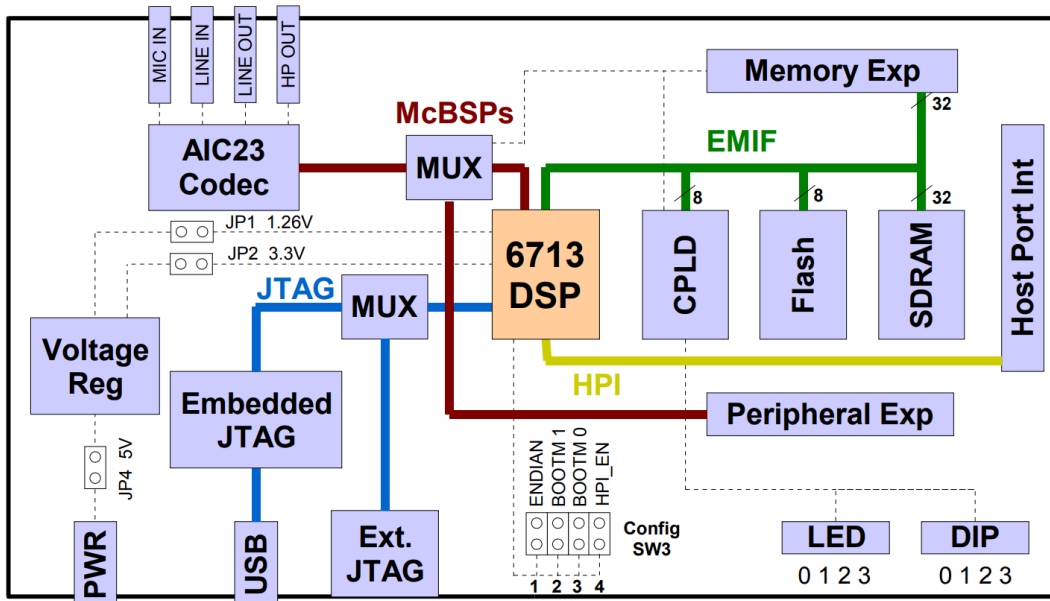
Figure 7.3: Block Diagram of the DSKC6713

7.3.2 HPI daughter board

The HPI daughter board provides an HPI between the host PC and the DSP without interrupting the central processor unit, providing serial, parallel and USB access to the HPI port in the DSK. With this access in place, a Matlab application can be used, and also stanD/Alone applications can be developed to permit a PC host to download software to the DSP and then control its operation. Fig. 7.4a shows the HPI daughter board mounted on the DSP.
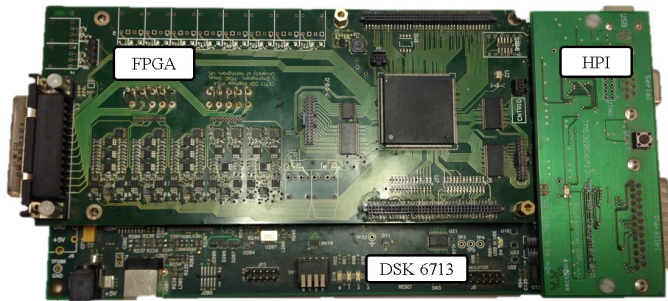
(a) Conventional control platform designed by the PEMC, including one DSP, FPGA and HPI.
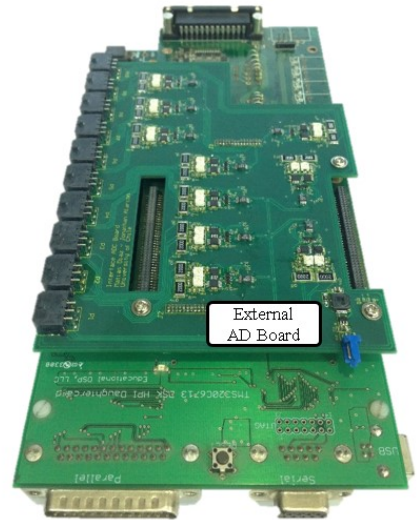
(b) Control Platform with the external A/D board on top.
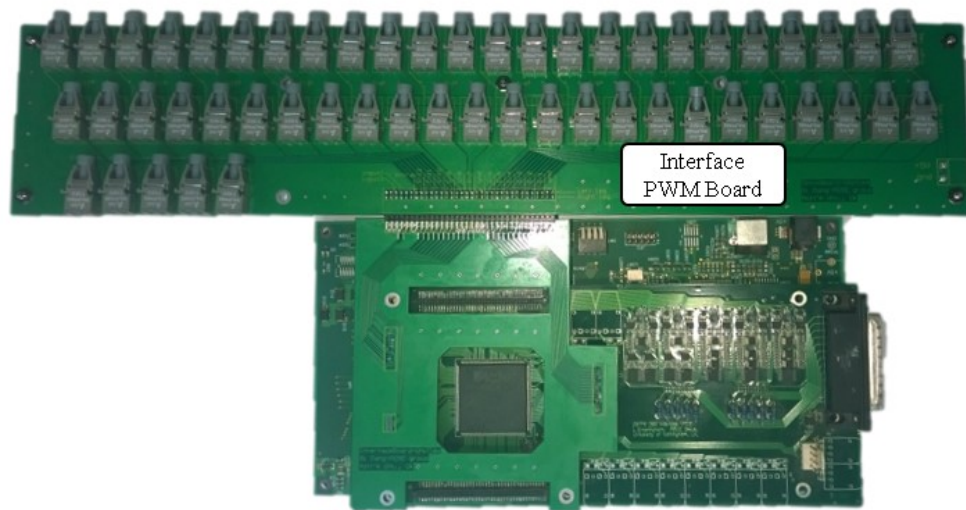
(c) Control Platform with the Interface PWM board on top.

Figure 7.4: Components of the Control Platform.

7.3.3 FPGA board

The FPGA board employed in this project was developed by the PEMC Group of the University of Nottingham, and it has proved to be a very flexible and versatile tool for several power electronics applications. This board features an ProASIC3 chip capable up to one million system gates, ten 14-bit A/D converters to measure analogue signals, three connectors with 52 digital input/output ports, connectors for DSP-FPGA data transmission, hardware comparators for over-current and/or over-voltage protection, optical transmitters for the PWM gate drive signals, etc. Among other functions, the FPGA boards are used to:

- Interruption signal generation

- Watchdog timer

- A/D and D/A conversion and data acquisition

- DSP memory interface

- Phase-shifter modulation implementation

- Trip generator

Due to the complexity of M^3C, three FPGA boards (a master and two slaves FPGA boards) plus one External A/D board plus one Interface PWM board have been connected and synchronised to handle the 42 measurements and 54 switching signals required for the experimental prototype. Fig. 7.5 illustrates the connection and main functions of each board.

The master FPGA generates an interrupt signal for the DSP and the slave FPGAs at 2.5 kHz. This interrupt signal triggers the execution of the interrupt service routine in the DSP and the execution of the Phase-Shifted PWM modules. Non-stop communication between the DSP and the FPGA is ensured using the watchdog timer. Whenever there is loss of communication between the DSP and the master FPGA, the watchdog service generates a trip signal which halts converter operation by setting all gate-signals to zero.

The Trip Generator features the watchdog, software and hardware trip decisions. Watchdog trip and hardware trip are implemented in the master FPGS board due to they require high-speed processing. The software trip which acts as a backup trip and it is implemented in the DSP code.

7.3.3.1 Phase-shifted PWM Implementation

Phase-Shifted PWM modules are programmed in the master and first slave FPGA boards. The modulation of eight clusters of the converter is programmed into the master FPGA, whereas the ninth cluster PWM is programmed in the first slave FPGA, as shown in Fig. 7.5(a).

The phase-shifted PWM modules are implemented as shown in Fig. 7.5(b), where the modulation of the cluster ar is illustrate as representative example. The voltage references for each power cell (obtained in) are held in 10-bit First-in First-Out (FIFO) memory registers. Carriers signals

with a delay of 120 degrees are programmed in the FPGAs. Then, the reference for each power cell is compared to the carrier signal using 10-bit comparators. The resulting gate drive signals are used to hold the logic states of the H-bridge power cells. To turn on the upper MOSFET device in an H-Bridge, an 1 state logic is written and a 0 is written to turn it off.

The gate drive signals obtained from the PWM modules are sent from the FPGAs to an Interface board for electrical-optic conversion. The Interface PWM board is equipped with fibre optic transmitters, model Avago HFBR-1521Z. The connection of the FPGA boards and the Interface PWM board is shown in Fig. 7.4b.

7.3.3.2   Data acquisition system

The Master, the first slave and the second slave FPGAs are used to measure 10 electrical variables each. The DSP can access to registers containing the sampled signals which are required for the closed loop control because the FPGA boards are mapped directly into the memory of the DSK board.

However, there are 12 signals that need to be measured to control the M^3C. Consequently, an external A/D board with 20 channels was designed during this PhD project to increase the measurement capability of the control platform. The External A/D board is connected to the second slave FPGA using its output connectors, as shown in Fig. 7.4b.
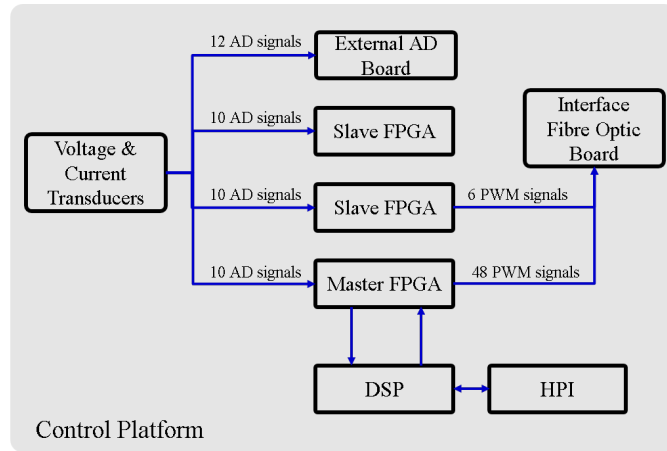
(a)
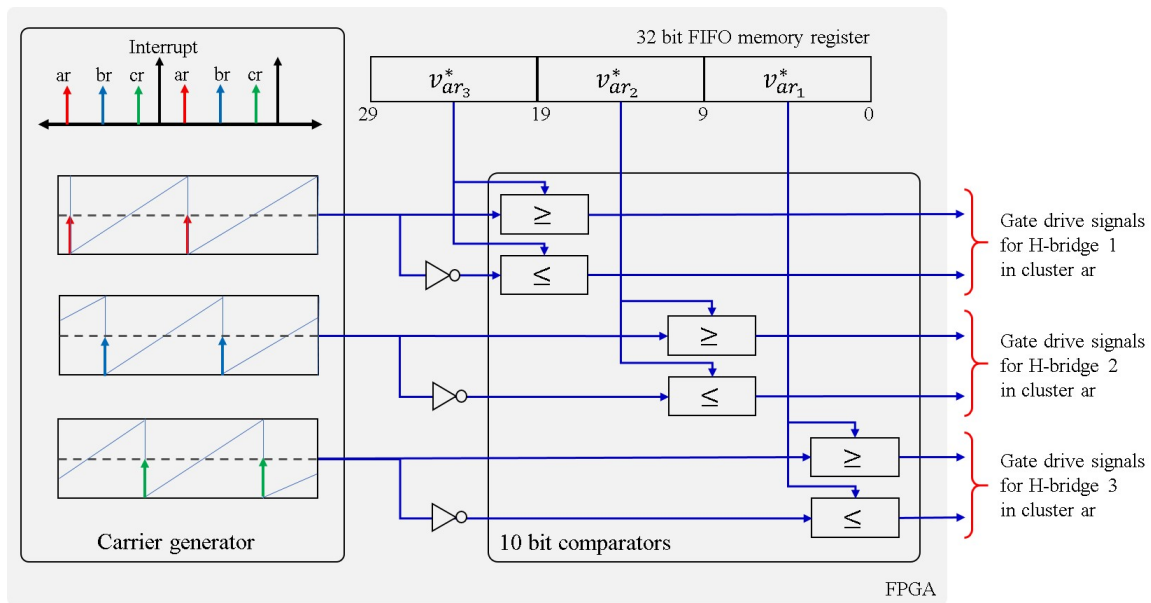
(b)

Figure 7.5: Details of the Control Platform. (a) Block Diagram of FPGA connections and its main functions. (b) Diagram block of the Phase-shifted PWM Modules programmed in the FPGAs.

7.3.4 Measurement boards

As mentioned in previous Subsection, 42 analogue signals have to be measured to control the M^3C. Therefore, several voltage and current transducers are considered in the experimental setup. Current transducers model LEM LA 55-P and the voltage transducers model LV 25-P are mounted on PCB boards, as shown in Figure 7.6. These two models are Hall effect closed loop transducers that present excellent accuracy, good linearity and a wide frequency bandwidth.

(a) Voltage Transducers Board using LEM LV 25-P.

(b) Current Transducers Board using LEM LA 55-P.
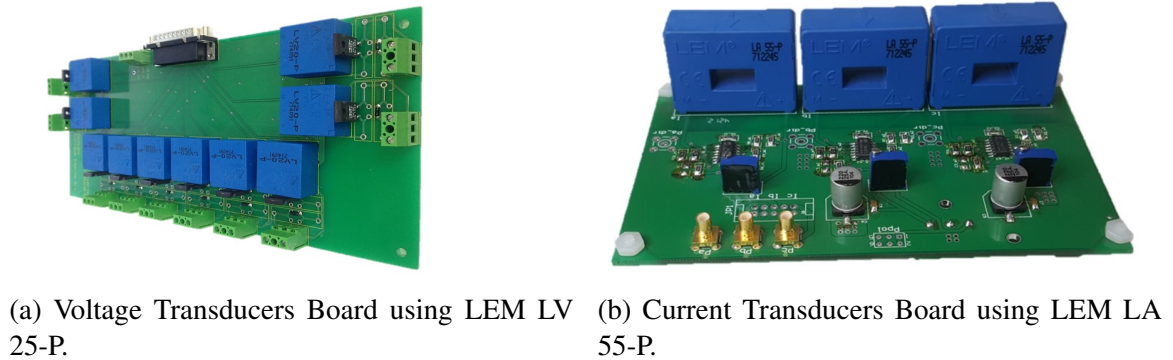
Figure 7.6: Measurement Boards

7.4 Power Stage

The power stage of the M^3C has been implemented using 27 H-Bridge power cells, arranged in nine clusters composed of cascade connection of three H-Bridges and an inductor. The input and output of the M^3C have been connected to Ametek Programmable power sources, Model CSW5550 and Model MX45, respectively. Parameters of the experimental system are given in Table 7.3.

7.4.1 H-Bridge Power Cells

Fig. 7.7a shows the H-Bridge power cells that were designed and built during this PhD project. Each power cell considers two double-MOSFET modules IRFP4868PBF from International Rectifier. The MOSFETs are rated for a nominal voltage of 300V and a nominal current of 70A. The schematic of the H-Bridge power cell is shown in 7.7b. This design considers an optic-electric stage to receive the optic signals from the FPGAs and transform them into electrical signals. A delay circuit composed of a trimmer and a capacitor is included to add dead time to the drive signals. Moreover, an optocoupler stage is implemented using the HCPL-3120 optocoupler, which is specifically designed for gate driver applications. Furthermore, an isolated $\pm$ 15V power supply is used to achieve the required isolation in the gate circuit. Finally, two Zener diodes Dz1 and Dz2 are used to prevent transient over-voltage of the MOSFETs gate signals and the pull-down resistor R10 connected between gate and emitter of the MOSFET ensures that the semiconductor remains off during the power-up sequence of the gate driver.

Parameters	Experimental setup
Nominal Power	6kVA
Cells per branch	3
Input Voltage	200V
Input Frequency	10-40 Hz
Cluster Inductor	2.5 mH
Single cell Capacitance	4.7 mF
Nominal Capacitor Voltage	150 V
Output Voltage.	185V
Output Frequency	50 Hz
Switching frequency	2.5 kHz

Table 7.3: Parameters of the experimental M^3C.
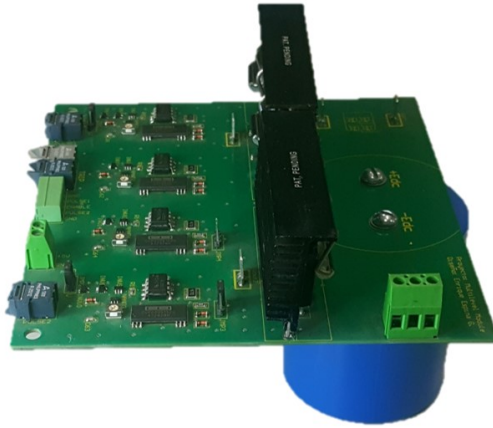
(a) H-Bridge Power Cell.
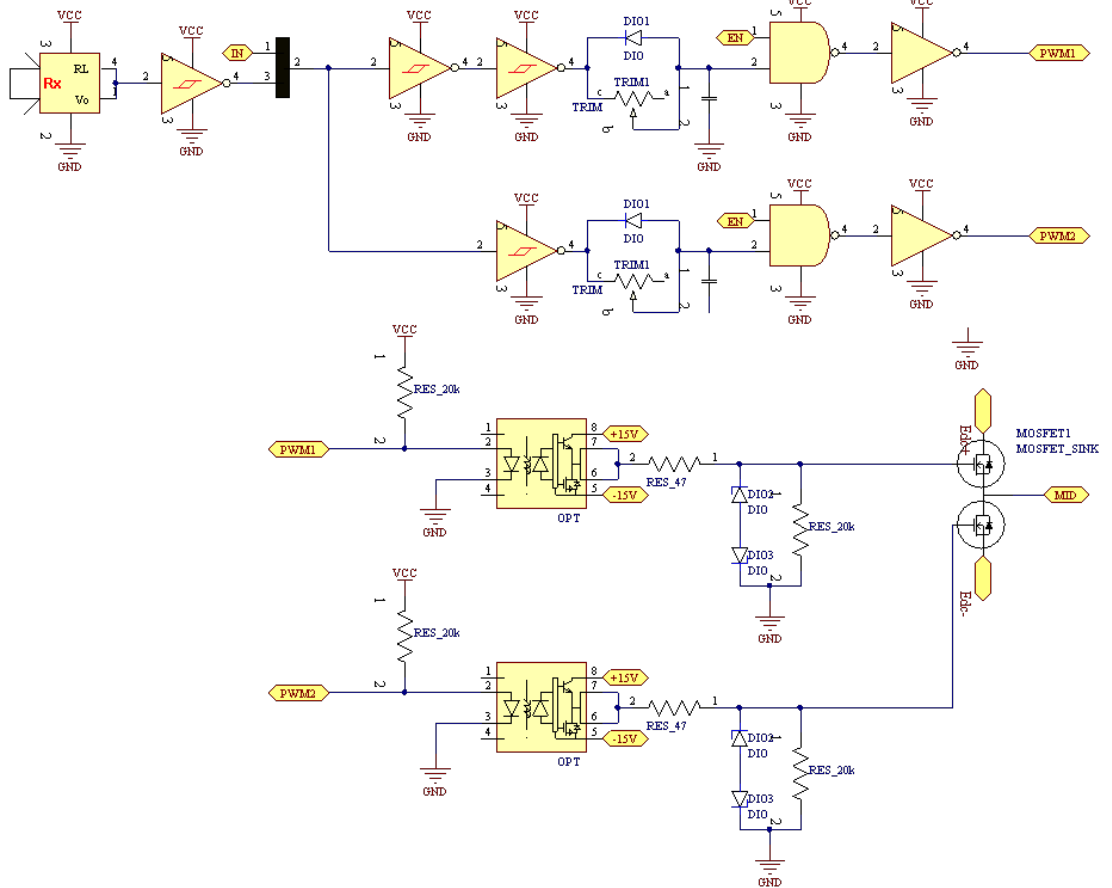
(b) Gate-Drive Circuit.

Figure 7.7: H-Bridge Power Cells

7.4.2 M^3C **passive element dimensioning**

7.4.2.1 M^3C **Power Cell Capacitor dimensioning**

To select the correct value of cell capacitance to be utilised in the implementation of the M^3C clusters is important [94, 108]. This capacitance has to be designed to buffer the peak-to-peak energy variations generated by the variable speed operation, maintaining the voltage oscillations inside an appropriate range.

In natural $abc - rst$ frame, the instantaneous power in each cluster is obtained as:

$$[P_{xy}] = ([v_{mx}] - [v_{gy}]) \circ \frac{1}{3}([i_{mx}] + [i_{gy}])$$ (7.1)

Where $x \in \{a, b, c\}$ and $y \in \{r, s, t\}$, $\circ$ denotes the Hadamard (element by element) product, and it is assumed that a third of the machine/grid phase currents is circulating in each cluster. Expanding (7.1), power terms with four oscillating frequencies are obtained: a term of frequency $2\omega_m$; a term of frequency $2\omega_g$; and two power terms of frequencies $\omega_g \pm \omega_m$ (produced by the input/output cross products, i.e. $v_{mx}i_{gy} - v_{gy}i_{mx}$). Using (3.16) the variation in the energy stored in the capacitors could be obtained from these four power terms as:

$$\Delta W_{xy} = C v_c^* \Delta v_{c_{xy}} = \int_0^t \left([P_{xy1}]_{\omega=2\omega_m} + [P_{xy2}]_{\omega=2\omega_g} + [P_{xy3}]_{\omega=\omega_g-\omega_m} + [P_{xy3}]_{\omega=\omega_g+\omega_m} \right) \mathrm{d}t$$ (7.2)

As discussed in Subsection 3.3, the capacitor voltage oscillations in the M^3C are more difficult to control when the input/output frequencies have similar values, i.e. $\omega_g \pm \omega_m$ is relatively small [93]. From (7.2) the cluster capacitance could be calculated as:

$$C \approx k_c \frac{\Delta W_{xy}}{\Delta v_{c_{xy}} v_c^*}$$ (7.3)

where ΔW_{xy} is the energy ripple, $\Delta v_{c_{xy}}$ is the maximum allowable capacitor voltage ripple and k_c represents an additional safety factor [108]. The factor k_c is selected to slightly oversize the capacitance considering that during LVRT the energy fluctuation in the capacitors could be increased. Moreover, it is assumed that f_g is 50Hz and the generator is operating between 10-40Hz. Furthermore, the capacitor voltage could be regulated between 100V-150V with a $\Delta v_{c_{xy}}$ of about 15V peak ($\approx 10\%$ of 150V).

Therefore, considering the experimental setup parameters and the above-mentioned conditions, the capacitance of each cell is C =4.58mF. Therefore, the experimental M^3C is implemented with 4.7mF capacitors (similar to the value used in the prototype of [108]). It is important to mention that the capacitance of the cell could be reduced by increasing the maximum allowable ripple level. Obviously, a higher ripple in the capacitors affects the lifetime of the capacitors. In practical appli-

cations, the M^3C capacitance should be dimensioned by trading between capacitor cost, efficiency and circulating current magnitude. Finally, even though the technical and economic analysis of the dimensioning of the M^3C components (number of cells, nominal voltage, capacitor voltage, type of semiconductor devices, switching frequency, etc.) for WECS applications is necessary, it is outside the scope of this PhD project.

7.4.2.2 Cluster Inductor dimensioning

The value of the cluster inductance is relatively simple to calculate by imposing a limit in the ripple of the current (usually set to 10%-15% of the nominal value). This value is calculated as [94, 109]:

$$L_b = \frac{0.5(\frac{v_c^*}{n} + \Delta v_{c_{xy}})}{\Delta i_{xy} f_{sw}} \tag{7.4}$$

Where Δi_{xy} is the maximum allowable cluster current ripple and f_{sw} is the output switching frequency. Considering the experimental setup parameters, and limiting the ripple in the cluster inductors to 10%, the inductance of each cluster is $L_b = 1.3$mH. For hardware availability reasons, 2.5mH inductors are used. In practical applications, the M^3C cluster inductance should be dimensioned by trading between inductor cost, circulating current magnitude, etc.

7.5 Summary

This chapter has described the design and implementation of a 27 power cells M^3C. This converter is used to validate the nested control systems proposed in Chapter4 and Chapter5.

The design, functions and components of the control platform have been described, focusing on the experimental M^3C requirements, such as electrical variables to be measured and gate drive switching signals.

The power stage of the experimental M^3C has been described and attention was paid to safety circuitry of the H-Bridges and the dimensioning of the M^3C capacitors and inductors.

CHAPTER 8

Results

8.1 Introduction

The 27-power cells experimental M^3C described in Chapter7 has been practically implemented to verify the theoretical and simulation work proposed in this thesis. This Chapter presents experimental results Control Strategies proposed in Chapter 4 to Chapter 5. Then, the following tests have been conducted to validate proper capacitor voltage balancing, Variable-Speed operation and fulfillment of grid codes:

- Fixed-Speed Steady State Operation

- Variable-Speed WECS emulation

- Grid-code compliance tests, including Symmetric and ASymmetric LVRT operation

- Similar Input-Output Frequencies Operation

The parameters considered for all test are shown in Table 7.3. Results are saved using the A/D channels on the FPGA boards described in Section 7.3 and a Keysight DSX Series 4000 oscilloscope using a combination of differential voltage and current probes.

The switching frequency used in all tests is set to 2500 Hz. Consequently, the sample time used for saving date is 400 μs.
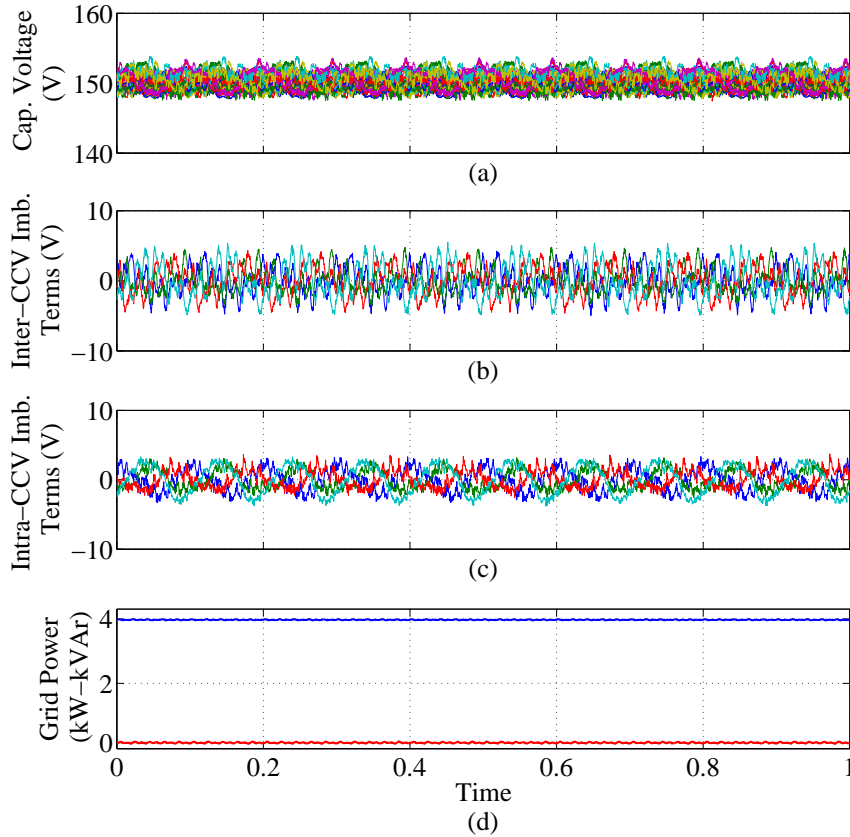
Figure 8.1: Experimental Results for Steady State Operation in LFM. (a) 27 Power Cells Capacitor Voltages. (b) Inter-CCV imbalance terms. (c) Intra-CCV Imbalace Terms. (d) Power Injected into the Grid.

8.2 Experimental Results for Fixed-Speed Steady State Operation

The steady state operation of the experimental M^3C for fixed generator frequency is presented in this Subsection. In this test, the generator frequency is set to 40 Hz, the grid frequency is 50 Hz, each capacitor is regulated to 150V and the M^3C is operating with unitary power factor.

Signals measured using the A/D converters available in the control platform are presented in Fig. 8.1-8.2. The capacitor voltages of the 27 power cells are regulated to 150V, as shown in Fig. 8.1(a). The Inter-CCV imbalance terms (i.e. $v_{c_{0\alpha}}$, $v_{c_{0\beta}}$, $v_{c_{\alpha 0}}$, $v_{c_{\beta 0}}$) are presented in Fig. 8.1(b), whereas the Intra-CCV imbalance terms (i.e $v_{c_{\alpha\alpha}}$, $v_{c_{\alpha\beta}}$, $v_{c_{\alpha\beta}}$, $v_{c_{\beta\beta}}$) are shown in Fig. 8.1(c). The eight imbalance terms are successfully regulated inside a ± 7 V band. Fig. 8.1(d) illustrates the unity power factor operation of the system injecting 4kW into the grid. The average CCV control loop presents excellent steady state tracking, as shown in Fig. 8.2. The term $v_{c_{00}}$ is regulated to $3nv_c^* = 1350$V in accordance with (3.20).

The generator and grid voltages are set to 200V and 215V (peak phase to neutral values), re-
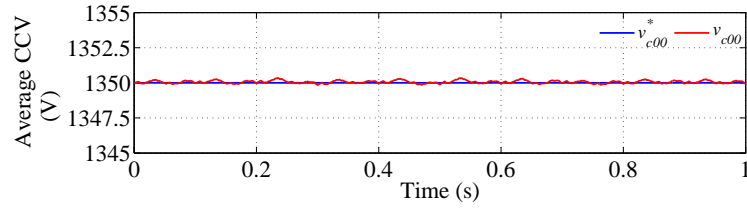
Figure 8.2: Experimental Results for Steady State Operation in LFM. Average Cluster Capacitor Voltage Tracking.

spectively, as shown in Fig. 8.3(a)−(b). The input and output currents are not much affected by the circulating currents produced by the balancing algorithms. As shown in Fig. 8.3(c)−(d), the input and output currents are balanced and present low harmonic distortion (THD $\approx 2\%$).

As the balancing of the CCVs is performed using a component of the circulating currents in phase with the generator voltages, any drift in the circulating current tracking can be reflected in the generator currents. Consequently, the circulating current reference tracking has to be accurate. As shown in Fig. 8.4, good tracking of the circulating current references is achieved using the control loop proposed in Subsection 4.3 and the negative sequence component of the generator current is $\approx 3\%$. Oscilloscope waveforms are presented in Fig. 8.5. From top to bottom, one of the capacitor voltages of the M^3C ($v_{c_{ar1}}$), the input voltage $v_{m_{ab}}$, the cluster voltage v_{ar} and the grid voltage $v_{g_{rt}}$ are presented in Fig. 8.5(a). The cluster voltage v_{ar} modulates both (generator and grid) voltages and the different levels produced by the phase shifted modulation are observed. The use of this modulation technique implies an output voltage of $2n + 1 = 7$ levels and an equivalent output switching frequency of $2nf_{sw} = 15$ kHz.

Analogously, from top to bottom, the cluster currents i_{ar} and i_{br}, the grid current i_{g_r} and the generator-side current i_{m_a} are presented in Fig. 8.5(b).

133

Figure 8.3: Experimental Results for Steady State Operation in LFM. (a) Grid Voltages. (b) Generator Voltages. (c) Grid Currents. (d) Generator Currents.
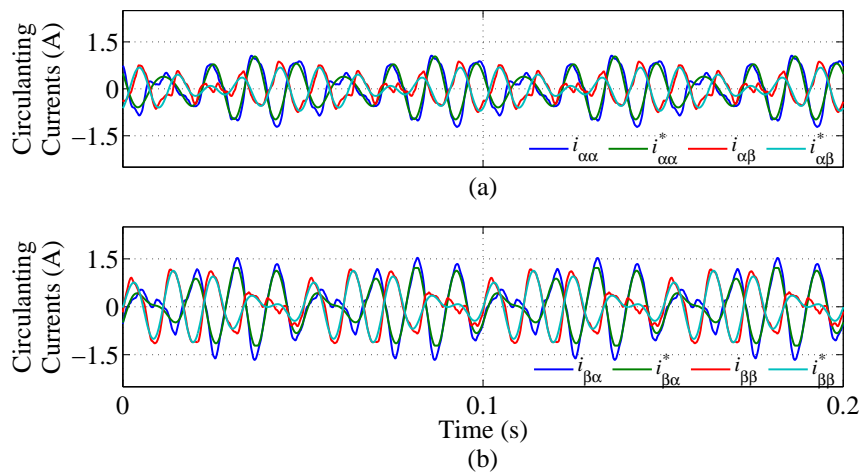
Figure 8.4: Experimental Results for Steady State Operation in LFM. (a)-(b) Circulating Currents tracking.
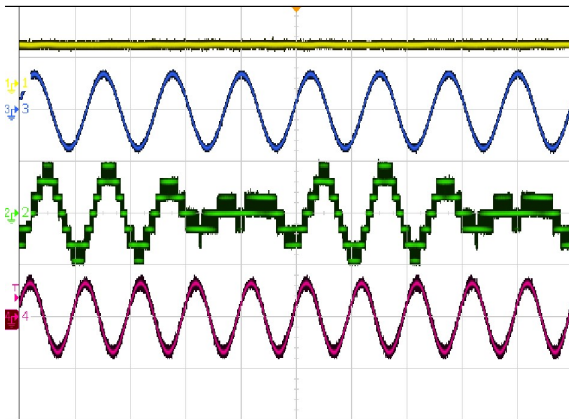
(a) Voltages.
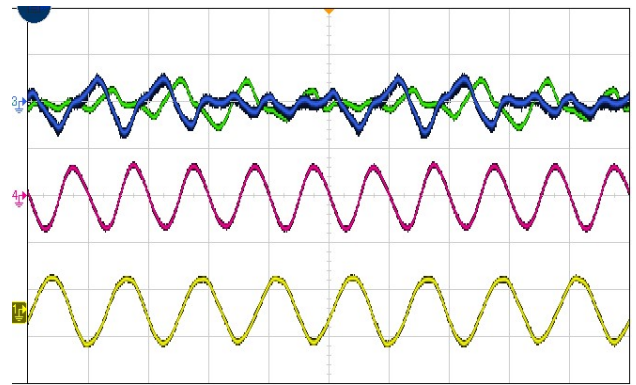
(b) Currents.

Figure 8.5: Scope Waveforms for Steady State Operation in LFM.

8.3   Experimental Results for Variable-Speed WECS Emulation

The operation of a 4kW PMSG based variable-speed wind turbine is simulated using a wind speed profile from Rutherford Appleton Laboratories. The frequency and voltage profiles obtained in this simulation are discretised and programmed in the generator-side power supply (ModelCSW5550) with a sample time of 400 μs. Consequently, the power source generates variable frequency and voltages emulating the behavior of a 4kW PMSG based wind turbine at the M^3C M3C input.

As observed in Fig. 8.6(a), the wind speed profile generates a variable rotational speed at the converter input, whereas the grid frequency remains constant at 50 Hz. In Fig. 8.6(b), the performance of the generator-side control system is shown. The generator-side control system tracks the maximum power point for each wind velocity, achieving MPPT operation through the regulation of the quadrature current [see (4.60)]. The 27 power cell capacitor voltages keep their voltage references throughout the test, regardless the generator frequency, as is depicted in Fig. 8.6(c). Finally, Fig. 8.6(d) presents the performance of the grid-side control, which is regulated to operate with unitary power factor, dispatching into the grid all the active power produced by the wind turbine.

Oscilloscope waveforms are presented in Fig. 8.7. From top to bottom, one of the capacitor voltages $v_{c_{ar1}}$, the cluster voltage v_{ar}, the grid voltage $v_{g_{rt}}$ (purple line) and the input voltage $v_{m_{ab}}$ (green line), are presented in Fig. 8.5(a). The cluster voltage v_{ar} modulates both (generator and grid) voltages and the different levels produced by the phase-shifted modulation are observed. In Fig. 8.7(a) a time window of 20s is used, whereas a zoomed image of the same test is presented in Fig. 8.7(b) with a time window of 200ms (20ms per division).
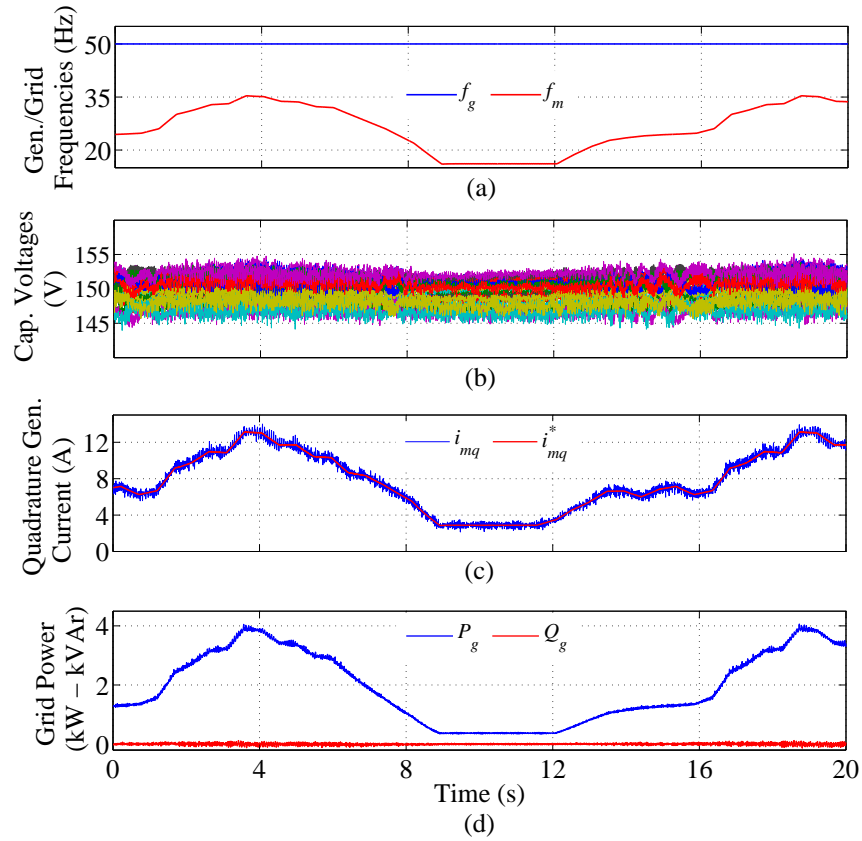
Figure 8.6: Experimental Results for Variable-Speed Wind Turbine Emulation. (a) Grid and Generator Frequencies. (b) 27 Power Cells Capacitor Voltages. (c) Quadrature generator-side current tracking. (d) Active and Reactive Power Injected into the grid.

(a) Voltages of the system.

(b) Amplified view of (a).
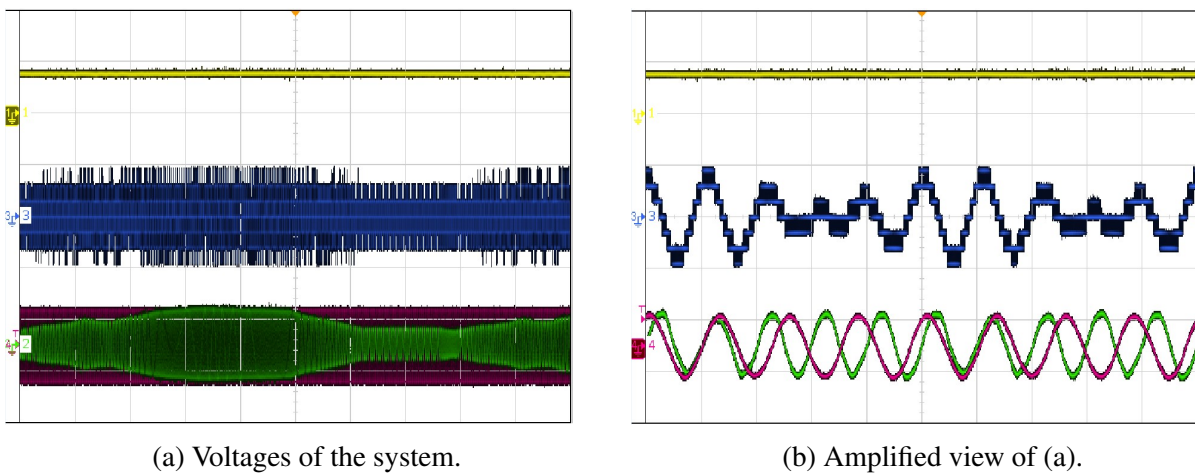
Figure 8.7: Oscilloscope Waveforms for Variable-Speed Wind Turbine Emulation.

8.4 Experimental Results for Symmetric LVRT operation

In this test, the MX45 power source is programmed to produce a symmetrical Dip type A, with the phase voltages being decreased to a 30% of the nominal value for 0.2s. During the next 0.6s, a profile for the recovery of the grid voltage is applied. The power source is programmed to generate this fault three consecutive times before returning to the nominal grid voltage parameters.

Oscilloscope waveforms are shown in Fig. 8.8. From top to bottom, one of the capacitor voltages of the M^3C ($v_{c_{ar1}}$), the input voltage $v_{m_{ab}}$, the cluster voltage v_{ar} and the grid voltage $v_{g_{rt}}$ are presented in Fig. 8.8(a). An amplified view of the dip is depicted in Fig. 8.8(b) considering a time window of 1s. When the dip voltage appears, the reduction of the number of levels in the cluster voltage is observed as the cluster voltage v_{ar} modulates both (generator and grid) voltages. Finally, experimental results −processed by the A/D channels of the control platform− for the grid and generator voltages are also depicted in Fig. 8.10(a)−(b).

The signals measured by the A/D channels of the control platform are presented in Fig. 8.9 and Fig. 8.10. The capacitor voltages of the 27 power cells are properly regulated to the set point ($v_c^* = 150$ V), as shown in Fig. 8.9(a). The Inter-CCV and the Intra-CCV imbalance terms are presented in Fig. 8.9(b)-(c), respectively. Those imbalance terms are successfully regulated inside a ± 7 V band through the fault. Moreover, the active and reactive power are controlled to fulfill LVRT requirements. When the fault is applied, the active power is regulated to 0A, and the M^3C starts supporting the grid voltage through the injection of reactive power. As shown in Fig. 8.9(d), for $t \approx 0.25$s, the M^3C supplies only reactive power to the grid.

To achieve LVRT requirements, the generator and grid currents have to follow the power references. Therefore, the grid currents commands are modified to inject 50% of reactive current during the fault. Due to the LVRT requirements demand to the control system, the M^3C stops the injection of active power into the grid during the fault. Consequently, the generator current is no longer controlled using the MPPT algorithm of (4.60) and the current reference is reduced to $0A$. As shown in Fig. 8.10(c)-(d), the generator and grid currents are balanced and present low harmonic distortion (THD $\approx 2\%$) during the test regardless the grid-voltage condition.

(a) Experimental results for LVRT Control. Voltages of the system.

(b) Amplified view of (a).

Figure 8.8: Oscilloscope Waveforms for LVRT control.
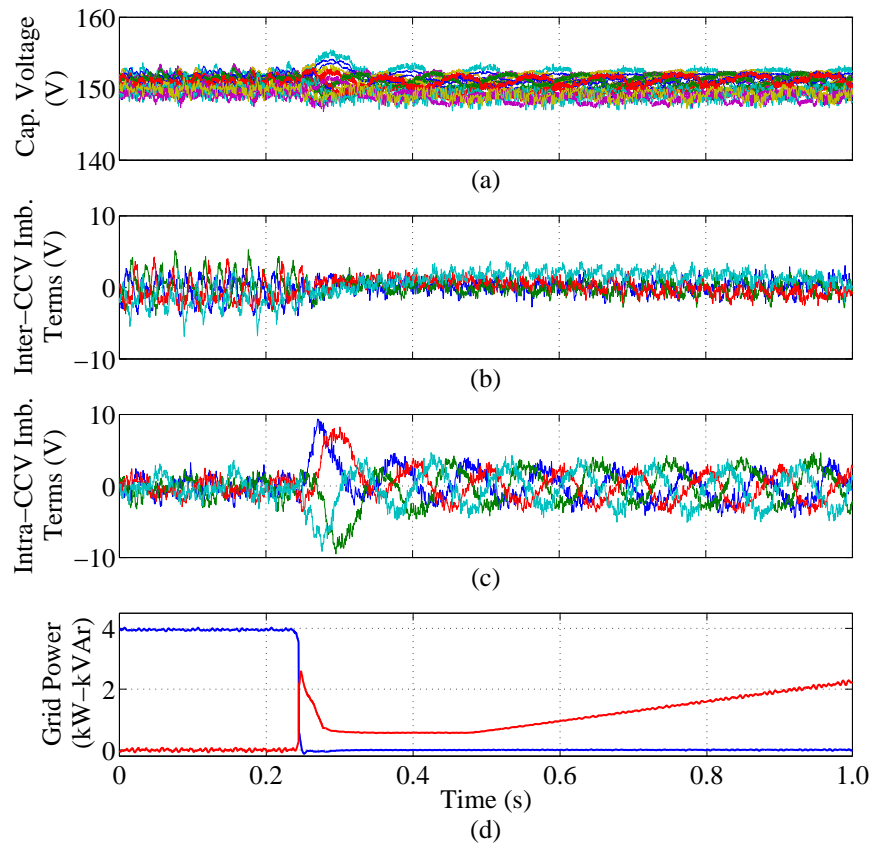
Figure 8.9: Experimental Results for LVRT Control. (a) 27 Power Cells Capacitor Voltages. (b) Inter-CCV imbalance terms. (c) Intra-CCV Imbalace Terms. (d) Power Injected into the Grid.
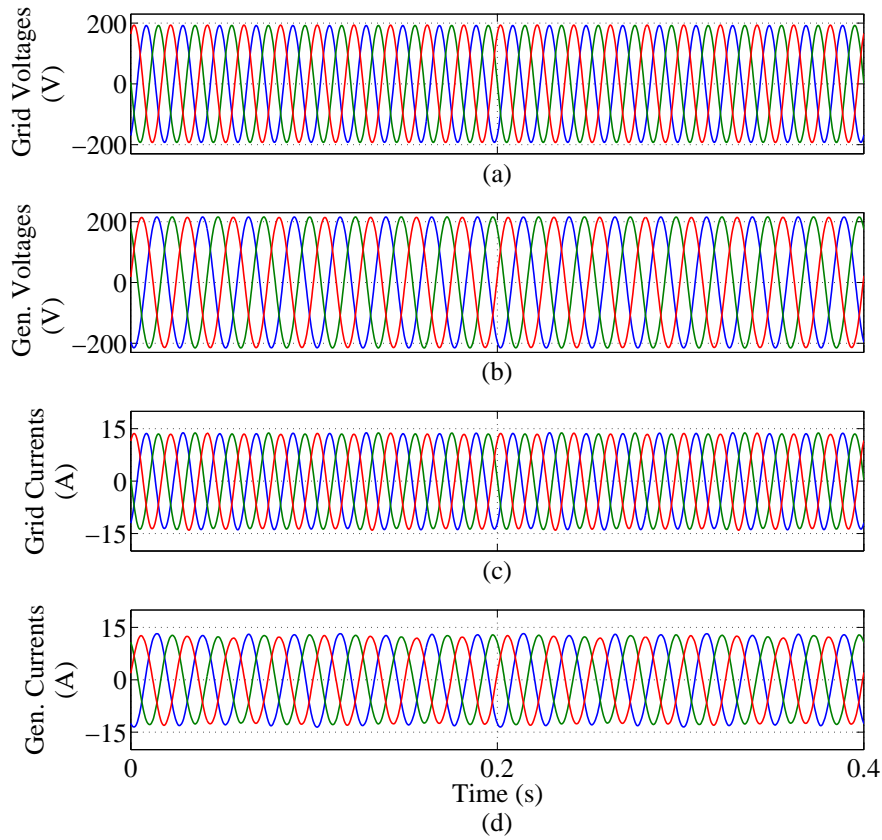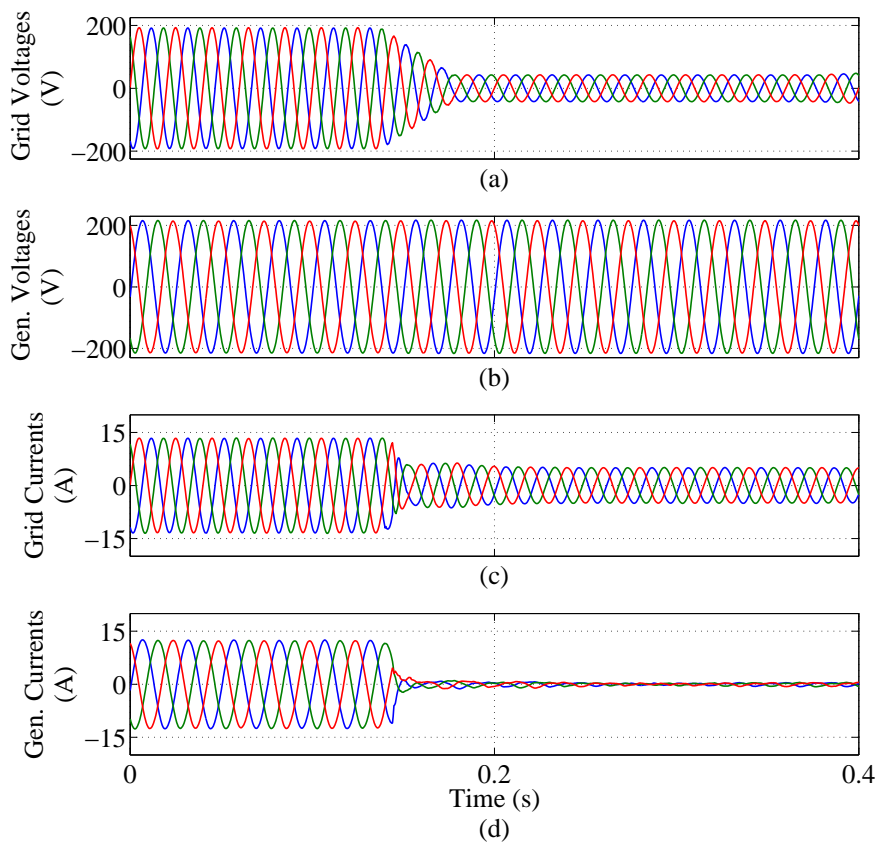
Figure 8.10: Experimental Results for LVRT Control. (a) Grid Voltages. (b) Generator Voltages. (c) Grid Currents. (d) Generator Currents.

## 8.5   Experimental Results for Symmetric ZVRT operation

In this test, the MX45 power source is also programmed to produce a symmetrical Dip type A, with the phase voltages being decreased to a 2% of the nominal value for 0.2s. During the next 0.6s, a profile for the recovery of the grid voltage is applied. Similarly to the previous test, the power source is programmed to generate this fault three consecutive times before returning to the nominal grid voltage parameters.

The main difference with the previous test is the magnitude of the grid voltage dip, which is almost 0V during the fault. Moreover, the requirement of reactive current injection during the fault is increased from 50% to 100% of the nominal current. Therefore, the M^3C has to be able to support to the grid with 100% of nominal current when the grid voltage decrease almost to 0%. This test meets the most demanding grid codes presented in [27].

Oscilloscope waveforms are shown in Fig. 8.11. From top to bottom, one of the capacitor voltages of the M^3C ($v_{c_{ar1}}$), the input voltage $v_{m_{ab}}$, the cluster voltage v_{ar} and the grid voltage $v_{g_{rt}}$ are presented in Fig. 8.11(a). An amplified view of the dip is depicted in Fig. 8.11(b) considering a time window of 1s, where it is visible the reduction of the number of levels in the cluster voltage during the fault. The grid and generator voltages are also presented in Fig. 8.13(a)-(b), where signals processed by the A/D channels of the control platform have been used.

Additional experimental results −measured by the A/D channels of the control platform− obtained to validate the ZVRT performance of the M^3C are presented in Fig. 8.12 and Fig. 8.13. The capacitor voltages of the 27 power cells are properly regulated to the desired set point during the fault [see Fig. 8.9(a)]. The Inter-CCV and the Intra-CCV imbalance terms are presented in Fig. 8.9(b)−(c), respectively. The average value of those imbalance terms is successfully regulated to zero and the oscillations generated during the fault are maintained inside a ±15 V band. It is important to note that the oscillations represent the 7% of the average Cluster Capacitor Voltage (450V). Fig. 8.9(d) presents the active and reactive powers injected into the grid during the fault. When the fault appears, the M^3C supplies only reactive power to the grid.

(a) Voltages of the system.   (b) Amplified view of (a).
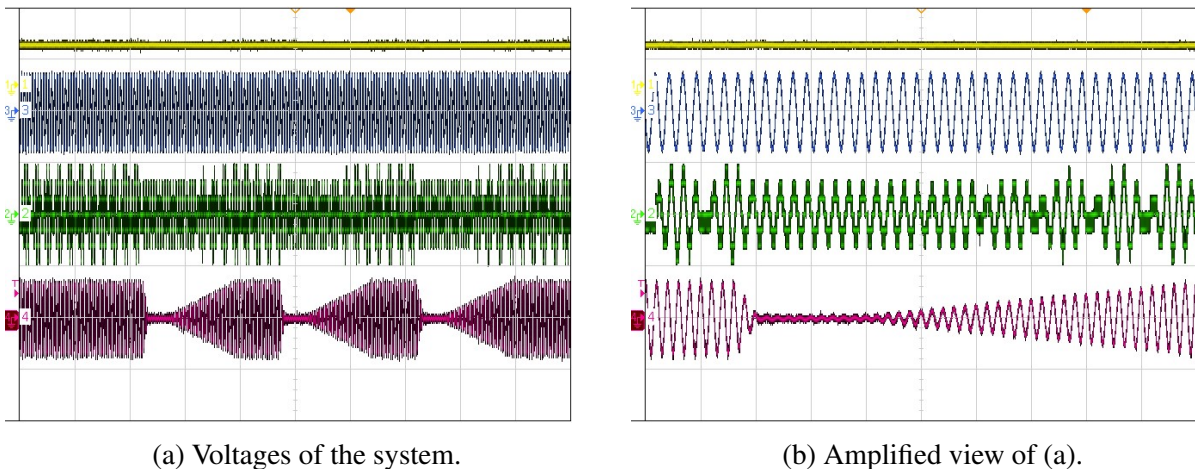
Figure 8.11: Oscilloscope Waveforms for ZVRT control.
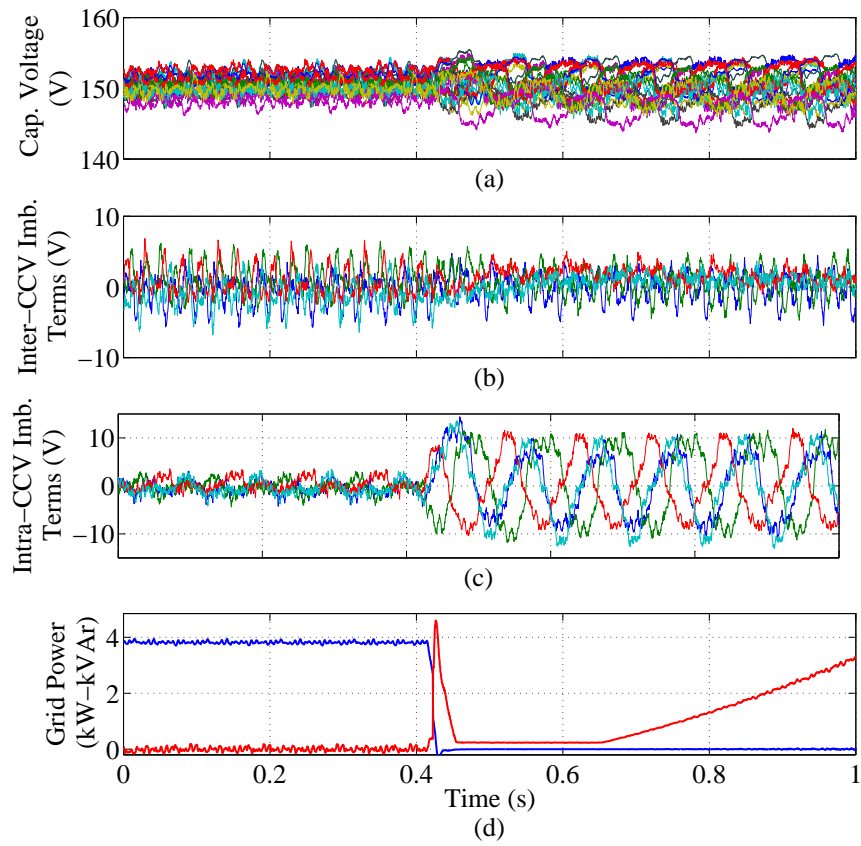
Figure 8.12: Experimental Results for ZVRT Control. (a) 27 Power Cells Capacitor Voltages. (b) Inter-CCV imbalance terms. (c) Intra-CCV Imbalace Terms. (d) Power Injected into the Grid.
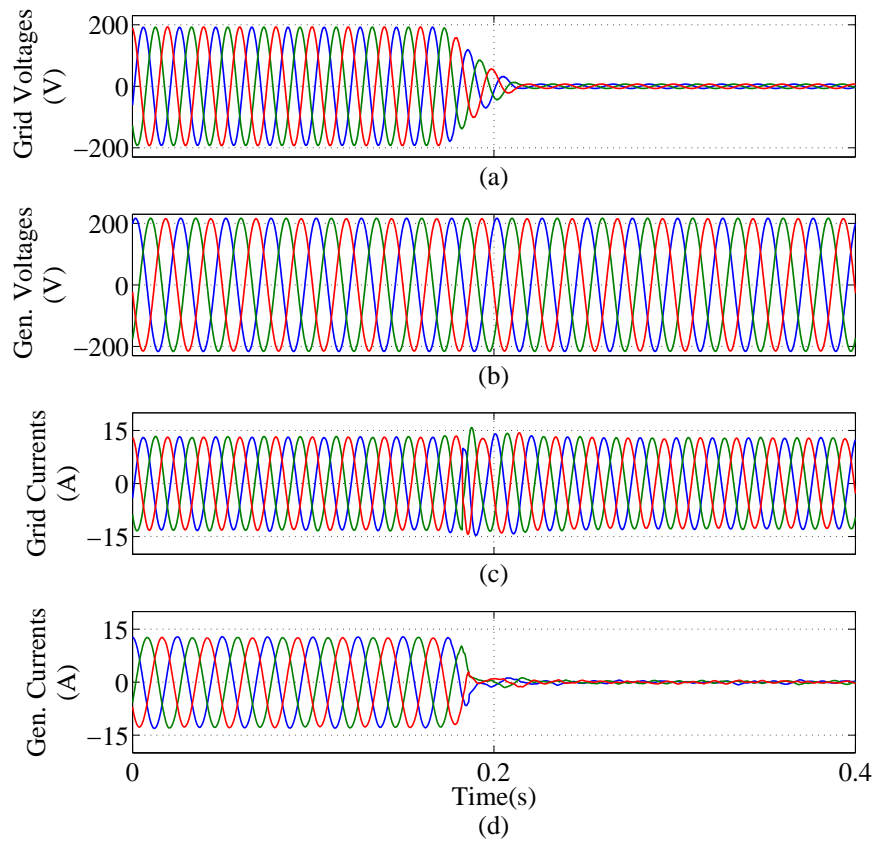
Figure 8.13: Experimental Results for ZVRT Control. (a) Grid Voltages. (b) Generator Voltages. (c) Grid Currents. (d) Generator Currents.
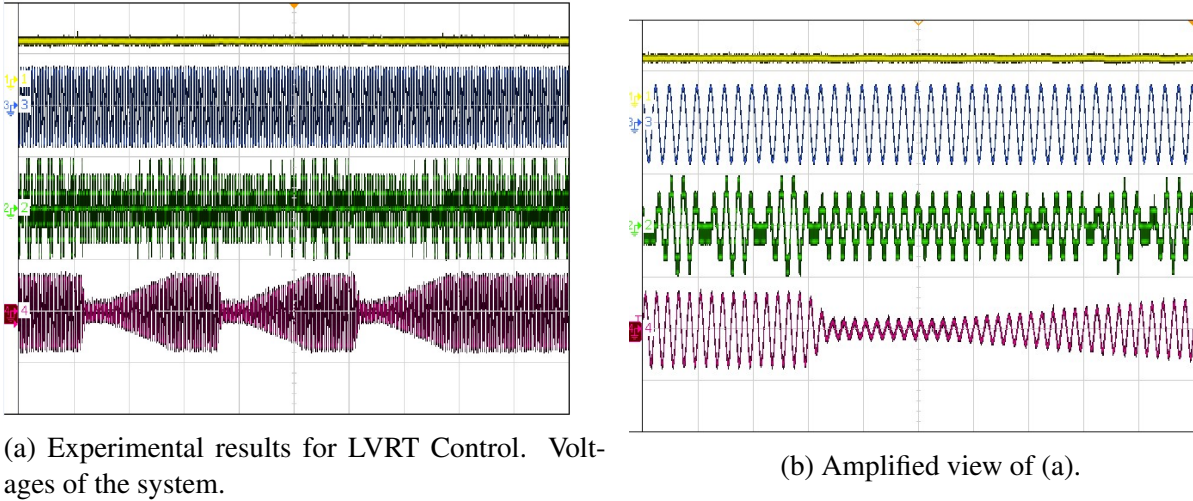
To accomplish the power LVRT requirement presented in 8.9(d), generator and grid currents have to be controlled as shown in Fig. 8.10(c)-(d). The grid current commands are modified to inject 100% of reactive current during the fault. At the same time, this information is feed-forwarded to the the generator current controller, which change its reference from MPPT to $0A$. As shown in Fig. 8.10(c)$-$(d), the generator and grid currents are balanced and present low harmonic distortion during the test regardless the grid-voltage condition.

8.6   Experimental Results for ASymmetric LVRT operation

The proposed control strategy has been tested considering a Type C Voltage Dip. In this case, two grid phases decrease their voltages to 50% of the nominal value for 0.2s. During the next 0.6s, the profile recovery shown in Fig. 8.14(a) is applied. The performance of the proposed DSC algorithm to estimate the positive and negative sequence voltages is presented in Fig. 8.14(b). In this test, the delay of the DSC algorithm is set to be 2ms.

The performance of the M^3C control system is depicted in Fig. 8.15. The capacitor voltages of the 27 power cells are properly regulated to the desired set point during the fault [see Fig. 8.15(a)]. The Inter-CCV and the Intra-CCV imbalance terms are presented in Fig. 8.9(b)-(c), respectively. The average value of those imbalance terms is successfully regulated to zero and the oscillations generated during the fault are maintained inside a ± 15 V band. Active and reactive powers injected into the grid during the fault are presented in Fig. 8.9(d). When the fault appears, the M^3C supplies only reactive power to the grid. However, as mentioned in Subsection 5.3.2.2, the four $\alpha\beta$ grid currents do not provide enough degrees of freedom to eliminate the oscillations in the reactive power which has a noticeable 100Hz component. On the other hand, active power supplied to the grid is virtually free of double frequency oscillations because the current calculation of (5.17) is obtained selecting k_{LVRT}=0.

As discussed in the Section 5.3.3, the grid-side control system regulates the positive and negative currents to mitigate the double-frequency power pulsations. Therefore, the unbalanced grid currents presented in Fig. 8.15(c) are injected to the grid.

Alternatively, the control system depicted in Fig. 5.4 is configured to reduce the power oscillation in the converter. In this case, $k_{LVRT} = 1$ and the grid is supplying the active power oscillations required by the filter. The experimental results are shown in Fig. 8.17. The capacitor voltages of the 27 power cells are properly regulated to the desired set point during the fault, as shown in see Fig. 8.17(a)]. The Inter-CCV and the Intra-CCV imbalance terms, presented in Fig. 8.17(b)-(c), are successfully regulated to zero and the oscillations generated during the fault are maintained inside a ± 15 V band. Active and reactive powers injected into the grid during the fault are presented in Fig. 8.17(d).

The performance of the control system is similar to the previuos case when $k_{LVRT} = 0$. This is due to the filter between the M^3C and the grid has a low internal resistance ($R_g = 0.2\Omega$). Therefore, small active power oscillations are produced in the filter when the grid voltage Dip appears. However, a slightly reduction can be observed in the capacitor waveforms when Fig. 8.17(a) is compared to Fig. 8.15(a).
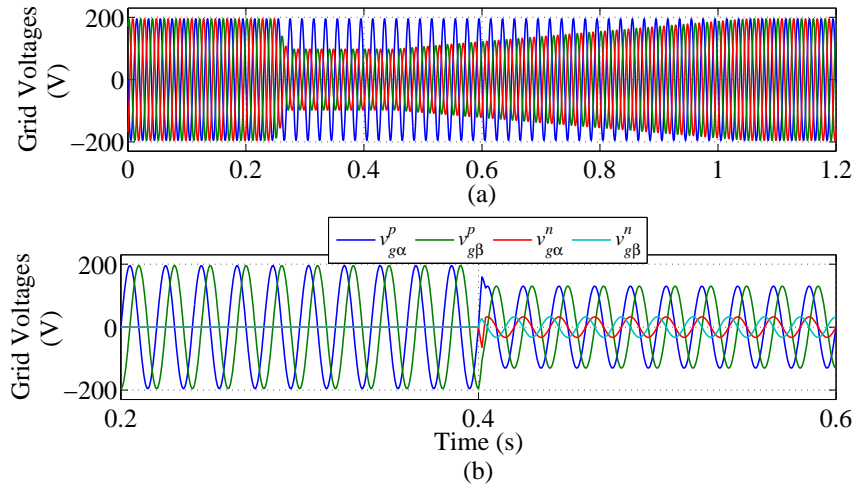
Figure 8.14: Grid Voltages for a 50% Dip Type C. (a) Grid Voltages. (b) Positive and Negative sequence components estimation using $\theta_{\rm d}$ =2m.
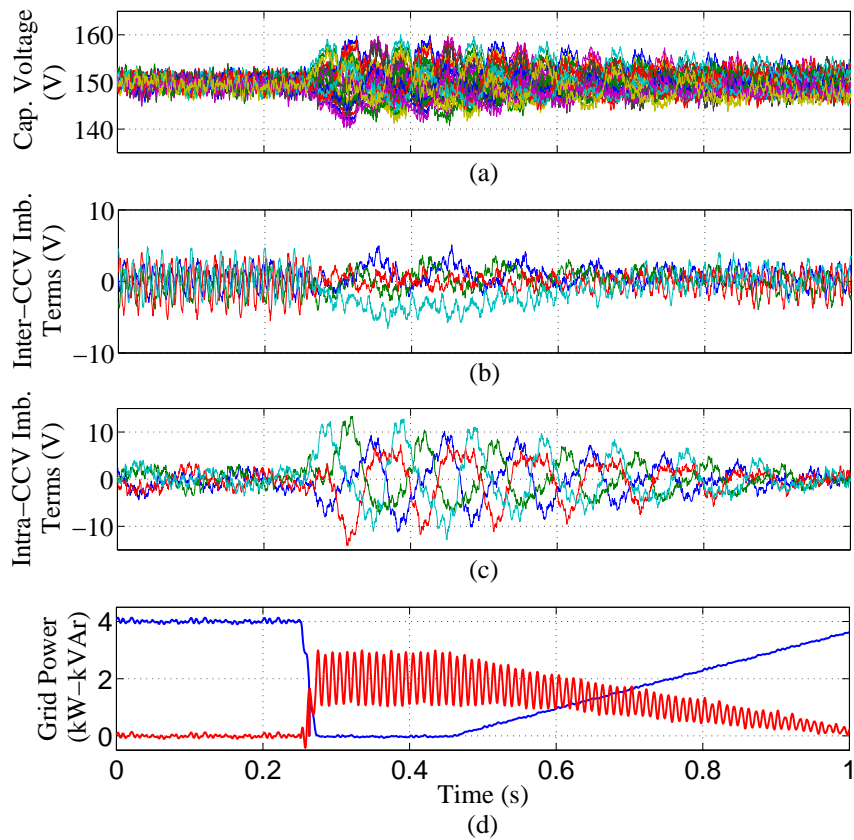
Figure 8.15: Experimental Results for LVRT Control using $k_{LVRT} = 0$. (a) 27 Power Cells Capacitor Voltages. (b) Inter-CCV imbalance terms. (c) Intra-CCV Imbalace Terms. (d) Power Injected into the Grid.
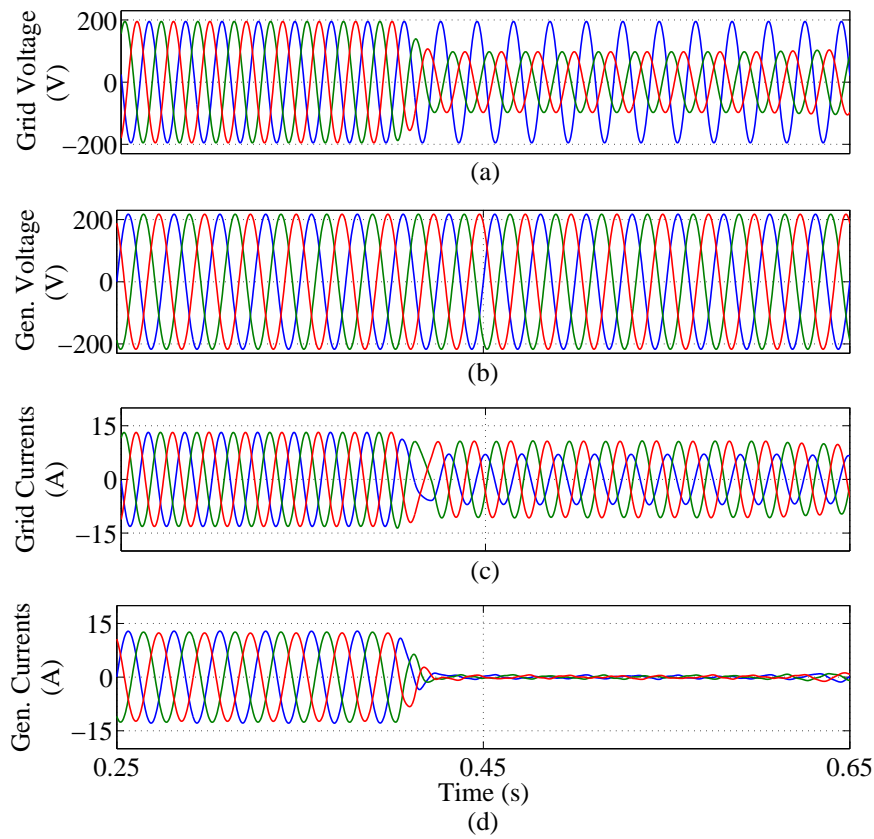
Figure 8.16:]
Experimental Results for LVRT Control using $k_{LVRT} = 0$. (a) Grid Voltages. (b) Generator Voltages. (c) Grid Currents. (d) Generator Currents.
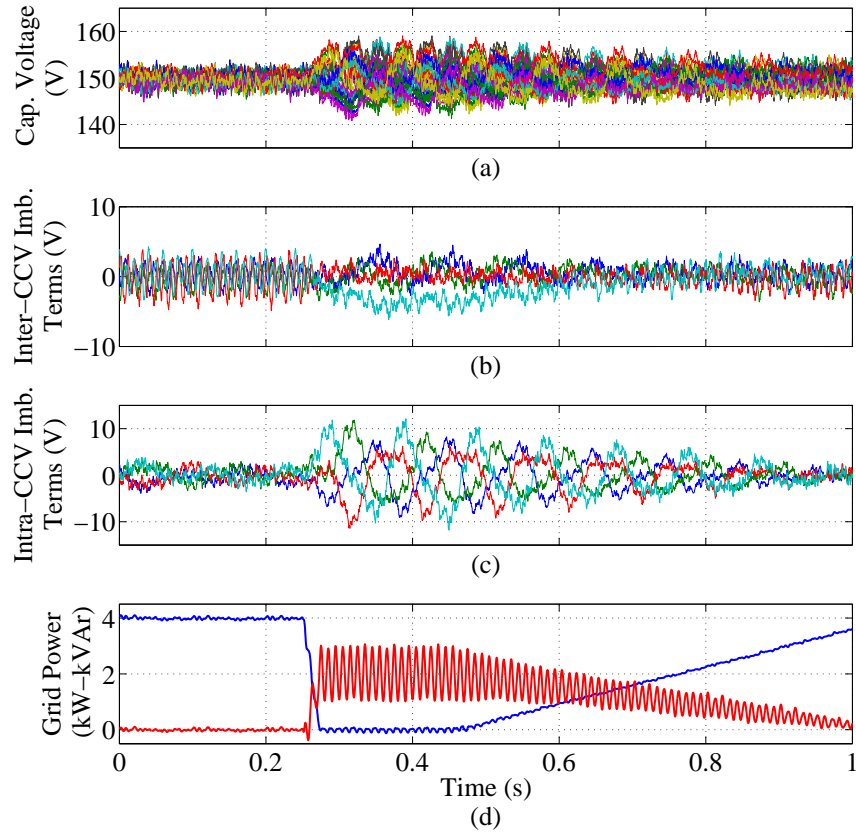
Figure 8.17: Experimental Results for LVRT Control using $k_{LVRT} = 1$. (a) 27 Power Cells Capacitor Voltages. (b) Inter-CCV imbalance terms. (c) Intra-CCV Imbalace Terms. (d) Power Injected into the Grid.

For better understanding, a zoomed view of the active power delivered to the grid in both cases is shown in Fig. 8.18. The red-line waveforms correspond to the case when $k_{LVRT} = 0$ and the blue line corresponds to the case when $k_{LVRT} = 1$. From the inspection of Fig. 8.18, it is concluded that when $k_{LVRT} = 1$ the active power oscillations are supplied by the grid and, consequently, the oscillations at the M3C output are successfully reduced. In some cases, e.g weak grids, resistive lines or massive short circuits, the oscillations in active power could be dangerous for the converter and should be desirable to mitigate them at the converter terminals.
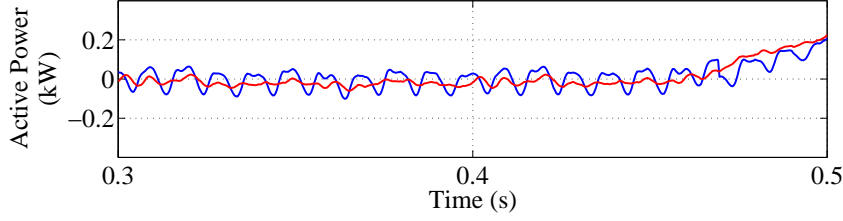
Figure 8.18: Blue line: Amplified view of Active Power Injected when $k_{LVRT} = 1$. Red line: Amplified view of Active Power Injected when $k_{LVRT} = 0$.

8.7 Experimental Results for similar Input-Output Frequencies Operation

In this section, similar Input-Output Frequencies operation of the M^3C is tested for the Vector control strategy. In this case, a ramp of generator-side frequency is applied during 20 s, considering a lower frequency limit of 16Hz (the inferior limit of the Ametek Power Source) and an upper limit of 45 Hz.

In this case, the vector control strategy is selected to balance the Cluster Capacitor Voltages using the Semi-controllable terms because the oscillations in the capacitors are within an acceptable range. Therefore, the injection of common-mode voltage is not required in this test. However, it has to be stated that for $f_m > 45$Hz, the mitigation control has to be performed using the Fully-controllable terms and, consequently, common-mode voltage need to be injected. Of course, this fact implies that each cluster of the experimental setup has to be designed to synthesise the generator voltage plus the grid voltage plus the common-mode voltage.

Results for the equal frequency operation of the M^3C using the Vector Control Strategy are presented in Fig. 8.19. As mentioned above, the generator frequency f_m follow a ramp between 16-45 Hz, as illustrated in Fig. 8.19(a). The 27 capacitor voltages are properly controlled to 150 V, as shown in Fig. 8.19(a). The Inter-CCV imbalance terms ($v_{c_{0\alpha}}$, $v_{c_{0\beta}}$, $v_{c_{\alpha 0}}$, $v_{c_{\beta 0}}$) and the Intra-CCV imbalance terms ($v_{c_{\alpha\alpha}}$, $v_{c_{\alpha\beta}}$, $v_{c_{\alpha\beta}}$, $v_{c_{\beta\beta}}$) are illustrated in Fig. 8.19(b)−(c), respectively. The ripple of the imbalance terms is bounded and it is not increased as f_m gets closer to f_g. In fact, the eight imbalance terms are bounded inside a $\pm$ 10 V band, which represents oscillations of $\approx 5\%$ of the CCV nominal value (which is $nv_c^* = 450$ V). Finally, Fig. 8.19(d) illustrates unity power factor operation of the system injecting 4 kW into the grid.

148
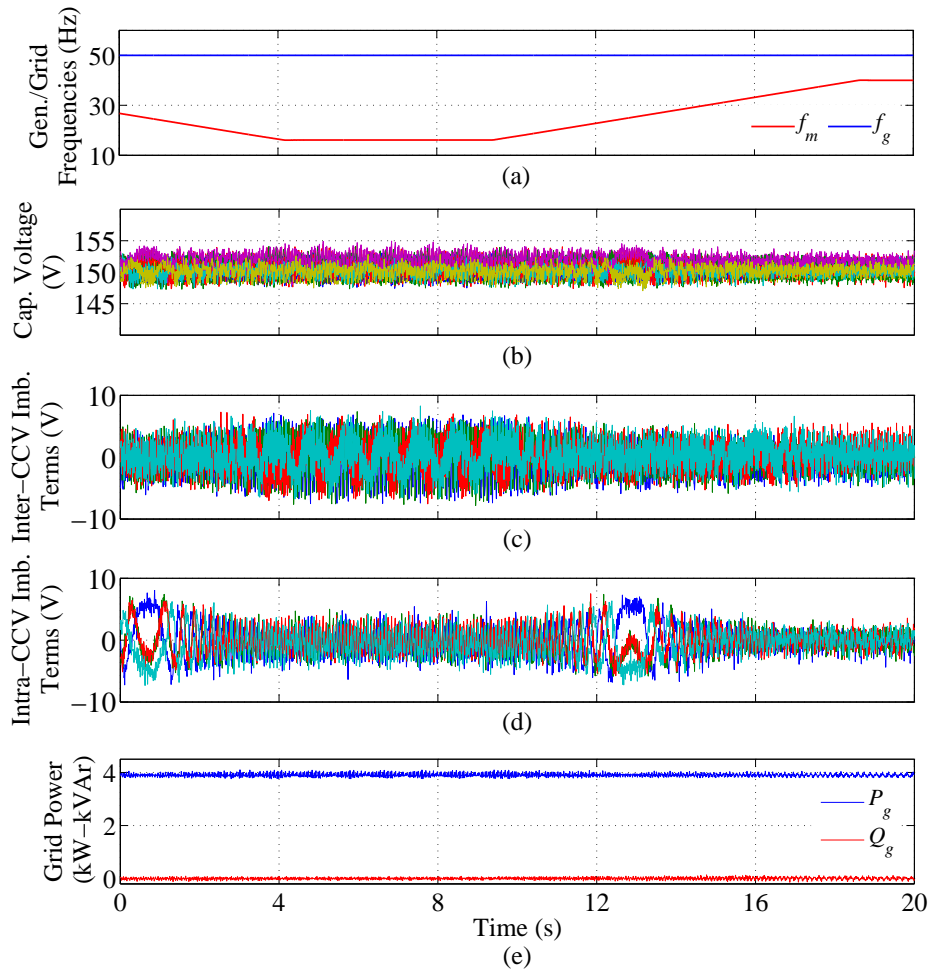
Figure 8.19: Experimental Results for around Equal Input-Output Frequencies Operation. (a) Generator and Grid Frequencies. (b) 27 Power Cells Capacitor Voltages. (c) Inter-CCV imbalance terms. (d) Intra-CCV imbalance terms. (e) Power Injected into the Grid.

8.8 Summary

In this Chapter, experimental results obtained with a 5kW downscale prototype have been presented to validate the theoretical work proposed in this project. The effectiveness of the control strategies proposed in Chapters 4-5 has been proved to be accurate for Variable-Speed operation, grid code compliance and capacitor voltage regulation. Furthermore, the experimental results are consistent with simulations results.

Similarly to Chapter 6 conclusion, both control strategies are equivalent for low-frequency operation of the M^3C. In LFM, fixed speed operation, variable-speed operation and the fulfilment of grid codes, such as LVRT and ZVRT, have been successfully tested for in the experimental prototype. In all test, the proposed control systems ensure proper capacitor voltage balancing, keeping the CCVs bounded and with low ripple. Additionally, the performance of the generator-side and grid-side control system had shown good dynamics response for grid-code compliance and MPPT, respectively.

As far as equal-frequency operation is concerned, the operation of the experimental setup up has been tested to follow a ramp of frequency which reaches $f_m{=}0.9f_g$ performing proper capacitor voltage tracking.

CHAPTER 9

Conclusions and Future Work

9.1 Conclusions

The continuous increase in the power level of WECSs is driving the power electronics technology towards MV operation. Research works on novel MV power converters, and advanced control schemes will play a major role in the development of the new generation of WECSs. Accordingly, the main goal of this thesis was to validate the use of the M^3C for Multi-MW WECS applications with emphasis on characteristics such as decoupled operation, variable-speed operation, grid-code fulfilment, modularity and scalability.

Owing to the results obtained in this thesis, it can be stated that the M^3C is a suitable power converter that can be successfully applied in WECS applications of 10 MW and beyond. Additionally, the major findings of this PhD project are highlighted below:

Decoupled operation:

- As the research has demonstrated, the regulation of the machine-side and grid-side systems connected to the M^3C is decoupled from the regulation of the converter. Consequently, M^3C based WECSs can be controlled similarly to the operation of conventional Back-to-Back Converters based WECSs, where the presence of a DC-link allows decoupled control of the ac-dc-ac conversion stages. In this case, the proposed control system, which relies on the representation of the M^3C in Double $\alpha\beta0$ coordinates, enables decoupled regulation. The grid-side and generator-side control systems are regulated using the input/output currents, whereas the regulation of the flying capacitors is achieved by the manipulation of the circulating currents.

Variable-Speed Operation:

- M^3C M^3C based WECSs can operate in variable-speed conditions, tracking the maximum power point for each wind speed. The Generator-side Control System has been designed considering that the M^3C based WECS features a PMSG. Consequently, the control system regulates the torque current imposing a reference that is a function of the wind speed and wind turbine parameters. Simulations and experimental results have confirmed the correct performance of the MPPT algorithm when the M^3C is tested with a real wind speed profile.

Grid-Code Compliance:

- M^3C based WECSs have FRT capability, and they can remain connected to the electrical network in case of faults. All the experimental results have proved that the M^3C can ride-through fault conditions such as LVRT and ZVRT at the same time that injection of reactive power provides voltage support.

Grid-Side Control System:

- The Grid-side Control System is simple because neither counter-revolving $\mathrm{d}q$ frames nor notch filters to achieve sequence separation are required and because positive and negative sequence components are regulated by the same controller (Resonant Controllers). Furthermore, the Grid-side Control System has a faster detection of grid-faults through the estimation of positive and negative sequence components achieved by the Fast DSC algorithm. Unlike the conventional DSC, the proposed Fast DSC can estimate the positive/negative-sequence signals within a small fraction of a cycle.

Scalability and Power Quality:

- Owing to the fact that the balancing of the CCVs is decoupled from the balancing of the power-cells within a cluster, it can be stated that the M^3C based WECSs features simplicity on reaching high voltage levels by increasing the number of power cells without affecting the structure of the control system. This statement can be corroborated analysing the Simulation and Experimental Results. All the Experimental Results were conducted with a M^3C with three power-cells per cluster. On the other hand, Simulations Results were carried out with a M^3C with seven power-cells per cluster. Regardless the number of cells per cluster, the control strategies proposed in this thesis are similar in both cases. The only difference relies on the implementation of the Single-Cell Control System, which has to balance three or seven power-cells. For a higher number of power-cells per cluster, the same principle is applicable.

- High power quality is achieved using the M^3C to interface Multi-MW WECSs. Single-Cell Control considers the use of phase-shifted modulation that leads to a low harmonic distortion and small voltage steps in the output voltages when a high number of cells are considered. As experimental and simulation results have proved, the use of this modulation technique implies an output voltage of $2n + 1$ levels and an equivalent output switching frequency of $2nf_{sw}$.

Capacitor Voltage Regulation

- The flying capacitors of the M^3C are properly bounded and with low ripple for a broad range of input-output frequencies operation. Additionally, the vector Power-CCV model of the M^3C in $\Sigma\Delta$ Double-$\alpha\beta0$ coordinates allows a simple analysis and implementation of control strategies in accordance with the operational frequencies. Then, the definition of LFM (balancing) and EFM (mitigation) are useful to realise the real control requirements of the M^3C. WECSs have a cut-in and a cut-out speed that are not close to the unstable frequencies of the M^3C. Therefore, just the balancing control of the CCVs is required as has been validated through simulations and experimental results. This is certainly an advantage of the M^3C based WECSs, because the injection of common-mode voltage and high-magnitude circulating currents are not needed in a normal speed range of operation.

Equal Frequency Operation

- Although it is not likely that a M^3C based Multi-MW WECS operate with equal generator-grid frequencies, the operation of the M^3C when the generator frequency is equal to the grid frequency has been proved to be successful. In EFM, mitigation control has to be applied to regulate the voltage oscillations in the capacitor voltages. In recent literature, all the proposed strategies enable EF operation using open-loop mitigation signals, similar to the Scalar CCV Control System proposal. However, open-loop mitigation signals cannot compensate non-linearities or simplifications in the power converter model. Thereby, the Vector CCV Control Strategy introduces a novel dq based vector control of the M^3C which is especially useful in this situation because it considers a closed-loop control of CCVs. Consequently, Vector CCV Control System has a better performance than Scalar Control Strategy and 0 steady state error is achieved in the regulation of the CCVs even when $f_m = f_g$.

9.2 Summary of contributions

- A comprehensive model of the M^3C dynamics has been developed in this work. Using this model, it is straightforward to identify the issues that arise from the variable-speed operation and to represent the dynamics of the capacitor voltages.

- Nested control strategies have been proposed to regulate the operation of the M^3C in Multi-MW WECS applications. This control system enables the operation of the converter for a broad range of frequency, including equal generator-grid frequencies.

- An enhanced Low Voltage Ride Through (LVRT) algorithm is proposed. This algorithm enables operation of the converter under symmetrical and unsymmetrical grid voltage sags, injecting reactive power during the faults.

- A fast-convergence DSC algorithm has been introduced to enhance the component-sequence separation of voltages and currents required to apply LVRT control strategies.

- An experimental prototype composed of 27 power cells has been constructed to validate the operation and control of M^3C based Multi-MW WECSs.

- To the best of this author knowledge, this is the first research work where LVRT control strategies for M^3C based WECSs are discussed, analysed and experimentally validated.

The work developed during this project has resulted in the publication of 9 international conference papers [41, 97, 100, 106, 110–113] and 5 journal papers [42, 114–118] submitted mostly to top-tier indexed journals. Additionally, 8 additional papers have been published as co-author [68, 69, 95, 96, 119–122]. The details of these publications and other contributions to papers related to multilevel converters are listed in Chapter 10.

9.3 Future Work

The following are some interesting topics in which further research can be undertaken to extend the scope of this project:

- The dimensioning procedure of the experimental prototype could be enhanced by reducing the size of the capacitor to an optimal value calculated by trading-off the application requirements and operational set-points. For operation only in LFM, the capacitance of the M^3C could be reduced approximately 50%.

- The circulating current control system could be enhanced by incorporating a more complex control structure. For instance, circulating currents could be regulated using multi-resonant controllers.

- The Vector CCV Control Strategy can be extended to operates in three sub-modes:

    Using the Fully-controllable terms of the CCV, as proposed in Chapter 4.

    Using the Semi-controllable terms of the CCV, similar to the Scalar CCV Control Strategy, but applying closed-loop regulation.

    Imposing equal-frequency and complementary power factor operation.

- An optimal mix of the three options mentioned above to operate in EFM can be obtained. In this manner, the injection of either circulating currents or common-mode voltage can be minimised.

- The proposed nested Vector CCV Control Strategy can be adapted to operate the M^3C as a motor drive. Accordingly, the analysis of its performance to drive induction and synchronous machines is interesting.

CHAPTER 10

Publications

10.1 Papers related to this Ph.D. project

10.1.1 Journal Papers

1. **M. Diaz**, R. Cardenas, M. Espinoza, F. Rojas, A. Mora, P. Wheeler, and J. Clare, "Control of Wind Energy Conversion Systems Based on the Modular Multilevel Matrix Converter," IEEE Trans. Ind. Electron, Nov. 2017. Q1

2. R. Cardenas, **M. Diaz**, F. Rojas, J. Clare and P. Wheeler, "Resonant Control System for Low-Voltage Ride-Through in Wind Energy Conversion Systems," IET Power Electron., vol. 9, no. 6, pp. 1–16, May 2016. Q1

3. R. Cardenas, **M. Diaz**, F. Rojas, and J. Clare, "Fast Convergence Delayed Signal Cancellation Method for Sequence Component Separation," in IEEE Transactions on Power Delivery, vol. 30, no. 4, pp. 2055-2057, Aug. 2015. Q1

4. **M. Diaz** and R. Cárdenas-Dobson, "Dual current control strategy to fulfill LVRT requirements in WECS," Int. J. Comput. Math. Electr. Electron. Eng., vol. 33, no. 5, pp. 1665–1677, Aug. 2014. Q4

5. **M. Diaz**, R. Cárdenas, F. Rojas, and J. Clare, "3-Phase 4-wire matrix converter-based voltage sag/swell generator to test low-voltage ride through in wind energy conversion systems," IET Power Electron., vol. 7, no. 12, pp. 3116–3125, Dec. 2014. Q1

10.1.2 Conference Papers

6. **M. Diaz,** M. Espinoza, F. Rojas, P. Wheeler, R. Cárdenas, "Vector Control Strategies to enable equal input-output frequencies operation of the Modular Multilevel Matrix Converter", submitted to the 9th International Conference on Power Electronics, Machines and Drives, PEMD 2018.

7. **M. Diaz**, M. Espinoza, F. Rojas, A. Mora, P. Wheeler, R. Cárdenas, "Closed Loop Vector Control of the Modular Multilevel Matrix Converter for equal frequency operation", 3rd IEEE Southern Power Electronics Conference (SPEC), Puerto Varas, Chile 2017.

8. **M. Diaz**, R. Cárdenas, M. Espinoza, A. Mora, and P. Wheeler, "Modelling and control of the Modular Multilevel Matrix Converter and its application to Wind Energy Conversion Systems," IECON 2016 - 42nd Annual Conference of the IEEE Industrial Electronics Society, Florence, 2016, pp. 5052-5057.

9. **M. Diaz**, M. Espinoza, A. Mora, R. Cardenas, and P. Wheeler, "The application of the modular multilevel matrix converter in high-power wind turbines," 2016 18th European Conference on Power Electronics and Applications (EPE'16 ECCE Europe), Karlsruhe, 2016, pp. 1-11.

10. **M. Diaz**, R. Cárdenas, B. Mauricio Espinoza, A. Mora, and F. Rojas, "A novel LVRT control strategy for Modular Multilevel Matrix Converter based high-power Wind Energy Conversion Systems," 2015 Tenth International Conference on Ecological Vehicles and Renewable Energies (EVER), Monte Carlo, 2015, pp. 1-11.

11. **M. Diaz** and R. Cardenas, "Analysis of synchronous and stationary reference frame control strategies to fulfill LVRT requirements in Wind Energy Conversion Systems," 2014 Ninth International Conference on Ecological Vehicles and Renewable Energies (EVER), Monte-Carlo, 2014, pp. 1-8.

12. **M. Diaz**, R. Cardenas, and G. Soto, "4-wire Matrix Converter based voltage sag/swell generator to test LVRT in renewable energy systems," 2014 Ninth International Conference on Ecological Vehicles and Renewable Energies (EVER), Monte-Carlo, 2014, pp. 1-10.

13. **M. Diaz** and R. Cardenas, "The application of resonant controller to fulfill LVRT requirements in grid connected VSI," 2013 Eighth International Conference and Exhibition on Ecological Vehicles and Renewable Energies (EVER), Monte Carlo, 2013, pp. 1-8.

14. **M. Diaz** and R. Cardenas, "Matrix converter based Voltage Sag Generator to test LVRT capability in renewable energy systems," 2013 Eighth International Conference and Exhibition on Ecological Vehicles and Renewable Energies (EVER), Monte Carlo, 2013, pp. 1-7.

10.2 Participation in other publications

10.2.1 Journal Papers

15. Espinoza, R. Cardenas, **M. Diaz**, and J. Clare, "An Enhanced $\mathrm{d}q$-Based Vector Control System for Modular Multilevel Converters Feeding Variable-Speed Drives," in IEEE Transactions on Industrial Electronics, vol. 64, no. 4, pp. 2620-2630, April 2017. Q1

16. F. Rojas, R. Kennel, R. Cardenas, R. Repenning, J. C. Clare, and **M. Diaz**, "A New Space-Vector-Modulation Algorithm for a Three-Level Four-Leg NPC Inverter," IEEE Trans. Energy Convers., vol. 32, no. 1, pp. 23–35, Mar. 2017. Q1

17. F. Rojas, R. Cardenas-Dobson, R. Kennel, J. Clare, and **M. Diaz**, "A Simplified Space Vector Modulation Algorithm for Four-Leg NPC Converters IEEE Transactions on Power Electronics," vol. 32, no. 11, pp. 8371-8380, Nov. 2017. Q1

10.2.2 Conference Papers

18. A. Mora, R. Cárdenas, M. Espinoza, **M. Díaz**, "Active power oscillation elimination in 4-leg grid-connected converters under unbalanced network conditions," IECON 2016 - 42nd Annual Conference of the IEEE Industrial Electronics Society, Florence, 2016, pp. 2229-2234.

19. M. Espinoza, R. Cardenas, **M. Diaz**, A. Mora, and D. Soto, "Modelling and control of the modular multilevel converter in back to back configuration for high power induction machine drives," in IECON 2016 - 42nd Annual Conference of the IEEE Industrial Electronics Society, 2016, pp. 5046–5051.

20. M. Espinoza, E. Espina, **M. Diaz**, A. Mora, R. Cárdenas, "Improved control strategy of the modular multilevel converter for high power drive applications in low frequency operation," 2016 18th European Conference on Power Electronics and Applications (EPE'16 ECCE Europe), Karlsruhe, 2016, pp. 1-10.

21. A. Mora, M. Espinoza, **M. Diaz**, and R. Cardenas, "Model Predictive Control of Modular Multilevel Matrix Converter," in 2015 IEEE 24th International Symposium on Industrial Electronics (ISIE), 2015, pp. 1074–1079.

22. M. Espinoza, A. Mora, **M. Diaz**, and R. Cardenas, "Balancing energy and low frequency operation of the Modular Multilevel Converter in Back to Back configuration," 2015 Tenth International Conference on Ecological Vehicles and Renewable Energies (EVER), Monte Carlo, 2015, pp. 1-9.

Bibliography

[1] C. B. Field, V. R. Barros, G. Dabelko, G. Hovelsrud, M. Levy, U. Oswald Spring, and C. Vogel, *Climate change 2014 : impacts, adaptation, and vulnerability Climate Change*, 2014.

[2] International Energy Agency, "World Energy Outlook 2016," Tech. Rep., 2016. [Online]. Available: https://www.iea.org/newsroom/news/2016/november/world-energy-outlook-2016.html

[3] A. Whiteman, T. Rinke, J. Esparrago, and S. Elsayed, "Renewable Capacity Statistics 2016," Tech. Rep., 2016. [Online]. Available: www.irena.org

[4] Global Wind Energy Council, "Global Wind Statisitcs 2015. GWEC," Tech. Rep. 9, 2015. [Online]. Available: http://www.gwec.net/wp-content/uploads/vip/GWEC-PRstats-2015{_}LR.pdf

[5] ——, "Global Wind Report Annual Market Update 2015," Tech. Rep., 2015. [Online]. Available: http://www.gwec.net/wp-content/uploads/vip/GWEC-Global-Wind-2015-Report{_}April-2016{_}22{_}04.pdf

[6] N. Fichaux, J. Beurskens, P. H. Jensen, and J. Wilkes, "Design limits and solutions for very large wind turbines: A 20 MW turbine is feasible," Tech. Rep. March, 2011.

[7] The European Wind Energy Association, "Aiming High Rewarding Ambition in Wind Energy," Tech. Rep.

[8] M. Liserre, R. Cardenas, M. Molinas, J. Rodriguez, R. Cárdenas, M. Molinas, J. Rodríguez, R. Cardenas, M. Molinas, and J. Rodriguez, "Overview of Multi-MW Wind Turbines and Wind Parks," *IEEE Trans. Ind. Electron.*, vol. 58, no. 4, pp. 1081–1095, apr 2011. [Online]. Available: http://ieeexplore.ieee.org/lpdocs/epic03/wrapper.htm?arnumber=5680636

[9] V. Yaramasu, B. Wu, P. C. Sen, S. Kouro, and M. Narimani, "High-power wind energy conversion systems: State-of-the-art and emerging technologies," *Proc. IEEE*, vol. 103, no. 5, pp. 740–788, 2015.

[10] The Wind Power - Wind Energy Market Intelligence, "Manufacturers and tur-
bines - The Wind Power." [Online]. Available: http://www.thewindpower.net/
turbines{_}manufacturers{_}en.php

[11] "Sway Turbine | Game changing Light weight Wind turbine." [Online]. Available:
http://www.swayturbine.no/

[12] "AMSC Wind Turbine Design Portfolio." [Online]. Available: http://www.amsc.com/
windtec/turbine{_}designs-licenses.html

[13] The European Wind Energy Association, "UpWind: Design limits and solutions
for very large wind turbines," Tech. Rep. 3, 2016. [Online]. Available: http:
//www.ewea.org/publications/reports/upwind/

[14] W. Erdman and M. Behnke, "Low Wind Speed Turbine Project Phase II : The Application
of Medium-Voltage Electrical Apparatus to the Class of Variable Speed Multi-Megawatt
Low Wind Speed Turbines Low Wind Speed Turbine Project Phase II : The Application
of Medium-Voltage Electrical A," no. November, p. 119, 2005. [Online]. Available:
http://www.osti.gov/energycitations/product.biblio.jsp?osti{_}id=861052

[15] V. Yaramasu and B. Wu, "Predictive control of a three-level boost converter and an NPC
inverter for high-power PMSG-based medium voltage wind energy conversion systems,"
IEEE Trans. Power Electron., vol. 29, no. 10, pp. 5308–5322, oct 2014. [Online]. Available:
http://ieeexplore.ieee.org/document/6671482/

[16] S. Alepuz, A. Calle, S. Busquets-Monge, S. Kouro, and B. Wu, "Use of stored energy
in PMSG rotor inertia for low-voltage ride-through in back-to-back NPC converter-based
wind power systems," *IEEE Trans. Ind. Electron.*, vol. 60, no. 5, pp. 1787–1796, may
2013. [Online]. Available: http://ieeexplore.ieee.org/lpdocs/epic03/wrapper.htm?arnumber=
6169988

[17] S. Alepuz, S. Busquets-Monge, J. Bordonau, P. Cortes, and S. Kouro, "Control
methods for Low Voltage Ride-Through compliance in grid-connected NPC converter
based wind power systems using predictive control," in *2009 IEEE Energy Convers.
Congr. Expo.*, no. 1. IEEE, sep 2009, pp. 363–369. [Online]. Available: http:
//ieeexplore.ieee.org/lpdocs/epic03/wrapper.htm?arnumber=5316139

[18] I. Erlich, F. Shewarega, C. Feltes, F. W. Koch, and J. Fortmann, "Offshore wind power
generation technologies," *Proc. IEEE*, vol. 101, no. 4, pp. 891–905, 2013.

[19] C. Ng, M. Parker, P. Tavner, J. Bumby, and E. Spooner, "A Multilevel Modular
Converter for a Large, Light Weight Wind Turbine Generator," *IEEE Trans. Power
Electron.*, vol. 23, no. 3, pp. 1062–1074, may 2008. [Online]. Available: http:
//ieeexplore.ieee.org/lpdocs/epic03/wrapper.htm?arnumber=4494751

[20] S. Debnath and M. Saeedifard, "A new hybrid modular multilevel converter for grid
connection of large wind turbines," *IEEE Trans. Sustain. Energy*, vol. 4, no. 4, pp.
1051–1064, oct 2013. [Online]. Available: http://ieeexplore.ieee.org/lpdocs/epic03/wrapper.
htm?arnumber=6550897

[21] S. S. Gjerde and T. M. Undeland, "A modular series connected converter for a 10 MW, 36 kV, transformer-less offshore wind power generator drive," *Energy Procedia*, vol. 24, no. January, pp. 68–75, 2012.

[22] A. Lesnicar and R. Marquardt, "An innovative modular multilevel converter topology suitable for a wide power range," in *2003 IEEE Bol. PowerTech - Conf. Proc.*, vol. 3. IEEE, 2003, pp. 272–277. [Online]. Available: http://ieeexplore.ieee.org/lpdocs/epic03/wrapper.htm?arnumber=1304403

[23] R. Marquardt, "Modular Multilevel Converter: An universal concept for HVDC-Networks and extended DC-bus-applications," in *2010 Int. Power Electron. Conf. - ECCE Asia -, IPEC 2010*. IEEE, jun 2010, pp. 502–507. [Online]. Available: http://ieeexplore.ieee.org/lpdocs/epic03/wrapper.htm?arnumber=5544594

[24] M. Saeedifard and R. Iravani, "Dynamic performance of a modular multilevel back-to-back HVDC system," *IEEE Trans. Power Deliv.*, vol. 25, no. 4, pp. 2903–2912, oct 2010. [Online]. Available: http://ieeexplore.ieee.org/lpdocs/epic03/wrapper.htm?arnumber=5565526

[25] M. Glinka and R. Marquardt, "A new AC/AC multilevel converter family," *IEEE Trans. Ind. Electron.*, vol. 52, no. 3, pp. 662–669, jun 2005. [Online]. Available: http://ieeexplore.ieee.org/document/1435677/

[26] H. Akagi, "Classification, terminology, and application of the modular multilevel cascade converter (MMCC)," *IEEE Trans. Power Electron.*, vol. 26, no. 11, pp. 3119–3130, nov 2011. [Online]. Available: http://ieeexplore.ieee.org/lpdocs/epic03/wrapper.htm?arnumber=5751701

[27] N. C. F. Iov, A. Hansen, P. Sørensen, F. Iov, A. D. Hansen, P. Sørensen, and N. A. Cutululis, "Mapping of grid faults and grid codes," *Wind Energy*, vol. 1617, no. July, pp. 1–41, 2007.

[28] Z. Chen, J. M. Guerrero, and F. Blaabjerg, "A review of the state of the art of power electronics for wind turbines," *IEEE Trans. Power Electron.*, vol. 24, no. 8, pp. 1859–1875, aug 2009. [Online]. Available: http://ieeexplore.ieee.org/document/5200696/

[29] R. Pena, R. Cardenas, and G. Asher, "Overview of control systems for the operation of DFIGs in wind energy applications," *IECON Proc. (Industrial Electron. Conf.*, vol. 60, no. 7, pp. 88–95, jul 2013. [Online]. Available: http://ieeexplore.ieee.org/document/6423899/

[30] D. J. Trudnowski, A. Gentile, J. M. Khan, and E. M. Petritz, "Fixed-speed wind-generator and wind-park modeling for transient stability studies," *IEEE Trans. Power Syst.*, vol. 19, no. 4, pp. 1911–1917, nov 2004. [Online]. Available: http://ieeexplore.ieee.org/document/1350830/

[31] A. D. Hansen, F. Iov, F. Blaabjerg, and L. H. Hansen, "Review of Contemporary Wind Turbine Concepts and their Market Penetration," *Wind Eng.*, vol. 28, no. 3, pp. 247–263, 2009. [Online]. Available: http://www.cerien.upc.edu/jornades/jiie2005/ponencies/powerelectronicsasefficientinterfaceindispersedpowergenerationsystempaper.pdf

[32] M. J. Hossain, H. R. Pota, V. A. Ugrinovskii, and R. A. Ramos, "Simultaneous STATCOM

and pitch angle control for improved LVRT capability of fixed-speed wind turbines," *IEEE Trans. Sustain. Energy*, vol. 1, no. 3, pp. 142–151, oct 2010. [Online]. Available: http://ieeexplore.ieee.org/document/5492220/

[33] "The Wind Power - Manufacturers and Turbines Database." [Online]. Available: http://www.thewindpower.net/turbines{_}manufacturers{_}en.php

[34] T. Thiringer, "Grid-friendly connecting of constant-speed wind turbines using external resistors," *IEEE Trans. Energy Convers.*, vol. 17, no. 4, pp. 537–542, dec 2002. [Online]. Available: http://ieeexplore.ieee.org/document/1159206/

[35] M. R. Khadraoui and M. Elleuch, "Comparison between OptiSlip and Fixed Speed wind energy conversion systems," in *2008 5th Int. Multi-Conference Syst. Signals Devices*. IEEE, jul 2008, pp. 1–6. [Online]. Available: http://ieeexplore.ieee.org/document/4632796/

[36] R. Pena, J. Clare, and G. Asher, "Doubly fed induction generator using back-to-back PWM converters and its application to variable-speed wind-energy generation," *IEE Proc. - Electr. Power Appl.*, vol. 143, no. 3, p. 231, 1996. [Online]. Available: http://digital-library.theiet.org/content/journals/10.1049/ip-epa{_}19960288

[37] R. Datta and V. T. Ranganathan, "Variable-speed wind power generation using doubly fed wound rotor induction machine - A comparison with alternative schemes," *IEEE Trans. Energy Convers.*, vol. 17, no. 3, pp. 414–421, sep 2002. [Online]. Available: http://ieeexplore.ieee.org/document/1033974/

[38] M. Jamil, R. Gupta, and M. Singh, "A review of power converter topology used with PMSG based wind power generation," in *2012 IEEE Fifth Power India Conf.* IEEE, dec 2012, pp. 1–6. [Online]. Available: http://ieeexplore.ieee.org/lpdocs/epic03/wrapper.htm?arnumber= 6479549

[39] M. Chinchilla, S. Arnaltes, and J. C. Burgos, "Control of permanent-magnet generators applied to variable-speed wind-energy systems connected to the grid," *IEEE Trans. Energy Convers.*, vol. 21, no. 1, pp. 130–135, mar 2006. [Online]. Available: http://ieeexplore.ieee.org/lpdocs/epic03/wrapper.htm?arnumber=1597329

[40] A. Hansen and G. Michalke, "Multi-pole permanent magnet synchronous generator wind turbines grid support capability in uninterrupted operation during grid faults," *IET Renew. Power Gener.*, vol. 3, no. 3, p. 333, 2009. [Online]. Available: http://digital-library.theiet.org/content/journals/10.1049/iet-rpg.2008.0055

[41] R. Cardenas, M. Diaz, F. Rojas, J. Clare, and P. Wheeler, "Resonant Control System for Low-Voltage Ride-Through in Wind Energy Conversion Systems," *IET Power Electron.*, vol. 9, no. 6, pp. 1–16, may 2016. [Online]. Available: http: //digital-library.theiet.org/content/journals/10.1049/iet-pel.2015.0488

[42] M. Diaz and R. Cardenas, "Analysis of synchronous and stationary reference frame control strategies to fulfill LVRT requirements in Wind Energy Conversion Systems," in *2014 9th Int. Conf. Ecol. Veh. Renew. Energies, EVER 2014.* IEEE, mar 2014, pp. 1–8. [Online]. Available: http://ieeexplore.ieee.org/articleDetails.jsp?arnumber=6844121

[43] K.-H. Kim, Y.-C. Jeung, D.-C. Lee, and H.-G. Kim, "LVRT Scheme of PMSG Wind Power Systems Based on Feedback Linearization," *IEEE Trans. Power Electron.*, vol. 27, no. 5, pp. 2376–2384, may 2012. [Online]. Available: http://ieeexplore.ieee.org/lpdocs/epic03/wrapper.htm?arnumber=6045345

[44] M. Altin, Ö. Göksu, R. Teodorescu, P. Rodriguez, B. B. Jensen, and L. Helle, "Overview of recent grid codes for wind power integration," in *Proc. Int. Conf. Optim. Electr. Electron. Equipment, OPTIM*, vol. 58. IEEE, may 2010, pp. 1152–1160. [Online]. Available: http://ieeexplore.ieee.org/lpdocs/epic03/wrapper.htm?arnumber=5510521

[45] M. H. Bollen, *Understanding Power Quality Problems: Voltage Sags and Interruptions*, 2001, no. IEEE Press Series on Power Engineering. [Online]. Available: http://ieeexplore.ieee.org/xpl/bkabstractplus.jsp?bkn=5270869

[46] M. H. J. Bollen and I. Y. Gu, *SIGNAL PROCESSING OF POWER QUALITY DISTURBANCES*. Hoboken, NJ, USA: John Wiley & Sons, Inc., 2006. [Online]. Available: http://doi.wiley.com/10.1002/9780471931317.fmatter

[47] P. Li, W. Hu, and Z. Chen, "Review on Integrated-Control Method of Variable Speed Wind Turbines Participation in Primary and Secondary Frequency," in *IECON 2016 - 42nd Annu. Conf. IEEE Ind. Electron. Soc.* IEEE, oct 2016, pp. 0–5. [Online]. Available: http://ieeexplore.ieee.org/document/7794127/

[48] J. Van De Vyver, J. D. M. De Kooning, B. Meersman, L. Vandevelde, and T. L. Vandoorn, "Droop Control as an Alternative Inertial Response Strategy for the Synthetic Inertia on Wind Turbines," *IEEE Trans. Power Syst.*, vol. 31, no. 2, pp. 1129–1138, mar 2016. [Online]. Available: http://ieeexplore.ieee.org/document/7104170/

[49] M. F. M. Arani and Y. A. R. I. Mohamed, "Analysis and impacts of implementing droop control in dfig-based wind turbines on microgrid/Weak-grid stability," *IEEE Trans. Power Syst.*, vol. 30, no. 1, pp. 385–396, jan 2015. [Online]. Available: http://ieeexplore.ieee.org/document/6820794/

[50] C. K. Vartanian, N. Bentley, and R. Foster, "Application of advanced battery energy storage systems for wind integration," in *2012 IEEE Power Energy Soc. Gen. Meet.* IEEE, jul 2012, pp. 1–4. [Online]. Available: http://ieeexplore.ieee.org/lpdocs/epic03/wrapper.htm?arnumber=6345476

[51] C. Abbey and G. Joos, "Supercapacitor energy storage for wind energy applications," *IEEE Trans. Ind. Appl.*, vol. 43, no. 3, pp. 769–776, 2007. [Online]. Available: http://ieeexplore.ieee.org/document/4214991/

[52] R. Cárdenas, R. Peña, G. M. Asher, J. Clare, and R. Blasco-Giménez, "Control strategies for power smoothing using a flywheel driven by a sensorless vector-controlled induction machine operating in a wide speed range," *IEEE Trans. Ind. Electron.*, vol. 51, no. 3, pp. 603–614, jun 2004. [Online]. Available: http://ieeexplore.ieee.org/document/1302337/

[53] R. Cárdenas, R. Peña, G. Asher, and J. Clare, "Power smoothing in wind generation systems using a sensorless vector controlled induction machine driving a flywheel," *IEEE*

Trans. Energy Convers., vol. 19, no. 1, pp. 206–216, mar 2004. [Online]. Available: http://ieeexplore.ieee.org/document/1268138/

[54] N. Thitichaiworakorn, M. Hagiwara, and H. Akagi, "A Medium-Voltage Large Wind Turbine Generation System Using an AC/AC Modular Multilevel Cascade Converter," *IEEE J. Emerg. Sel. Top. Power Electron.*, vol. 4, no. 2, pp. 534–546, jun 2016. [Online]. Available: http://ieeexplore.ieee.org/document/7169511/

[55] S. Kouro, M. Malinowski, K. Gopakumar, J. Pou, L. G. Franquelo, B. Wu, J. Rodriguez, M. A. Perez, and J. I. Leon, "Recent advances and industrial applications of multilevel converters," *IEEE Trans. Ind. Electron.*, vol. 57, no. 8, pp. 2553–2580, aug 2010. [Online]. Available: http://ieeexplore.ieee.org/lpdocs/epic03/wrapper.htm?arnumber=5482117

[56] R.-D. Klug and N. Klaassen, "High power medium voltage drives-innovations, portfolio, trends," in *Power Electron. Appl. 2005 Eur. Conf.* IEEE, 2005, pp. 10–pp. [Online]. Available: http://ieeexplore.ieee.org/document/1665859/

[57] R. José, L. G. Franquelo, K. Samir, J. I. León, R. C. Portillo, M. Á. M. Prats, and M. A. Pérez, "Multilevel converters: An enabling technology for high-poer applications," *Proc. IEEE*, vol. 97, no. 11, pp. 1786–1817, nov 2009. [Online]. Available: http://ieeexplore.ieee.org/document/5290111/

[58] J. Dixon, L. Moran, J. Rodriguez, and R. Domke, "Reactive power compensation technologies: State-of-the-art review," *Proc. IEEE*, vol. 93, no. 12, pp. 2144–2164, dec 2005. [Online]. Available: http://ieeexplore.ieee.org/lpdocs/epic03/wrapper.htm?arnumber= 1545768{%}5Cnhttp://ieeexplore.ieee.org/xpls/abs{_}all.jsp?arnumber=1545768

[59] M. Calais, V. G. Agelidis, L. J. Borle, and M. S. Dymond, "Transformerless five level cascaded inverter based single phase photovoltaic system," in *PESC Rec. - IEEE Annu. Power Electron. Spec. Conf.*, vol. 3. IEEE, 2000, pp. 1173–1178. [Online]. Available: http://ieeexplore.ieee.org/lpdocs/epic03/wrapper.htm?arnumber=880477

[60] M. Winkelnkemper, A. Korn, and P. Steimer, "A modular direct converter for transformerless rail interties," in *IEEE Int. Symp. Ind. Electron.* IEEE, jul 2010, pp. 562–567. [Online]. Available: http://ieeexplore.ieee.org/document/5637826/

[61] M. Narimani, B. Wu, Z. Cheng, and N. R. Zargari, "A new nested neutral point-clamped (NNPC) converter for medium-voltage (MV) power conversion," *IEEE Trans. Power Electron.*, vol. 29, no. 12, pp. 6375–6382, dec 2014. [Online]. Available: http://ieeexplore.ieee.org/lpdocs/epic03/wrapper.htm?arnumber=6740051

[62] T. M. Iversen, S. S. Gjerde, and T. Undeland, "Multilevel converters for a 10 MW, 100 kV transformer-less offshore wind generator system," in *2013 15th Eur. Conf. Power Electron. Appl. EPE 2013*. IEEE, sep 2013, pp. 1–10. [Online]. Available: http://ieeexplore.ieee.org/document/6634753/

[63] T. Nakanishi, K. Orikawa, and J.-i. Itoh, "Modular Multilevel Converter for wind power generation system connected to micro-grid," in *2014 Int. Conf. Renew. Energy Res. Appl.* IEEE, oct 2014, pp. 653–658. [Online]. Avail-

able: http://www.scopus.com/inward/record.url?eid=2-s2.0-84925390121{&}partnerID=
tZOtx3y1http://ieeexplore.ieee.org/document/7016466/

[64] A. Lesnicar and R. Marquardt, "A new modular voltage source inverter topology," in *Proc. 10th Eur. Conf. Power Electron. Appl. EPE 2003*, 2003.

[65] J. D. Ainsworth, M. Davies, P. J. Fitz, K. E. Owen, and D. R. Trainer, "Static VAr compensator (STATCOM) based on single-phase chain circuit converters," *IEE Proceedings-Generation, Transm. Distrib.*, vol. 145, no. 4, pp. 381–386, 1998. [Online]. Available: http://ieeexplore.ieee.org/ielx4/2195/15290/00707083.pdf?tp={&}arnumber=707083{&}isnumber=15290

[66] P. W. Hammond, "A new approach to enhance power quality for medium voltage AC drives," *Ind. Appl. IEEE Trans.*, vol. 33, no. 1, pp. 202–208, 1997. [Online]. Available: http://ieeexplore.ieee.org/lpdocs/epic03/wrapper.htm?arnumber=567113

[67] M. Davies, M. Dommaschk, J. Dorn, J. Lang, D. Retzmann, and D. So-erangr, "HVDC PLUS – Basics and Principle of Operation," Tech. Rep. [On-line]. Available: http://www.energy.siemens.com/us/pool/hq/power-transmission/HVDC/HVDC{_}Plus{_}BasicandPrincipals.pdf

[68] M. Espinoza, R. Cardenas, M. Diaz, and J. Clare, "An Enhanced dq-Based Vector Control System for Modular Multilevel Converters Feeding Variable Speed Drives," *IEEE Trans. Ind. Electron.*, no. November, pp. 1–1, 2016. [Online]. Available: http://ieeexplore.ieee.org/document/7781663/

[69] B. Mauricio Espinoza, A. Mora, M. Diaz, and R. Cárdenas, "Balancing energy and low frequency operation of the modular multilevel converter in back to back configuration," in *2015 10th Int. Conf. Ecol. Veh. Renew. Energies, EVER 2015*. IEEE, mar 2015, pp. 1–9. [Online]. Available: http://ieeexplore.ieee.org/document/7113005/http://ieeexplore.ieee.org/articleDetails.jsp?arnumber=7113005

[70] P. Khamphakdi, K. Sekiguchi, M. Hagiwara, and H. Akagi, "A transformerless back-to-back (BTB) system using modular multilevel cascade converters for power distribution systems," *IEEE Trans. Power Electron.*, vol. 30, no. 4, pp. 1866–1875, apr 2015. [Online]. Available: http://ieeexplore.ieee.org/document/6824816/

[71] H. Polinder, D. Bang, R. van Rooij, A. McDonald, and M. Mueller, "10 MW Wind Turbine Direct-Drive Generator Design with Pitch or Active Speed Stall Control," in *2007 IEEE Int. Electr. Mach. Drives Conf.* IEEE, 2007, pp. 1390–1395. [Online]. Available: http://ieeexplore.ieee.org/document/4270852/

[72] L. Baruschka and A. Mertens, "A new three-phase AC/AC modular multilevel converter with six branches in hexagonal configuration," *IEEE Trans. Ind. Appl.*, vol. 49, no. 3, pp. 1400–1410, may 2013. [Online]. Available: http://ieeexplore.ieee.org/document/6479302/

[73] D. Karwatzki, L. Baruschka, and A. Mertens, "Survey on the Hexverter topology - A modular multilevel AC/AC converter," in *9th Int. Conf. Power Electron. - ECCE Asia "Green World with Power Electron. ICPE 2015-ECCE Asia*. IEEE, jun 2015, pp.

1075–1082. [Online]. Available: http://ieeexplore.ieee.org/document/7167914/

[74] J. Kucka, D. Karwatzki, and A. Mertens, "AC/AC modular multilevel converters in wind energy applications: Design considerations," in *2016 18th Eur. Conf. Power Electron. Appl. (EPE'16 ECCE Eur.* IEEE, sep 2016, pp. 1–10. [Online]. Available: http://ieeexplore.ieee.org/document/7695542/

[75] R. Erickson and O. Al-Naseem, "A new family of matrix converters," in *IECON'01. 27th Annu. Conf. IEEE Ind. Electron. Soc. (Cat. No.37243)*, vol. 2, no. Xcx. IEEE, 2001, pp. 1515–1520. [Online]. Available: http://ieeexplore.ieee.org/document/976015/

[76] R. Erickson, S. Angkititrakul, and K. Almazeedi, "A New Family of Multilevel Matrix Converters for Wind Power Applications: Final Report," University of Colorado, Tech. Rep. December, 2006. [Online]. Available: http://www.nrel.gov/wind/pdfs/40051.pdf

[77] F. Kammerer, J. Kolb, and M. Braun, "Fully decoupled current control and energy balancing of the Modular Multilevel Matrix Converter," in *15th Int. Power Electron. Motion Control Conf. Expo. EPE-PEMC 2012 ECCE Eur.* IEEE, sep 2012, pp. LS2a.3–1–LS2a.3–8. [Online]. Available: http://ieeexplore.ieee.org/lpdocs/epic03/wrapper. htm?arnumber=6397408

[78] W. Kawamura, M. Hagiwara, and H. Akagi, "Control and experiment of a modular multilevel cascade converter based on triple-star bridge cells," *IEEE Trans. Ind. Appl.*, vol. 50, no. 5, pp. 3536–3548, sep 2014. [Online]. Available: http://ieeexplore.ieee.org/lpdocs/epic03/wrapper.htm?arnumber=6767095

[79] T. Nakamori, M. A. Sayed, Y. Hayashi, T. Takeshita, S. Hamada, and K. Hirao, "Independent Control of Input Current, Output Voltage, and Capacitor Voltage Balancing for a Modular Matrix Converter," *IEEE Trans. Ind. Appl.*, vol. 51, no. 6, pp. 4623–4633, nov 2015. [Online]. Available: http://ieeexplore.ieee.org/document/7155537/

[80] W. Kawamura, Y. Chiba, and H. Akagi, "A broad range of speed control of a permanent magnet synchronous motor driven by a modular multilevel TSBC converter," in *2016 IEEE Energy Convers. Congr. Expo.*, 2016, pp. 1–6. [Online]. Available: http://ieeexplore.ieee.org/document/7854652/

[81] Y. Miura, T. Mizutani, M. Ito, and T. Ise, "Modular multilevel matrix converter for low frequency AC transmission," in *2013 IEEE 10th Int. Conf. Power Electron. Drive Syst.* IEEE, apr 2013, pp. 1079–1084. [Online]. Available: http://ieeexplore.ieee.org/lpdocs/epic03/wrapper.htm?arnumber=6527180

[82] B. Fan, K. Wang, C. Gu, P. Wheeler, and Y. Li, "A branch current reallocation based energy balancing strategy for the Modular multilevel matrix converter operating around equal frequency," *IECON Proc. (Industrial Electron. Conf.*, pp. 3111–3116, 2016. [Online]. Available: http://ieeexplore.ieee.org/document/7883960/

[83] D. Soto and J. Borquez, "Control of a modular multilevel matrix converter for high power applications," *Stud. Informatics Control*, vol. 21, no. 1, pp. 85–92, mar 2012. [Online]. Available: http://sic.ici.ro/?page{_}id=1435https://sic.ici.ro/

control-of-a-modular-multilevel-matrix-converter-for-high-power-applications/

[84] Y. Hayashi, T. Takeshita, M. Muneshima, and Y. Tadano, "Independent control of input current and output voltage for Modular Matrix Converter," in *Ind. Electron. Soc. IECON 2013 - 39th Annu. Conf. IEEE*, vol. 51, no. 6.   IEEE, nov 2013, pp. 888–893. [Online]. Available: http://ieeexplore.ieee.org/lpdocs/epic03/wrapper.htm?arnumber=6699251

[85] A. Korn, M. Winkelnkemper, P. Steimer, and J. Kolar, "Direct modular multi-level converter for gearless low-speed drives," in *Power Electron. Appl. (EPE 2011), Proc. 2011-14th Eur. Conf.*, no. direct MMC, 2011, pp. 1–7.

[86] D. Arancibia, M. A. Perez, and J. Rodriguez, "Decoupled control of a three-phase to three-phase modular multilevel matrix converter," in *2013 IEEE Energy Convers. Congr. Expo. ECCE 2013*.   IEEE, sep 2013, pp. 404–408. [Online]. Available: http://ieeexplore.ieee.org/document/6646729/

[87] F. Kammerer, J. Kolb, and M. Braun, "A novel cascaded vector control scheme for the Modular Multilevel Matrix Converter," in *IECON Proc. (Industrial Electron. Conf.*   IEEE, nov 2011, pp. 1097–1102. [Online]. Available: http://ieeexplore.ieee.org/lpdocs/epic03/wrapper.htm?arnumber=6119461

[88] F. Kammerer, M. Gommeringer, J. Kolb, and M. Braun, "Energy balancing of the Modular Multilevel Matrix Converter based on a new transformed arm power analysis," in *2014 16th Eur. Conf. Power Electron. Appl. EPE-ECCE Eur. 2014*.   IEEE, aug 2014, pp. 1–10. [Online]. Available: http://ieeexplore.ieee.org/document/6910939/

[89] H. Akagi, S. Inoue, and T. Yoshii, "Control and Performance of a Transformerless Cascade PWM STATCOM With Star Configuration," *IEEE Trans. Ind. Appl.*, vol. 43, no. 4, pp. 1041–1049, 2007. [Online]. Available: http://ieeexplore.ieee.org/lpdocs/epic03/wrapper.htm?arnumber=4276838

[90] W. Kawamura, M. Hagiwara, and H. Akagi, "A broad range of frequency control for the modular multilevel cascade converter based on triple-star bridge-cells (MMCC-TSBC)," in *2013 IEEE Energy Convers. Congr. Expo. ECCE 2013*.   IEEE, sep 2013, pp. 4014–4021. [Online]. Available: http://ieeexplore.ieee.org/document/6647233/

[91] W. Kawamura, K.-L. Chen, M. Hagiwara, and H. Akagi, "A Low-Speed, High-Torque Motor Drive Using a Modular Multilevel Cascade Converter Based on Triple-Star Bridge Cells (MMCC-TSBC)," *IEEE Trans. Ind. Appl.*, vol. 51, no. 5, pp. 3965–3974, sep 2015. [Online]. Available: http://ieeexplore.ieee.org/document/7065290/

[92] W. Kawamura, Y. Chiba, M. Hagiwara, and H. Akagi, "Experimental Verification of an Electrical Drive Fed by a Modular Multilevel TSBC Converter When the Motor Frequency Gets Closer or Equal to the Supply Frequency," *IEEE Trans. Ind. Appl.*, vol. 53, no. 3, pp. 1–1, may 2017. [Online]. Available: http://ieeexplore.ieee.org/document/7845641/

[93] Y. Okazaki, W. Kawamura, M. Hagiwara, H. Akagi, T. Ishida, M. Tsukakoshi, and R. Nakamura, "Which is more suitable for MMCC-based medium-voltage motor drives, a DSCC inverter or a TSBC converter?" in *9th Int. Conf. Power Electron. - ECCE*

Asia "Green World with Power Electron. ICPE 2015-ECCE Asia. IEEE, jun 2015, pp. 1053–1060. [Online]. Available: http://ieeexplore.ieee.org/document/7167911/

[94] J. Kolb, F. Kammerer, and M. Braun, "Dimensioning and design of a modular multilevel converter for drive applications," in *15th Int. Power Electron. Motion Control Conf. Expo. EPE-PEMC 2012 ECCE Eur.* IEEE, sep 2012, pp. LS1a–1.1–1–LS1a–1.1–8. [Online]. Available: http://ieeexplore.ieee.org/document/6397380/

[95] M. Espinoza, R. Cárdenas, M. Díaz, A. Mora, and D. Soto, "Modelling and control of the modular multilevel converter in back to back configuration for high power induction machine drives," in *IECON Proc. (Industrial Electron. Conf.* IEEE, oct 2016, pp. 5046–5051. [Online]. Available: http://ieeexplore.ieee.org/document/7793979/

[96] M. Espinoza, E. Espina, M. Diaz, A. Mora, and R. Cardenas, "Improved control strategy of the modular multilevel converter for high power drive applications in low frequency operation," in *2016 18th Eur. Conf. Power Electron. Appl. (EPE'16 ECCE Eur.* IEEE, sep 2016, pp. 1–10. [Online]. Available: http://ieeexplore.ieee.org/document/7695557/

[97] M. Diaz and R. Cardenas, "The application of resonant controller to fulfill LVRT requirements in grid connected VSI," in *2013 8th Int. Conf. Exhib. Ecol. Veh. Renew. Energies, EVER 2013.* IEEE, mar 2013, pp. 1–8. [Online]. Available: http://ieeexplore.ieee.org/articleDetails.jsp?arnumber=6521528

[98] S. Alepuz, S. Busquets-Monge, J. Bordonau, J. A. Martinez-Velasco, C. A. C. Silva, J. Pontt, and J. Rodriguez, "Control Strategies Based on Symmetrical Components for Grid-Connected Converters Under Voltage Dips," *IEEE Trans. Ind. Electron.*, vol. 56, no. 6, pp. 2162–2173, jun 2009. [Online]. Available: http://ieeexplore.ieee.org/lpdocs/epic03/wrapper.htm?arnumber=4801749

[99] M. Díaz, R. Cárdenas, B. Mauricio Espinoza, A. Mora, and F. Rojas, "A novel LVRT control strategy for modular multilevel matrix converter based high-power wind energy conversion systems," in *2015 10th Int. Conf. Ecol. Veh. Renew. Energies, EVER 2015.* IEEE, mar 2015, pp. 1–11. [Online]. Available: http://ieeexplore.ieee.org/document/7113026/http://ieeexplore.ieee.org/articleDetails.jsp?arnumber=7113026

[100] M. Díaz and R. Cárdenas-Dobson, "Dual current control strategy to fulfill LVRT requirements in WECS," *COMPEL - Int. J. Comput. Math. Electr. Electron. Eng.*, vol. 33, no. 5, pp. 1665–1677, aug 2014. [Online]. Available: http://www.emeraldinsight.com/doi/abs/10.1108/COMPEL-09-2013-0305

[101] J. Svensson, M. Bongiorno, and A. Sannino, "Practical Implementation of Delayed Signal Cancellation Method for Phase-Sequence Separation," *IEEE Trans. Power Deliv.*, vol. 22, no. 1, pp. 18–26, jan 2007. [Online]. Available: http://ieeexplore.ieee.org/lpdocs/epic03/wrapper.htm?arnumber=4039479

[102] Y. F. Wang and Y. W. Li, "Grid synchronization PLL based on cascaded delayed signal cancellation," *IEEE Trans. Power Electron.*, vol. 26, no. 7, pp. 1987–1997, jul 2011. [Online]. Available: http://ieeexplore.ieee.org/document/5668509/

[103] L. F. A. Pereira, J. V. Flores, G. Bonan, D. F. Coutinho, J. M. Gomes Da Silva, and J. M. G. da Silva, "Multiple resonant controllers for uninterruptible power supplies - A systematic robust control design approach," *IEEE Trans. Ind. Electron.*, vol. 61, no. 3, pp. 1528–1538, mar 2014. [Online]. Available: http://ieeexplore.ieee.org/lpdocs/epic03/wrapper.htm?arnumber=6507601

[104] A. G. Yepes, F. D. Freijedo, J. Doval-Gandoy, O. Lopez, J. Malvar, and P. Fernandez-Comesana, "Effects of discretization methods on the performance of resonant controllers," *IEEE Trans. Power Electron.*, vol. 25, no. 7, pp. 1692–1712, jul 2010. [Online]. Available: http://ieeexplore.ieee.org/lpdocs/epic03/wrapper.htm?arnumber=5398914

[105] R. Cardenas, E. Espina, J. Clare, and P. Wheeler, "Self-tuning resonant control of a seven-leg back-to-back converter for interfacing variable-speed generators to four-wire loads," *IEEE Trans. Ind. Electron.*, vol. 62, no. 7, pp. 4618–4629, 2015. [Online]. Available: http://www.scopus.com/inward/record.url?eid=2-s2.0-84930505651{&}partnerID=tZOtx3y1

[106] R. Cardenas, M. Diaz, F. Rojas, and J. Clare, "Fast Convergence Delayed Signal Cancellation Method for Sequence Component Separation," *IEEE Trans. Power Deliv.*, vol. 30, no. 4, pp. 2055–2057, aug 2015. [Online]. Available: http://ieeexplore.ieee.org/lpdocs/epic03/wrapper.htm?arnumber=6963423

[107] H. Fujita, S. Tominaga, and H. Akagi, "Analysis and design of a DC voltage-controlled static var compensator using quad-series voltage-source inverters," *IEEE Trans. Ind. Appl.*, vol. 32, no. 4, pp. 970–978, 1996. [Online]. Available: http://ieeexplore.ieee.org/document/511656/

[108] F. Kammerer, J. Kolb, and M. Braun, "Optimization of the passive components of the modular multilevel matrix converter for drive applications," in *PCIM Eur. Conf. Proc.* Mesago PCIM GmbH [u.a.], 2012, pp. 702–709. [Online]. Available: https://publikationen.bibliothek.kit.edu/1000031470

[109] B. Li, S. Zhou, D. Xu, R. Yang, D. Xu, C. Buccella, and C. Cecati, "An Improved Circulating Current Injection Method for Modular Multilevel Converters in Variable-Speed Drives," *IEEE Trans. Ind. Electron.*, vol. 63, no. 11, pp. 7215–7225, nov 2016. [Online]. Available: http://ieeexplore.ieee.org/document/7442889/

[110] M. Diaz, R. Cardenas, M. Espinoza, F. Rojas, A. Mora, J. C. Clare, and P. Wheeler, "Control of Wind Energy Conversion Systems Based on the Modular Multilevel Matrix Converter," *IEEE Trans. Ind. Electron.*, pp. 1–1, 2017. [Online]. Available: http://ieeexplore.ieee.org/document/7995125/

[111] M. Díaz, R. Cárdenas, F. Rojas, and J. Clare, "3-Phase 4-wire matrix converter-based voltage sag/swell generator to test low-voltage ride through in wind energy conversion systems," *IET Power Electron.*, vol. 7, no. 12, pp. 3116–3125, dec 2014. [Online]. Available: http://ieeexplore.ieee.org/articleDetails.jsp?arnumber=6983694

[112] M. Diaz, R. Cardenas, and G. Soto, "4-wire Matrix Converter based voltage sag/swell generator to test LVRT in renewable energy systems," in *2014 9th Int. Conf. Ecol. Veh. Renew. Energies, EVER 2014.* IEEE, mar 2014, pp. 1–10. [Online]. Available:

http://ieeexplore.ieee.org/document/6844123/

[113] M. Diaz and R. Cardenas, "Matrix converter based Voltage Sag Generator to test LVRT capability in renewable energy systems," in *2013 8th Int. Conf. Exhib. Ecol. Veh. Renew. Energies, EVER 2013*, 2013.

[114] M. Diaz, R. Cardenas, M. Espinoza, F. Rojas, A. Mora, and P. Wheeler, "Vector Control Strategies to enable equal input-output frequencies operation of the Modular Multilevel Matrix Converter," in *Submitt. to PEMD*, Liverpool, 2018.

[115] M. Diaz, R. Cardenas, M. Espinoza, A. Mora, F. Rojas, and P. Wheeler, "Closed Loop Vector Control of the Modular Multilevel Matrix Converter for equal frequency operation," in *Submitt. to SPEC*, 2017.

[116] M. Diaz, R. Cárdenas, M. Espinoza, A. Mora, and P. Wheeler, "Modelling and Control of the Modular Multilevel Matrix Converter and its application to Wind Energy Conversion Systems," in *IECON 2016 - 42nd Annu. Conf. IEEE Ind. Electron. Soc.*, no. 1140337. IEEE, oct 2016, pp. 0–5. [Online]. Available: http://ieeexplore.ieee.org/document/7793945/

[117] M. Diaz, M. Espinoza, A. Mora, R. Cardenas, and P. Wheeler, "The application of the modular multilevel matrix converter in high-power wind turbines," in *2016 18th Eur. Conf. Power Electron. Appl. (EPE'16 ECCE Eur.* IEEE, sep 2016, pp. 1–11. [Online]. Available: http://ieeexplore.ieee.org/document/7695437/

[118] M. Díaz, R. Cárdenas, B. Mauricio Espinoza, A. Mora, and F. Rojas, "A novel LVRT control strategy for modular multilevel matrix converter based high-power wind energy conversion systems," in *2015 10th Int. Conf. Ecol. Veh. Renew. Energies, EVER 2015*. IEEE, mar 2015, pp. 1–11. [Online]. Available: http://ieeexplore.ieee.org/document/7113026/

[119] F. Rojas, R. Kennel, R. Cardenas, R. Repenning, J. C. Clare, and M. Diaz, "A New Space-Vector-Modulation Algorithm for a Three-Level Four-Leg NPC Inverter," *IEEE Trans. Energy Convers.*, vol. 32, no. 1, pp. 23–35, mar 2017. [Online]. Available: http://ieeexplore.ieee.org/document/7558237/

[120] F. Rojas, R. Cardenas, R. Kennel, J. C. Clare, and M. Diaz, "A Simplified Space-Vector Modulation Algorithm for Four-Leg NPC Converters," *IEEE Trans. Power Electron.*, vol. 32, no. 11, pp. 8371–8380, 2017. [Online]. Available: http://ieeexplore.ieee.org/document/7592426/

[121] A. Mora, R. Cárdenas, M. Espinoza, and M. Díaz, "Active power oscillation elimination in 4-leg grid-connected converters under unbalanced network conditions," in *IECON Proc. (Industrial Electron. Conf.*, 2016, pp. 2229–2234.

[122] A. Mora, M. Espinoza, M. Diaz, and R. Cardenas, "Model Predictive Control of Modular Multilevel Matrix Converter," in *2015 IEEE 24th Int. Symp. Ind. Electron.* IEEE, jun 2015, pp. 1074–1079. [Online]. Available: http://ieeexplore.ieee.org/document/7281621/

APPENDIX A

Double-$\alpha\beta 0$ Transformation of the Voltage-Current Model

The Voltage-Current Model of the M^3C presented in (3.3) can be re-written in separate equations for each Sub-Converter as follows:

- Sub-Converter 1 linking input phases (a, b, c) to output phase r.

$$
\begin{bmatrix} v_{ma} \\ v_{mb} \\ v_{mc} \end{bmatrix} = L_c \frac{\mathrm{d}}{\mathrm{d}t} \begin{bmatrix} i_{ar} \\ i_{br} \\ i_{cr} \end{bmatrix} + \begin{bmatrix} v_{ar} \\ v_{br} \\ v_{cr} \end{bmatrix} + \begin{bmatrix} v_{gr} \\ v_{gr} \\ v_{gr} \end{bmatrix} + \begin{bmatrix} v_n \\ v_n \\ v_n \end{bmatrix} \tag{A.1}
$$

- Sub-Converter 2 linking input phases (a, b, c) to output phase s.

$$
\begin{bmatrix} v_{ma} \\ v_{mb} \\ v_{mc} \end{bmatrix} = L_c \frac{\mathrm{d}}{\mathrm{d}t} \begin{bmatrix} i_{as} \\ i_{bs} \\ i_{cs} \end{bmatrix} + \begin{bmatrix} v_{as} \\ v_{bs} \\ v_{cs} \end{bmatrix} + \begin{bmatrix} v_{gs} \\ v_{gs} \\ v_{gs} \end{bmatrix} + \begin{bmatrix} v_n \\ v_n \\ v_n \end{bmatrix} \tag{A.2}
$$

- Sub-Converter 3 linking input phases (a, b, c) to output phase t.

$$
\begin{bmatrix} v_{ma} \\ v_{mb} \\ v_{mc} \end{bmatrix} = L_c \frac{\mathrm{d}}{\mathrm{d}t} \begin{bmatrix} i_{at} \\ i_{bt} \\ i_{ct} \end{bmatrix} + \begin{bmatrix} v_{at} \\ v_{bt} \\ v_{ct} \end{bmatrix} + \begin{bmatrix} v_{gt} \\ v_{gt} \\ v_{gt} \end{bmatrix} + \begin{bmatrix} v_n \\ v_n \\ v_n \end{bmatrix} \tag{A.3}
$$

A.1 First $\alpha\beta 0$ Transformation - System connected to the input port

A.1.1 Sub-Converter 1

Applying the power invariant Clarke transformation of (3.4) to the system described in (A.1):

$$
\begin{bmatrix} v_{m\alpha} \\ v_{m\beta} \\ v_{m0} \end{bmatrix} = \sqrt{\frac{2}{3}} \begin{bmatrix} L_c(1\frac{d}{dt}i_{ar} - \frac{1}{2}\frac{d}{dt}i_{br} - \frac{1}{2}\frac{d}{dt}i_{cr}) \\ L_c(0 + \frac{\sqrt{3}}{2}\frac{d}{dt}i_{br} - \frac{\sqrt{3}}{2}\frac{d}{dt}i_{cr}) \\ L_c(\frac{1}{\sqrt{2}}\frac{d}{dt}i_{ar} + \frac{1}{\sqrt{2}}\frac{d}{dt}i_{br} + \frac{1}{\sqrt{2}}\frac{d}{dt}i_{cr}) \end{bmatrix} + \sqrt{\frac{2}{3}} \begin{bmatrix} v_{ar} - \frac{1}{2}v_{br} - \frac{1}{2}v_{cr} \\ 0 + \frac{\sqrt{3}}{2}v_{br} - \frac{\sqrt{3}}{2}v_{cr} \\ \frac{1}{\sqrt{2}}v_{ar} + \frac{1}{\sqrt{2}}v_{br} + \frac{1}{\sqrt{2}}v_{cr} \end{bmatrix}
$$
$$
+ \sqrt{\frac{2}{3}} \begin{bmatrix} v_{gr} - \frac{1}{2}v_{gr} - \frac{1}{2}v_{gr} \\ 0 + \frac{\sqrt{3}}{2}v_{gr} - \frac{\sqrt{3}}{2}v_{gr} \\ \frac{1}{\sqrt{2}}v_{gr} + \frac{1}{\sqrt{2}}v_{gr} + \frac{1}{\sqrt{2}}v_{gr} \end{bmatrix} + \sqrt{\frac{2}{3}} \begin{bmatrix} v_n - \frac{1}{2}v_n - \frac{1}{2}v_n \\ 0 + \frac{\sqrt{3}}{2}v_n - \frac{\sqrt{3}}{2}v_n \\ \frac{1}{\sqrt{2}}v_n + \frac{1}{\sqrt{2}}v_n + \frac{1}{\sqrt{2}}v_n \end{bmatrix} \tag{A.4}
$$

After some manipulations, (A.4) yields to:

$$
\begin{bmatrix} v_{m\alpha} \\ v_{m\beta} \\ v_{m0} \end{bmatrix} = L_c \frac{d}{dt} \begin{bmatrix} i_{\alpha r} \\ i_{\beta r} \\ i_{0r} \end{bmatrix} + \begin{bmatrix} v_{\alpha r} \\ v_{\beta r} \\ v_{0r} \end{bmatrix} + \begin{bmatrix} 0 \\ 0 \\ \sqrt{3}v_{gr} \end{bmatrix} + \begin{bmatrix} 0 \\ 0 \\ \sqrt{3}v_n \end{bmatrix} \tag{A.5}
$$

Being:

$$
i_{\alpha r} = \sqrt{\frac{2}{3}}(i_{ar} - \frac{1}{2}(i_{br} + i_{cr}))
$$
$$
i_{\beta r} = \sqrt{2}/2(i_{br} - i_{cr})
$$
$$
i_{0r} = 1/\sqrt{3}(i_{ar} + i_{br} + i_{cr})
$$
$$
v_{\alpha r} = \sqrt{\frac{2}{3}}(v_{ar} - \frac{1}{2}(v_{br} + v_{cr})) \tag{A.6}
$$
$$
v_{\beta r} = \frac{\sqrt{2}}{2}(v_{br} - v_{cr})
$$
$$
v_{0r} = \frac{1}{\sqrt{3}}(v_{ar} + v_{br} + v_{cr})
$$

A.1.2 Sub-Converter 2

Applying the power invariant Clarke transformation of (3.4) to the system described in (A.2) and after some manipulations:

$$\begin{bmatrix} v_{m\alpha} \\ v_{m\beta} \\ v_{m0} \end{bmatrix} = L_c \frac{\mathrm{d}}{\mathrm{d}t} \begin{bmatrix} \mathrm{i}_{\alpha s} \\ \mathrm{i}_{\beta s} \\ \mathrm{i}_{0s} \end{bmatrix} + \begin{bmatrix} v_{\alpha s} \\ v_{\beta s} \\ v_{0s} \end{bmatrix} + \begin{bmatrix} 0 \\ 0 \\ \sqrt{3}v_{gs} \end{bmatrix} + \begin{bmatrix} 0 \\ 0 \\ \sqrt{3}v_{n} \end{bmatrix} \tag{A.7}$$

Being:

$$\begin{aligned} \mathrm{i}_{\alpha s} &= \sqrt{\frac{2}{3}}(\mathrm{i}_{as} - \frac{1}{2}(\mathrm{i}_{bs} + \mathrm{i}_{cs})) \\ \mathrm{i}_{\beta s} &= \sqrt{2}/2(\mathrm{i}_{bs} - \mathrm{i}_{cs}) \\ \mathrm{i}_{0s} &= 1/\sqrt{3}(\mathrm{i}_{as} + \mathrm{i}_{bs} + \mathrm{i}_{cs}) \\ v_{\alpha s} &= \sqrt{\frac{2}{3}}(v_{as} - \frac{1}{2}(v_{bs} + v_{cs})) \\ v_{\beta s} &= \sqrt{2}/2(v_{bs} - v_{cs}) \\ v_{0s} &= 1/\sqrt{3}(v_{as} + v_{bs} + v_{cs}) \end{aligned} \tag{A.8}$$

A.1.3   Sub-Converter 3

Applying the power invariant Clarke transformation of (3.4) to the system described in (A.3) and after some manipulations:

$$\begin{bmatrix} v_{m\alpha} \\ v_{m\beta} \\ v_{m0} \end{bmatrix} = L_c \frac{\mathrm{d}}{\mathrm{d}t} \begin{bmatrix} \mathrm{i}_{\alpha t} \\ \mathrm{i}_{\beta t} \\ \mathrm{i}_{0t} \end{bmatrix} + \begin{bmatrix} v_{\alpha t} \\ v_{\beta t} \\ v_{0t} \end{bmatrix} + \begin{bmatrix} 0 \\ 0 \\ \sqrt{3}v_{gt} \end{bmatrix} + \begin{bmatrix} 0 \\ 0 \\ \sqrt{3}v_{n} \end{bmatrix} \tag{A.9}$$

Being:

$$\begin{aligned} \mathrm{i}_{\alpha t} &= \sqrt{2/3}(\mathrm{i}_{at} - \frac{1}{2}(\mathrm{i}_{bt} + \mathrm{i}_{ct})) \\ \mathrm{i}_{\beta t} &= \sqrt{2}/2(\mathrm{i}_{bt} - \mathrm{i}_{ct}) \\ \mathrm{i}_{0t} &= 1/\sqrt{3}(\mathrm{i}_{at} + \mathrm{i}_{bt} + \mathrm{i}_{ct}) \\ v_{\alpha t} &= \sqrt{2/3}(v_{at} - \frac{1}{2}(v_{bt} + v_{ct})) \\ v_{\beta t} &= \sqrt{2}/2(v_{bt} - v_{ct}) \\ v_{0t} &= 1/\sqrt{3}(v_{at} + v_{bt} + v_{ct}) \end{aligned} \tag{A.10}$$

A.1.4 Matrix Representation

Using (A.6), (A.8) and (A.10), the following expression is obtained:

$$
\begin{bmatrix} v_{m\alpha} & v_{m\beta} & v_{m0} \\ v_{m\alpha} & v_{m\beta} & v_{m0} \\ v_{m\alpha} & v_{m\beta} & v_{m0} \end{bmatrix} = L_c \frac{\mathrm{d}}{\mathrm{d}t} \begin{bmatrix} i_{\alpha r} & i_{\beta r} & i_{0r} \\ i_{\alpha s} & i_{\beta s} & i_{0s} \\ i_{\alpha t} & i_{\beta r} & i_{0t} \end{bmatrix} + \begin{bmatrix} v_{\alpha r} & v_{\beta r} & v_{0r} \\ v_{\alpha s} & v_{\beta s} & v_{0s} \\ v_{\alpha t} & v_{\beta r} & v_{0t} \end{bmatrix}
$$
$$
+ \begin{bmatrix} 0 & 0 & \sqrt{3}v_{gr} \\ 0 & 0 & \sqrt{3}v_{gs} \\ 0 & 0 & \sqrt{3}v_{gt} \end{bmatrix} + \begin{bmatrix} 0 & 0 & \sqrt{3}v_n \\ 0 & 0 & \sqrt{3}v_n \\ 0 & 0 & \sqrt{3}v_n \end{bmatrix}
$$

(A.11)

The three phases of the output system are represented in the columns of (A.11). Accordingly, (A.11) is re-ordered as follows:

$$
\begin{bmatrix} v_{m\alpha} \\ v_{m\alpha} \\ v_{m\alpha} \end{bmatrix} = L_c \frac{\mathrm{d}}{\mathrm{d}t} \begin{bmatrix} i_{\alpha r} \\ i_{\alpha s} \\ i_{\alpha t} \end{bmatrix} + \begin{bmatrix} v_{\alpha r} \\ v_{\alpha s} \\ v_{\alpha t} \end{bmatrix}
$$

(A.12)

$$
\begin{bmatrix} v_{m\beta} \\ v_{m\beta} \\ v_{m\beta} \end{bmatrix} = L_c \frac{\mathrm{d}}{\mathrm{d}t} \begin{bmatrix} i_{\beta r} \\ i_{\beta s} \\ i_{\beta t} \end{bmatrix} + \begin{bmatrix} v_{\beta r} \\ v_{\beta s} \\ v_{\beta t} \end{bmatrix}
$$

(A.13)

$$
\begin{bmatrix} v_{m0} \\ v_{m0} \\ v_{m0} \end{bmatrix} = L_c \frac{\mathrm{d}}{\mathrm{d}t} \begin{bmatrix} i_{0r} \\ i_{0s} \\ i_{0t} \end{bmatrix} + \begin{bmatrix} v_{0r} \\ v_{0s} \\ v_{0t} \end{bmatrix} + \sqrt{3} \begin{bmatrix} v_{gr} \\ v_{gs} \\ v_{gt} \end{bmatrix} + \sqrt{3} \begin{bmatrix} v_n \\ v_n \\ v_n \end{bmatrix}
$$

(A.14)

A.2 Second $\alpha\beta0$ Transformation - System connected to the output port

A.2.1 Sub-Converter 1, $(r, s, t) \rightarrow \alpha$

Applying the power invariant Clarke transformation of (3.4) to the system described in (A.12) yields to:

$$
\sqrt{3} \begin{bmatrix} 0 \\ 0 \\ v_{m\alpha} \end{bmatrix} = L_c \frac{\mathrm{d}}{\mathrm{d}t} \begin{bmatrix} i_{\alpha\alpha} \\ i_{\alpha\beta} \\ i_{\alpha0} \end{bmatrix} + \begin{bmatrix} v_{\alpha\alpha} \\ v_{\alpha\beta} \\ v_{\alpha0} \end{bmatrix}
$$

(A.15)

174

Where:

$$i_{\alpha\alpha} = \sqrt{2/3}(i_{\alpha r} - \frac{1}{2}(i_{\alpha s} + i_{\alpha t}))$$

$$i_{\alpha\beta} = \sqrt{2}/2(i_{\alpha s} - \beta_{\alpha t})$$

$$i_{\alpha 0} = 1/\sqrt{3}(i_{\alpha r} + i_{\alpha s} + i_{\alpha t})$$

$$v_{\alpha\alpha} = \sqrt{2/3}(v_{\alpha r} - \frac{1}{2}(v_{\alpha s} + v_{\alpha t}))$$

$$v_{\alpha\beta} = \sqrt{2}/2(v_{\alpha s} - v_{\alpha t})$$

$$v_{\alpha 0} = 1/\sqrt{3}(v_{\alpha r} + v_{\alpha s} + v_{\alpha t})$$

(A.16)

A.2.2 Sub-Converter 2, $(r, s, t) \rightarrow \beta$

Applying the power invariant Clarke transformation of (3.4) to the system described in (A.13):

$$\sqrt{3} \begin{bmatrix} 0 \\ 0 \\ v_{m\beta} \end{bmatrix} = L_c \frac{\mathrm{d}}{\mathrm{d}t} \begin{bmatrix} i_{\beta\alpha} \\ i_{\beta\beta} \\ i_{\beta 0} \end{bmatrix} + \begin{bmatrix} v_{\beta\alpha} \\ v_{\beta\beta} \\ v_{\beta 0} \end{bmatrix}$$

(A.17)

Where:

$$i_{\beta\alpha} = \sqrt{2/3}(i_{\beta r} - \frac{1}{2}(i_{\beta s} + i_{\beta t}))$$

$$i_{\beta\beta} = \sqrt{2}/2(i_{\beta s} - \beta_{\beta t})$$

$$i_{\beta 0} = 1/\sqrt{3}(i_{\beta r} + i_{\beta s} + i_{\beta t})$$

$$v_{\beta\alpha} = \sqrt{2/3}(v_{\beta r} - \frac{1}{2}(v_{\beta s} + v_{\beta t}))$$

$$v_{\beta\beta} = \sqrt{2}/2(v_{\beta s} - v_{\beta t})$$

$$v_{\beta 0} = 1/\sqrt{3}(v_{\beta r} + v_{\beta s} + v_{\beta t})$$

(A.18)

A.2.3 Sub-Converter 3, $(r, s, t) \rightarrow 0$

Applying the power invariant Clarke transformation of (3.4) to the system described in (A.14):

$$\sqrt{3} \begin{bmatrix} 0 \\ 0 \\ v_{m0} \end{bmatrix} = L_c \frac{\mathrm{d}}{\mathrm{d}t} \begin{bmatrix} i_{0\alpha} \\ i_{0\beta} \\ i_{00} \end{bmatrix} + \begin{bmatrix} v_{0\alpha} \\ v_{0\beta} \\ v_{00} \end{bmatrix} + \sqrt{3} \begin{bmatrix} v_{g\alpha} \\ v_{g\beta} \\ v_{g0} \end{bmatrix} + \begin{bmatrix} 0 \\ 0 \\ 3v_n \end{bmatrix}$$

(A.19)

Where:

$$i_{0\alpha} = \sqrt{2/3}(i_{0r} - \frac{1}{2}(i_{0s} + i_{0t}))$$

$$i_{0\beta} = \sqrt{2}/2(i_{0s} - i_{0t})$$

$$i_{00} = 1/\sqrt{3}(i_{0r} + i_{0s} + i_{0t})$$

$$v_{0\alpha} = \sqrt{2/3}(v_{0r} - \frac{1}{2}(v_{0s} + v_{0t}))$$

$$v_{0\beta} = \sqrt{2}/2(v_{0s} - v_{0t})$$

$$v_{00} = 1/\sqrt{3}(v_{0r} + v_{0s} + v_{0t})$$

$$v_{g\alpha} = \sqrt{2/3}(v_{gr} - \frac{1}{2}(v_{gs} + v_{gt}))$$

$$v_{g\beta} = \sqrt{2}/2(v_{gs} - v_{gt})$$

$$v_{g0} = 1/\sqrt{3}(v_{gr} + v_{gs} + v_{gt})$$

(A.20)

A.3 Voltage-Current model of the M^3C in Double $\alpha\beta0$ coordinates

Expressing (A.15), (A.17), and (A.19) in matrix form, the Voltage-Current model of the M^3C is obtained:

$$\sqrt{3}\begin{bmatrix} 0 & 0 & 0 \\ 0 & 0 & 0 \\ v_{m\alpha} & v_{m\beta} & v_{m0} \end{bmatrix} = L_c\frac{d}{dt}\begin{bmatrix} i_{\alpha\alpha} & i_{\beta\alpha} & i_{0\alpha} \\ i_{\alpha\beta} & i_{\beta\beta} & i_{0\beta} \\ i_{\alpha0} & i_{\beta0} & i_{00} \end{bmatrix} + \begin{bmatrix} v_{\alpha\alpha} & v_{\beta\alpha} & v_{0\alpha} \\ v_{\alpha\beta} & v_{\beta\beta} & v_{0\beta} \\ v_{\alpha0} & v_{\beta0} & v_{00} \end{bmatrix} + \sqrt{3}\begin{bmatrix} 0 & 0 & v_{g\alpha} \\ 0 & 0 & v_{g\beta} \\ 0 & 0 & v_{g0} \end{bmatrix}$$
$$+ \begin{bmatrix} 0 & 0 & 0 \\ 0 & 0 & 0 \\ 0 & 0 & 3v_n \end{bmatrix}$$

(A.21)

Notice that (A.21) is equal to (3.5).

A.4 Input/Output Current analyses

A.4.1 Generator-side Currents

Using Kirchhoff current law in Fig. 3.2, the following relationships are obtained:

176

$$i_{ma} = i_{ar} + i_{as} + i_{at}$$
$$i_{mb} = i_{br} + i_{bs} + i_{bt} \quad (A.22)$$
$$i_{mc} = i_{cr} + i_{cs} + i_{ct}$$

Moreover, the $(\alpha, \beta, 0)$ components of the generator-side system are given by:

$$
\begin{bmatrix} i_{m\alpha} \\ i_{m\beta} \\ i_{m0} \end{bmatrix} = \sqrt{\frac{2}{3}} \begin{bmatrix} 1 & -1/2 & -1/2 \\ 0 & \sqrt{3}/2 & -\sqrt{3}/2 \\ 1/\sqrt{2} & 1/\sqrt{2} & 1/\sqrt{2} \end{bmatrix} \begin{bmatrix} i_{ma} \\ i_{mb} \\ i_{mc} \end{bmatrix} \quad (A.23)
$$

- Replacing (A.23) into (A.22) and factorising for $i_{m\alpha}$:

$$
i_{m\alpha} = \overbrace{\sqrt{\frac{2}{3}}(i_{ar} - 1/2i_{br} - 1/2i_{cr})}^{i_{\alpha r}} + \overbrace{\sqrt{\frac{2}{3}}(i_{as} - 1/2i_{bs} - 1/2i_{cs})}^{i_{\alpha s}} + \overbrace{\sqrt{\frac{2}{3}}(i_{at} - 1/2i_{bt} - 1/2i_{ct}))}^{i_{\alpha t}}
$$
$$(A.24)$$

Using the expression of (A.6) for $i_{\alpha r}$, (A.8) for $i_{\alpha s}$ and (A.10) for $i_{\alpha r}$, (A.24) becomes:

$$i_{m\alpha} = i_{\alpha r} + i_{\alpha s} + i_{\alpha t} \quad (A.25)$$

At this point it is useful to use the expression of given in (A.16) [i.e. $i_{\alpha 0} = \frac{1}{\sqrt{3}}(i_{\alpha r} + i_{\alpha s} + i_{\alpha t})$]. Therefore, (A.25) yields to:

$$i_{m\alpha} = \sqrt{3}i_{\alpha 0} \quad (A.26)$$

- Replacing (A.23) into (A.22) and factorising for $i_{m\beta}$:

$$i_{m\beta} = \frac{\sqrt{2}}{2}(i_{br} - i_{cr}) + \frac{\sqrt{2}}{2}(i_{bs} - i_{cs}) + \frac{\sqrt{2}}{2}(i_{bt} - i_{ct}) \quad (A.27)$$

Using the expression of (A.6) for $i_{\beta r}$, (A.8) for $i_{\beta s}$ and (A.10) for $i_{\beta r}$, (A.27) becomes:

$$i_{m\beta} = i_{\beta r} + i_{\beta s} + i_{\beta t} \quad (A.28)$$

At this point it is useful to use the expression of given in (A.18) [i.e. $i_{\beta 0} = 1/\sqrt{3}(i_{\beta r} + i_{\beta s} + i_{\beta t})$]. Therefore, (A.28) yields to:

$$i_{m\beta} = \sqrt{3}i_{\beta 0} \quad (A.29)$$

A.4.2 Grid-side Currents

Using Kirchhoff current law in Fig. 3.2, the following relationships are obtained:

$$i_{gr} = i_{ar} + i_{br} + i_{cr}$$
$$i_{gs} = i_{as} + i_{bs} + i_{cs} \qquad \text{(A.30)}$$
$$i_{gt} = i_{at} + i_{bt} + i_{ct}$$

Moreover, the $(\alpha, \beta, 0)$ components of the grid-side system are given by:

$$\begin{bmatrix} i_{g\alpha} \\ i_{g\beta} \\ i_{g0} \end{bmatrix} = \sqrt{\frac{2}{3}} \begin{bmatrix} 1 & -1/2 & -1/2 \\ 0 & \sqrt{3}/2 & -\sqrt{3}/2 \\ 1/\sqrt{2} & 1/\sqrt{2} & 1/\sqrt{2} \end{bmatrix} * \begin{bmatrix} i_{gr} \\ i_{gs} \\ i_{gt} \end{bmatrix} \qquad \text{(A.31)}$$

- Replacing (A.31) into (A.30) and factorising for $i_{g\alpha}$:

$$i_{g\alpha} = \sqrt{\frac{2}{3}}((i_{ar} + i_{br} + i_{cr}) - \frac{1}{2}(i_{as} + i_{bs} + i_{cs}) - \frac{1}{2}(i_{at} + i_{bt} + i_{ct})) \qquad \text{(A.32)}$$

Using the expression of (A.6) for i_{0r}, (A.8) for i_{0s} and (A.10) for i_{0t}, (A.32) becomes:

$$i_{g\alpha} = \sqrt{\frac{2}{3}}(\sqrt{3}(i_{0r} - \tfrac{1}{2}i_{\alpha s} - \tfrac{1}{2}i_{\alpha t}) \qquad \text{(A.33)}$$

At this point it is useful to use the expression of given in (A.20) [i.e. $i_{0\alpha} = \sqrt{\frac{2}{3}}(i_{0r} - \frac{1}{2}(i_{0s} + i_{0t})]$. Therefore, (A.33) yields to:

$$i_{g\alpha} = \sqrt{3}i_{0\alpha} \qquad \text{(A.34)}$$

- Replacing (A.23) into (A.30) and factorising for $i_{g\beta}$:

$$i_{g\beta} = \frac{\sqrt{2}}{2}(i_{as} + i_{bs} + i_{cs} - (i_{at} + i_{bt} + i_{ct})) \qquad \text{(A.35)}$$

Using the expression of (A.8) for i_{0s} and (A.10) for i_{0t}, (A.35) becomes:

$$i_{m\beta} = \frac{\sqrt{2}}{2}(\sqrt{3}(i_{0s} - i_{0t})) \qquad \text{(A.36)}$$

At this point it is useful to use the expression of given in (A.20) [i.e. $i_{0\beta} = \frac{\sqrt{2}}{2}(i_{0s} - i_{0t}]$. Therefore, (A.36) yields to:

$$i_{g\beta} = \sqrt{3}i_{0\beta} \qquad \text{(A.37)}$$

A.5 Extended currents equations in Double $\alpha\beta 0$ coordinates

Summarising:

$$i_{\alpha\alpha} = \tfrac{2}{3}i_{ar} - \tfrac{1}{3}i_{as} - \tfrac{1}{3}i_{at} - \tfrac{1}{3}i_{br} + \tfrac{1}{6}i_{bs} + \tfrac{1}{6}i_{bt} - \tfrac{1}{3}i_{cr} + \tfrac{1}{6}i_{cs} + \tfrac{1}{6}i_{ct}$$

$$i_{\beta\alpha} = \tfrac{1}{\sqrt{3}}i_{br} - \tfrac{1}{2\sqrt{3}}i_{bs} - \tfrac{1}{2\sqrt{3}}i_{bt} - \tfrac{1}{\sqrt{3}}i_{cr} + \tfrac{1}{2\sqrt{3}}i_{cs} + \tfrac{1}{2\sqrt{3}}i_{ct}$$

$$i_{0\alpha} = \tfrac{\sqrt{2}}{3}i_{ar} - \tfrac{\sqrt{2}}{6}i_{as} - \tfrac{\sqrt{2}}{3}i_{at} + \tfrac{\sqrt{2}}{3}i_{br} - \tfrac{\sqrt{2}}{6}i_{bs} - \tfrac{\sqrt{6}}{3}i_{bt} + \tfrac{\sqrt{2}}{3}i_{cr} - \tfrac{\sqrt{2}}{6}i_{cs} - \tfrac{\sqrt{2}}{6}i_{ct}$$

$$i_{\alpha\beta} = \tfrac{1}{\sqrt{3}}i_{as} - \tfrac{1}{\sqrt{3}}i_{at} - \tfrac{1}{2\sqrt{3}}i_{bs} + \tfrac{1}{2\sqrt{3}}i_{bt} - \tfrac{1}{2\sqrt{3}}i_{cs} + \tfrac{1}{2\sqrt{3}}i_{ct}$$

$$i_{\beta\beta} = \tfrac{1}{2}i_{bs} - \tfrac{1}{2}i_{bt} - \tfrac{1}{2}i_{cs} + \tfrac{1}{2}i_{ct}$$

$$i_{0\beta} = \tfrac{\sqrt{6}}{6}i_{as} + \tfrac{\sqrt{6}}{6}i_{bs} + \tfrac{\sqrt{6}}{6}i_{cs} - \tfrac{\sqrt{6}}{6}i_{at} - \tfrac{\sqrt{6}}{6}i_{bt} - \tfrac{\sqrt{6}}{6}i_{ct} \tag{A.38}$$

$$i_{\alpha 0} = \tfrac{\sqrt{2}}{3}i_{ar} + \tfrac{\sqrt{2}}{3}i_{as} + \tfrac{\sqrt{2}}{3}i_{at} - \tfrac{\sqrt{2}}{6}i_{br} - \tfrac{\sqrt{2}}{6}i_{bs} - \tfrac{\sqrt{2}}{6}i_{bt} - \tfrac{\sqrt{2}}{6}i_{cr} - \tfrac{\sqrt{2}}{6}i_{cs} - \tfrac{\sqrt{2}}{6}i_{ct}$$

$$i_{\beta 0} = \tfrac{\sqrt{6}}{6}i_{br} + \tfrac{\sqrt{6}}{6}i_{bs} + \tfrac{\sqrt{6}}{6}i_{bt} - \tfrac{\sqrt{6}}{6}i_{cr} - \tfrac{\sqrt{6}}{6}i_{cs} - \tfrac{\sqrt{6}}{6}i_{ct}$$

$$i_{00} = \tfrac{1}{3}i_{ar} + \tfrac{1}{3}i_{as} + \tfrac{1}{3}i_{at} + \tfrac{1}{3}i_{br} + \tfrac{1}{3}i_{bs} + \tfrac{1}{3}i_{bt} + \tfrac{1}{3}i_{cr} + \tfrac{1}{3}i_{cs} + \tfrac{1}{3}i_{ct}$$

APPENDIX B

Double-$\alpha\beta0$ Transformation of the Power-CCV Model

The Power-CCV Model of the M^3C presented in (3.19) can be re-written in separate equations for each Sub-Converter as follows:

- Sub-Converter 1 linking input phases (a, b, c) to output phase r.

$$
\begin{bmatrix} v_{c_{ar}} \\ v_{c_{br}} \\ v_{c_{cr}} \end{bmatrix} \approx \frac{1}{Cv^*} \int \begin{bmatrix} P_{ar} \\ P_{br} \\ P_{cr} \end{bmatrix} \mathrm{d}t + nv_c^* \begin{bmatrix} 1 \\ 1 \\ 1 \end{bmatrix}
\tag{B.1}
$$

- Sub-Converter 2 linking input phases (a, b, c) to output phase s.

$$
\begin{bmatrix} v_{c_{as}} \\ v_{c_{bs}} \\ v_{c_{cs}} \end{bmatrix} \approx \frac{1}{Cv^*} \int \begin{bmatrix} P_{as} \\ P_{bs} \\ P_{cs} \end{bmatrix} \mathrm{d}t + nv_c^* \begin{bmatrix} 1 \\ 1 \\ 1 \end{bmatrix}
\tag{B.2}
$$

- Sub-Converter 3 linking input phases (a, b, c) to output phase t.

$$
\begin{bmatrix} v_{c_{at}} \\ v_{c_{bt}} \\ v_{c_{ct}} \end{bmatrix} \approx \frac{1}{Cv^*} \int \begin{bmatrix} P_{at} \\ P_{bt} \\ P_{ct} \end{bmatrix} \mathrm{d}t + nv_c^* \begin{bmatrix} 1 \\ 1 \\ 1 \end{bmatrix}
\tag{B.3}
$$

B.1 First $\alpha\beta 0$ Transformation - System connected to the input port

B.1.1 Sub-Converter 1

Applying the power invariant Clarke transformation of (3.4) to the system described in (B.1):

$$\sqrt{\frac{2}{3}} \begin{bmatrix} 1 & -1/2 & -1/2 \\ 0 & \sqrt{3}/2 & -\sqrt{3}/2 \\ 1/\sqrt{2} & 1/\sqrt{2} & 1/\sqrt{2} \end{bmatrix} \begin{bmatrix} v_{c_{ar}} \\ v_{c_{br}} \\ v_{c_{cr}} \end{bmatrix} \approx \frac{\sqrt{2}}{Cv_c^*\sqrt{3}} \int \begin{bmatrix} P_{ar} - \frac{1}{2}P_{br} - \frac{1}{2}P_{cr} \\ 0 + \frac{\sqrt{3}}{2}P_{br} - \frac{\sqrt{3}}{2}P_{cr} \\ \frac{1}{\sqrt{2}}P_{ar} + \frac{1}{\sqrt{2}}P_{br} + \frac{1}{\sqrt{2}}P_{cr} \end{bmatrix} \mathrm{d}t$$
$$+ \frac{\sqrt{2}nv_c^*}{\sqrt{3}} \begin{bmatrix} 1 - \frac{1}{2} - \frac{1}{2} \\ 0 + \frac{\sqrt{3}}{2} - \frac{\sqrt{3}}{2} \\ \frac{1}{\sqrt{2}} + \frac{1}{\sqrt{2}} + \frac{1}{\sqrt{2}} \end{bmatrix} \tag{B.4}$$

After some manipulations, (B.4) yields to:

$$\begin{bmatrix} v_{c_{\alpha r}} \\ v_{c_{\beta r}} \\ v_{c_{0r}} \end{bmatrix} \approx \frac{1}{Cv_c^*} \int \begin{bmatrix} P_{\alpha r} \\ P_{\beta r} \\ P_{0r} \end{bmatrix} \mathrm{d}t + nv_c^* \begin{bmatrix} 0 \\ 0 \\ \sqrt{3} \end{bmatrix} \tag{B.5}$$

Being:

$$P_{\alpha r} = \sqrt{\frac{2}{3}} \left(P_{ar} - \frac{1}{2}(P_{br} + P_{cr}) \right)$$
$$P_{\beta r} = \frac{\sqrt{2}}{2} \left(P_{br} - P_{cr} \right) \tag{B.6}$$
$$P_{0r} = \frac{1}{\sqrt{3}}(P_{ar} + P_{br} + P_{cr})$$

B.1.2 Sub-Converter 2

Applying the power invariant Clarke transformation of (3.4) to the system described in (B.2) and after some manipulations:

$$\begin{bmatrix} v_{c_{\alpha s}} \\ v_{c_{\beta s}} \\ v_{c_{0s}} \end{bmatrix} \approx \frac{1}{Cv_c^*} \int \begin{bmatrix} P_{\alpha s} \\ P_{\beta s} \\ P_{0s} \end{bmatrix} \mathrm{d}t + nv_c^* \begin{bmatrix} 0 \\ 0 \\ \sqrt{3} \end{bmatrix} \tag{B.7}$$

Being:

$$P_{\alpha s} = \sqrt{\frac{2}{3}} \left(P_{as} - \frac{1}{2}(P_{bs} + P_{cs}) \right)$$

$$P_{\beta s} = \frac{\sqrt{2}}{2} (P_{bs} - P_{cs}) \tag{B.8}$$

$$P_{0s} = \frac{1}{\sqrt{3}}(P_{as} + P_{bs} + P_{cs})$$

B.1.3   Sub-Converter 3

Applying the power invariant Clarke transformation of (3.4) to the system described in (B.3) and after some manipulations:

$$\begin{bmatrix} v_{c\alpha t} \\ v_{c\beta t} \\ v_{c0t} \end{bmatrix} \approx \frac{1}{Cv_c^*} \int \begin{bmatrix} P_{\alpha t} \\ P_{\beta t} \\ P_{0t} \end{bmatrix} dt + n v_c^* \begin{bmatrix} 0 \\ 0 \\ \sqrt{3} \end{bmatrix} \tag{B.9}$$

Being:

$$P_{\alpha t} = \sqrt{\frac{2}{3}} \left(P_{at} - \frac{1}{2}(P_{bt} + P_{ct}) \right)$$

$$P_{\beta t} = \frac{\sqrt{2}}{2} (P_{bt} - P_{ct}) \tag{B.10}$$

$$P_{0t} = \frac{1}{\sqrt{3}}(P_{at} + P_{bt} + P_{ct})$$

B.1.4   Matrix Representation

Using (B.5), (B.7) and (B.9), the following expression is obtained:

$$\begin{bmatrix} v_{c\alpha r} & v_{c\alpha s} & v_{c\alpha t} \\ v_{c\beta r} & v_{c\beta s} & v_{c\beta t} \\ v_{c0r} & v_{c0s} & v_{c0t} \end{bmatrix} \approx \frac{1}{Cv_c^*} \int \begin{bmatrix} P_{\alpha r} & P_{\alpha s} & P_{\alpha t} \\ P_{\beta r} & P_{\beta s} & P_{\beta t} \\ P_{0r} & P_{0s} & P_{0t} \end{bmatrix} dt + \sqrt{3} n v_c^* \begin{bmatrix} 0 & 0 & 0 \\ 0 & 0 & 0 \\ 1 & 1 & 1 \end{bmatrix} \tag{B.11}$$

The three phases of the output system are represented in the rows of (B.11). Accordingly, (B.11) is re-ordered as follows:

$$\begin{bmatrix} v_{c\alpha r} \\ v_{c\alpha s} \\ v_{c\alpha t} \end{bmatrix} \approx \frac{1}{Cv^*} \int \begin{bmatrix} P_{\alpha r} \\ P_{\alpha s} \\ P_{\alpha t} \end{bmatrix} dt \tag{B.12}$$

182

$$
\begin{bmatrix} v_{c_{\beta r}} \\ v_{c_{\beta s}} \\ v_{c_{\beta t}} \end{bmatrix} \approx \frac{1}{Cv^*} \int \begin{bmatrix} P_{\beta r} \\ P_{\beta s} \\ P_{\beta t} \end{bmatrix} \mathrm{d}t \tag{B.13}
$$

$$
\begin{bmatrix} v_{c_{0r}} \\ v_{c_{0s}} \\ v_{c_{0t}} \end{bmatrix} \approx \frac{1}{Cv_c^*} \int \begin{bmatrix} P_{0r} \\ P_{0s} \\ P_{0t} \end{bmatrix} \mathrm{d}t + \sqrt{3} n v_c^* \begin{bmatrix} 1 \\ 1 \\ 1 \end{bmatrix} \tag{B.14}
$$

B.2   Second $\alpha\beta 0$ Transformation - System connected to the output port

B.2.1   Sub-Converter 1, $(r, s, t) \rightarrow \alpha$

Applying the power invariant Clarke transformation of (3.4) to the system described in (B.12):

$$
\begin{bmatrix} v_{c_{\alpha\alpha}} \\ v_{c_{\alpha\beta}} \\ v_{c_{\alpha 0}} \end{bmatrix} \approx \frac{1}{Cv_c^*} \int \begin{bmatrix} P_{\alpha\alpha} \\ P_{\alpha\beta} \\ P_{\alpha 0} \end{bmatrix} \mathrm{d}t \tag{B.15}
$$

Being:

$$
P_{\alpha\alpha} = \sqrt{\frac{2}{3}} \left(P_{\alpha r} - \frac{1}{2}(P_{\alpha s} + P_{\alpha t}) \right)
$$

$$
P_{\alpha\beta} = \frac{\sqrt{2}}{2} \left(P_{\alpha s} - P_{\alpha t} \right) \tag{B.16}
$$

$$
P_{\alpha 0} = \frac{1}{\sqrt{3}} (P_{\alpha r} + P_{\alpha s} + P_{\alpha t})
$$

B.2.2   Sub-Converter 2, $(r, s, t) \rightarrow \beta$

Applying the power invariant Clarke transformation of (3.4) to the system described in (B.13):

$$
\begin{bmatrix} v_{c_{\beta\alpha}} \\ v_{c_{\beta\beta}} \\ v_{c_{\beta 0}} \end{bmatrix} \approx \frac{1}{Cv_c^*} \int \begin{bmatrix} P_{\beta\alpha} \\ P_{\beta\beta} \\ P_{\beta 0} \end{bmatrix} \mathrm{d}t \tag{B.17}
$$

Where:

$$P_{\beta\alpha} = \sqrt{\frac{2}{3}}\left(P_{\beta r} - \frac{1}{2}(P_{\beta s} + P_{\beta t})\right)$$

$$P_{\beta\beta} = \frac{\sqrt{2}}{2}(P_{\beta s} - P_{\beta t}) \tag{B.18}$$

$$P_{\beta 0} = \frac{1}{\sqrt{3}}(P_{\beta r} + P_{\beta s} + P_{\beta t})$$

B.2.3 Sub-Converter 3, $(r, s, t) \to 0$

Applying the power invariant Clarke transformation of (3.4) to the system described in (B.13):

$$\begin{bmatrix} v_{c_{0\alpha}} \\ v_{c_{0\beta}} \\ v_{c_{00}} \end{bmatrix} \approx \frac{1}{Cv^*}\int \begin{bmatrix} P_{0\alpha} \\ P_{0\beta} \\ P_{00} \end{bmatrix} \mathrm{d}t + \begin{bmatrix} 0 \\ 0 \\ 3nv_c^* \end{bmatrix} \tag{B.19}$$

Where:

$$P_{0\alpha} = \sqrt{\frac{2}{3}}\left(P_{0r} - \frac{1}{2}(P_{0s} + P_{0t})\right)$$

$$P_{0\beta} = \frac{\sqrt{2}}{2}(P_{0s} - P_{0t}) \tag{B.20}$$

$$P_{00} = \frac{1}{\sqrt{3}}(P_{0r} + P_{0s} + P_{0t})$$

B.3 Power-CCV model of the M^3C in Double $\alpha\beta 0$ coordinates

Expressing (B.19), (B.19), and (B.19) in matrix form, the Power-CCV model of the M^3C of (3.20) is obtained:

$$\begin{bmatrix} P_{ar} & P_{as} & P_{at} \\ P_{br} & P_{bs} & P_{bt} \\ P_{cr} & P_{cs} & P_{ct} \end{bmatrix} = \begin{bmatrix} v_{ar}i_{ar} & v_{as}i_{as} & v_{at}i_{at} \\ v_{br}i_{br} & v_{bs}i_{bs} & v_{bt}i_{bt} \\ v_{cr}i_{cr} & v_{cs}i_{cs} & v_{ct}i_{ct} \end{bmatrix} \tag{B.21}$$

APPENDIX C

Power Components in Double $\alpha\beta0$ coordinates

The power components of the left-side of (3.20) are expressed as a function of the transformed currents and voltages of the M^3C in Double-$\alpha\beta0$ coordinates. This procedure is explained in following subsections.

C.1 First $\alpha\beta0$ Transformation - System connected to the input port

C.1.1 Sub-Converter 1

Firstly, the power invariant Clarke Transformation is applied to the system composed of $[P_{ar}\ P_{br}\ P_{cr}]^T$:

$$\begin{bmatrix} P_{\alpha r} \\ P_{\beta r} \\ P_{0r} \end{bmatrix} = \sqrt{\frac{2}{3}} \begin{bmatrix} 1 & -1/2 & -1/2 \\ 0 & \sqrt{3}/2 & -\sqrt{3}/2 \\ 1/\sqrt{2} & 1/\sqrt{2} & 1/\sqrt{2} \end{bmatrix} \begin{bmatrix} v_{ar}\mathrm{i}_{cr} \\ v_{br}\mathrm{i}_{cr} \\ v_{cr}\mathrm{i}_{cr} \end{bmatrix} \tag{C.1}$$

The voltages and currents of the right-side of (C.1) can be expressed in $\alpha\beta0$ coordinates as follows:

$$\begin{bmatrix} v_{ar} \\ v_{br} \\ v_{cr} \end{bmatrix} = [C_{\alpha\beta0}]^T \begin{bmatrix} v_{\alpha r} \\ v_{\beta r} \\ v_{0r} \end{bmatrix} \quad ; \quad \begin{bmatrix} \mathrm{i}_{ar} \\ \mathrm{i}_{br} \\ \mathrm{i}_{cr} \end{bmatrix} = [C_{\alpha\beta0}]^T \begin{bmatrix} \mathrm{i}_{\alpha r} \\ \mathrm{i}_{\beta r} \\ \mathrm{i}_{0r} \end{bmatrix} \tag{C.2}$$

- $P_{\alpha r}$ **Calculation**:

From (C.1), $P_{\alpha r}$ can be written as follows:

$$
P_{\alpha r} = \begin{bmatrix} v_{ar} \\ v_{br} \\ v_{cr} \end{bmatrix}^T \overbrace{\sqrt{\frac{2}{3}} \begin{bmatrix} 1 & 0 & 0 \\ 0 & -\frac{1}{2} & 0 \\ 0 & 0 & -\frac{1}{2} \end{bmatrix}}^{[C_\alpha]} \begin{bmatrix} i_{ar} \\ i_{br} \\ i_{cr} \end{bmatrix}
\tag{C.3}
$$

Replacing (C.2) into (C.3) yields to:

$$
P_{\alpha r} = \left([C_{\alpha\beta 0}]^T \begin{bmatrix} v_{\alpha r} \\ v_{\beta r} \\ v_{0r} \end{bmatrix} \right)^T [C_\alpha][C_{\alpha\beta 0}]^T \begin{bmatrix} i_{\alpha r} \\ i_{\beta r} \\ i_{0r} \end{bmatrix}
\tag{C.4}
$$

Using the Properties of Transpose Matrices, i.e. $(A * B)^T = B^T * A^T$, in (C.4):

$$
P_{\alpha r} = \begin{bmatrix} v_{\alpha r} \\ v_{\beta r} \\ v_{0r} \end{bmatrix}^T [C_{\alpha\beta 0}][C_\alpha][C_{\alpha\beta 0}]^T \begin{bmatrix} i_{\alpha r} \\ i_{\beta r} \\ i_{0r} \end{bmatrix}
\tag{C.5}
$$

Where:

$$
[C_{\alpha\beta 0}] [C_\alpha][C_{\alpha\beta 0}]^T = \begin{bmatrix} \frac{\sqrt{6}}{6} & 0 & \frac{\sqrt{3}}{3} \\ 0 & -\frac{\sqrt{6}}{6} & 0 \\ \frac{\sqrt{3}}{3} & 0 & 0 \end{bmatrix}
\tag{C.6}
$$

Replacing (C.6) into (C.5), the following expression for $P_{\alpha r}$ is obtained:

$$
P_{\alpha r} = \frac{1}{\sqrt{6}}(v_{\alpha r}i_{\alpha r} - v_{\beta r}i_{\beta r}) + \frac{1}{\sqrt{3}}(v_{\alpha r}i_{0r} + v_{0r}i_{\alpha r})
\tag{C.7}
$$

- $P_{\beta r}$ **Calculation**:

From (C.1), $P_{\alpha r}$ can be written as follows:

$$P_{\beta r} = \begin{bmatrix} v_{ar} \\ v_{br} \\ v_{cr} \end{bmatrix}^T \overbrace{\sqrt{\frac{2}{3}} \begin{bmatrix} 0 & 0 & 0 \\ 0 & \frac{\sqrt{3}}{2} & 0 \\ 0 & 0 & -\frac{\sqrt{3}}{2} \end{bmatrix}}^{[C_\beta]} \begin{bmatrix} i_{ar} \\ i_{br} \\ i_{cr} \end{bmatrix} \tag{C.8}$$

Replacing (C.6) into (C.8) and using the above-mentioned Properties of Transpose Matrices, (C.8) becomes:

$$P_{\beta r} = \begin{bmatrix} v_{\alpha r} \\ v_{\beta r} \\ v_{0r} \end{bmatrix}^T [C_{\alpha\beta 0}][C_\beta][C_{\alpha\beta 0}]^T \begin{bmatrix} i_{\alpha r} \\ i_{\beta r} \\ i_{0r} \end{bmatrix} \tag{C.9}$$

Where:

$$[C_{\alpha\beta 0}][C_\beta][C_{\alpha\beta 0}] = \begin{bmatrix} 0 & -\frac{\sqrt{6}}{6} & 0 \\ -\frac{\sqrt{6}}{6} & 0 & \frac{\sqrt{3}}{3} \\ 0 & \frac{\sqrt{3}}{3} & 0 \end{bmatrix} \tag{C.10}$$

Replacing (C.10) into (C.9), the following expression for $P_{\beta r}$ is obtained:

$$P_{\beta r} = -\frac{1}{\sqrt{6}}(v_{\alpha r}i_{\beta r} + v_{\beta r}i_{\alpha r}) + \frac{1}{\sqrt{3}}(v_{\beta r}i_{0r} + v_{0r}i_{\beta r}) \tag{C.11}$$

- P_{0r} **Calculation**:

From (C.1), P_{0r} can be written as follows:

$$P_{0r} = \begin{bmatrix} v_{ar} \\ v_{br} \\ v_{cr} \end{bmatrix}^T \overbrace{\sqrt{\frac{2}{3}} \begin{bmatrix} \frac{1}{\sqrt{2}} & 0 & 0 \\ 0 & \frac{1}{\sqrt{2}} & 0 \\ 0 & 0 & \frac{1}{\sqrt{2}} \end{bmatrix}}^{[C_0]} \begin{bmatrix} i_{ar} \\ i_{br} \\ i_{cr} \end{bmatrix} \tag{C.12}$$

Replacing (C.6) into (C.12) and using the above-mentioned Properties of Transpose Matrices, (C.12) becomes:

$$P_{0r} = \begin{bmatrix} v_{\alpha r} \\ v_{\beta r} \\ v_{0r} \end{bmatrix}^T [C_{\alpha\beta 0}][C_0][C_{\alpha\beta 0}]^T \begin{bmatrix} i_{\alpha r} \\ i_{\beta r} \\ i_{0r} \end{bmatrix} \tag{C.13}$$

Where:

$$[C_{\alpha\beta0}]\,[C_0][C_{\alpha\beta0}] = \begin{bmatrix} \frac{\sqrt{3}}{3} & 0 & 0 \\ 0 & \frac{\sqrt{3}}{3} & 0 \\ 0 & 0 & \frac{\sqrt{3}}{3} \end{bmatrix} \tag{C.14}$$

Replacing (C.14) into (C.13), the following expression for P_{0r} is obtained:

$$P_{0r} = \frac{1}{\sqrt{3}}(v_{\alpha r}\mathrm{i}_{\alpha r} + v_{\beta r}\mathrm{i}_{\beta r} + v_{0r}\mathrm{i}_{0r}) \tag{C.15}$$

C.1.2 Sub-Converter 2

Firstly, the power invariant Clarke Transformation is applied to the system composed of $[P_{as}\ P_{bs}\ P_{cs}]^T$:

$$\begin{bmatrix} P_{\alpha s} \\ P_{\beta s} \\ P_{0s} \end{bmatrix} = \sqrt{\frac{2}{3}} \begin{bmatrix} 1 & -1/2 & -1/2 \\ 0 & \sqrt{3}/2 & -\sqrt{3}/2 \\ 1/\sqrt{2} & 1/\sqrt{2} & 1/\sqrt{2} \end{bmatrix} \begin{bmatrix} v_{as}\mathrm{i}_{as} \\ v_{bs}\mathrm{i}_{as} \\ v_{cs}\mathrm{i}_{as} \end{bmatrix} \tag{C.16}$$

The voltages and currents of the right-side of (C.16) can be expressed in $\alpha\beta0$ coordinates as follows:

$$\begin{bmatrix} v_{as} \\ v_{bs} \\ v_{cs} \end{bmatrix} = [C_{\alpha\beta0}]^T \begin{bmatrix} v_{\alpha s} \\ v_{\beta s} \\ v_{0s} \end{bmatrix} \quad ; \quad \begin{bmatrix} \mathrm{i}_{as} \\ \mathrm{i}_{bs} \\ \mathrm{i}_{cs} \end{bmatrix} = [C_{\alpha\beta0}]^T \begin{bmatrix} \mathrm{i}_{\alpha s} \\ \mathrm{i}_{\beta s} \\ \mathrm{i}_{0s} \end{bmatrix} \tag{C.17}$$

- $P_{\alpha s}$ **Calculation**:

Using the procedure explained in previous Subsection, the term $P_{\alpha s}$ can be calculated as follows:

$$P_{\alpha s} = \begin{bmatrix} v_{\alpha s} \\ v_{\beta s} \\ v_{0s} \end{bmatrix}^T [C_{\alpha\beta0}][C_\alpha][C_{\alpha\beta0}]^T \begin{bmatrix} \mathrm{i}_{\alpha s} \\ \mathrm{i}_{\beta s} \\ \mathrm{i}_{0s} \end{bmatrix} \tag{C.18}$$

Replacing (C.6) into (C.18), the following expression for $P_{\alpha s}$ is obtained:

$$P_{\alpha s} = \frac{1}{\sqrt{6}}(v_{\alpha s}\mathrm{i}_{\alpha s} - v_{\beta s}\mathrm{i}_{\beta s}) + \frac{1}{\sqrt{3}}(v_{\alpha s}\mathrm{i}_{os} + v_{0s}\mathrm{i}_{\alpha s}) \tag{C.19}$$

- $P_{\beta s}$ **Calculation**:

The term $P_{\beta s}$ can be calculated as follows:

$$P_{\beta r} = \begin{bmatrix} v_{\alpha s} \\ v_{\beta s} \\ v_{0s} \end{bmatrix}^{T} [C_{\alpha\beta 0}][C_{\beta}][C_{\alpha\beta 0}]^{T} \begin{bmatrix} i_{\alpha s} \\ i_{\beta s} \\ i_{0s} \end{bmatrix} \qquad (C.20)$$

Replacing (C.10) into (C.20), the following expression for $P_{\beta s}$ is obtained:

$$P_{\beta s} = -\frac{1}{\sqrt{6}}(v_{\alpha s}i_{\beta s} + v_{\beta s}i_{\alpha s}) + \frac{1}{\sqrt{3}}(v_{\beta s}i_{0s} + v_{0s}i_{\beta s}) \qquad (C.21)$$

- P_{0s} **Calculation**:

The term P_{0s} can be calculated as follows:

$$P_{0s} = \begin{bmatrix} v_{\alpha s} \\ v_{\beta s} \\ v_{0s} \end{bmatrix}^{T} [C_{\alpha\beta 0}][C_{0}][C_{\alpha\beta 0}]^{T} \begin{bmatrix} i_{\alpha s} \\ i_{\beta s} \\ i_{0s} \end{bmatrix} \qquad (C.22)$$

Replacing (C.14) into (C.22), the following expression for P_{0s} is obtained:

$$P_{0s} = \frac{1}{\sqrt{3}}(v_{\alpha s}i_{\alpha s} + v_{\beta s}i_{\beta s} + v_{0s}i_{0s}) \qquad (C.23)$$

C.1.3   Sub-Converter 3

Firstly, the power invariant Clarke Transformation is applied to the system composed of $[P_{at}\ P_{bt}\ P_{ct}]^{T}$:

$$\begin{bmatrix} P_{\alpha t} \\ P_{\beta t} \\ P_{0t} \end{bmatrix} = \sqrt{\frac{2}{3}} \begin{bmatrix} 1 & -1/2 & -1/2 \\ 0 & \sqrt{3}/2 & -\sqrt{3}/2 \\ 1/\sqrt{2} & 1/\sqrt{2} & 1/\sqrt{2} \end{bmatrix} \begin{bmatrix} v_{at}i_{at} \\ v_{bt}i_{at} \\ v_{ct}i_{at} \end{bmatrix} \qquad (C.24)$$

The voltages and currents of the right-side of (C.24) can be expressed in $\alpha\beta 0$ coordinates as follows:

$$\begin{bmatrix} v_{at} \\ v_{bt} \\ v_{ct} \end{bmatrix} = [C_{\alpha\beta 0}]^{T} \begin{bmatrix} v_{\alpha t} \\ v_{\beta t} \\ v_{0t} \end{bmatrix} \quad ; \quad \begin{bmatrix} i_{at} \\ i_{bt} \\ i_{ct} \end{bmatrix} = [C_{\alpha\beta 0}]^{T} \begin{bmatrix} i_{\alpha t} \\ i_{\beta t} \\ i_{0t} \end{bmatrix} \qquad (C.25)$$

- $P_{\alpha t}$ **Calculation**:

The term $P_{\alpha t}$ can be calculated as follows:

$$P_{\alpha t} = \begin{bmatrix} v_{\alpha t} \\ v_{\beta t} \\ v_{0t} \end{bmatrix}^T [C_{\alpha\beta 0}][C_\alpha][C_{\alpha\beta 0}]^T \begin{bmatrix} i_{\alpha t} \\ i_{\beta t} \\ i_{0t} \end{bmatrix} \qquad (C.26)$$

Replacing (C.6) into (C.26), the following expression for $P_{\alpha t}$ is obtained:

$$P_{\alpha t} = \frac{1}{\sqrt{6}}(v_{\alpha t}i_{\alpha t} - v_{\beta t}i_{\beta t}) + \frac{1}{\sqrt{3}}(v_{\alpha t}i_{0t} + v_{0t}i_{\alpha t}) \qquad (C.27)$$

- $P_{\beta t}$ **Calculation**:

The term $P_{\beta t}$ can be calculated as follows:

$$P_{\beta t} = \begin{bmatrix} v_{\alpha t} \\ v_{\beta t} \\ v_{0t} \end{bmatrix}^T [C_{\alpha\beta 0}][C_\beta][C_{\alpha\beta 0}]^T \begin{bmatrix} i_{\alpha t} \\ i_{\beta t} \\ i_{0t} \end{bmatrix} \qquad (C.28)$$

Replacing (C.10) into (C.28), the following expression for $P_{\beta t}$ is obtained:

$$P_{\beta t} = -\frac{1}{\sqrt{6}}(v_{\alpha t}i_{\beta t} + v_{\beta t}i_{\alpha t}) + \frac{1}{\sqrt{3}}(v_{\beta t}i_{0t} + v_{0t}i_{\beta t}) \qquad (C.29)$$

- P_{0t} **Calculation**:

The term P_{0t} can be calculated as follows:

$$P_{0t} = \begin{bmatrix} v_{\alpha t} \\ v_{\beta t} \\ v_{0t} \end{bmatrix}^T [C_{\alpha\beta 0}][C_0][C_{\alpha\beta 0}]^T \begin{bmatrix} i_{\alpha t} \\ i_{\beta t} \\ i_{0t} \end{bmatrix} \qquad (C.30)$$

Replacing (C.14) into (C.30), the following expression for P_{0t} is obtained:

$$P_{0t} = \frac{1}{\sqrt{3}}(v_{\alpha t}i_{\alpha t} + v_{\beta t}i_{\beta t} + v_{0t}i_{0t}) \qquad (C.31)$$

C.2 Second $\alpha\beta0$ Transformation - System connected to the output port

C.2.1 Sub-Converter 1, $(r, s, t) \rightarrow \alpha$

Firstly, the power invariant Clarke Transformation is applied to the system composed of $[P_{\alpha r}\ P_{\alpha s}\ P_{\alpha t}]^T$:

$$
\begin{bmatrix} P_{\alpha\alpha} \\ P_{\alpha\beta} \\ P_{\alpha 0} \end{bmatrix} = \sqrt{\frac{2}{3}} \begin{bmatrix} 1 & -1/2 & -1/2 \\ 0 & \sqrt{3}/2 & -\sqrt{3}/2 \\ 1/\sqrt{2} & 1/\sqrt{2} & 1/\sqrt{2} \end{bmatrix} \begin{bmatrix} P_{\alpha r} \\ P_{\alpha s} \\ P_{\alpha t} \end{bmatrix}
\tag{C.32}
$$

- $P_{\alpha\alpha}$ **Calculation**:

Replacing $P_{\alpha r}$ from (B.6), $P_{\alpha s}$ from (B.8) and $P_{\alpha t}$ from (B.10), the following expression for $P_{\alpha\alpha}$ is obtained:

$$
\begin{aligned}
P_{\alpha\alpha} = &\frac{1}{\sqrt{6}} \left[\sqrt{\frac{2}{3}}\left(v_{\alpha r}i_{\alpha r} - \frac{1}{2}v_{\alpha s}i_{\alpha s} - \frac{1}{2}v_{\alpha t}i_{\alpha t}\right) - \sqrt{\frac{2}{3}}\left(v_{\beta r}i_{\beta r} - \frac{1}{2}v_{\beta s}i_{\beta s} - \frac{1}{2}v_{\beta t}i_{\beta t}\right) \right] \\
&+ \frac{1}{\sqrt{3}} \left[\sqrt{\frac{2}{3}}\left(v_{\alpha r}i_{0r} - \frac{1}{2}v_{\alpha s}i_{0s} - \frac{1}{2}v_{\alpha t}i_{0t}\right) + \sqrt{\frac{2}{3}}\left(v_{0r}i_{\alpha r} - \frac{1}{2}v_{0s}i_{\alpha s} - \frac{1}{2}v_{0t}i_{\alpha t}\right) \right]
\end{aligned}
\tag{C.33}
$$

Expressing (C.33) in matrix form:

$$
\begin{aligned}
P_{\alpha\alpha} = &\frac{1}{\sqrt{6}} \left[\begin{bmatrix} v_{\alpha r} \\ v_{\alpha s} \\ v_{\alpha t} \end{bmatrix}^T [C_\alpha] \begin{bmatrix} i_{\alpha r} \\ i_{\alpha s} \\ i_{\alpha t} \end{bmatrix} - \begin{bmatrix} v_{\beta r} \\ v_{\beta s} \\ v_{\beta t} \end{bmatrix}^T [C_\alpha] \begin{bmatrix} i_{\beta r} \\ i_{\beta s} \\ i_{\beta t} \end{bmatrix} \right] \\
&+ \frac{1}{\sqrt{3}} \left[\begin{bmatrix} v_{\alpha r} \\ v_{\alpha s} \\ v_{\alpha t} \end{bmatrix}^T [C_\alpha] \begin{bmatrix} i_{0r} \\ i_{0s} \\ i_{0t} \end{bmatrix} + \begin{bmatrix} v_{0r} \\ v_{0s} \\ v_{0t} \end{bmatrix}^T [C_\alpha] \begin{bmatrix} i_{\alpha r} \\ i_{\alpha s} \\ i_{\alpha t} \end{bmatrix} \right]
\end{aligned}
\tag{C.34}
$$

The voltages and currents of (C.34) can be expressed in $\alpha\beta0$ coordinates as follows:

$$
\begin{bmatrix} v_{\alpha r} \\ v_{\alpha s} \\ v_{\alpha t} \end{bmatrix} = [C_{\alpha\beta0}]^T \begin{bmatrix} v_{\alpha\alpha} \\ v_{\alpha\beta} \\ v_{\alpha 0} \end{bmatrix} \quad ; \quad \begin{bmatrix} i_{\alpha r} \\ i_{\alpha s} \\ i_{\alpha t} \end{bmatrix} = [C_{\alpha\beta0}]^T \begin{bmatrix} i_{\alpha\alpha} \\ i_{\alpha\beta} \\ i_{\alpha 0} \end{bmatrix}
\tag{C.35}
$$

Replacing (C.35) into (C.34) yields to:

$$P_{\alpha\alpha} = \frac{1}{\sqrt{6}} \left[\begin{bmatrix} v_{\alpha\alpha} \\ v_{\alpha\beta} \\ v_{\alpha 0} \end{bmatrix}^T [C_{\alpha\beta 0}] [C_\alpha] [C_{\alpha\beta 0}]^T \begin{bmatrix} i_{\alpha\alpha} \\ i_{\alpha\beta} \\ i_{\alpha 0} \end{bmatrix} - \begin{bmatrix} v_{\beta\alpha} \\ v_{\beta\beta} \\ v_{\beta 0} \end{bmatrix}^T [C_{\alpha\beta 0}] [C_\alpha] [C_{\alpha\beta 0}]^T \begin{bmatrix} i_{\beta\alpha} \\ i_{\beta\beta} \\ i_{\beta 0} \end{bmatrix} \right]$$
$$+ \frac{1}{\sqrt{3}} \left[\begin{bmatrix} v_{\alpha\alpha} \\ v_{\alpha\beta} \\ v_{\alpha 0} \end{bmatrix}^T [C_{\alpha\beta 0}] [C_\alpha] [C_{\alpha\beta 0}]^T \begin{bmatrix} i_{0\alpha} \\ i_{0\beta} \\ i_{00} \end{bmatrix} + \begin{bmatrix} v_{0\alpha} \\ v_{0\beta} \\ v_{00} \end{bmatrix}^T [C_{\alpha\beta 0}] [C_\alpha] [C_{\alpha\beta 0}]^T \begin{bmatrix} i_{\alpha\alpha} \\ i_{\alpha\beta} \\ i_{\alpha 0} \end{bmatrix} \right] \tag{C.36}$$

Replacing the expression of $[C_{\alpha\beta 0}][C_\alpha][C_{\alpha\beta 0}]^T$ [see (C.6)] into (C.36), the following expression for $P_{\alpha\alpha}$ is obtained:

$$P_{\alpha\alpha} = \frac{1}{\sqrt{6}} \left[\frac{1}{\sqrt{6}} (v_{\alpha\alpha} i_{\alpha\alpha} - v_{\alpha\beta} i_{\alpha\beta}) + \frac{1}{\sqrt{3}} (v_{\alpha\alpha} i_{\alpha 0} + v_{\alpha 0} i_{\alpha\beta}) - \frac{1}{\sqrt{6}} (v_{\beta\alpha} i_{\beta\alpha} - v_{\beta\beta} i_{\beta\beta}) - \frac{1}{\sqrt{3}} (v_{\beta\alpha} i_{\beta 0} + v_{\beta 0} i_{\beta\alpha}) \right]$$
$$+ \frac{1}{\sqrt{3}} \left[\frac{1}{\sqrt{6}} (v_{\alpha\alpha} i_{0\alpha} - v_{\alpha\beta} i_{0\beta}) + \frac{1}{\sqrt{3}} (v_{\alpha\alpha} i_{00} + v_{\alpha 0} i_{0\alpha}) - \frac{1}{\sqrt{6}} (v_{0\alpha} i_{\alpha\alpha} - v_{0\beta} i_{\alpha\alpha}) - \frac{1}{\sqrt{3}} (v_{0\alpha} i_{\alpha 0} + v_{00} i_{\alpha\alpha}) \right] \tag{C.37}$$

- $P_{\alpha\beta}$ **Calculation**:

Replacing $P_{\alpha r}$ from (B.6), $P_{\alpha s}$ from (B.8) and $P_{\alpha t}$ from (B.10), the following expression for $P_{\alpha\beta}$ is obtained:

$$P_{\alpha\beta} = \frac{1}{\sqrt{6}} \left[\sqrt{\frac{2}{3}} (\frac{\sqrt{3}}{2} v_{\alpha s} i_{\alpha s} - \frac{\sqrt{3}}{2} v_{\alpha t} i_{\alpha t}) - \sqrt{\frac{2}{3}} (\frac{\sqrt{3}}{2} v_{\beta s} i_{\beta s} - \frac{\sqrt{3}}{2} v_{\beta t} i_{\beta t}) \right]$$
$$+ \frac{1}{\sqrt{3}} \left[\sqrt{\frac{2}{3}} (\frac{\sqrt{3}}{2} v_{\alpha s} i_{0s} - \frac{\sqrt{3}}{2} v_{\alpha t} i_{0t}) + \sqrt{\frac{2}{3}} (\frac{\sqrt{3}}{2} v_{0s} i_{\alpha s} - \frac{\sqrt{3}}{2} v_{0t} i_{\alpha t}) \right] \tag{C.38}$$

Expressing (C.38) in matrix form:

$$P_{\alpha\beta} = \frac{1}{\sqrt{6}} \left[\begin{bmatrix} v_{\alpha r} \\ v_{\alpha s} \\ v_{\alpha t} \end{bmatrix}^T [C_\beta] \begin{bmatrix} i_{\alpha r} \\ i_{\alpha s} \\ i_{\alpha t} \end{bmatrix} - \begin{bmatrix} v_{\beta r} \\ v_{\beta s} \\ v_{\beta t} \end{bmatrix}^T [C_\beta] \begin{bmatrix} i_{\beta r} \\ i_{\beta s} \\ i_{\beta t} \end{bmatrix} \right]$$
$$+ \frac{1}{\sqrt{3}} \left[\begin{bmatrix} v_{\alpha r} \\ v_{\alpha s} \\ v_{\alpha t} \end{bmatrix}^T [C_\beta] \begin{bmatrix} i_{0r} \\ i_{0s} \\ i_{0t} \end{bmatrix} + \begin{bmatrix} v_{0r} \\ v_{0s} \\ v_{0t} \end{bmatrix}^T [C_\beta] \begin{bmatrix} i_{\alpha r} \\ i_{\alpha s} \\ i_{\alpha t} \end{bmatrix} \right] \tag{C.39}$$

Voltages and currents of (C.39) can be expressed in $\alpha\beta 0$ coordinates as shown in (C.35). Consequently, (C.39) becomes:

$$P_{\alpha\beta} = \frac{1}{\sqrt{6}} \left[\begin{bmatrix} v_{\alpha\alpha} \\ v_{\alpha\beta} \\ v_{\alpha 0} \end{bmatrix}^T [C_{\alpha\beta 0}] [C_\beta] [C_{\alpha\beta 0}]^T \begin{bmatrix} i_{\alpha\alpha} \\ i_{\alpha\beta} \\ i_{\alpha 0} \end{bmatrix} - \begin{bmatrix} v_{\beta\alpha} \\ v_{\beta\beta} \\ v_{\beta 0} \end{bmatrix}^T [C_{\alpha\beta 0}] [C_\beta] [C_{\alpha\beta 0}]^T \begin{bmatrix} i_{\beta\alpha} \\ i_{\beta\beta} \\ i_{\beta 0} \end{bmatrix} \right]$$

$$+ \frac{1}{\sqrt{3}} \left[\begin{bmatrix} v_{\alpha\alpha} \\ v_{\alpha\beta} \\ v_{\alpha 0} \end{bmatrix}^T [C_{\alpha\beta 0}] [C_\beta] [C_{\alpha\beta 0}]^T \begin{bmatrix} i_{0\alpha} \\ i_{0\beta} \\ i_{00} \end{bmatrix} + \begin{bmatrix} v_{0\alpha} \\ v_{0\beta} \\ v_{00} \end{bmatrix}^T [C_{\alpha\beta 0}] [C_\beta] [C_{\alpha\beta 0}]^T \begin{bmatrix} i_{\alpha\alpha} \\ i_{\alpha\beta} \\ i_{\alpha 0} \end{bmatrix} \right] \tag{C.40}$$

Replacing the expression of $[C_{\alpha\beta 0}][C_\beta][C_{\alpha\beta 0}]^T$ [see (C.10)] into (C.40), the following expression for $P_{\alpha\beta}$ is obtained:

$$P_{\alpha\beta} = \frac{1}{\sqrt{6}} \left[\frac{-v_{\alpha\alpha} i_{\alpha\beta}}{\sqrt{6}} + v_{\alpha\beta} \left(\frac{-i_{\alpha\alpha}}{\sqrt{6}} + \frac{i_{\alpha 0}}{\sqrt{3}} \right) + \frac{v_{\alpha 0} i_{\alpha\beta}}{\sqrt{3}} + \frac{v_{\beta\alpha} i_{\beta\beta}}{\sqrt{6}} + v_{\beta\beta} \left(\frac{-i_{\beta\alpha}}{\sqrt{6}} + \frac{i_{\beta 0}}{\sqrt{3}} \right) + \frac{v_{\beta 0} i_{\beta\beta}}{\sqrt{3}} \right]$$

$$+ \frac{1}{\sqrt{3}} \left[\frac{-v_{\alpha\alpha} i_{0\beta}}{\sqrt{6}} + v_{\alpha\beta} \left(\frac{-i_{0\alpha}}{\sqrt{6}} + \frac{i_{00}}{\sqrt{3}} \right) + \frac{v_{\alpha 0} i_{0\beta}}{\sqrt{3}} - \frac{v_{0\alpha} i_{\alpha\beta}}{\sqrt{6}} + v_{0\beta} \left(\frac{-i_{\alpha\alpha}}{\sqrt{6}} + \frac{i_{\alpha 0}}{\sqrt{3}} \right) + \frac{v_{00} i_{\alpha\beta}}{\sqrt{3}} \right] \tag{C.41}$$

- $P_{\alpha 0}$ **Calculation**:

Replacing $P_{\alpha r}$ from (B.6), $P_{\alpha s}$ from (B.8) and $P_{\alpha t}$ from (B.10), the following expression for $P_{\alpha 0}$ is obtained:

$$P_{\alpha 0} = \frac{1}{\sqrt{6}} \left[\sqrt{\frac{2}{3}} \left(\frac{1}{\sqrt{2}} v_{\alpha r} i_{\alpha r} + \frac{1}{\sqrt{2}} v_{\alpha s} i_{\alpha s} + \frac{1}{\sqrt{2}} v_{\alpha t} i_{\alpha t} \right) - \sqrt{\frac{2}{3}} \left(\frac{1}{\sqrt{2}} v_{\beta r} i_{\beta r} + \frac{1}{\sqrt{2}} v_{\beta s} i_{\beta s} + \frac{1}{\sqrt{2}} v_{\beta t} i_{\beta t} \right) \right]$$

$$+ \frac{1}{\sqrt{3}} \left[\sqrt{\frac{2}{3}} \left(\frac{1}{\sqrt{2}} v_{\alpha r} i_{0r} + \frac{1}{\sqrt{2}} v_{\alpha s} i_{0s} + \frac{1}{\sqrt{2}} v_{\alpha t} i_{0t} \right) + \sqrt{\frac{2}{3}} \left(\frac{1}{\sqrt{2}} v_{0r} i_{\alpha r} + \frac{1}{\sqrt{2}} v_{0s} i_{\alpha s} + \frac{1}{\sqrt{2}} v_{0t} i_{\alpha t} \right) \right] \tag{C.42}$$

Expressing (C.42) in matrix form:

$$P_{\alpha 0} = \frac{1}{\sqrt{6}} \left[\begin{bmatrix} v_{\alpha r} \\ v_{\alpha s} \\ v_{\alpha t} \end{bmatrix}^T [C_0] \begin{bmatrix} i_{\alpha r} \\ i_{\alpha s} \\ i_{\alpha t} \end{bmatrix} - \begin{bmatrix} v_{\beta r} \\ v_{\beta s} \\ v_{\beta t} \end{bmatrix}^T [C_0] \begin{bmatrix} i_{\beta r} \\ i_{\beta s} \\ i_{\beta t} \end{bmatrix} \right]$$

$$+ \frac{1}{\sqrt{3}} \left[\begin{bmatrix} v_{\alpha r} \\ v_{\alpha s} \\ v_{\alpha t} \end{bmatrix}^T [C_0] \begin{bmatrix} i_{0r} \\ i_{0s} \\ i_{0t} \end{bmatrix} + \begin{bmatrix} v_{0r} \\ v_{0s} \\ v_{0t} \end{bmatrix}^T [C_0] \begin{bmatrix} i_{\alpha r} \\ i_{\alpha s} \\ i_{\alpha t} \end{bmatrix} \right] \tag{C.43}$$

Voltages and currents of (C.43) can be expressed in $\alpha\beta0$ coordinates as shown in (C.35). Consequently, (C.43) becomes:

$$
P_{\alpha0} = \frac{1}{\sqrt{6}} \left[\left[\begin{array}{c} v_{\alpha\alpha} \\ v_{\alpha\beta} \\ v_{\alpha0} \end{array} \right]^T [C_{\alpha\beta0}][C_0][C_{\alpha\beta0}]^T \left[\begin{array}{c} i_{\alpha\alpha} \\ i_{\alpha\beta} \\ i_{\alpha0} \end{array} \right] - \left[\begin{array}{c} v_{\beta\alpha} \\ v_{\beta\beta} \\ v_{\beta0} \end{array} \right]^T [C_{\alpha\beta0}][C_0][C_{\alpha\beta0}]^T \left[\begin{array}{c} i_{\beta\alpha} \\ i_{\beta\beta} \\ i_{\beta0} \end{array} \right] \right]
$$

$$
+ \frac{1}{\sqrt{3}} \left[\left[\begin{array}{c} v_{\alpha\alpha} \\ v_{\alpha\beta} \\ v_{\alpha0} \end{array} \right]^T [C_{\alpha\beta0}][C_0][C_{\alpha\beta0}]^T \left[\begin{array}{c} i_{0\alpha} \\ i_{0\beta} \\ i_{00} \end{array} \right] + \left[\begin{array}{c} v_{0\alpha} \\ v_{0\beta} \\ v_{00} \end{array} \right]^T [C_{\alpha\beta0}][C_0][C_{\alpha\beta0}]^T \left[\begin{array}{c} i_{\alpha\alpha} \\ i_{\alpha\beta} \\ i_{\alpha0} \end{array} \right] \right]
$$

(C.44)

Replacing the expression of $[C_{\alpha\beta0}][C_0][C_{\alpha\beta0}]^T$ [see (C.30)] into (C.44), the following expression for $P_{\alpha\beta}$ is obtained:

$$
P_{\alpha0} = \frac{1}{\sqrt{6}} \left[\frac{1}{\sqrt{3}} (v_{\alpha\alpha}i_{\alpha\alpha} + v_{\alpha\beta}i_{\alpha\beta} + v_{\alpha0}i_{i\alpha0}) - \frac{1}{\sqrt{3}} (v_{\beta\alpha}i_{\beta\alpha} + v_{\beta\beta}i_{\beta\beta} + v_{0\beta}i_{\beta0}) \right]
$$

$$
+ \frac{1}{\sqrt{3}} \left[\frac{1}{\sqrt{3}} (v_{\alpha\alpha}i_{0\alpha} + v_{\alpha\beta}i_{0\beta} + v_{\alpha0}i_{i00}) + \frac{1}{\sqrt{3}} (v_{0\alpha}i_{\alpha\alpha} + v_{0\beta}i_{\alpha\beta} + v_{00}i_{\alpha0}) \right]
$$

(C.45)

C.2.2 Sub-Converter 2, $(r, s, t) \rightarrow \beta$

The power invariant Clarke Transformation is applied to the system composed of $[P_{\beta r}\ P_{\beta s}\ P_{\beta t}]^T$:

$$
\left[\begin{array}{c} P_{\beta\alpha} \\ P_{\beta\beta} \\ P_{\beta0} \end{array} \right] = \sqrt{\frac{2}{3}} \left[\begin{array}{ccc} 1 & -1/2 & -1/2 \\ 0 & \sqrt{3}/2 & -\sqrt{3}/2 \\ 1/\sqrt{2} & 1/\sqrt{2} & 1/\sqrt{2} \end{array} \right] \left[\begin{array}{c} P_{\beta r} \\ P_{\beta s} \\ P_{\beta t} \end{array} \right]
$$

(C.46)

- $P_{\beta\alpha}$ **Calculation**:

Replacing $P_{\beta r}$ from (B.6), $P_{\beta s}$ from (B.8) and $P_{\beta t}$ from (B.10) into (C.46), the following expression for $P_{\beta\alpha}$ is obtained:

$$
P_{\beta\alpha} = \frac{-1}{\sqrt{6}} \left[\sqrt{\frac{2}{3}} (v_{\alpha r}i_{\beta r} - \frac{1}{2}v_{\alpha s}i_{\beta s} - \frac{1}{2}v_{\alpha t}i_{\beta t}) + \sqrt{\frac{2}{3}} (v_{\beta r}i_{\alpha r} - \frac{1}{2}v_{\beta s}i_{\alpha s} - \frac{1}{2}v_{\beta t}i_{\alpha t}) \right]
$$

$$
+ \frac{1}{\sqrt{3}} \left[\sqrt{\frac{2}{3}} (v_{\beta r}i_{0r} - \frac{1}{2}v_{\beta s}i_{0s} - \frac{1}{2}v_{\beta t}i_{0t}) + \sqrt{\frac{2}{3}} (v_{0r}i_{\beta r} - \frac{1}{2}v_{0s}i_{\beta s} - \frac{1}{2}v_{0t}i_{\beta t}) \right]
$$

(C.47)

Expressing (C.42) in matrix form:

$$
P_{\beta\alpha} = \frac{-1}{\sqrt{6}} \left[\begin{bmatrix} v_{\alpha r} \\ v_{\alpha s} \\ v_{\alpha t} \end{bmatrix}^T [C_\alpha] \begin{bmatrix} i_{\beta r} \\ i_{\beta s} \\ i_{\beta t} \end{bmatrix} + \begin{bmatrix} v_{\beta r} \\ v_{\beta s} \\ v_{\beta t} \end{bmatrix}^T [C_\alpha] \begin{bmatrix} i_{\alpha r} \\ i_{\alpha s} \\ i_{\alpha t} \end{bmatrix} \right]
$$
$$
+ \frac{1}{\sqrt{3}} \left[\begin{bmatrix} v_{\beta r} \\ v_{\beta s} \\ v_{\beta t} \end{bmatrix}^T [C_\alpha] \begin{bmatrix} i_{0r} \\ i_{0s} \\ i_{0t} \end{bmatrix} + \begin{bmatrix} v_{0r} \\ v_{0s} \\ v_{0t} \end{bmatrix}^T \sqrt{\frac{2}{3}}[C_\alpha] \begin{bmatrix} i_{\beta r} \\ i_{\beta s} \\ i_{\beta t} \end{bmatrix} \right]
$$

(C.48)

Voltages and currents of (C.48) can be expressed in $\alpha\beta 0$ coordinates as follows:

$$
\begin{bmatrix} v_{\beta r} \\ v_{\beta s} \\ v_{\beta t} \end{bmatrix} = [C_{\alpha\beta 0}]^T \begin{bmatrix} v_{\beta\alpha} \\ v_{\beta\beta} \\ v_{\beta 0} \end{bmatrix} \quad ; \quad \begin{bmatrix} i_{\beta r} \\ i_{\beta s} \\ i_{\beta t} \end{bmatrix} = [C_{\alpha\beta 0}]^T \begin{bmatrix} i_{\beta\alpha} \\ i_{\beta\beta} \\ i_{\beta 0} \end{bmatrix}
$$

(C.49)

Replacing (C.49) into (C.48) yields to:

$$
P_{\beta\alpha} = \frac{-1}{\sqrt{6}} \left[\begin{bmatrix} v_{\alpha\alpha} \\ v_{\alpha\beta} \\ v_{\alpha 0} \end{bmatrix}^T [C_{\alpha\beta 0}][C_\alpha][C_{\alpha\beta 0}]^T \begin{bmatrix} i_{\beta\alpha} \\ i_{\beta\beta} \\ i_{\beta 0} \end{bmatrix} + \begin{bmatrix} v_{\beta\alpha} \\ v_{\beta\beta} \\ v_{\beta 0} \end{bmatrix}^T [C_{\alpha\beta 0}][C_\alpha][C_{\alpha\beta 0}]^T \begin{bmatrix} i_{\alpha\alpha} \\ i_{\alpha\beta} \\ i_{\alpha 0} \end{bmatrix} \right]
$$
$$
+ \frac{1}{\sqrt{3}} \left[\begin{bmatrix} v_{\beta\alpha} \\ v_{\beta\beta} \\ v_{\beta 0} \end{bmatrix}^T [C_{\alpha\beta 0}][C_\alpha][C_{\alpha\beta 0}]^T \begin{bmatrix} i_{0\alpha} \\ i_{0\beta} \\ i_{00} \end{bmatrix} + \begin{bmatrix} v_{0\alpha} \\ v_{0\beta} \\ v_{00} \end{bmatrix}^T [C_{\alpha\beta 0}][C_\alpha][C_{\alpha\beta 0}]^T \begin{bmatrix} i_{\beta\alpha} \\ i_{\beta\beta} \\ i_{\beta 0} \end{bmatrix} \right]
$$

(C.50)

Replacing the expression of $[C_{\alpha\beta 0}][C_\alpha][C_{\alpha\beta 0}]^T$ [see (C.6)] into (C.50), the following expression for $P_{\alpha\beta}$ is obtained:

$$
P_{\beta\alpha} = \frac{-1}{\sqrt{6}} \left[v_{\alpha\alpha}\left(\frac{i_{\beta\alpha}}{\sqrt{6}} + \frac{i_{\beta 0}}{\sqrt{3}}\right) - \frac{v_{\alpha\beta}i_{\beta\beta}}{\sqrt{6}} + \frac{v_{\alpha 0}i_{\beta\alpha}}{\sqrt{3}} + v_{\beta\alpha}\left(\frac{i_{\alpha\alpha}}{\sqrt{6-}} + \frac{i_{\alpha 0}}{\sqrt{3}}\right) + \frac{-v_{\beta\beta}i_{\alpha\beta}}{\sqrt{6}} + \frac{v_{\beta 0}i_{\alpha\alpha}}{\sqrt{3}} \right]
$$
$$
+ \frac{1}{\sqrt{3}} \left[v_{\beta\alpha}\left(\frac{i_{0\alpha}}{\sqrt{6}} + \frac{i_{00}}{\sqrt{3}}\right) - \frac{v_{\beta\beta}i_{0\beta}}{\sqrt{6}} + \frac{v_{\beta 0}i_{0\alpha}}{\sqrt{3}} + v_{0\alpha}\left(\frac{i_{\beta\alpha}}{\sqrt{6}} + \frac{i_{\beta 0}}{\sqrt{3}}\right) + \frac{-1v_{0\beta}i_{\beta\beta}}{\sqrt{6}} + \frac{v_{00}i_{\beta\alpha}}{\sqrt{3}} \right]
$$

(C.51)

- $P_{\beta\beta}$ **Calculation**:

Replacing $P_{\beta r}$ from (B.6), $P_{\beta s}$ from (B.8) and $P_{\beta t}$ from (B.10) into (C.46), the following expression for $P_{\beta\beta}$ is obtained:

$$P_{\beta\beta}=\frac{-1}{\sqrt{6}}\left[\sqrt{\frac{2}{3}}\frac{\sqrt{3}}{2}v_{\alpha s}i_{\beta s}-\frac{\sqrt{3}}{2}v_{\alpha t}i_{\beta t})+\sqrt{\frac{2}{3}}(\frac{\sqrt{3}}{2}v_{\beta s}i_{\alpha s}-\frac{\sqrt{3}}{2}v_{\beta t}i_{\alpha t})\right]$$
$$+\frac{1}{\sqrt{3}}\left[\sqrt{\frac{2}{3}}(\frac{\sqrt{3}}{2}v_{\beta s}i_{0s}-\frac{\sqrt{3}}{2}v_{\beta t}i_{0t})+\sqrt{\frac{2}{3}}(\frac{\sqrt{3}}{2}v_{0s}i_{\beta s}-\frac{\sqrt{3}}{2}v_{0t}i_{\beta t})\right] \quad\text{(C.52)}$$

In matrix form:

$$P_{\beta\beta}=\frac{-1}{\sqrt{6}}\left[\begin{bmatrix}v_{\alpha r}\\v_{\alpha s}\\v_{\alpha t}\end{bmatrix}^{T}[C_{\beta}]\begin{bmatrix}i_{\beta r}\\i_{\beta s}\\i_{\beta t}\end{bmatrix}+\begin{bmatrix}v_{\beta r}\\v_{\beta s}\\v_{\beta t}\end{bmatrix}^{T}[C_{\beta}]\begin{bmatrix}i_{\alpha r}\\i_{\alpha s}\\i_{\alpha t}\end{bmatrix}\right]$$
$$+\frac{1}{\sqrt{3}}\left[\begin{bmatrix}v_{\beta r}\\v_{\beta s}\\v_{\beta t}\end{bmatrix}^{T}[C_{\beta}]\begin{bmatrix}i_{0r}\\i_{0s}\\i_{0t}\end{bmatrix}+\begin{bmatrix}v_{0r}\\v_{0s}\\v_{0t}\end{bmatrix}^{T}[C_{\beta}]\begin{bmatrix}i_{\beta r}\\i_{\beta s}\\i_{\beta t}\end{bmatrix}\right] \quad\text{(C.53)}$$

Replacing the voltages and currents of (C.49) into (C.53):

$$P_{\beta\beta}=\frac{-1}{\sqrt{6}}\left[\begin{bmatrix}v_{\alpha\alpha}\\v_{\alpha\beta}\\v_{\alpha 0}\end{bmatrix}^{T}[C_{\alpha\beta 0}][C_{\beta}][C_{\alpha\beta 0}]^{T}\begin{bmatrix}i_{\beta\alpha}\\i_{\beta\beta}\\i_{\beta 0}\end{bmatrix}+\begin{bmatrix}v_{\beta\alpha}\\v_{\beta\beta}\\v_{\beta 0}\end{bmatrix}^{T}[C_{\alpha\beta 0}][C_{\beta}][C_{\alpha\beta 0}]^{T}\begin{bmatrix}i_{\alpha\alpha}\\i_{\alpha\beta}\\i_{\alpha 0}\end{bmatrix}\right]$$
$$+\frac{1}{\sqrt{3}}\left[\begin{bmatrix}v_{\beta\alpha}\\v_{\beta\beta}\\v_{\beta 0}\end{bmatrix}^{T}[C_{\alpha\beta 0}][C_{\beta}][C_{\alpha\beta 0}]^{T}\begin{bmatrix}i_{0\alpha}\\i_{0\beta}\\i_{00}\end{bmatrix}+\begin{bmatrix}v_{0\alpha}\\v_{0\beta}\\v_{00}\end{bmatrix}^{T}[C_{\alpha\beta 0}][C_{\beta}][C_{\alpha\beta 0}]^{T}\begin{bmatrix}i_{\beta\alpha}\\i_{\beta\beta}\\i_{\beta 0}\end{bmatrix}\right]$$
$$\text{(C.54)}$$

Additionally, using the expression of $[C_{\alpha\beta 0}][C_{\beta}][C_{\alpha\beta 0}]^{T}$ [see (C.10)], the following expression for $P_{\beta\beta}$ is obtained:

$$P_{\beta\beta}=\frac{-1}{\sqrt{6}}[\frac{-v_{\alpha\alpha}i_{\beta\beta}}{\sqrt{6}}+v_{\alpha\beta}(\frac{-i_{\beta\alpha}}{\sqrt{6}}+\frac{i_{\beta 0}}{\sqrt{3}})+\frac{v_{\alpha 0}i_{\beta\beta}}{\sqrt{3}}+v_{\beta\alpha}\frac{-i_{\alpha\beta}}{\sqrt{6}}+v_{\beta\beta}(\frac{-i_{\alpha\alpha}}{\sqrt{6}}+\frac{i_{\alpha 0}}{\sqrt{3}})+\frac{v_{\beta 0}i_{\alpha\beta}}{\sqrt{3}}]$$
$$+\frac{1}{\sqrt{3}}[-\frac{v_{\beta\alpha}i_{0\beta}}{\sqrt{6}}+v_{\beta\beta}(\frac{-i_{0\alpha}}{\sqrt{6}}+\frac{i_{00}}{\sqrt{3}})+\frac{v_{\beta 0}i_{0\beta}}{\sqrt{3}}+\frac{-v_{0\alpha}i_{\beta\beta}}{\sqrt{6}}+v_{0\beta}(\frac{-i_{\beta\alpha}}{\sqrt{6}}+\frac{i_{\beta 0}}{\sqrt{3}})+\frac{v_{00}i_{\beta\beta}}{\sqrt{3}}] \quad\text{(C.55)}$$

- $P_{\beta 0}$ **Calculation**:

Replacing $P_{\beta r}$ from (B.6), $P_{\beta s}$ from (B.8) and $P_{\beta t}$ from (B.10) into (C.46), the following expression for $P_{\beta 0}$ is obtained:

$$P_{\beta0}=\frac{-1}{\sqrt{6}}\left[\sqrt{\frac{2}{3}}(\frac{1}{\sqrt{2}}v_{\alpha r}i_{\beta r}+\frac{1}{\sqrt{2}}v_{\alpha s}i_{\beta s}+\frac{1}{\sqrt{2}}v_{\alpha t}i_{\beta t})+\sqrt{\frac{2}{3}}(\frac{1}{\sqrt{2}}v_{\beta r}i_{\alpha r}+\frac{1}{\sqrt{2}}v_{\beta s}i_{\alpha s}+\frac{1}{\sqrt{2}}v_{\beta t}i_{\alpha t})\right]$$
$$+\frac{1}{\sqrt{3}}\left[\sqrt{\frac{2}{3}}(\frac{1}{\sqrt{2}}v_{\beta r}i_{0r}+\frac{1}{\sqrt{2}}v_{\beta s}i_{0s}+\frac{1}{\sqrt{2}}v_{\beta t}i_{0t})+\sqrt{\frac{2}{3}}(\frac{1}{\sqrt{2}}v_{0r}i_{\beta r}+\frac{1}{\sqrt{2}}v_{0s}i_{\beta s}+\frac{1}{\sqrt{2}}v_{0t}i_{\beta t})\right]$$

(C.56)

In matrix form:

$$P_{\beta0}=\frac{-1}{\sqrt{6}}\left[\begin{bmatrix}v_{\alpha r}\\v_{\alpha s}\\v_{\alpha t}\end{bmatrix}^{T}[C_0]\begin{bmatrix}i_{\beta r}\\i_{\beta s}\\i_{\beta t}\end{bmatrix}+\begin{bmatrix}v_{\beta r}\\v_{\beta s}\\v_{\beta t}\end{bmatrix}^{T}[C_0]\begin{bmatrix}i_{\alpha r}\\i_{\alpha s}\\i_{\alpha t}\end{bmatrix}\right]$$
$$+\frac{1}{\sqrt{3}}\left[\begin{bmatrix}v_{\beta r}\\v_{\beta s}\\v_{\beta t}\end{bmatrix}^{T}[C_0]\begin{bmatrix}i_{0r}\\i_{0s}\\i_{0t}\end{bmatrix}+\begin{bmatrix}v_{0r}\\v_{0s}\\v_{0t}\end{bmatrix}^{T}[C_0]\begin{bmatrix}i_{\beta r}\\i_{\beta s}\\i_{\beta t}\end{bmatrix}\right]$$

(C.57)

Replacing the voltages and currents of (C.57) by their components in $\alpha\beta0$ [see(C.49)]:

$$P_{\beta0}=\frac{-1}{\sqrt{6}}\left[\begin{bmatrix}v_{\alpha\alpha}\\v_{\alpha\beta}\\v_{\alpha0}\end{bmatrix}^{T}[C_{\alpha\beta0}][C_0][C_{\alpha\beta0}]^{T}\begin{bmatrix}i_{\beta\alpha}\\i_{\beta\beta}\\i_{\beta0}\end{bmatrix}+\begin{bmatrix}v_{\beta\alpha}\\v_{\beta\beta}\\v_{\beta0}\end{bmatrix}^{T}[C_{\alpha\beta0}][C_0][C_{\alpha\beta0}]^{T}\begin{bmatrix}i_{\alpha\alpha}\\i_{\alpha\beta}\\i_{\alpha0}\end{bmatrix}\right]$$
$$+\frac{1}{\sqrt{3}}\left[\begin{bmatrix}v_{\beta\alpha}\\v_{\beta\beta}\\v_{\beta0}\end{bmatrix}^{T}[C_{\alpha\beta0}][C_0][C_{\alpha\beta0}]^{T}\begin{bmatrix}i_{0\alpha}\\i_{0\beta}\\i_{00}\end{bmatrix}+\begin{bmatrix}v_{0\alpha}\\v_{0\beta}\\v_{00}\end{bmatrix}^{T}[C_{\alpha\beta0}][C_0][C_{\alpha\beta0}]^{T}\begin{bmatrix}i_{\beta\alpha}\\i_{\beta\beta}\\i_{\beta0}\end{bmatrix}\right]$$

(C.58)

Additionally, using the expression of $[C_{\alpha\beta0}][C_0][C_{\alpha\beta0}]^{T}$ [see (C.14)], the following expression for $P_{\beta0}$ is obtained:

$$P_{\beta0}=\frac{-1}{\sqrt{6}}[\frac{1}{\sqrt{3}}(v_{\alpha\alpha}i_{\beta\alpha}+v_{\alpha\beta}i_{\beta\beta}+v_{\alpha0}i_{\beta0})+\frac{1}{\sqrt{3}}(v_{\beta\alpha}i_{\alpha\alpha}+v_{\beta\beta}i_{\alpha\beta}+v_{0\beta}i_{\alpha0})]$$
$$+\frac{1}{\sqrt{3}}[\frac{1}{\sqrt{3}}(v_{\beta\alpha}i_{0\alpha}+v_{\beta\beta}i_{0\beta}+v_{\beta0}i_{00})+\frac{1}{\sqrt{3}}(v_{0\alpha}i_{\alpha\alpha}+v_{0\beta}i_{\alpha\beta}+v_{00}i_{\alpha0})]$$

(C.59)

C.2.3 Sub-Converter 3, $(r, s, t) \to 0$

The power invariant Clarke Transformation is applied to the system composed of $[P_{0r} \ P_{0s} \ P_{0t}]^T$:

$$\begin{bmatrix} P_{0\alpha} \\ P_{0\beta} \\ P_{00} \end{bmatrix} = \sqrt{\frac{2}{3}} \begin{bmatrix} 1 & -1/2 & -1/2 \\ 0 & \sqrt{3}/2 & -\sqrt{3}/2 \\ 1/\sqrt{2} & 1/\sqrt{2} & 1/\sqrt{2} \end{bmatrix} * \begin{bmatrix} P_{0r} \\ P_{0s} \\ P_{0t} \end{bmatrix}$$

- $P_{0\alpha}$ **Calculation**:

Replacing P_{0r} from (B.6), P_{0s} from (B.8) and P_{0t} from (B.10) into (C.46), the following expression for $P_{0\alpha}$ is obtained:

$$
\begin{aligned}
P_{0\alpha} = \frac{1}{\sqrt{3}} \Big[&\sqrt{\frac{2}{3}} \big(v_{\alpha r} i_{\alpha r} - \frac{1}{2} v_{\alpha s} i_{\alpha s} - \frac{1}{2} v_{\alpha t} i_{\alpha t}\big) + \sqrt{\frac{2}{3}} \big(v_{\beta r} i_{\beta r} - \frac{1}{2} v_{\beta s} i_{\beta s} - \frac{1}{2} v_{\beta t} i_{\beta t}\big) \\
&+ \sqrt{\frac{2}{3}} \big(v_{0r} i_{0r} - \frac{1}{2} v_{0s} i_{0s} - \frac{1}{2} v_{0t} i_{0t}\big) \Big]
\end{aligned}
\tag{C.60}
$$

Expressing (C.60) in matrix form:

$$
P_{0\alpha} = \frac{1}{\sqrt{3}} \left[\begin{bmatrix} v_{\alpha r} \\ v_{\alpha s} \\ v_{\alpha t} \end{bmatrix}^T [C_\alpha] \begin{bmatrix} i_{\alpha r} \\ i_{\alpha s} \\ i_{\alpha t} \end{bmatrix} + \begin{bmatrix} v_{\beta r} \\ v_{\beta s} \\ v_{\beta t} \end{bmatrix}^T [C_\alpha] \begin{bmatrix} i_{\beta r} \\ i_{\beta s} \\ i_{\beta t} \end{bmatrix} + \begin{bmatrix} v_{0r} \\ v_{0s} \\ v_{0t} \end{bmatrix}^T [C_\alpha] \begin{bmatrix} i_{0r} \\ i_{0s} \\ i_{0t} \end{bmatrix} \right]
\tag{C.61}
$$

Voltages and currents of (C.61) can be expressed in $\alpha\beta 0$ coordinates as follows:

$$
\begin{bmatrix} v_{0r} \\ v_{0s} \\ v_{0t} \end{bmatrix} = [C_{\alpha\beta 0}]^T \begin{bmatrix} v_{0\alpha} \\ v_{0\beta} \\ v_{00} \end{bmatrix} \quad ; \quad \begin{bmatrix} i_{0r} \\ i_{0s} \\ i_{0t} \end{bmatrix} = [C_{\alpha\beta 0}]^T \begin{bmatrix} i_{0\alpha} \\ i_{0\beta} \\ i_{00} \end{bmatrix}
\tag{C.62}
$$

Replacing (C.62) into (C.61) yields to:

$$P_{0\alpha}=\frac{1}{\sqrt{3}}\left[\left[\begin{array}{c} v_{\alpha\alpha} \\ v_{\alpha\beta} \\ v_{\alpha 0} \end{array}\right]^{T}[C_{\alpha\beta 0}][C_{\alpha}][C_{\alpha\beta 0}]^{T}\left[\begin{array}{c} i_{\alpha\alpha} \\ i_{\alpha\beta} \\ i_{\alpha 0} \end{array}\right]+\left[\begin{array}{c} v_{\beta\alpha} \\ v_{\beta\beta} \\ v_{\beta 0} \end{array}\right]^{T}[C_{\alpha\beta 0}][C_{\alpha}][C_{\alpha\beta 0}]^{T}\left[\begin{array}{c} i_{\beta\alpha} \\ i_{\beta\beta} \\ i_{\beta 0} \end{array}\right]\right.$$
$$\left.+\left[\begin{array}{c} v_{0\alpha} \\ v_{0\beta} \\ v_{00} \end{array}\right]^{T}[C_{\alpha\beta 0}][C_{\alpha}][C_{\alpha\beta 0}]^{T}\left[\begin{array}{c} i_{0\alpha} \\ i_{0\beta} \\ i_{00} \end{array}\right]\right]$$

(C.63)

Replacing the expression of $[C_{\alpha\beta 0}][C_{\alpha}][C_{\alpha\beta 0}]^{T}$ [see (C.6)] into (C.63), the following expression for $P_{0\alpha}$ is obtained:

$$P_{0\alpha}=\frac{1}{\sqrt{3}}\left[v_{\alpha\alpha}(\frac{1}{\sqrt{6}}i_{\alpha\alpha}+\frac{1}{\sqrt{3}}i_{\alpha 0})+\frac{-1}{\sqrt{6}}v_{\alpha\beta}i_{\alpha\beta}+\frac{1}{\sqrt{3}}v_{\alpha 0}i_{\alpha\alpha}+v_{\beta\alpha}(\frac{1}{\sqrt{6}}i_{\beta\alpha}+\frac{1}{\sqrt{3}}i_{\beta 0})\right.$$
$$\left.+\frac{-1}{\sqrt{6}}v_{\beta\beta}i_{\beta\beta}+\frac{1}{\sqrt{3}}v_{\beta 0}i_{\beta\alpha}+v_{0\alpha}(\frac{1}{\sqrt{6}}i_{0\alpha}+\frac{1}{\sqrt{3}}i_{00})+\frac{-1}{\sqrt{6}}v_{0\beta}i_{0\beta}+\frac{1}{\sqrt{3}}i_{0\alpha}v_{00}\right]$$

(C.64)

- $P_{0\beta}$ **Calculation**:

Replacing P_{0r} from (B.6), P_{0s} from (B.8) and P_{0t} from (B.10) into (C.46), the following expression for $P_{0\beta}$ is obtained:

$$P_{0\beta}=\frac{1}{\sqrt{3}}\left[\sqrt{\frac{2}{3}}(\frac{\sqrt{3}}{2}v_{\alpha s}i_{\alpha s}-\frac{\sqrt{3}}{2}v_{\alpha t}i_{\alpha t})+\sqrt{\frac{2}{3}}(\frac{\sqrt{3}}{2}v_{\beta s}i_{\beta s}-\frac{\sqrt{3}}{2}v_{\beta t}i_{\beta t})\right.$$
$$\left.+\sqrt{\frac{2}{3}}(\frac{\sqrt{3}}{2}v_{0s}i_{0s}-\frac{\sqrt{3}}{2}v_{0t}i_{0t})\right]$$

(C.65)

In matrix form:

$$P_{0\beta}=\frac{1}{\sqrt{3}}\left[\left[\begin{array}{c} v_{\alpha r} \\ v_{\alpha s} \\ v_{\alpha t} \end{array}\right]^{T}[C_{\beta}]\left[\begin{array}{c} i_{\alpha r} \\ i_{\alpha s} \\ i_{\alpha t} \end{array}\right]+\left[\begin{array}{c} v_{\beta r} \\ v_{\beta s} \\ v_{\beta t} \end{array}\right]^{T}[C_{\beta}]\left[\begin{array}{c} i_{\beta r} \\ i_{\beta s} \\ i_{\beta t} \end{array}\right]\right.$$
$$\left.+\left[\begin{array}{c} v_{0r} \\ v_{0s} \\ v_{0t} \end{array}\right]^{T}[C_{\beta}]\left[\begin{array}{c} i_{0r} \\ i_{0s} \\ i_{0t} \end{array}\right]\right]$$

(C.66)

Replacing the voltages and currents of (C.66) by their components in $\alpha\beta 0$ [see(C.62)]:

$$
P_{0\beta}=\frac{1}{\sqrt{3}}\left[\left[\begin{array}{c} v_{\alpha\alpha} \\ v_{\alpha\beta} \\ v_{\alpha0} \end{array}\right]^{T} [C_{\alpha\beta0}][C_{\beta}][C_{\alpha\beta0}]^{T} \left[\begin{array}{c} i_{\alpha\alpha} \\ i_{\alpha\beta} \\ i_{\alpha0} \end{array}\right] + \left[\begin{array}{c} v_{\beta\alpha} \\ v_{\beta\beta} \\ v_{\beta0} \end{array}\right]^{T} [C_{\alpha\beta0}][C_{\beta}][C_{\alpha\beta0}]^{T} \left[\begin{array}{c} i_{\beta\alpha} \\ i_{\beta\beta} \\ i_{\beta0} \end{array}\right] \right.
$$
$$
\left. + \left[\begin{array}{c} v_{0\alpha} \\ v_{0\beta} \\ v_{00} \end{array}\right]^{T} [C_{\alpha\beta0}][C_{\beta}][C_{\alpha\beta0}]^{T} \left[\begin{array}{c} i_{0\alpha} \\ i_{0\beta} \\ i_{00} \end{array}\right] \right]
$$
(C.67)

Additionally, replacing the expression of $[C_{\alpha\beta0}][C_{\beta}][C_{\alpha\beta0}]^{T}$ [see (C.10)] into(C.67), the following expression for $P_{0\beta}$ is obtained:

$$
P_{0\beta}=\frac{1}{\sqrt{3}}\left[\frac{-1}{\sqrt{6}}v_{\alpha\alpha}i_{\alpha\beta}+v_{\alpha\beta}(-\frac{1}{\sqrt{6}}i_{\alpha\alpha}+\frac{1}{\sqrt{3}}i_{\alpha0})+\frac{1}{\sqrt{3}}v_{\alpha0}i_{\alpha\beta}+\frac{-1}{\sqrt{6}}v_{\beta\alpha}i_{\beta\beta} \right.
$$
$$
\left. +v_{\beta\beta}(\frac{-1}{\sqrt{6}}i_{\beta\alpha}+\frac{1}{\sqrt{3}}i_{\beta0})+\frac{1}{\sqrt{3}}v_{\beta0}i_{\beta\beta}-\frac{1}{\sqrt{6}}v_{0\alpha}i_{0\beta}+v_{0\beta}(\frac{-1}{\sqrt{6}}i_{0\alpha}+\frac{1}{\sqrt{3}}i_{00})+\frac{1}{\sqrt{3}}v_{00}i_{0\beta}\right]
$$
(C.68)

- P_{00} **Calculation**:

Replacing P_{0r} from (B.6), P_{0s} from (B.8) and P_{0t} from (B.10) into (C.46), the following expression for P_{00} is obtained:

$$
P_{00}=\frac{1}{\sqrt{3}}\left[\sqrt{\frac{2}{3}}(\frac{1}{\sqrt{2}}v_{\alpha r}i_{\alpha r}+\frac{1}{\sqrt{2}}v_{\alpha s}i_{\alpha s}+\frac{1}{\sqrt{2}}v_{\alpha t}i_{\alpha t})+\sqrt{\frac{2}{3}}(\frac{1}{\sqrt{2}}v_{\beta r}i_{\beta r}+\frac{1}{\sqrt{2}}v_{\beta s}i_{\beta s}+\frac{1}{\sqrt{2}}v_{\beta t}i_{\beta t}) \right.
$$
$$
\left. +\sqrt{\frac{2}{3}}(\frac{1}{\sqrt{2}}v_{0r}i_{0r}+\frac{1}{\sqrt{2}}v_{0s}i_{0s}+\frac{1}{\sqrt{2}}v_{0t}i_{0t})\right]
$$
(C.69)

In matrix form:

$$
P_{00}=\frac{1}{\sqrt{3}}\left[\left[\begin{array}{c} v_{\alpha\alpha} \\ v_{\alpha\beta} \\ v_{\alpha0} \end{array}\right]^{T} [C_{0}] \left[\begin{array}{c} i_{\alpha\alpha} \\ i_{\alpha\beta} \\ i_{\alpha0} \end{array}\right] + \left[\begin{array}{c} v_{\beta\alpha} \\ v_{\beta\beta} \\ v_{\beta0} \end{array}\right]^{T} [C_{0}] \left[\begin{array}{c} i_{\beta\alpha} \\ i_{\beta\beta} \\ i_{\beta0} \end{array}\right] \right.
$$
$$
\left. + \left[\begin{array}{c} v_{0\alpha} \\ v_{0\beta} \\ v_{00} \end{array}\right]^{T} [C_{0}] \left[\begin{array}{c} i_{0\alpha} \\ i_{0\beta} \\ i_{00} \end{array}\right] \right]
$$
(C.70)

Replacing the voltages and currents of (C.70) by their components in $\alpha\beta0$ [see(C.62)]:

$$P_{00}=\frac{1}{\sqrt{3}}\left[\left[\begin{array}{c}v_{\alpha\alpha}\\v_{\alpha\beta}\\v_{\alpha0}\end{array}\right]^{T}[C_{\alpha\beta0}][C_{0}][C_{\alpha\beta0}]^{T}\left[\begin{array}{c}i_{\alpha\alpha}\\i_{\alpha\beta}\\i_{\alpha0}\end{array}\right]+\left[\begin{array}{c}v_{\beta\alpha}\\v_{\beta\beta}\\v_{\beta0}\end{array}\right]^{T}[C_{\alpha\beta0}][C_{0}][C_{\alpha\beta0}]^{T}\left[\begin{array}{c}i_{\beta\alpha}\\i_{\beta\beta}\\i_{\beta0}\end{array}\right]\right.$$
$$\left.+\left[\begin{array}{c}v_{0\alpha}\\v_{0\beta}\\v_{00}\end{array}\right]^{T}[C_{\alpha\beta0}][C_{0}][C_{\alpha\beta0}]^{T}\left[\begin{array}{c}i_{0\alpha}\\i_{0\beta}\\i_{00}\end{array}\right]\right]$$

<div align="right">(C.71)</div>

Additionally, replacing the expression of $[C_{\alpha\beta0}][C_{0}][C_{\alpha\beta0}]^{T}$ [see (C.14)] into (C.71), the following expression for (C.71) is obtained:

$$P_{00}=\frac{1}{\sqrt{3}}\left[\frac{1}{\sqrt{3}}v_{\alpha\alpha}i_{\alpha\alpha}+\frac{1}{\sqrt{3}}v_{\alpha\beta}i_{\alpha\beta}+\frac{1}{\sqrt{3}}v_{\alpha0}i_{\alpha0}+\frac{1}{\sqrt{3}}v_{\beta\alpha}i_{\beta\alpha}+\frac{1}{\sqrt{3}}v_{\beta\beta}i_{\beta\beta}+\frac{1}{\sqrt{3}}v_{\beta0}i_{\beta0}\right.$$
$$\left.+\frac{1}{\sqrt{3}}v_{0\alpha}i_{0\alpha}+\frac{1}{\sqrt{3}}v_{0\beta}i_{0\beta}+\frac{1}{\sqrt{3}}v_{00}i_{00}\right]$$

<div align="right">(C.72)</div>

C.3 Final equations

From (A.26)−(A.29) and (A.34)−(A.37) it is known that:

- $i_{\alpha0}=\frac{1}{\sqrt{3}}i_{m\alpha}$; $i_{\beta0}=\frac{1}{\sqrt{3}}i_{m\alpha}$

- $i_{0\alpha}=\frac{1}{\sqrt{3}}i_{g\beta}$; $i_{0\alpha}=\frac{1}{\sqrt{3}}i_{g\alpha}$

Additionally, it is assumed that there is not current path between neutral points N and n (i.e. $i_{00}=0$), the voltages connected to the input-output ports are balanced (i.e. $v_{g0}=v_{m0}=0$) and the voltage drop in the cluster inductors is small and can be neglected. Accordingly, the Voltage-Current Model in Double $\alpha\beta0$ coordinates of (3.20) becomes:

$$\left[\begin{array}{ccc}v_{\alpha\alpha}&v_{\beta\alpha}&v_{0\alpha}\\v_{\alpha\beta}&v_{\beta\beta}&v_{0\beta}\\v_{\alpha0}&v_{\beta0}&v_{00}\end{array}\right]=\sqrt{3}\left[\begin{array}{ccc}0&0&0\\0&0&0\\v_{m\alpha}&v_{m\beta}&0\end{array}\right]-\sqrt{3}\left[\begin{array}{ccc}0&0&v_{g\alpha}\\0&0&v_{g\beta}\\0&0&0\end{array}\right]-\left[\begin{array}{ccc}0&0&0\\0&0&0\\0&0&3v_{n}\end{array}\right]$$

<div align="right">(C.73)</div>

Therefore:

$$\begin{array}{ccc} v_{\alpha\alpha}=0 & v_{\beta\alpha}=0 & v_{0\alpha}=-\sqrt{3}v_{g\alpha} \\ v_{\alpha\beta}=0 & v_{\beta\beta}=0 & v_{0\beta}=-\sqrt{3}v_{g\beta} \\ v_{\alpha0}=\sqrt{3}v_{m\alpha} & v_{\beta0}=\sqrt{3}v_{00} & v_{00}-3v_n \end{array} \tag{C.74}$$

Finally, the power components given in (3.22)$-$(3.30) are obtained as follows:

- Replacing (C.73) into (C.37) yields to (3.22)

- Replacing (C.73) into (C.41) yields to (3.23)

- Replacing (C.73) into (C.51) yields to (3.24)

- Replacing (C.73) into (C.55) yields to (3.25)

- Replacing (C.73) into (C.45) yields to (3.26)

- Replacing (C.73) into (C.59) yields to (3.27)

- Replacing (C.73) into (C.64) yields to (3.28)

- Replacing (C.73) into (C.68) yields to (3.29)

- Replacing (C.73) into (C.72) yields to (3.30)